NTNU
Norwegian University of
Science and Technology

Micromechanical modeling of plasticity, damage and fracture in aluminium alloys

Vetle Espeseth

Master of Science in Mechanical Engineering	
Submission date:	June 2018
Supervisor:	Odd Sture Hopperstad, KT
Co-supervisor:	Tore Børvik, KT Lars Edvard Dæhli, KT

Norwegian University of Science and Technology
Department of Structural Engineering

Department of Structural Engineering
Faculty of Engineering
NTNU- Norwegian University of Science and Technology

ACCESSIBILITY	
OPEN	

MASTER THESIS 2018

SUBJECT AREA: Computational Mechanics	DATE: June 11, 2018	NO. OF PAGES: 20 + 154 + 27

TITLE:

Micromechanical modeling of plasticity, damage and fracture in aluminium alloys

Mikromekanisk modellering av plastisitet, skade og brudd i aluminiumslegeringer

BY:

Vetle Espeseth

SUMMARY:

A microstructure-based modeling framework for ductile damage and failure has been examined and validated with experiments for an AlMgSi aluminium alloy. A limited number of material tests has been used to calibrate a porous plasticity model and different fracture models.

The nucleation, growth, and coalescence of voids characterize the mechanisms of ductile damage and fracture. Simulations on an initially voided 3D micromechanical unit cell have been conducted to assess the growth phase and onset of coalescence. The ductility of the unit cell was found to decrease with increasing stress triaxiality. Furthermore, the stress-strain response of the unit cell was used to optimize the Gurson-Tvergaard model. In general, the softening predicted by this calibrated model was found to be too modest compared to experimental data. An examination on coalescence was also performed to assess the critical porosity level.

Strain localization analyses have been conducted to evaluate when the strain localizes into a narrow band, which is a frequent precursor to failure. An imperfection band approach has been used, where the band material was modeled by applying the Gurson-Tvergaard model optimized from both unit cells and experiments. Inadequate predictions of the global failure strain were obtained from the model calibrated from unit cells. The localization analysis was also utilized to calibrate the material parameters of the band material using the failure strain from a single smooth axisymmetric tensile specimen. This approach was found to give satisfactory results.

Numerical analyses of a pre-damaged plate subjected to a blast load were conducted to examine how the different calibrated failure criteria perform in a large-scale problem. Considerable differences were found between the different criteria. The calibration approach of using a smooth specimen test with the localization analysis provided the most convincing results. It is suggested that a purely microstructure-based modeling framework is ambitious.

RESPONSIBLE TEACHER: Odd Sture Hopperstad

SUPERVISOR(S): Tore Børvik og Lars Edvard Dæhli

CARRIED OUT AT: SIMLab, the Department of Structural Engineering, NTNU

Institutt for konstruksjonsteknikk
Fakultet for ingeniørvitenskap
NTNU- Norges teknisk- naturvitenskapelige universitet

TILGJENGELIGHET

ÅPEN

MASTEROPPGAVE 2018

FAGOMRÅDE:	DATO:	ANTALL SIDER:
Beregningsmekanikk	11. juni 2018	20 + 154 + 27

TITTEL:

Mikromekanisk modellering av plastisitet, skade og brudd i aluminiumslegeringer

Micromechanical modeling of plasticity, damage and fracture in aluminium alloys

UTFØRT AV:

Vetle Espeseth

SAMMENDRAG:

Et mikrostrukturbasert modelleringsramme for duktil skade og brudd har blitt undersøkt og validert med eksperimenter for en AlMgSi aluminiumslegering. Et begrenset antall materialtester har blitt brukt til å kalibrere en porøs plastisitetsmodell og forskjellige bruddmodeller.

Kjernedannelse, veksten og koalesering av hulrom karakteriserer mekanismer for duktil skade og brudd. Simuleringer på en 3D mikromekanisk enhetscelle med innledende hulrom har blitt utført for å vurdere vekstfasen og begynnelsen av koalesering. Duktiliteten til enhetscellen ble funnet å synke med økende spennings triaksialitet. Videre ble spenning-tøyningsresponsen til enhetscellen brukt til å optimalisere Gurson-Tvergaard modellen. Generelt viste det seg at mykningen predikert av denne kalibrerte modellen var for beskjeden sammenlignet med eksperimentelle data. En undersøkelse på koalesering ble også utført for å vurdere det kritiske porøsitetsnivået.

Tøyningslokaliseringsanalyser har blitt utført for å evaluere når tøyingen lokaliseres i et smalt band, som er en hyppig forløper til feil. En imperfeksjonsbåndstilnærming har blitt brukt, hvor båndmaterialet ble modellert ved å anvende Gurson-Tvergaard modellen optimalisert fra både enhetsceller og eksperimenter. Utilstrekkelige predikeringer av den globale bruddtøyningen ble oppnådd fra modellen kalibrert fra enhetsceller.Lokaliseringsanalysen ble også benyttet for å kalibrere materialparametrene til båndmaterialet ved å bruke bruddspenningen fra en enkelt glatt aksisymmetrisk strekkprøve. Denne tilnærmingen ble funnet å gi tilfredsstillende resultater.

Numeriske analyser av en for-skadet plate utsatt for en eksplosjonslast ble utført for å undersøke hvordan de forskjellige kalibrerte feilkriteriene utfører i et stortskala problem. Det ble funnet betydelige forskjeller mellom de ulike kriteriene. Kalibreringsmetoden ved bruk av et glatt prøvestykke med lokaliseringsanalysen ga de mest overbevisende resultatene. Det foreslås at et rent mikrostrukturbasert modelleringsramme er ambisiøst.

FAGLÆRER: Odd Sture Hopperstad

VEILEDER(E): Tore Børvik og Lars Edvard Dæhli

UTFØRT VED: SIMLab, Institutt for konstruksjonsteknikk, NTNU

Department of Structural Engineering
FACULTY OF ENGINEERING SCIENCE
NTNU – Norwegian University of Science and Technology

MASTER'S THESIS 2018

for

Vetle Espeseth

Micromechanical modeling of plasticity, damage and fracture in aluminium alloys

In the design of aluminium structures against failure, the material's strength and ductility are important factors. To design lightweight structures it is often necessary to use high strength aluminium alloys, while taking advantage of ductility in full. For aluminium alloys, increased strength often comes at the expense of ductility of the material. This can increase the risk of structural failure. Therefore, it is important to have good models for ductility of aluminium alloys under different load situations.

In this project, the main objective is to assess a novel microstructure-based modeling framework for ductile fracture in aluminium alloys. It involves modeling and simulation at multiple scales (nano-, micro-, and macroscales) and customized laboratory experiments for validation purposes.

Besides building a basic understanding of ductile fracture in aluminium alloys, the modeling framework enables designers and engineers to select the most suitable aluminium alloy for a given structure with less time-consuming and costly mechanical tests. The framework can also be used to tailor alloys with ideal strength and ductility of a given structure. This could pave the way for a completely new way to design aluminium structures.

The main tasks of the research project are as follows:

1. To perform a literature review on plasticity, damage and fracture in aluminium alloys, including experiments, modeling and simulations.
2. To conduct an experimental study to characterize the plastic, damage and fracture in an aluminium alloy AA6082 in selected tempers.
3. To perform unit cell analyses based on nano- and microstructure modeling in order to calibrate a porous plasticity model.
4. To use localization analyses to estimate the critical strain for a range of stress states.
5. To run simulations of material and component tests to assess the accuracy of the calibrated constitutive models.
6. To report the research work.

Supervisors: Odd Sture Hopperstad, Tore Børvik, Lars Edvard Dæhli (NTNU)

The report should be written in the style of a scientific article and submitted to the Department of Structural Engineering, NTNU, no later than June 11, 2018.

NTNU, January 15th, 2018

Odd Sture Hopperstad
Professor

Preface

This thesis was prepared at the Structural Impact Laboratory (SIMLab) at the Norwegian University of Science and Technology (NTNU) in the spring of 2018. The master thesis is the final requirement for the degree of Master of Science in Mechanical Engineering at NTNU and is weighted with 30 credits. Altogether, the duration was 20 weeks between January to June 2018.

The thesis was prepared under the supervision of Professor Odd Sture Hopperstad at the Department of Structural Engineering at NTNU. Tore Børvik and Lars Edvard Dæhli from the same department contributed as co-supervisors.

Acknowledgment

First, I would like to thank Senior Engineer Trond Auestad at the Department of Structural Engineering for helping with the material tests carried out. Also, thanks to Ph.D. Candidate Susanne Thomesen at the Department of Structural Engineering for providing Scanning Electron Microscope pictures of the fracture surface and Ph.D. Candidate Emil Christiansen at the Department of Physics for help with the preparation of the specimens for the Scanning Electron Microscope process.

I want to thank Ph.D. Candidate Sondre Bergo at the Department of Structural Engineering for providing me with a script for pre-processing the specimen geometry and Researcher Egil Fagerholt for his guidance in the software eCorr. I would also like to express my appreciation to Ph.D. Candidate Henrik Granum at the Department of Structural Engineering for providing me with FE-models for a blast problem on a pre-damaged plate.

Further, I wish to thank Associate Professor David Morin at the Department of Structural Engineering for the valuable guidance with the SIMLab Localization Module and SIMLab Metal Model. Your theoretical knowledge and feedback have been of great value in my work.

A large thanks to my co-supervisor Postdoctoral Researcher Lars Edvard Dæhli at the Department of Structural Engineering for the assistance and valuable insight to the unit cell analysis. Lars Edvard also provided me with Python script and Fortran code for the 3D unit cell model. I appreciate all the time and effort you have put into the guidance.

I wish to give my appreciation to Professor Tore Børvik at the Department of Structural Engineering for his role as co-supervisor. All guidance and advice you have provided through the weekly meetings have been very helpful, and it has been a pleasure working with you.

Last, but not least, I would like to express my very great appreciation to my main supervisor, Professor Odd Sture Hopperstad at the Department of Structural Engineering, for all the valuable guidance and support through the weekly meetings, e-mails, and

additional hours when needed. Your knowledge and enthusiasm have been highly inspirational. Thanks for the prompt response to my emails and always keeping your office door open. I never hesitated to ask you if something came up and I am grateful for having you as my supervisor.

Trondheim
June 10, 2018

Vetle

Vetle Espeseth

Abstract

A microstructure-based modeling framework for ductile damage and failure has been examined and validated with experiments for an AlMgSi aluminium alloy. A limited number of material tests has been used to calibrate a porous plasticity model and different fracture models.

The nucleation, growth, and coalescence of voids characterize the mechanisms of ductile damage and fracture. Simulations on an initially voided 3D micromechanical unit cell have been conducted to assess the growth phase and onset of coalescence. The ductility of the unit cell was found to decrease with increasing stress triaxiality. Furthermore, the stress-strain response of the unit cell was used to optimize the Gurson-Tvergaard model. In general, the softening predicted by this calibrated model was found to be too modest compared to experimental data. An examination on coalescence was also performed to assess the critical porosity level.

Strain localization analyses have been conducted to evaluate when the strain localizes into a narrow band, which is a frequent precursor to failure. An imperfection band approach has been used, where the band material was modeled by applying the Gurson-Tvergaard model optimized from both unit cells and experiments. Inadequate predictions of the global failure strain were obtained from the model calibrated from unit cells. The localization analysis was also utilized to calibrate the material parameters of the band material using the failure strain from a single smooth axisymmetric tensile specimen. This approach was found to give satisfactory results.

Numerical analyses of a pre-damaged plate subjected to a blast load were conducted to examine how the different calibrated failure criteria perform in a large-scale problem. Considerable differences were found between the different criteria. The calibration approach of using a smooth specimen test with the localization analysis provided the most convincing results. It is suggested that a purely microstructure-based modeling framework is ambitious.

Contents

Nomenclature

Abbreviations

CL	Cockcroft-Latham
DIC	Digital Image Correlation
E^2RT	Extended^2 Rice Tracey
ECL	Extended Cockcroft-Latham
FE	Finite Element
GC	Generalized Compression
GS	Generalized Shear
GT	Generalized Tension
GT	Gurson-Tvergaard
JC	Johnson-Cook
MJC	Modified Johnson-Cook
MPC	Multi-Point Constraint
PPM	Porous Plasticity Model
PSD	Particle Size Distribution
PST	Plane Strain Tension
RP	Rigid Point
RT	Room Temperature
RVE	Representative Volume Element
SEM	Scanning Electron Microscope
SLM	SIMLab Localization Modul
SMM	SIMLab Metal Model
SPPM	SIMLab Porous Plasticity Model
UC	Unit Cell
VM	Von Mises
VVF	Void Volume Fraction
WQ	Water Quenching

Greek Letters

α	A constant in Equation (7.2) with a numerical value close to 0.3
$\beta_1, \beta_2, \beta_3$	Normalized principal stress ratios
δ_{ij}	Kronecker delta
ε_{eng}	Engineering strain
ε_f	The global fracture strain
ε_{ij}, $\boldsymbol{\varepsilon}$	Strain tensor
$\varepsilon_{ij}^{'}$	Deviatoric part of the strain tensor
ε_{ij}^e, ε_{ij}^p	Elastic and plastic strain tensor
ε_{kk}, ε_v	Volumetric part of the strain tensor
ε_l, ε_{lu}	Logarithmic strain and logarithmic strain at necking
$\dot{\varepsilon}_{ij}$, $\dot{\boldsymbol{\varepsilon}}$	Strain rate tensor
$\dot{\varepsilon}_{ij}^e$, $\dot{\varepsilon}_{ij}^p$	Elastic and plastic strain rate tensor
$\dot{\varepsilon}_{kk}^p$, $\dot{\varepsilon}_v^p$	Plastic volumetric strain rate
ϕ	A positive homogeneous function (but a material parameter in Equation (2.30))
$\dot{\Phi}$	The rate form of the yield function
Φ, $\dot{\Phi}$	The yield function
$\dot{\lambda}$	The plastic parameter
ν	Poisson's ratio
ω	Damage parameter
ρ_g, ρ_s, ρ_t	The geometrically necessary dislocation density, the statically stored dislocation density, and the total dislocation density
ϕ_0, θ_0	Initial azimuthal angle and polar angle, Figure 2.10
θ_L	Lode angle
Θ	Temperature
Θ^*, Θ_r, Θ_m	The homologous temperature, ambient temperature, and melting temperature
$\Delta\sigma_d$	Net contribution from dislocation hardening to flow stress
σ_j	Stress tensor in integration point j
$\sigma_{0.2}$	0.2% proof stress
σ_0	Initial yield stress

σ_{eng}	Engineering stress
σ_{eq}, σ_{eq}^{VM}	Equivalent stress and the von Mises equivalent stress
σ_H	Hydrostatic part of the stress tensor
σ_{ij}, $\boldsymbol{\sigma}$	Stress tensor
$\sigma_{ij}^{'}$, $\boldsymbol{\sigma}^{'}$	Deviatoric part of the stress tensor
σ_I, σ_{II}, σ_{III}	Principal stress components. Note that $\sigma_I \geq \sigma_{II} \geq \sigma_{III}$
σ_i, σ_{ss}, σ_p	The intrinsic yield strength of pure aluminium, the solid solution hardening contribution, and the overall precipitation hardening contribution
σ_M	Flow stress of the matrix material
σ_{sat}	Saturation stress
σ_t	True/Cauchy stress
σ_y	Overall yield strength
$\dot{\sigma}_{ij}$	Stress rate tensor
Σ_{eq}^{VM}	Macroscopic equivalent von Mises stress
Σ_H	Hydrostatic part of the macroscopic stress tensor
Σ_{ij}, $\boldsymbol{\Sigma}$	Macroscopic stress tensor
$\Sigma_{ij}^{'}$, $\boldsymbol{\Sigma}^{'}$	Deviatoric part of the macroscopic stress tensor
Σ_I, Σ_{II}, Σ_{III}	The macroscopic principal stress components. Note that $\Sigma_I \geq \Sigma_{II} \geq \Sigma_{III}$
χ	Amplification factor in Equation (2.27)
ξ	Coordinate along **n** in the localization analysis
κ	Stress dependent function
ψ, κ_g, κ_{s1}, κ_{s2}	Model parameters in the Extended^2 Rice-Tracey fracture criterion
ψ_i	The normalized principal stress ratios in direction i

Roman Letters

a	The radius of the current cross-section
$\overline{A}^t$	Acoustic tensor in the localization analysis
A, A_0	Current and initial cross-section area
$A(p), A_n$	Nucleation rate function. Constant nucleation rate
$\mathbf{b}$	Magnitude of the Burgers vector
b	The exponential decay coefficient
ΔD_i	Boundary displacement of the unit cell face in direction i
$D_1, ..., D_6$	Model parameters in the modified Johnson-Cook fracture criterion
D_i, $D_{0,i}$	Current and initial diameter in direction i
$\boldsymbol{\mathfrak{D}}$	Plastic dissipation
e, e_Σ, e_f	Different errors
E	Young's modulus
E_{eq}^c	The critical macroscopic equivalent strain
E_{eq}^{VM}	Macroscopic equivalent von Mises strain
E_{ij}, $\boldsymbol{E}$	Macroscopic strain tensor
E_{ij}'	Deviatoric part of the macroscopic strain tensor
E_I, E_{II}, E_{III}	Macroscopic principal logarithmic strain
f	Porosity (void volume fraction)
f^*	Effective porosity (void volume fraction)
f_0	Initial porosity (void volume fraction)
f_c, f_f, f_u	Critical porosity, the porosity when the material loses its load-carrying capacity, and fitting parameter in Equation (2.49)
f_N, s_N, p_N	The total volume fraction of void nucleation particles, the associated standard deviation, and mean plastic strain for nucleation
$\dot{f}$	Rate of change in porosity
$\dot{f}_g$	Rate of change in porosity due to growth
$\dot{f}_n$	Rate of change in porosity due to nucleation of voids
$\dot{f}_s$	Rate of change in damage (porosity) due to softening in shear
$\mathbf{F}$	Deformation gradient
F	Tensile force
G	Shear modulus

I_σ	The first principal invariant of the stress tensor
J_2, J_3	The second and third deviatoric stress invariant
k_s	Magnitude of damage growth rate in pure shear
L	Lode parameter
L_{ij}, $\overline{L}_{ij}$	Velocity gradient field outside and inside the band material in the localization analysis
L_i	Length of side i in a unit cell
$\bar{L}$	Length of the sides of the 1/8 model of the unit cell
m	The Hershey exponent
m_i, $\mathbf{m}$	The parallel vector to the band in the localization analysis
M	Taylor factor
n_{int}, n_{els}	Number of integration points and number of elements
n_i, $\mathbf{n}$, $\mathbf{n}_0$	Current and initial normal vector to the band in the localization analysis
N_{SS}	Total number of stress states
p	Equivalent plastic strain
p_f	The plastic failure strain
$\dot{p}$	Equivalent plastic strain rate
$\dot{p}^*$, $\dot{p}_0$	Dimensionless plastic strain rate and a user-defined reference strain rate
$\bar{p}_f$	The plastic failure strain p_f for proportional loading
$\dot{P}_{ij}$, $\dot{\overline{P}}_{ij}$	Rate of the nominal stress tensor
C^{ep}_{ijkl}, $\overline{C}^{ep}_{ijkl}$	Elastic-plastic tangent modulus of the material outside and inside the band in the localization analysis
C^{t}_{ijkl}, $\overline{C}^{t}_{ijkl}$	Tangent modulus of the material outside and inside the band in the localization analysis
$P(t), P_r$	Pressure-time history and peak reflective pressure
q_1, q_2, q_3	Material parameters in the Gurson-Tvergaard model
$\dot{q}_i$, $\dot{\mathbf{q}}$	Rate of deformation non-uniformity
Q_i, C_i	Hardening parameters in Voce rule
$\dot{R}$	Rate of change in void radius
R	Radius of the void and the radius of the curvature of the neck
R_i	Radius of the void in direction i in the unit cell model

$\bar{R}$	Radius of the void for the 1/8 model of the unit cell
t	Time
t_+	The duration of the positive phase
T	Stress triaxiality ratio
ΔU_i, $\Delta \widetilde{U}_i$	The displacement component of the cell wall and the displacement component of a fictitious node in direction i
V_{RVE}	The volume of the RVE (and the volume of the void in the unit cell model)
$\mathbf{v}$	Global velocity field in the localization analysis
$\Delta\mathbf{v}$	Non-uniformity of the velocity field inside the band
V, V_f, V_M	Total volume of RVE, volume of the void and volume of the matrix material
V_j, V_{mat}	Volume associated with integration point j, and total material volume
w	Aspect ratio of void radius
w_Σ, w_f	Weight of error e_Σ and e_f
W_c, γ, ϕ	Model parameters in the Extended Cockcroft-Latham fracture criterion

1 | Introduction

Aluminium alloys are frequently used in structures due to their high energy absorption capabilities, excellent formability, and low weight. They also provide exceptional durability and low maintenance. It is often essential to use high strength alloys while fully taking advantage of the ductility when designing lightweight structures. However, increasing the strength of aluminium alloys comes at the expense of the ductility, enhancing the risk of severe damage and failure under deformation. This is why access to accurate and reliable material models for aluminium alloys is essential in a design process.

The mechanisms of ductile fracture are characterized by the nucleation, growth, and coalescence of voids [1]. These mechanisms are often complex and depend on a large variety of factors such as stress state, strain rate, material hardening, temperature, and the content, distribution, and shape of secondary particles and voids [2]. Consequently, a large number of mechanical tests are often required to calibrate material models adequately. These calibrations are often quite costly and time-consuming in a design process where it is crucial for the engineers to select the most suitable aluminium alloy for a given structure. A novel microstructure-based modeling framework might substitute some of these tests. This involves modeling and simulation at nano-, micro-, and macroscales. Besides making the design phase more time and cost efficient, such a framework provides a greater knowledge of the ductile failure processes that occur. Essentially, this permits the possibility to tailor alloys with ideal strength and ductility for a particular application, paving the way for an entirely new way to design aluminium structures.

The FractAl project [3] at the Norwegian University of Science and Technology received in 2016 a 24.6 MNOK FRIPRO Toppforsk grant to investigate new ways of designing aluminium structures against failure [4, 5]. The project aims to "enable design of both material and structure in an optimal combination without having to use time-consuming and expensive mechanical tests" [4]. The FRIPRO Toppforsk scheme of the Norwegian Research Council aims at developing more world-leading research environments in Norway [6]. This really emphasizes the interests of a microstructure-based modeling framework.

The work on ductile fracture is extensive, and a vast variety of models have been proposed in the literature the past decades. Two widely used ductile damage models are the Johnson-Cook criterion [7] and the Cockcroft-Latham criterion [8]. Gruben et al. [9] proposed an extended version of the latter criterion to access better control on the influence of the Lode parameter and stress triaxiality ratio. Experiments have shown that the stress state regarding these two parameters significantly influences the fracture strains [10]. Furthermore, these damage models in their original form are uncoupled, and the accumulated damage will not affect the load-carrying capacity of the material. Nor are they based on any physical mechanisms of ductile failure.

McClintock, in 1968, and Rice and Tracey the following year were the first to address an analytical description of void growth in a porous material. Gurson established in 1977 a constitutive model that accounted for the evolution of voids in a uniformly voided continuum during plastic deformation [11], thus providing a basic framework for porous plasticity models. Tvergaard later modified the Gurson model [12, 13] to obtain better agreements with numerical simulations on voided materials by making it more flexible. This model is commonly referred to as the Gurson-Tvergaard model and accounts only for the spherical growth of voids. Extensions to account for nucleation [14], coalescence [15] and shearing [16] of voids have been proposed in the literature. A vast variety of other improvements to the Gurson models also exist. Among others; the inclusion of material anisotropy [17, 18], void size effects [19], the effect of rate-dependent plasticity [20], kinematic hardening in the matrix material [21], and the influence of a non-quadratic yield surface [22].

The growth and coalescence of voids on a microscopic level are difficult to observe experimentally. In order to get a better understanding of these mechanisms, it is desirable to use micro-scale models. The finite element micromechanical unit cell approach has proven to be a powerful tool in the improvement of ductile fracture models ever since it was first introduced by Needleman [23] and Tvergaard [12, 13]. Furthermore, Dæhli et al. [24, 25] used the unit cell response in a recent study to calibrate the material parameters in the Gurson-Tvergaard model.

Another approach to ductile failure is the strain localization analysis. A frequent precursor to failure is the localization of strain in a narrow band [26, 27]. The theory of Hill [28] and MK-analysis [29] have been applied to predict ductile failure for sheet metals in plane stress, such as forming applications, for decades. Rice [30, 31] proposed in 1975 a more general framework on localization in a 3D continuum. Recent work performed by Morin et al. [32] has shown that the imperfection band approach of strain localization (See Section 2.3.1) provides similar results to the unit cell simulations, but with considerably less computational effort.

A nano-scale material model (NaMo) can be used to predict the strength and work hardening of tempered aluminium alloys [33, 34], which may entirely substitute expensive material tests in a design process. The foundation for these predictions is the chemical composition and thermal history. Several extensive studies have validated the model for the aluminium 6xxx-series in different tempers [34, 35]. Also, a solidification and homogenization microstructure model (Alstruc) that can estimate the particle and solute element content has been developed [36, 37, 38].

The objective of this thesis is to assess a microstructure-based modeling framework on ductile behavior and fracture of an aluminium alloy. This consists of performing unit cell analyses based on nano- and microstructure modeling to calibrate a porous plasticity model. Localization analysis will be used to predict the failure strain for various loads, and to calibrate different failure criteria.

The ultimate goal is a pure "bottom-up" approach which links the atomic scale to the macroscopic response through real mechanisms founded on physics and chemistry. Such an approach may use NaMo and Alstruc to predict the yield stress, isotropic hardening, and particle content. Unit cell analyses could be used to evaluate the growth and coalescence of voids, and localization analysis to predict the fracture strain. The gray, blue and red arrows in Figure 1.1 illustrate such an approach. The calibration is also done using experimental data on a smooth and various notched axisymmetric tensile specimens. The difference between the different methods will be discussed further.

In this thesis, experimental data of a cast and homogenized AlMgSi aluminium alloy is used [38, 39]. The yield stress and hardening parameters are determined from experiments. These variables, however, could have been determined numerically by NaMo. A 6082 alloy was initially intended for this work, but experiments showed a rather brittle fracture behavior, making this material unsuited for the objective herein. Chapter 7 addresses this alloy in greater details. The predictive capabilities of NaMo are also addressed in this chapter.

An overview is presented in the following.

Chapter 2 – Theory
This chapter explains the theory used. It includes relevant theory in the field of material mechanics, ductile failure processes, porous plasticity models, the unit cell analysis and the strain localization analysis.

Chapter 3 – Material and Experimental Study
Here, the AlMgSi aluminium alloy used for the majority of this thesis is examined. The particle content from ALSTRUC, material behavior and results from various tensile tests are examined. A mesh study on the finite element model for all the tensile specimens are also performed. The plastic strain, the stress triaxiality ratio and the Lode parameter along the cross-section elements are evaluated in the end.

Chapter 4 – Calibration of the GT Model
Unit cell simulations are conducted to examine the growth and coalescence of voids. The material parameters in the Gurson-Tvergaard model are calibrated using both a unit cell approach and experimental data. A parametric study is performed to evaluate how different parameters affect the calibration process.

Chapter 5 – Numerical Approach to Fracture
This chapter assesses material failure using the unit cell and the strain localization analysis. A methodology that can calibrate all material parameters using a single smooth tensile specimen is presented at the end of this chapter.

Chapter 6 – Case Study - Blast Load
This chapter will use the failure models in Chapter 5 to predict crack growth in a pre-damaged plate subjected to a blast load. No experiments have been carried out, so the aim is only to assess the performance of the different failure models in a numerical simulation.

Chapter 7 – Aluminium Alloy 6082 T6
The work done on the 6082 aluminum alloy is presented in this chapter. This includes prediction from NAMO, an investigation on the actual geometry, and SEM fractographies of the failure surfaces.

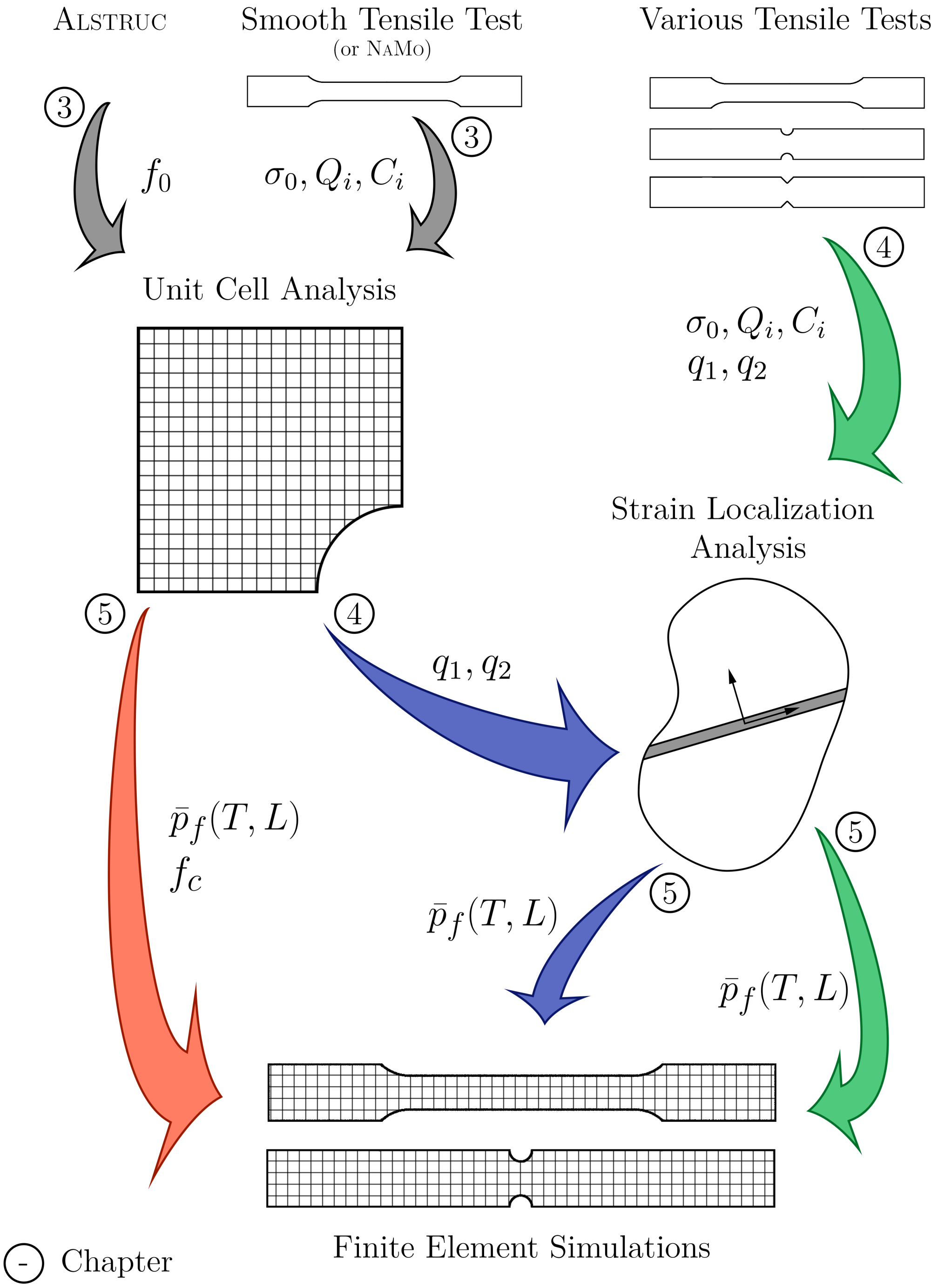

Figure 1.1: *An overview of the different approaches taken in this thesis. The numbers inside the circles correspond to the chapter which covers the approach.*

2 | Theory

This chapter addresses relevant theory for this thesis. Some fundamental theories in the field of material mechanics are presented first. This includes the constitute relations in classical plasticity, experimental measurements of stress and strain, and a section on important stress invariants for damage in porous metals. Then, the damage and failure processes in ductile materials are addressed, followed by theories in ductile damage and porous plasticity. Most of these sections are based on Hopperstad and Børvik [26, 40], Anderson [1], and on a review paper by Benzerga and Leblond [10].

The fundamental concepts of the 3D unit cell model are presented in Section 2.2, which is based on the work of Dæhli et al. [24, 25]. Lastly, an overview on the theory of localization of deformation for a 3D continuum is addressed.

2.1 Material Mechanics

2.1.1 Constitutive Relations

Various constitutive relations are used to describe the behavior of materials. This section presents a classical elastic-plastic formulation. The theory of plasticity often neglects the effects of voids, and the equations in this section govern the bulk material response. Rate and thermal effects will be neglected. It should be mentioned that the formulation presented in this section is restricted to small deformations. It can, however, easily be extended to a hypoelastic-plastic formulation, which is adopted in most finite element codes. In the theory of plasticity, it is accepted to additively split the strain rate tensor into an elastic and a plastic part

$$\dot{\varepsilon}_{ij} = \dot{\varepsilon}^{e}_{ij} + \dot{\varepsilon}^{p}_{ij} \tag{2.1}$$

where $\dot{\varepsilon}^{e}_{ij}$ and $\dot{\varepsilon}^{p}_{ij}$ represent the elastic and plastic part, respectively. The generalized Hooke's law governs the elastic response. The material response is assumed to be isotropic in this study. Thus, the rate form of the generalized Hooke's law is given by

$$\dot{\sigma}_{ij} = \frac{E}{1+\nu}\dot{\varepsilon}'^{e}_{ij} + \frac{E}{3(1-2\nu)}\dot{\varepsilon}^{e}_{kk}\delta_{ij} \tag{2.2}$$

where E is the Young's modulus and ν is the Poisson's ratio. The deviatoric and volumetric parts of the elastic strain rate tensor are denoted $\dot{\varepsilon}'^{e}_{ij}$ and $\dot{\varepsilon}^{e}_{kk}$, respectively. The Kronecker delta, δ_{ij}, equals 1 for $i = j$ and 0 otherwise. A yield criterion restrains the stress, which states that

$$\Phi(\boldsymbol{\sigma}, p) = \phi\left(\boldsymbol{\sigma}\right) - \sigma_y(p) \leq 0 \tag{2.3}$$

Here, $\phi\left(\boldsymbol{\sigma}\right) = \sigma_{eq}$ is the equivalent stress and $\sigma_y(p)$ is the flow stress of the material. Elastic domain is indicated by $\Phi < 0$, while $\Phi > 0$ is inadmissible. Plastic deformation occurs only for $\Phi = 0$. A two-term Voce rule can be used to describe the isotropic hardening

$$\sigma_y(p) = \sigma_0 + \sum_{i=1}^{2} Q_i\left(1 - \exp(-C_i p)\right) \tag{2.4}$$

where, σ_0 is the initial yield stress and p is the accumulated plastic strain. The material constants σ_0, Q_i, and C_i are normally fitted from experiments. Section 7.4 shows how these parameters can be obtained numerically using the nanostructure model NaMo.

A high-exponent yield criterion, known as the Hershey criterion, can be used to define the equivalent stress in Equation (2.3).

$$\sigma_{eq} = \left(\frac{1}{2}\left[\left|\sigma_I - \sigma_{II}\right|^m + \left|\sigma_{II} - \sigma_{III}\right|^m + \left|\sigma_{III} - \sigma_I\right|^m\right]\right)^{\frac{1}{m}} \tag{2.5}$$

The exponent $m \geq 1$ determines the curvature of the yield surface. In the special case of $m = 2$, this equation takes the form of the von Mises equivalent stress, which is represented by a quadratic yield surface. Plasticity that considers the von Mises equivalent stress is frequently referred to as J2 plasticity. Hosford [41] proposed an exponent of $m = 8$ for face-centered cubic (FCC) materials, such as many aluminium alloys. Consequently, a non-quadratic yield surface is obtained, as shown in Figure 2.1. A cylinder represents the surface in the case of $m = 2$, making yielding unaffected by the third deviatoric stress invariant, J_3. The opposite applies to a non-quadratic yield surface. A user-defined subroutine from the library SIMLab Metal Model (SMM) [42] has been used to include the Hershey yield criterion in the finite element simulations.

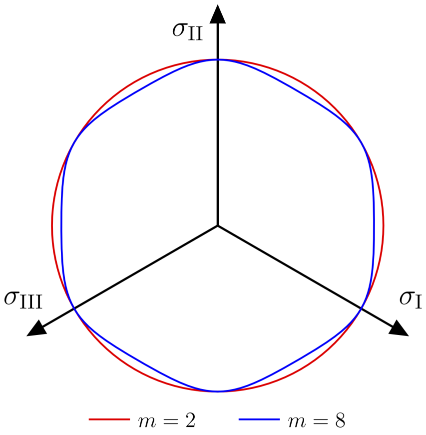

Figure 2.1: *Plot of the yield surface for* $m = 2$ *and* $m = 8$ *in the* Π*-plane. The figure is taken from Dæhli et al. [25].*

Furthermore, the plastic strain rate tensor is governed by the associated flow rule, defined as

$$\dot{\varepsilon}_{ij}^{p} = \dot{\lambda}\frac{\partial \Phi}{\partial \sigma_{ij}} \tag{2.6}$$

The flow rule ensures non-negative dissipation. The plastic parameter, $\dot{\lambda}$, is a non-negative scalar ($\dot{\lambda} \geq 0$) which is determined based on the consistency condition. This condition states that the stress must stay at the yield surface during plastic deformation. Mathematically, this is expressed as $\dot{\lambda}\dot{\Phi} = 0$, where $\dot{\Phi}$ denotes the rate form of the yield surface. The accumulated plastic strain is found from the rate of plastic dissipation, defined as $\mathfrak{D} = \dot{\varepsilon}_{ij}^{p}\sigma_{ij} = \dot{p}\sigma_{eq}$. It follows that

$$p = \int_0^t \dot{p}dt, \qquad \dot{p} \equiv \dot{\lambda} = \frac{\dot{\varepsilon}_{ij}^{p}\sigma_{ij}}{\sigma_{eq}} \tag{2.7}$$

It can easily be shown that in the special case of von Mises equivalent stress, $\dot{p}$ equals to [40]

$$\dot{p} = \sqrt{\frac{2}{3}\dot{\varepsilon}_{ij}^{p}\dot{\varepsilon}_{ij}^{p}} \tag{2.8}$$

2.1.2 Experimental Measurements

Section 3 presents tensile tests on different axisymmetric specimens. Some experimental measurements used later will be defined here. The true, or Cauchy, stress σ_t and logarithmic strain ε_l are calculated as

$$\sigma_t = \frac{F}{A}, \qquad \varepsilon_l = \ln\frac{A_0}{A} \tag{2.9}$$

The applied force is denoted F, while A_0 and A are the initial and current cross-section area, respectively. Under the assumption of elliptical cross-section, these are defined as

$$A_0 = \frac{\pi}{4}D_{0,x}D_{0,y}, \qquad A = \frac{\pi}{4}D_xD_y \tag{2.10}$$

where $D_{0,i}$ and D_i are the initial and current diameter in the two perpendicular directions x and y. It is assumed that the initial cross-section area is spherical, hence $D_{0,x} = D_{0,y} = D_0$. The stress and strain might also be expressed with respect to the initial configuration. These are defined as the engineering stress and engineering strain and are given here as

$$\sigma_{eng} = \frac{F}{A_0}, \qquad \varepsilon_{eng} = \frac{A_0}{A} - 1 \tag{2.11}$$

It follows from Equation (2.9) that $\sigma_t = \sigma_{eng}(1 + \varepsilon_{eng})$ and $\varepsilon_l = \ln(1 + \varepsilon_{eng})$. In a uniaxial tensile state, the plastic strain is defined as

$$p = \varepsilon^p = \varepsilon - \varepsilon^e = \varepsilon - \frac{\sigma}{E} \tag{2.12}$$

where ε is the total strain, $\varepsilon^e = \sigma/E$ is the elastic strain, and E is the Young's modulus. In a uniaxial stress state, $\sigma_{eq} = \sigma$, where σ is the stress in longitudinal direction. This is true for an axisymmetric smooth tensile specimen. At large plastic strains, a neck will form in the gauge section of the specimen. This neck introduces a complex stress state where the equivalent stress no longer equals to the stress in the longitudinal direction due to radial and transverse stress components. In contrast, owing the fact that the strain is determined by the minimum cross-section area in Equation (2.9), the plastic strain p can be found using Equation (2.12), even after necking. The point of necking is defined as the point when maximum force is applied, i.e., $dF = 0$, or equivalently, $d\sigma_{eng} = 0$.

Since the formation of radial and transverse stress components will increase the longitudinal stress required for plastic flow, the stress measurement needs to be corrected. Under certain assumption, defined in [43], the equivalent stress after necking can be estimated using the Bridgman correction

$$\sigma_{eq} = \frac{\sigma_t}{\left(1 + \frac{R}{a}\right)\left[\ln\left(1 + \frac{1}{2}\frac{a}{R}\right)\right]} \tag{2.13}$$

Here, R is the radius of the curvature of the neck and a is the radius of the current cross-section of the specimen. Le Roy et al. [44] proposed an empirical model for the a/R-ratio, given as

$$\frac{a}{R} = 1.1\left(p - \varepsilon_{lu}^{p}\right), \qquad p > \varepsilon_{lu}^{p} \tag{2.14}$$

where ε_{lu}^{p} is the logarithmic plastic strain at necking.

It should be emphasized that the measurements in Equation (2.9) and (2.11) are only physical meaningful in the case of a smooth specimen before a neck forms. In the case of the notched specimens, the stresses and strains are not uniform throughout the cross-section. Thus, these equations are only valid in an average sense. However, they prove to be useful when comparing numerical simulations with experiments, and will therefore be adopted here as well.

2.1.3 Stress Invariants

Three important stress invariants can describe the stress state in an isotropic material, namely the von Mises equivalent stress σ_{eq}^{VM}, the stress triaxiality ratio T and the Lode parameter L. Experiments have shown that these invariants play a crucial role in describing damage evolution and failure [10]. Studying different combinations of the stress triaxiality and Lode parameter will give vital insight into the material response upon ductile failure. Thus, these invariants will be used to impose various proportional stress states in the unit cell and the localization analysis. They are also important factors in different fracture criteria, as will be explained later in Section 2.1.5.

An arbitrary stress state $\boldsymbol{\sigma}$ is plotted in the Haigh-Westergaard space in Figure 2.2a. The Cauchy stress tensor is divided into a deviatoric and a hydrostatic part by the following relation

$$\sigma_{ij} = \sigma_{ij}^{'} + \sigma_H \delta_{ij}, \qquad \sigma_H = \frac{1}{3}\sigma_{kk} = \frac{1}{3}(\sigma_I + \sigma_{II} + \sigma_{III}) \tag{2.15}$$

where $\sigma_{ij}^{'}$ is the deviatoric stress tensor and σ_H is the hydrostatic stress. Moreover, $\sigma_I \geq \sigma_{II} \geq \sigma_{III}$ are the principal stresses. The von Mises equivalent stress, which is the first stress invariant to be presented, is given by

$$\sigma_{eq}^{VM} = \sqrt{3J_2} = \sqrt{\frac{3}{2}\sigma_{ij}^{'}\sigma_{ij}^{'}} \tag{2.16}$$

This relation is equivalent with Equation (2.5) for $m = 2$. If nothing else is stated, σ_{eq} is defined as the von Mises equivalent stress. The second principal invariant of $\boldsymbol{\sigma}'$, J_2, is defined as

$$J_2 = \frac{1}{2}\sigma'_{ij}\sigma'_{ij} = \frac{1}{2}\left[(\sigma_I - \sigma_H)^2 + (\sigma_{II} - \sigma_H)^2 + (\sigma_{III} - \sigma_H)^2\right] \tag{2.17}$$

Further, the ratio of the hydrostatic stress to the von Mises equivalent stress expresses the stress triaxiality T. Hence, T is a non-dimensional measurement defined by the following equation

$$T \equiv \frac{\sigma_H}{\sigma_{eq}^{VM}} = \frac{I_\sigma}{3\sqrt{3J_2}} \tag{2.18}$$

The effect of stress triaxiality on ductile fracture is strongly evidenced by experiments [10, 45, 46]. The higher the stress triaxiality, the lower the fracture strain. This is mainly because the stress triaxiality is crucial for the growth of voids. Marini et al. [47] reported that the fracture strain decreased exponentially with increasing triaxiality ratio. Moreover, the void growth increased exponentially with T, which corresponds well with predictions from unit cell simulations. The stress triaxiality can be systematically varied over a range of specimen geometries, covering most practical applications. Smooth and notched axisymmetric tensile specimens, plane strain specimens and shear specimens are commonly used for this purpose. Also, cracked specimens may be used to obtain high triaxialities.

While the stress triaxiality has an important role on the ductility, studies show that the Lode parameter L, which is characterized by the deviatoric stress state, also influences the failure strain. This parameter is commonly expressed as

$$L = \frac{2\sigma_{II} - \sigma_I - \sigma_{III}}{\sigma_I - \sigma_{III}} \tag{2.19}$$

This effect has, among others, been demonstrated by Bao and Wierzbicki [48], and Barsoum and Faleskog [49]. It has been reported that the effect of the Lode parameter is mainly prominent in the lower range of stress triaxialities, where the ductility is found to be lower in shear dominated stress states than in axisymmetric stress states.

The same invariant might be expressed in terms of the angle θ_L between the deviatoric stress tensor $\boldsymbol{\sigma}'$ and the main principal stress direction σ_I in the Π-plane. This is illustrated in Figure 2.2b. The Lode angle is defined as [40]

$$\cos 3\theta_L \equiv \frac{J_3}{2}\left(\frac{3}{J_2}\right)^{\frac{3}{2}} = \frac{27J_3}{2\sigma_{eq}^3} \tag{2.20}$$

where $J_3 = \det \boldsymbol{\sigma}'$ is the third principal invariant of the deviatoric stress tensor. The

Lode angle ranges from $0 \leq \theta_L \leq \frac{\pi}{3}$. A relation between the Lode parameter and Lode angle is given by the equation

$$L = \sqrt{3} \tan \left(\theta_L - \frac{\pi}{6} \right) \tag{2.21}$$

The Lode parameter is defined such that $L = -1$, 0 and 1 correspond to $\theta_L = 0°$, 30° and 60°, respectively. These values represent the states of generalized tension (GT), generalized shear (GS) and generalized compression (GC) in the same order as above. Figure 2.2b illustrates how these states relate to the Π-plane. From the relation presented above, one can conclude that the Lode parameter is not affected by the hydrostatic stress. Thus, it is exclusively related to the deviatoric stress state.

Finally, the ordered principal stresses can be related to these invariant by decomposing the stress tensor into a deviatoric and hydrostatic part [40]

$$\begin{aligned} \left\{ \begin{matrix} \sigma_I \\ \sigma_{II} \\ \sigma_{III} \end{matrix} \right\} &= \frac{2}{3} \left\{ \begin{matrix} \cos\left(\theta_L\right) \\ \cos\left(\frac{2\pi}{3} - \theta_L\right) \\ \cos\left(\frac{2\pi}{3} + \theta_L\right) \end{matrix} \right\} \sigma_{eq}^{VM} + \sigma_H \left\{ \begin{matrix} 1 \\ 1 \\ 1 \end{matrix} \right\} \\ &= \sigma_{eq}^{VM} \left(\frac{2}{3} \left\{ \begin{matrix} \cos\left(\theta_L\right) \\ \cos\left(\frac{2\pi}{3} - \theta_L\right) \\ \cos\left(\frac{2\pi}{3} + \theta_L\right) \end{matrix} \right\} + T \left\{ \begin{matrix} 1 \\ 1 \\ 1 \end{matrix} \right\} \right) \end{aligned} \tag{2.22}$$

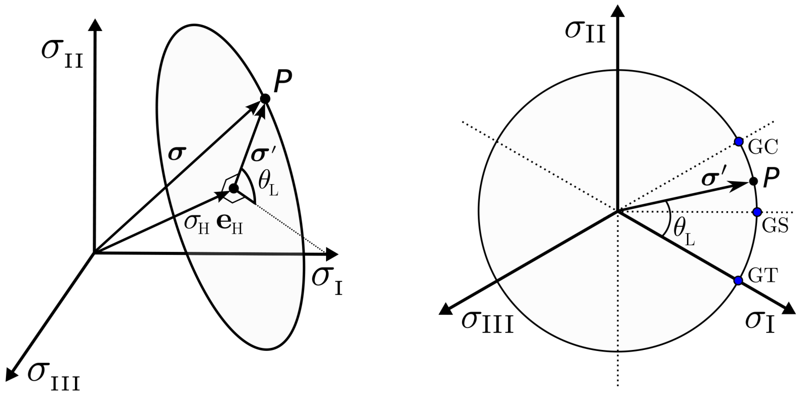

(a) *Haigh-Westergaard space* ***(b)*** Π*-plane*

Figure 2.2: *(a) An illustration of the stress tensor $\boldsymbol{\sigma}$ and its components (σ_H and $\boldsymbol{\sigma}'$) in the deviatoric space, commonly known as the Haigh-Westergaard space. (b) The principal stress tensor $\boldsymbol{\sigma}'$ and the deviatoric angle θ_L plotted in the* Π*-plane. The case of generalized tension (GT), generalized shear (GS) and generalized compression (GC) are also marked in the figure. The illustration is taken from Dæhli et al. [25].*

2.1.4 Damage and Failure in Ductile Metals

Figure 2.3 illustrates the three most common fracture micromechanisms in metals and alloys; intergranular fracture, cleavage fracture, and ductile fracture [1]. Cracks will under normal circumstances not form and propagate along the grain boundaries, as shown in Figure 2.3a. Cleavage, which is defined as rapid crack propagation along particular crystallographic planes, is generally associated with brittle materials. This process is shown in Figure 2.3b. The latter case, Figure 2.3c, is associated with ductile materials, such as many aluminium alloys. Three distinct processes identify the main mechanisms governing this failure behavior [1]; void nucleation, growth, and coalescence. Figure 2.4 illustrates these processes.

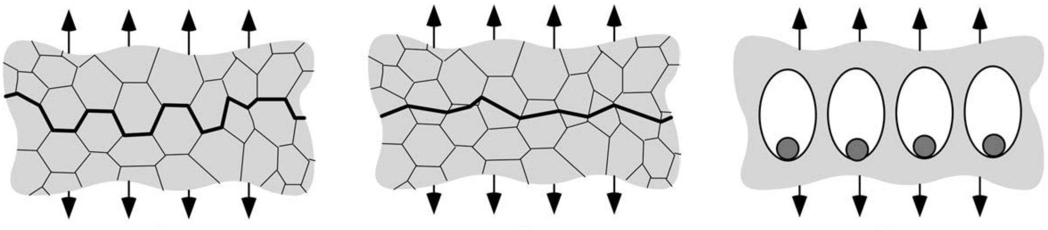

(a) *Intergranular fracture* ***(b)*** *Cleavage fracture* ***(c)*** *Ductile fracture*

Figure 2.3: *The three mechanisms of fracture. From Anderson [1].*

Void nucleation is associated with the formation of free surface at a second-phase particle or inclusion. This process is illustrated in Figure 2.4a and 2.4b. Voids will nucleate when the stress on particles is sufficient to induce particle cracking or decohesion of the material-particle bond. Many factors govern these processes. For instance, the size and shape of the particles are important. Decohesion occurs more readily for large particles than small particles since they contain more surface defects. Moreover, particle cracking is more prominent for a matrix material with a higher yield stress and hardening exponents. Larger particles are also often more likely to crack since they normally contain more defects [1]. The stress triaxiality plays an important role, where higher triaxiality tends to promote decohesion. Void nucleation is often the critical step when there is a strong bond between the particles and the bulk material, and fracture occurs shortly after. In the cases where nucleation occurs with ease, growth and coalescence are the governing mechanisms. Microscopic voids may also already be induced to the material due to the manufacturing process. There exist numerous models on void nucleation. However, this thesis will mainly focus on the growth and coalescence of voids.

Voids will continue to grow due to plastic strain and hydrostatic stress. Eventually, coalescence will occur. These processes are illustrated in Figure 2.4c – 2.4f. The co-

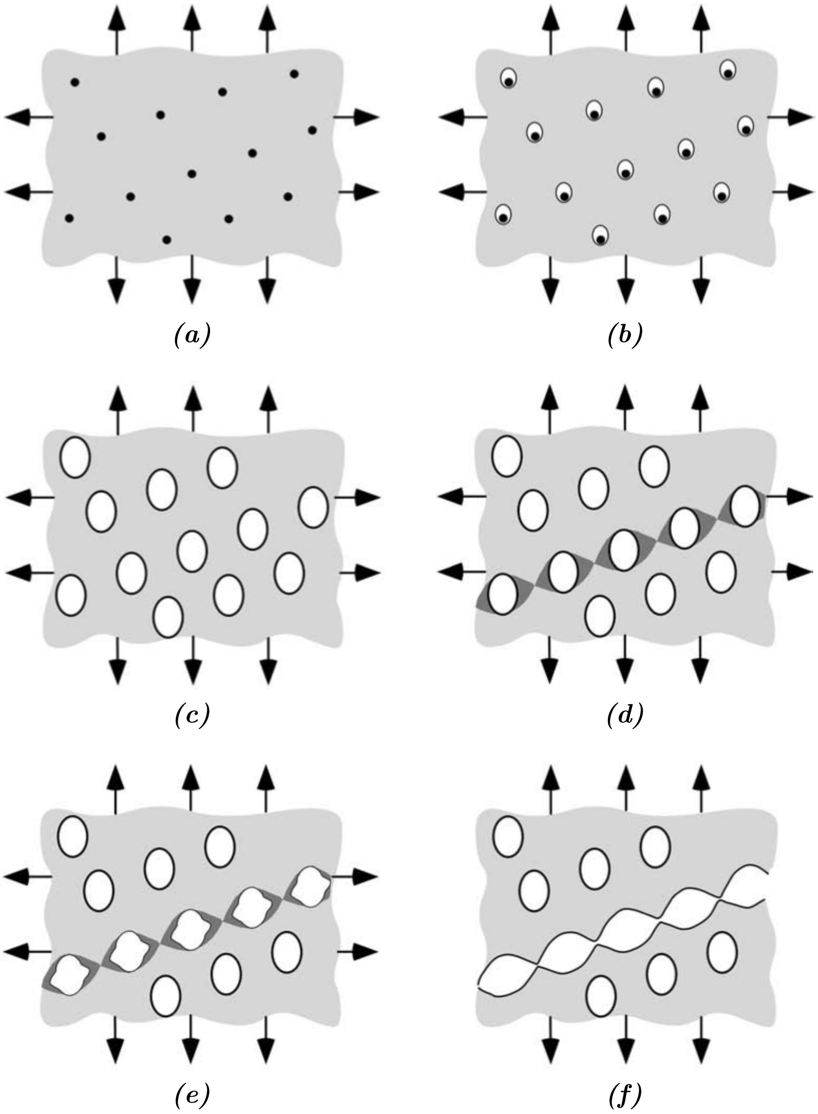

Figure 2.4: *Void nucleation, growth, and coalescence in ductile materials. (a) inclusions in a ductile matrix, (b) void nucleation, (c) void growth, (d) strain localization between voids, (e) necking between voids, and (f) void coalescence and fracture. From Anderson [1].*

alescence of voids indicates the end of the material lifespan, and fracture occurs soon after. Void growth is strongly dependent on the stress state, and the stress triaxiality introduced in Section 2.1.3 plays a vital role. The deviatoric stress state, represented by the Lode parameter, also plays an important role on the damage evolution in ductile materials, especially at low stress triaxialities. The coalescence can be divided into three main modes [10]; internal necking, void-sheeting, and necklace coalescence. Internal necking is the most common coalescence mode and is defined by the necking down of the inter-void ligament. Void-sheeting and necklace coalescence are more favorable at low triaxiality ratios.

2.1.5 Failure Criteria and Ductile Damage Models

The physical damage and failure mechanisms described in Section 2.1.4 must be characterized by some ductile damage model and failure criteria to predict material failure accurately. The prediction of failure is of particular importance in problems exhibiting large plastic deformations where the energy absorption is of interest. Some relevant applications are car bumper systems and protective structures. The literature presents numerous damage modeling approaches. They can be formulated either coupled or uncoupled to the constitutive relations of the material.

An uncoupled damage model is convenient due to the simple identification of the damage parameters. Here, the damage variable ω, which is used to keep a measure on the accumulated damage during deformation, evolves as a function of the stress state and plastic strain. Failure is assumed to occur when the damage variable reaches a critical value. An uncoupled approach does not, however, integrate the damage variable into the constitutive formulation. Consequently, the damage does not affect the material response. A coupled damage model, on the other hand, will link the damage to the material response. If the damage evolution exceeds the work hardening, strain softening occurs. Thus, the damage is related to material degradation, making coupled damage models more physical trustworthy, but also harder to calibrate.

Damage models may be divided into three categories [26]; (1) criteria defined by a fracture surface, (2) stress-based criteria, and (3) criteria driven by plastic straining but amplified by a factor that accounts for the stress state. As discussed in Section 2.1.3, ductile damage and failure are both dependent on the stress triaxiality T and the Lode parameter L. Hence, a criterion should depend on these two invariants in order to prescribe damage in a suitable way. Many traditional ductile damage models do not take the influence of the Lode parameter into account, making them only suitable for the application they are calibrated to, but too simple to accurately describe the failure of material for a wide range of loading conditions.

Many finite element codes use an accumulation rule to account for the damage. The first category follows this. A failure surface $\bar{p}_f = \bar{p}_f(T, L)$ is assumed to exist for proportional stress paths with constant Lode parameter and stress triaxiality. The damage is accumulated by the following relation to account for non-proportional loading,

$$\omega = \int_0^p \frac{dp}{\bar{p}_f(T, L)} \tag{2.23}$$

Here, p is the accumulated plastic strain and $\bar{p}_f$ is the plastic failure strain obtained under proportional loading. Fracture is normally assumed to occur when $\omega = 1$. Category (2) and (3) can be represented by a fracture surface as well under the assumption of proportional loading.

This section will examine different uncoupled approaches of defining damage. Three well-known models will be presented along with some extensions proposed in the literature to increase versatility. Section 2.1.6 will address a porous plasticity model, more precisely the Gurson-Tvergaard model. This model is a special branch of coupled damage models, which couples the damage through physical mechanisms.

Johnson-Cook Fracture Model

The Johnson-Cook (JC) fracture model [7] is a particularly important uncoupled fracture model that also accounts for the effects of rate dependency and temperature. It is defined as a fracture surface, putting it into category (1). This model does not account for the Lode dependency in its original form. The modified Johnson-Cook (MJC) fracture model is obtained by introducing the Lode angle into the Johnson-Cook equation [26] and is defined as

$$\bar{p}_f(T, \theta_L, \dot{p}, \Theta) = \left[D_1 + D_2 \exp\left(D_3 T\right)\right]\left(1 + D_4 \ln(\dot{p}^*)\right)\left(1 + D_5 \Theta^*\right)\left[1 - D_6 \kappa(\theta_L)\right] \tag{2.24}$$

where $D_1, ..., D_6$ are model constants. The dimensionless strain rate $\dot{p}^*$ and homologous temperature Θ^* are defined as

$$\dot{p}^* = \frac{\dot{p}}{\dot{p}_0}, \qquad \Theta^* = \frac{\Theta - \Theta_r}{\Theta_m - \Theta_r} \tag{2.25}$$

Here, $\dot{p}_0$ is a user-defined reference strain rate, Θ_r is the ambient temperature and Θ_m is the melting temperature of the material. In the case of quasi-static loading under constant temperature, D_4 and D_5 can be set to zero without loss of accuracy since $\dot{p} \approx \dot{p}_0$ and $\Theta = \Theta_r$. Furthermore, the stress-dependent function $\kappa(\theta_L)$ is defined as [16]

$$\kappa(\theta_L) \equiv 1 - \cos^2\left(3\theta_L\right), \qquad 0 \leq \theta_L \leq \frac{\pi}{3} \tag{2.26}$$

where θ_L is the Lode angle. The last factor in Equation (2.24) will reduce the fracture strain $\bar{p}_f$ for generalized shear, while keeping the case of generalized tension and compression unaltered. Note that $0 \leq D_6 \leq 1$ in order to avoid negative $\bar{p}_f$. It should be emphasized that the model presented in Equation (2.24) is symmetric about $L = 0$, which is generally not the case.

The Cockcroft-Latham Failure Criterion

Approach (3) assumes that the damage evolution is driven by plastic straining, but amplified by a factor $\chi = \chi(\boldsymbol{\sigma})$ which accounts for the stress state. Thus, a general damage evolution rule can be formulated by

$$\omega = \int_0^p \chi(\boldsymbol{\sigma}) dp \tag{2.27}$$

Failure is normally assumed to occur when $\omega = 1$.

The Cockcroft-Latham (CL) criterion [8] is a simple phenomenological one-parameter model which states that the damage parameter only depends on plastic straining and stress state through the maximum principal stress

$$\omega = \frac{1}{W_C} \int_0^p \max(\sigma_I, 0) dp \tag{2.28}$$

Calibration of W_C, which is the only model parameter, is done from a single tensile test. The Cockcroft-Latham criterion can be expressed by the stress triaxiality, the Lode angle and the von Mises equivalent stress by substituting σ_I with the first component in Equation (2.22)

$$\omega = \frac{1}{W_C} \int_0^p \max\left(T + \frac{2}{3}\cos(\theta_L), 0\right) \sigma_{eq} dp \tag{2.29}$$

Even though the Cockcroft-Latham criterion can display some effects of the triaxiality ratio and Lode parameter, these effects are only implicit and can not appropriately describe the trends seen in experiments. A more versatile damage model is the extended Cockcroft-Latham (ECL) criterion proposed by Gruben et al. [9], which defines the damage parameter as

$$\omega = \frac{1}{W_C} \int_0^p \max\left(\phi \frac{\sigma_I}{\sigma_{eq}} + (1-\phi)\left(\frac{\sigma_I - \sigma_{III}}{\sigma_{eq}}\right), 0\right)^{\gamma} \sigma_{eq} dp \tag{2.30}$$

This model consists of two additional model parameters, $0 \leq \phi \leq 1$ and $\gamma \geq 0$. Note that the extended Cockcroft-Latham reduces to the original criterion by taking $\phi = \gamma = 1$.

A fracture surface $\bar{p}_f(T, L)$ can be obtained from the extended Cockcroft-Latham criterion by assuming proportional loading. Failure occurs when $\omega = 1$, thus

$$\omega = \frac{1}{W_C} \int_0^{p_f} \mathfrak{H} \sigma_{eq} dp = 1 \tag{2.31}$$

where

$$\mathfrak{H} = \mathfrak{H}(\sigma_I, \sigma_{III}, \sigma_{eq}) = \max\left(\phi\frac{\sigma_I}{\sigma_{eq}} + (1-\phi)\left(\frac{\sigma_I - \sigma_{III}}{\sigma_{eq}}\right), 0\right)^{\gamma} \tag{2.32}$$

It can easily be shown that $\mathfrak{H}$ depends only on the triaxiality ratio and Lode parameter by using Equation (2.22). Thus $\mathfrak{H} = \mathfrak{H}(T, L)$. Consequently, $\mathfrak{H}$ is a constant function in the case of proportional loading. Assuming the Voce hardening in Equation (2.4), Equation (2.31) becomes

$$\frac{W_c}{\mathfrak{H}(T,L)} = \sigma_0 \bar{p}_f + \sum_{i=1}^{2} Q_i \left(\bar{p}_f + \frac{1}{C_i}\left(\exp(-C_i\bar{p}_f) - 1\right)\right) \tag{2.33}$$

The fracture surface $\bar{p}_f(T, L)$ can be calculated numerically from Equation (2.33) for a suiting set of model parameters.

The Rice-Tracey Criterion

Rice and Tracey proposed in 1969 an uncoupled fracture criterion that describes the growth of a spherical void in an infinite medium [50]. The normalized growth rate of the radius R is defined by

$$\frac{\dot{R}}{R} = \kappa_g \exp\left(\psi T\right)\dot{\varepsilon}^p \tag{2.34}$$

where κ_g and ψ are constants. Theoretically, these equal to 0.283 and 1.5, but might also be fitted from experiments. Fracture is assumed to occur when the ratio $\dot{R}/R$ reaches a critical limit. Marini et al. [47] reported the same exponential growth. Rousselier [51] expressed the Rice-Tracey criterion in terms of the void volume fraction f in the following way

$$\dot{f} = 3\kappa_g f(1-f)\exp\left(\psi T\right)\dot{\varepsilon}^p \tag{2.35}$$

In order to account for softening in shear-dominated stress states for low stress triaxiality ratios, an additional term, $\kappa_{s1}\omega_{s1}(L) f\dot{\varepsilon}^p$, can be added to the growth rate $\dot{f}$ (see Gruben et al. [9]). This way, a Lode dependency can be added to the problem. Moreover, Morin [52] proposed to add a third term to account for the void distortion, consequently tilting the failure surface. The new criterion will be referred to as the extended^2 Rice-Tracey model (E^{2}RT) and defines the growth rate as

$$\dot{f} = 3\kappa_g f(1-f)\exp\left(\psi T\right)\dot{\varepsilon}^p + \kappa_{s1}\omega_{s1}(L) f\dot{\varepsilon}^p + \kappa_{s2}\omega_{s2}(L) f\dot{\varepsilon}^p \tag{2.36}$$

where κ_{s1} and κ_{s2} are additional fitting parameters. The two functions $\omega_{s1}(L)$ and

$\omega_{s2}(L)$ are defined here as

$$\omega_{s1} = 1 - \frac{(9L - L^3)^2}{(L^2+3)^3} \tag{2.37a}$$

$$\omega_{s2} = \frac{1}{2}\left(1 + \cos(3\theta_L)\right), \qquad \theta_L = \arctan\left(\frac{L}{\sqrt{3}}\right) + \frac{\pi}{6} \tag{2.37b}$$

These functions could also be defined differently to get other variations of the Lode dependency. A fracture surface is possible to obtain from Equation (2.36) by assuming proportional loading. The proportional plastic fracture strain, $\bar{p}_f$, is reached at a critical porosity f_c. Hence, by integrating over the plastic strain from Equation (2.36), we obtain

$$\begin{aligned}\bar{p}_f = \int_0^{\bar{p}_f} d\varepsilon^p &= \int_{f_0}^{f_c} \frac{df}{3\kappa_g f(1-f)\exp\left(\psi T\right) + \left(\kappa_{s1}\omega_{s1} + \kappa_{s2}\omega_{s2}\right) f} \\ &= \frac{1}{3\kappa_g \exp\left(\psi T\right) + \left(\kappa_{s1}\omega_{s1} + \kappa_{s2}\omega_{s2}\right)} \cdot \\ &\qquad \ln \frac{f_c\left(3\kappa_g(1-f_0)\exp\left(\psi T\right) + \kappa_{s1}\omega_{s1} + \kappa_{s2}\omega_{s2}\right)}{f_0\left(3\kappa_g(1-f_c)\exp\left(\psi T\right) + \kappa_{s1}\omega_{s1} + \kappa_{s2}\omega_{s2}\right)}\end{aligned} \tag{2.38}$$

It is further assumed that f_0 and f_c are small compared with unit, which implies that $1 - f_0 = 1 - f_c \approx 1$. Thus, Equation (2.38) becomes

$$\bar{p}_f = \frac{\ln(f_c/f_0)}{3\kappa_g \exp\left(\psi T\right) + \kappa_{s1}\omega_{s1} + \kappa_{s2}\omega_{s2}} \tag{2.39}$$

Four parameters must be fitted from either experiments or micro-mechanical simulations; ψ, $\kappa_g/\ln(f_c/f_0)$, $\kappa_{s1}/\ln(f_c/f_0)$, and $\kappa_{s2}/\ln(f_c/f_0)$.

Figure 2.5 shows how the three terms in the denominator of Equation (2.39) influence the failure surface. Higher T and the state of generalized shear decreases the fracture strain. Moreover, the state of generalized tension has a lower failure strain than the state of generalized compression, as illustrated by Figure 2.5c. Note that the secondary axis is not in scale.

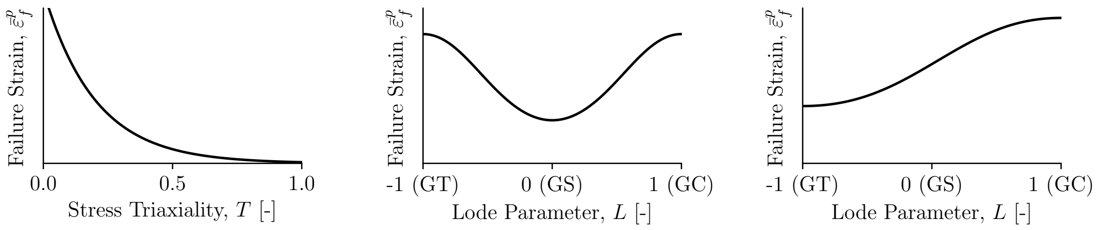

(a) $3\kappa_g \exp(\psi T)$ ***(b)*** $\kappa_{s1}\omega_{s1}$ ***(c)*** $\kappa_{s2}\omega_{s2}$

Figure 2.5: *An illustration on how the three terms in the denominator of Equation* (2.39) *affect the yield surface. (a) represents the original Rice-Tracey criteria. (b) illustrates the modification by Gruben et al. [9] due to shear softening. (c) shows the tilting of the fracture surface.*

2.1.6 Porous Plasticity

Porous plasticity models (PPM) are physically-based material models which combine the underlying physical mechanisms at a microscopic level to the constitutive relations. Ductile materials experience nucleation, growth and coalescence of micro-cracks and voids, as presented in Section 2.1.4. Porous models possess the ability to describe such micro-mechanical processes at a macroscopic scale. A material element is consequently assumed to consist of a matrix material and voids. The work-hardening of the matrix increases the strength of the material, while these micro-mechanical mechanisms tend to soften the material behavior. Consequently, there will be a competition between these two effects until the localization of strains occurs due to excessive damage. As a consequence, porous plasticity models couple the damage to the material response. Additionally, the assumption of pressure insensitive material behavior, which applies to many material models, is no longer valid.

Even though the processes of ductile failure are categorized into distinct regimes, in reality, these mechanics are related to several additional factors. Factors such that the distribution, shape, and size of second-phase particles and voids, stress state, strain rate and temperature [2] may all contribute to the ductility. Consequently, the employment of many approximations and simplifications is often necessary to reach a solution. The material constants are normally determined from experiments, and may therefore account for such factors in an average sense. Whether or not void-based damage models are preferable to coupled continuum damage models, as those presented in Section 2.1.5, is debatable. In the end, the most compelling aspect is if the model can predict real material behavior or not.

The following section presents the Gurson-Tvergaard model. This model accounts for the growth of voids, which is the most understood stage of ductile fracture. Void growth is a continuum plastic deformation process and, therefore, more convenient to model than nucleation and coalescence [2]. Extensions that account for nucleation and coalescence will also be presented here, along with a model for shearing of voids. A Gurson-type of model for the Hershey yield criterion is presented in the end.

The Gurson-Tvergaard Model

Gurson [11] proposed a porous plasticity model in 1977 which accounts for the growth of voids in the constitutive relation. The model is based on the upper-bound limit analysis in the theory of plasticity. Gurson assumed a periodic distribution of voids in the material and derived a yield criteria based on a thick-walled hollow sphere. Tvergaard later modified the model to become more adaptable [12, 13], which the literature frequently refers to as the Gurson-Tvergaard (GT) model. The model is given in terms of a macroscopic yield criterion and is defined by

$$\Phi(\boldsymbol{\sigma}, f, \sigma_M) = \left(\frac{\sigma_{eq}^{VM}}{\sigma_M}\right)^2 + 2fq_1 \cosh\left(\frac{3}{2}q_2\frac{\sigma_H}{\sigma_M}\right) - 1 - q_3 f^2 \leq 0 \tag{2.40}$$

where q_1, q_2 and q_3 are the material parameters introduced by Tvergaard. The original Gurson model was found to be overly stiff. The introduction of these variables encourage void growth and serves artificially softening. It is common to assume $q_3 = q_1^2$. For most ductile materials, $q_1 \approx 1.25 - 1.50$ and $q_2 \approx 1.0$ [2]. The flow stress of the matrix material is represented by σ_M. The Voce rule, given by Equation (2.4), will be utilized in this thesis. Moreover, σ_H and σ_{eq}^{VM} are the macroscopic hydrostatic stress and the macroscopic von Mises equivalent stress, respectively. Moreover, the Gurson-Tvergaard model is, in its original form, independent of the third invariant J_3, and thus the Lode parameter L.

The void volume fraction f, also called porosity, is the only microstructural variable in the Gurson-Tvergaard model and is defined as [26]

$$f = \frac{V_f}{V} = \frac{V_f}{V_f + V_M} \tag{2.41}$$

where $0 \leq V_f < V$ is the volume of voids in a representative volume element (see Section 2.2) and V_M is the total volume of matrix material. The Gurson model explicitly includes the porosity f in the yield function. Consequently, this is a coupled model where void growth results in softening of the macroscopic response. By using the underlying assumption of matrix incompressibility, i.e., $\dot{V}_M = 0$, it is possible to express

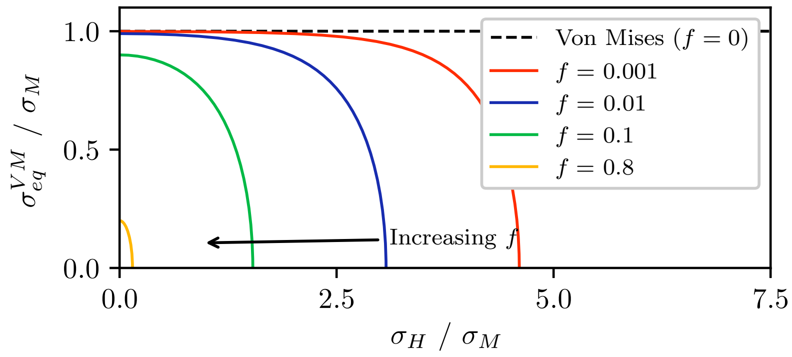

(a) *Varying porosity.* $q_1 = q_2 = 1.0$

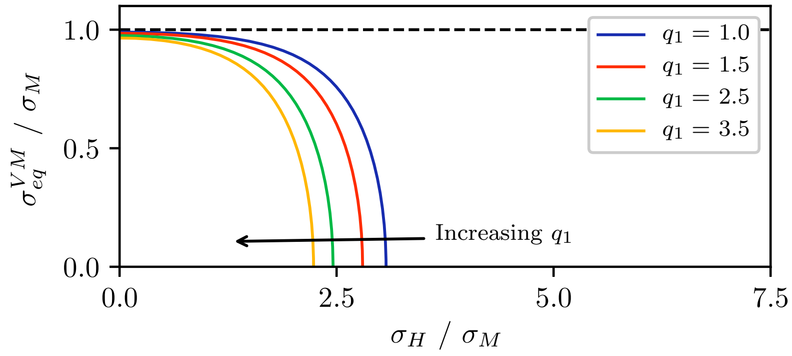

(b) *Varying* q_1. $f = 0.01$ *and* $= q_2 = 1.0$

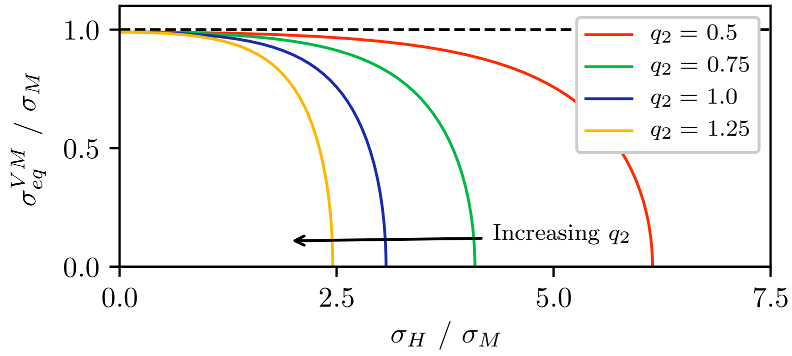

(c) *Varying* q_2. $f = 0.01$ *and* $= q_1 = 1.0$

Figure 2.6: *An illustration on how the different model parameters affect the yield surface* $\Phi = 0$. *The surface is plotted in the* σ_H–σ_{eq}^{VM}*–space and shows the reduction in macroscopic equivalent stress with the increase in hydrostatic stress for different (a) porosity levels, (b)* q_1 *and (c)* q_2. *The arrow shows the direction of increasing parameters. The blue curves represent the same set of parameters for all plots, i.e.,* $f_0 = 0.01$, $q_1 = 1$, *and* q_2.

the evolution of the porosity as

$$\dot{f} = \frac{\dot{V}_f}{V}\left(1 - \frac{V_f}{V}\right) = (1-f)\dot{\varepsilon}_v^p \tag{2.42}$$

where $\dot{\varepsilon}_v^p = \frac{\dot{V}_f}{V}$ is the plastic volumetric strain rate. By adopting the associated flow rule, given by Equation (2.6), the plastic strain rate tensor is found by the relation [26]

$$\dot{\varepsilon}_{ij}^p = \dot{\lambda}\frac{\partial \Phi}{\partial \sigma_{ij}} = \dot{\lambda}\left[\frac{3}{\sigma_M^2}\sigma_{ij}^{'} + \frac{f q_1 q_2}{\sigma_M}\sinh\left(\frac{3}{2}q_1\frac{\sigma_H}{\sigma_M}\delta_{ij}\right)\right] \tag{2.43}$$

The first term on the right-hand side is the deviatoric part and the second term is the volumetric part of the plastic strain rate tensor. By combining Equation (2.42) and the volumetric part in Equation (2.43), one can finally express the evolution of porosity due to growth as

$$\dot{f} = \dot{f}_g = (1-f)\dot{\varepsilon}_v^p = \dot{\lambda}(1-f)\frac{f q_1 q_2}{\sigma_M}\sinh\left(\frac{3}{2}q_1\frac{\sigma_H}{\sigma_M}\delta_{ij}\right) \tag{2.44}$$

Some important aspects of the Gurson model will be discussed. Figure 2.6 shows how the normalized macroscopic equivalent stress varies with increasing hydrostatic stress, and thus increasing stress triaxiality ratio, for different configurations of the model parameters. At zero porosity, i.e., $f = 0$, the yield function reduces to

$$\Phi = \left(\frac{\sigma_{eq}^{VM}}{\sigma_M}\right)^2 - 1 = 0 \tag{2.45}$$

which is another form of the yield function for the matrix material, given by Equation (2.3). The horizontal dashed line in Figure 2.6 illustrates this particular case. Obviously, the von Mises yield criterion is independent on the hydrostatic stress, and thus the triaxiality ratio. This follows by the definition of a von Mises material, where yielding is only affected by the deviatoric stress state. The macroscopic equivalent stress is reduced as the porosity increases. The yield function is fulfilled for zero stresses ($\sigma_{eq}^{VM} = \sigma_H = 0$) at a certain porosity level, defined by $f = \frac{1}{q_1}$. Consequently, this implies that the yield function collapses into a single point and the material losses its load-carrying capacity. The porosity must therefore stay within $f_0 \leq f < q_1^{-1}$.

Increasing all model parameters tends to decrease the yield surface, resulting in a softer material response. Increasing the porosity, which is the only parameter that changes during plastic deformation, exhibit the most significant impact on the surface. The effects of changing q_2 are more prominent than changing q_1. Changes in q_1 does not influence the response at zero hydrostatic stress. Also, yielding can take place in the case of vanishing deviatoric stresses, i.e., $\sigma_{eq}^{VM} = 0$. It can be seen from Equation (2.40) that this can result in yielding for a pure hydrostatic stress state, which is not possible in classical J2 flow theory.

One deficiency with the Gurson model is the assumption that the voids remain spherical during deformation. This assumption might be acceptable at intermediate to high stress triaxiality, but void growth is clearly not spherical in the lower triaxiality domain. Moreover, the model does not account for the effect of the Lode parameter, which is essential at low triaxiality ratios. Another insufficiency is the assumption of initially spherical voids. A study on unit cells by Gao and Kim [53] concluded that the shape of the voids significantly influenced void growth and coalescence. Improvements of the Gurson model have been proposed, but at the expense of the simplicity of the original model.

Nucleation of Voids

The Gurson-Tvergaard model, in its original form, accounts only for void growth and does not include void nucleation or coalescence. Chu and Needleman [14] expressed the evolution of porosity as

$$\dot{f} = \dot{f}_n + \dot{f}_g \tag{2.46}$$

to account for void nucleation. Here, $\dot{f}_n$ is the change in porosity due to nucleation of new voids, and $\dot{f}_g$ is defined by Equation (2.44). Nucleation is assumed to be either stress- or strain-driven. In the case of strain-driven nucleation [1, 26]

$$\dot{f}_n = A(p)\dot{p} \tag{2.47}$$

where

$$A(p) = \frac{f_N}{s_N\sqrt{2\pi}} \exp\left[-\frac{1}{2}\left(\frac{p - p_N}{s_N}\right)^2\right] \tag{2.48}$$

Here, f_N is the total volume fraction of void nucleating particles, s_N is the associated standard deviation and p_N is the mean plastic strain for nucleation. The introduction of void nucleation to the Gurson-Tvergaard model results in three additional fitting parameters.

An alternative strain-driven nucleation model, called the continuous nucleation model, assumes that a constant fraction of voids is nucleated per strain increment. Then $A(p) = A_n$ is assumed to be constant. The nucleation stops once a critical porosity is reached. Although this model is quite simple, good results have been reported for steel and aluminium alloys [54, 55]. It is noted that the continuous nucleation model is a special case of Equation (2.48) where s_N is large.

Coalescence of Voids

Fracture occurs when voids coalesce. A straightforward way of defining a fracture criterion is to assume that void coalescence occurs at a critical porosity f_c, at which point fracture initiates. Rapid void growth tends to happen when the void fraction exceeds 10 to 20 % [1]. Consequently, the material loses its load-carrying capacity rapidly. Tvergaard and Needleman [15] introduced a phenomenological way of accounting for this accelerating void growth by replacing f in Equation (2.40) with an effective void volume fraction f^*

$$f^* = \begin{cases} f & \text{if } f \leq f_c. \\ f_c + \dfrac{f_u - f_c}{f_f - f_c}(f - f_c) & \text{if } f > f_c. \end{cases} \tag{2.49}$$

where $f_u = \frac{1}{q_1}$, and f_f is the void volume fraction when the material loses its load-carrying capacity. Note that $f^*(f_f) = f_u$, which indicates that the yield function collapses into a single point. The contribution from the hydrostatic stress is amplified when $f > f_c$, which in turns accelerates the onset of plastic instability. It is probably sufficient to assume failure when the porosity exceeds f_c for all practical purposes, and the marginal benefit of applying Equation (2.49) is outweighed by the need to define the additional parameters [1].

Shearing of Voids

A deficiency with the Gurson model is its inability to represent the case of low stress triaxialities, for example in shear-dominated stress states. The model is founded on the formulation of spherical void growth. However, the voids will not remain spherical as the hydrostatic stresses are reduced, eventually resulting in the loss of its physical foundation.

In order to describe damage evolution for low stress triaxialities, Nahshon and Hutchinson [16] proposed an extension to the Gurson model that takes the evolution of damage $\dot{f}_s$ due to shear softening because of void distortion and inter-void linking into account.

Equation (2.46) is now expressed as

$$\dot{f} = \dot{f}_n + \dot{f}_g + \dot{f}_s \tag{2.50}$$

where the evolution of shear damage f_s is defined as

$$\dot{f}_s = k_s f \kappa\left(\theta_L\right) \frac{\sigma'_{ij}\dot{\varepsilon}^p_{ij}}{\sigma_{eq}} \tag{2.51}$$

Here, k_s is a constant and $\kappa\left(\theta_L\right)$ is a stress-dependent factor, defined as

$$\kappa\left(\theta_L\right) \equiv 1 - \cos^2(3\theta_L), \qquad 0 \leq \theta_L \leq \frac{\pi}{3} \tag{2.52}$$

From the definition of the Lode angle in Section 2.1.3, it can easily be shown that $\kappa = 0$ in the case of generalized tension and compression, and $\kappa = 1$ in the case of generalized shear. Thus $\dot{f}_s$ equals to zero for all axisymmetric stress states while shear-dominated stress states tend to accelerate the damage evolution. It must be emphasized that the porosity f no longer represents the volume fraction of voids, given by Equation (2.41). It can instead be viewed as a damage parameter that accounts for the softening due to void distortion and growth.

A Gurson-Type Model for the Hershey Yield Criterion

It is possible to obtain a Gurson-type model for isotropic porous solids that obeys the Hershey yield criterion by heuristically replacing the von Mises equivalent stress with the Hershey equivalent stress. Such a modification of the model incorporates effects of the Lode parameter and has been proposed by Dæhli et al. [25] in a recent study. The Gurson-Tvergaard model takes the form

$$\Phi(\boldsymbol{\sigma}, f, \sigma_M) = \left(\frac{\sigma_{eq}}{\sigma_M}\right)^2 + 2fq_1 \cosh\left(\frac{3}{2}q_2\frac{\sigma_H}{\sigma_M}\right) - 1 - (q_1 f)^2 \leq 0 \tag{2.53}$$

where σ_{eq} is the Hershey equivalent stress from Equation 2.5. The other parameters are the same as in the original Gurson model. This modification is implemented in the SIMLab Porous Plasticity Model (SPPM) [56].

2.2 Computational Unit Cell

Unit cell models provide a powerful numerical tool for understanding material behavior and fracture on a microscopic scale. It consists of modeling the microstructure of the material by applying assumptions such as a uniform and periodic distribution of voids, and a homogenized matrix material which does not include any secondary voids or particles. The voids are often approximated as spheroids. Needleman [23] first introduced these kinds of analyses in 1972, and they have been extensively used in the literature ever since. Large-scale experiments can not efficiently calibrate many material models which build on underlying physical phenomenons. The unit cell can in such cases generate useful data for the calibration process. Unit cell models may also give essential insight into mechanisms observed in experiments. The approach presented in this section is taken from the work by Dæhli et al. [24, 25, 57], and the reader is referred to these papers if nothing else is cited.

First, the idealization approach of unit cell models and the FE-model used are presented. The last section gives a brief overview on the definition of macroscopic stress states and the boundary conditions for the unit cell model.

2.2.1 The Unit Cell Model

Figure 2.7 shows the approximation of a representative volume element (RVE) in a polycrystalline solid [57]. The microstructure of alloys consists of grains, particles, and micro-voids, as shown in Figure 2.7a. In the case of randomly ordered grains, which is true for many polycrystalline materials, the material is expected to exhibit isotropic behavior on a macroscopic scale [26] and a homogenized matrix can approximate the microstructure. This process is shown in Figure 2.7b. The microstructure, which consists of randomly distributed and irregular particles, is further idealized by assuming a structure of evenly distributed particles of equal shape and size. Figure 2.7c illustrates this. From this fairly simple idealization, one can extract the resulting unit cell model, given in Figure 2.7d

Hence the representative volume element consists of a single void or particle embedded by an isotropic bulk material, which is described by the elastic-plastic constitutive relations given in Section 2.1.1. The primary purpose of the unit cell in this thesis is to observe void growth under proportional loading, and to fit the material constants in the Gurson-Tvergaard model, given in Equation (2.40).

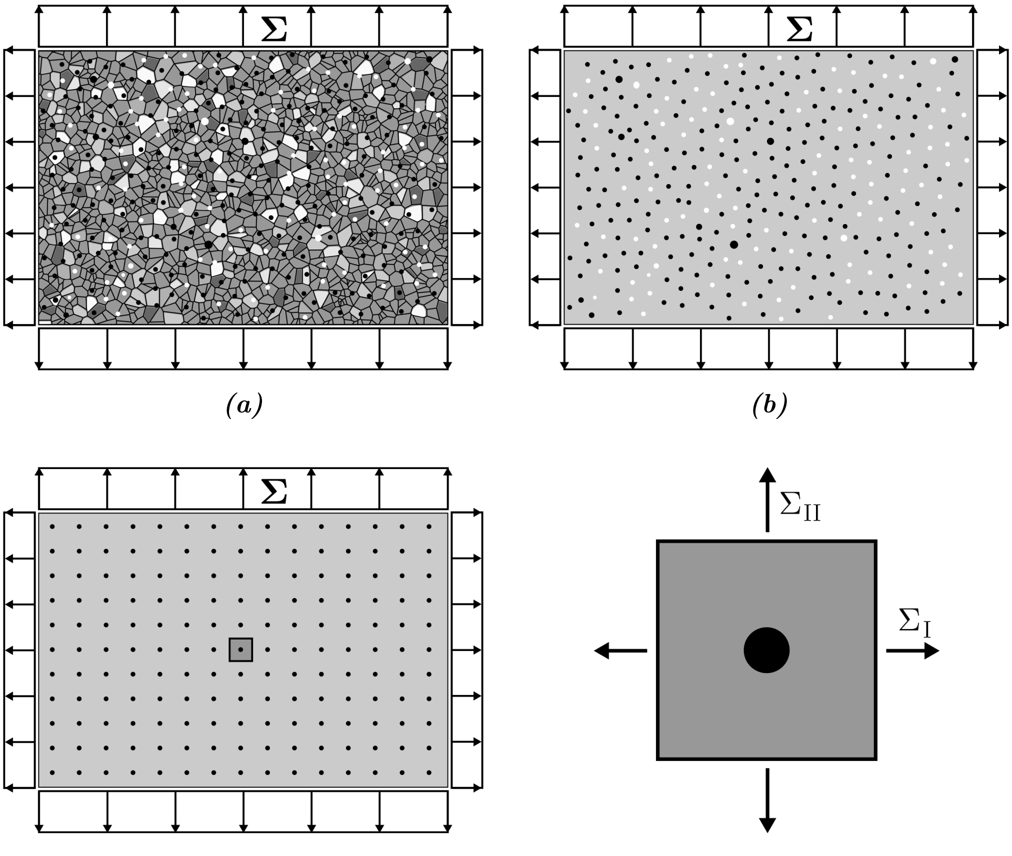

(a) *(b)* *(c)* *(d)*

Figure 2.7: *The process of simplifying a polycrystalline solid into an RVE. (a) Realistic micro-structure consisting of grains, voids, and particles. (b) Homogenized matrix description. (c) Evenly distributed and equal sized particles. (d) The resulting unit cell model. From Dæhli [57].*

2.2.2 A Finite Element Approach of the Cell Model

The 3D unit cell model consists of a cube with a spherical void located at the center, as illustrated in Figure 2.8a. Only normal stress components act on the unit cell and shear effects are precluded in the simulations. Moreover, the void surface is free from any traction. Only 1/8 of the cell is model due to the symmetry of the problem. In this study, the cube sides are of equal size, given by $L_i = 2\bar{L}$, where $\bar{L}$ is the length of the 1/8 model. The void is assumed to be initially spherical, hence $R_i = \bar{R}$. The initial void fraction is given by

$$f_0 = \frac{V_V}{V_{RVE}} = \frac{\pi \bar{R}^3}{6\bar{L}^3} \tag{2.54}$$

where V_V and V_{RVE} are the volume of the void and RVE, respectively. Axisymmetric tests of smooth and various notched specimens are normally used to fit f_0 from the Gurson model. This thesis, however, mainly uses the non-commercial Alstruc microstructure solidification model for industrial aluminium to determine the initial porosity [36, 37, 38]. The external cell boundaries translate as rigid faces in the perpendicular direction to enforce the requirement of periodic boundary conditions. Moreover, the symmetry planes are restricted from movement in the perpendicular direction. The 1/8 FE-model is shown in Figure 2.8b. The implicit finite element code Abaqus/Standard [58] was used to conduct the finite element (FE) simulations.

Due to the assumption of an initially voided material, the effects of nucleation and matrix-particle interaction are neglected. This is reasonable for matrix-particle systems that exhibit low cohesive energy, and at intermediate to high triaxiality stress states.

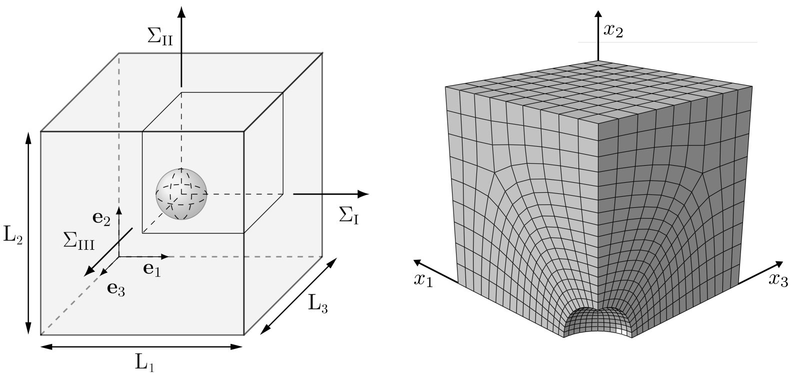

(a) *(b)*

Figure 2.8: *Illustration of the unit cell. (a) shows the unite with a spherical void located in the center. The macroscopic stresses are given as Σ_i. (b) illustrates an FE-model of the* 1/8 *unit cell. From Dæhli et al. [25].*

At negative or low stress triaxiality, however, closing of the void occurs. Consequently, including a particle is necessary.

2.2.3 Macroscopic Stress States

The unit cell is normally restricted to proportional macroscopic loads in order to systematically evaluate the cell response under different stress states. Due to the nature of the stress triaxiality T and the Lode parameter L on ductile damage and failure, these parameters will be kept constant during deformation. Thus, the translation of the rigid faces must be enforced by a set of equations to ensure correct stress state.

As indicated in Figure 2.8a, the cell is subjected to macroscopic stresses and strains. Capital letters are used to denote these variables here. The von Mises equivalent stress measurement is exploited, which is given by

$$\Sigma_{eq}^{VM} = \sqrt{\frac{3}{2}\Sigma'_{ij}\Sigma'_{ij}} \tag{2.55}$$

where Σ'_{ij} is the macroscopic deviatoric stress tensor. Accordingly, the macroscopic work conjugate equivalent von Mises strain is defined as

$$E_{eq}^{VM} = \sqrt{\frac{2}{3}E'_{ij}E'_{ij}} \tag{2.56}$$

where E'_{ij} is the macroscopic deviatoric logarithmic strain tensor. Further, Equation (2.22) can be expressed in terms of the macroscopic stresses

$$\begin{Bmatrix} \Sigma_I \\ \Sigma_{II} \\ \Sigma_{III} \end{Bmatrix} = \Sigma_{eq}^{VM} \left(\frac{3}{2} \begin{Bmatrix} \cos\left(\theta_L\right) \\ \cos\left(\frac{2\pi}{3} - \theta_L\right) \\ \cos\left(\frac{2\pi}{3} + \theta_L\right) \end{Bmatrix} + T \begin{Bmatrix} 1 \\ 1 \\ 1 \end{Bmatrix} \right) \tag{2.57}$$

The Lode angle, θ_L, and the stress triaxiality, T, are defined by

$$\theta_L = \arctan\left(\frac{L}{\sqrt{3}}\right) + \frac{\pi}{6}, \qquad L = \frac{2\Sigma_{II} - \Sigma_I - \Sigma_{III}}{\Sigma_I - \Sigma_{III}} \tag{2.58a}$$

$$T \equiv \frac{\Sigma_H}{\Sigma_{eq}^{VM}}, \qquad \Sigma_H = \frac{1}{3}(\Sigma_I + \Sigma_{II} + \Sigma_{III}) \tag{2.58b}$$

As indicated by Equation (2.57), the ratios between the different principal stress components are functions of only θ_L and T. The stress state can, therefore, be imposed simply and concisely. The normalized principal stress ratios are expressed on the form [24, 59]

$$\psi_1 = \frac{\Sigma_I}{\Sigma_{max}}, \qquad \psi_2 = \frac{\Sigma_{II}}{\Sigma_{max}}, \qquad \psi_3 = \frac{\Sigma_{III}}{\Sigma_{max}} \tag{2.59}$$

where $\Sigma_{max} = \max(\Sigma_I, \Sigma_{II}, \Sigma_{III})$, and thus $\psi_i = \psi_i(T, \theta_L) \leq 0$. These ratios are the only quantities needed in the kinematic constraints used to ensure proportional loading of the cell. Dæhli et al. [24] showed that, under the assumption of uniform boundary conditions, the three orthogonal boundary displacement components of the rigid faces could be connected to a single fictitious node through the following sets of equations

$$\Delta U_1 = l_1 \left(\beta_1 \Delta\widetilde{U}_1 + \beta_2 \Delta\widetilde{U}_2 + \beta_3 \Delta\widetilde{U}_3 \right) \tag{2.60a}$$

$$\Delta U_2 = l_2 \left(\beta_2 \Delta\widetilde{U}_1 - \frac{\beta_3^2 + \beta_1 \beta_2^2}{\beta_2^2 + \beta_3^2} \Delta\widetilde{U}_2 + \frac{\beta_2 \beta_3 (1 - \beta_1)}{\beta_2^2 + \beta_3^2} \Delta\widetilde{U}_3 \right) \tag{2.60b}$$

$$\Delta U_3 = l_3 \left(\beta_3 \Delta\widetilde{U}_1 + \frac{\beta_2 \beta_3 (1 - \beta_1)}{\beta_2^2 + \beta_3^2} \Delta\widetilde{U}_2 - \frac{\beta_2^2 + \beta_1 \beta_3^2}{\beta_2^2 + \beta_3^2} \Delta\widetilde{U}_3 \right) \tag{2.60c}$$

Here, ΔU_i are the displacement components of the rigid faces for a given set of ψ_i, l_i denotes the current length of the unit cell edges, and $\Delta\widetilde{U}_i$ are the displacements of the fictitious node located outside of the model. These connectivity equations can be imposed by using a multi-point constraint (MPC) subroutine in ABAQUS/Standard. The β_i parameters are explicitly given by the normalized principal stress ratios

$$\beta_1 = \frac{\psi_1}{\overline{\psi}}, \qquad \beta_2 = \frac{\psi_2}{\overline{\psi}}, \qquad \beta_3 = \frac{\psi_3}{\overline{\psi}}, \qquad \overline{\psi} = \sqrt{\psi_1^2 + \psi_2^2 + \psi_3^2} \tag{2.61}$$

2.3 Localization of Strains

Experiments show that ductile fracture is frequently preceded by the localization of strains [26]. The localization may take place due to softening from damage evolution or adiabatic heating, which results in non-unique solutions of the boundary value problem. In such cases, other solutions than the fundamental solution are possible, eventually leading to localized plastic deformation within a narrow band. By the assumption that localization initiates material failure, this theory can, to an extent, be a reliable tool for calibration different failure criteria. This assumption is often reasonable since intense deformation in a confined region is usually followed by local crack initiation and propagation [25].

Two cases of the localization analysis exist; bifurcation analysis and imperfection band analysis [26]. In the bifurcation analysis, localization occurs in a homogeneously deformed solid due to instabilities in the constitutive equation leading to the possibility of bifurcation modes. In contrast, the imperfection band analysis introduces a planer band of initial imperfection to the material. The material properties inside the band differ slightly from the surrounding material properties, which reduces the strength of the band material. It must be emphasized that the localization theory is not a ductile fracture model by itself. Studies show, however, good correlations between unit cell simulations and the imperfection band analyses. The bifurcation analysis, on the other hand, tends to over-predict the strain at localization [25, 32]. Moreover, the strain localization analysis is superior to the unit cell when concerning the computational effort [32].

2.3.1 The Imperfection Band Analysis

The governing idea of the imperfection band analysis, proposed by Rice in 1976 [31], is that a small portion of the material has slightly different properties from the surrounding material, permitting concentrated deformation within this inhomogeneity. A homogeneous and homogeneously deformed solid body will be considered, in which there exists an initial narrow band of imperfections. This is illustrated in Figure 2.9. Properties outside and inside the band will be denoted $(\bullet)$ and $\overline{(\bullet)}$, respectively.

The stress and deformation rates, as well as the constitutive relations, inside this band, are allowed to take values which differs from the surrounding material. It is assumed that some of the material properties will vary slightly inside the band, which is used

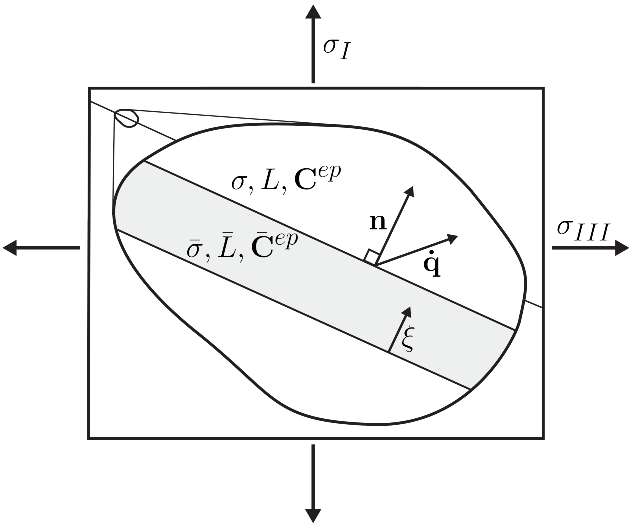

Figure 2.9: *Illustration of the strain localization approach. From Dæhli et al. [25].*

to explain the reason for this discontinuity, or non-uniformity, in the material. The requirement of equilibrium and compatibility, however, must be enforced across the band.

It is assumed that non-uniformities in the velocity gradient field inside the planar band may occur, while the velocity field $\mathbf{v}$ outside the band remains continuous and the partial derivatives of $\mathbf{v}$ in the direction parallel to the band remain uniform. Compatibility requires that the velocity gradient field $\overline{L}_{ij}$ only vary along the normal direction to the band. Thus, the compatibility equation becomes [26]

$$\overline{L}_{ij} = L_{ij} + \dot{q}_i n_j \tag{2.62}$$

where $\mathbf{n}$ denotes the unit normal vector to the planer band. The band orientation rotates due to the global deformation of the body. Hence, $\mathbf{n}$ is not fixed. The vector $\dot{\mathbf{q}} \equiv \partial \Delta \mathbf{v} / \partial \xi$ represents the rate of deformation non-uniformity, and $\Delta \mathbf{v}(\xi, t)$ is the non-uniformity of the velocity field inside the band. Note that the only directional coordinate for $\mathbf{v}$, and therefore $\dot{\mathbf{q}}$, is ξ, which is defined as the coordinate along $\mathbf{n}$, as illustrated in Figure 2.9.

The unit vector $\mathbf{m}$ parallel to the vector $\dot{\mathbf{q}}$ is used to define the localization mode. If $\mathbf{m}$ is orthogonal to $\mathbf{n}$, i.e., $\mathbf{m} \cdot \mathbf{n} = 0$, the band is a shear band. In contrary, if $\mathbf{m} \cdot \mathbf{n} = 1$, the two vectors are parallel and a dilatation band is obtained. Everything in between these two extremes are a mixed mode of localization.

The continuing equilibrium of the traction across the band can be expressed as [32]

$$n_i \dot{\overline{P}}_{ij} = n_i \dot{P}_{ij} \tag{2.63}$$

where $\dot{\mathbf{P}}$ is the rate of the nominal stress tensor. Equation (2.62) and (2.63) are the two governing equations in the imperfection band analysis. Also, the constitutive relations defining the material response inside and outside the band are included. By combining these equations, an equation for the rate of deformation non-uniformity vector $\dot{\mathbf{q}}$ can be derived [25, 32]

$$\left(n_i \overline{C}^t_{ijkl} n_l \right) \dot{q}_k = n_i \left(C^t_{ijkl} - \overline{C}^t_{ijkl} \right) L_{kl} \tag{2.64}$$

where $\mathbf{C}^t$ is the tangent modulus defined as [25, 32]

$$C^t_{ijkl} = C^{ep}_{ijkl} - \frac{1}{2}\sigma_{ik}\delta_{jl} + \frac{1}{2}\sigma_{il}\delta_{kj} - \frac{1}{2}\sigma_{jl}\delta_{ik} - \frac{1}{2}\sigma_{jk}\delta_{il} + \sigma_{ij}\delta_{kl} \tag{2.65}$$

Here, δ_{ij} is the Kronecker delta, σ_{ij} is the Cauchy stress tensor, and C^{ep}_{ijkl} is the elastic-plastic tangent modulus tensor. It follows that strain localization occurs when the acoustic tensor, defined as $\overline{\mathbf{A}}^t(\mathbf{n}) = \mathbf{n} \cdot \overline{\mathbf{C}}^t \cdot \mathbf{n}$, becomes singular, hence

$$\det\left(n_i \overline{C}^t_{ijkl} n_l\right) = 0 \tag{2.66}$$

This condition implies that the rate of deformation non-uniformity vector $\dot{\mathbf{q}}$ is no longer uniquely defined. Localization of the strains is normally not possible in materials undergoing associative plastic flow unless strain softening is present in the constitutive response of the material inside the band. As mentioned in the introduction, materials prone to ductile damage or thermal softening often experience strain softening. Accordingly, a natural way to account for softening in the constitutive relations is to use a porous plasticity model. The Gurson-Tvergaard model presented in Section 2.1.6 will be used herein.

In the imperfection analysis, a proportional load path is prescribed outside the band. The proportional load path can be defined by the stress triaxiality T and Lode parameter L. The constitutive relations determine the stress and internal variables. Localization is assumed to occur when the determinant of the acoustic tensor $\overline{\mathbf{A}}^t(\mathbf{n})$ becomes negative for the first time. Since this loss of ellipticity can arise for several band orientations, it is essential to search for the orientation for which the ductility is lowest [32]. The initial unit normal vector to the band is defined in terms of spherical coordinates

$$\mathbf{n_0} = \begin{Bmatrix} \cos\phi_0 \\ \cos\theta_0 \sin\phi_0 \\ \sin\theta_0 \sin\phi_0 \end{Bmatrix} \tag{2.67}$$

where the $\theta_0 \in [0, 2\pi]$ and $\phi_0 \in [0, \pi]$ are the initial azimuthal angle and polar angle, respectively. Figure 2.10 illustrates the normal vector and corresponding angles. The

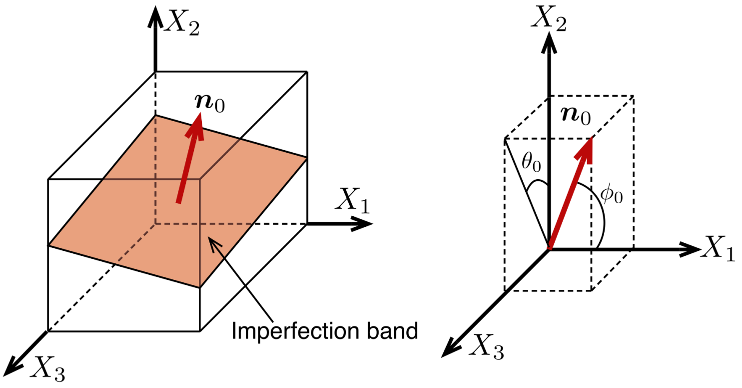

Figure 2.10: *The normal vector* $\mathbf{n_0}$ *to the imperfection band. From Morin et al. [60].*

band orientation vector at time t is calculated by,

$$\mathbf{n}(t) = \frac{\mathbf{n_0} \cdot \mathbf{F^{-1}}(t)}{|\mathbf{n_0} \cdot \mathbf{F^{-1}}(t)|} \tag{2.68}$$

where $\mathbf{F}(t)$ is the deformation gradient outside the imperfection band.

2.3.2 The Bifurication Analysis

In the bifurcation analysis, a homogeneous and homogeneously deformed body is also considered. The imperfection band, however, is not initially present in the un-deformed body. The body is subjected to a uniform stress field σ, and we search for conditions "for which continued deformation may result in an incipient non-uniformity field in which deformation rates vary with position across a planar band but remain uniform outside the band" [30].

The bifurcation approach is obtained by setting $\overline{\mathbf{C}}^t = \mathbf{C}^t$ in Equation (2.69). Hence, bifurcation occurs when [32]

$$\det\left(n_i C^t_{ijkl} n_l\right) = 0 \tag{2.69}$$

As for the imperfection band, some sort of softening mechanism must be included in the constitutive material relations in order for localization to occur.

3 | Material and Experimental Study

A cast and homogenized aluminium alloy in the AA6xxx-series is used in this study. Westermann et al. [38] reported this particular alloy, where the microstructure, strength, work-hardening, and ductile failure were extensively investigated. The experimental data from smooth and notched axisymmetric specimens used herein are taken from this paper. The same material has been examined subsequently in [38, 61, 62]. Holmen et al. [39] were investigating the prediction of failure in the same particular alloy using a numerical approach. This article also presents experimental data from a plane stress tension test which will be used in this thesis to investigate the effect of the Lode parameter.

3.1 Material

The material samples were taken from a DC-cast ingot produced at the laboratory casting facilities at Hydro Aluminum R&D Sunndal. The chemical composition is 0.2 Fe, 0.5 Mg, 0.4 Si and Al balanced, all in wt%. TiB was also added as grain refiner to control the grain size and avoid abnormal grains during casting. The ingot was homogenized using a laboratory furnace to ensure isotropic plastic flow. The homogenization procedure is given in Table 3.1. Pedersen et al. [61] could report a constant strain ratio (r-value) equal to unity for the cast and homogenized material. Thus, the material will hereafter be assumed isotropic. For consistency, the aluminium alloy will be referred to as AlMgSi.

Calculation from ALSTRUC estimated a particle content of 0.452% [38]. The Alstruc code is based on standard solidification and diffusion theory. The reader is referred to Dons et al. [36, 37] for more information about the code. More detailed information about the material and microstructure can be found in Westermann et al. [38].

3.2 Axisymmetric Tensile Tests

Westermann et al. [38] performed tensile tests on a smooth and two types of notched axisymmetric specimens. Tests were conducted on three samples, orientated along the longitudinal axis of the ingot, of each type. The geometries of the specimens are given in Figure 3.7 – 3.9. All tests were performed at room temperature with a cross-head velocity of 1.2 mm/min. This corresponds to an average strain rate of $5 \cdot 10^{-4}$ s^{-1} before necking for the smooth specimens.

The tensile force and diameter of the minimum cross-section of the specimen were continuously measurement until failure. A AEROEL XLS13XY laser micrometer with 1 μm resolution was used to measure the diameter in two perpendicular directions, denoted here as D_x and D_y. A $13 \times 13 \times 0.1$ mm^3 box of laser light was created by two perpendicular lasers around the cross-section of the specimen. The laser micrometer was mounted on a mobile frame which can move in the vertical direction. This is to ensure that the minimum cross section is always measured. The samples were scanned with a frequency of 1200 Hz during elongation.

The Cauchy stress versus the logarithmic strain curves for all 9 samples are plotted in Figure 3.1, which have been calculated using Equation (2.9) and (2.10). It must be emphasized that for the notched tests, the stress and strain measurements represent an average value over the minimum cross-section. The same holds true for the smooth specimen after incipient necking. Moreover, plastic incompressibility was assumed in order to obtain the logarithmic strain, which might not be true at large strains since void formation and growth may introduce change in the volume.

The measured stress after necking can be corrected using the Bridgman correction in Equation (2.13) with the Le Roy's empirical model in Equation (2.14). Both stresses are plotted in Figure 3.2. The plastic strain is calculated using Equation (2.12). The Young's modulus is given in Table 3.2.

Table 3.1: *Homogenization procedure for the AlMgSi-alloy [38].*

Heating rate	Holding temperature	Holding time	Cooling rate to RT
100 °C/h	585 °C	2.5 h	300 °C/h

Table 3.2: *Young's Modulus, E, and Poisson's ratio, ν, for a typical AA6xxx aluminum alloy.*

Young's Modulus, E	Poisson's ratio, ν
70,000 MPa	0.30

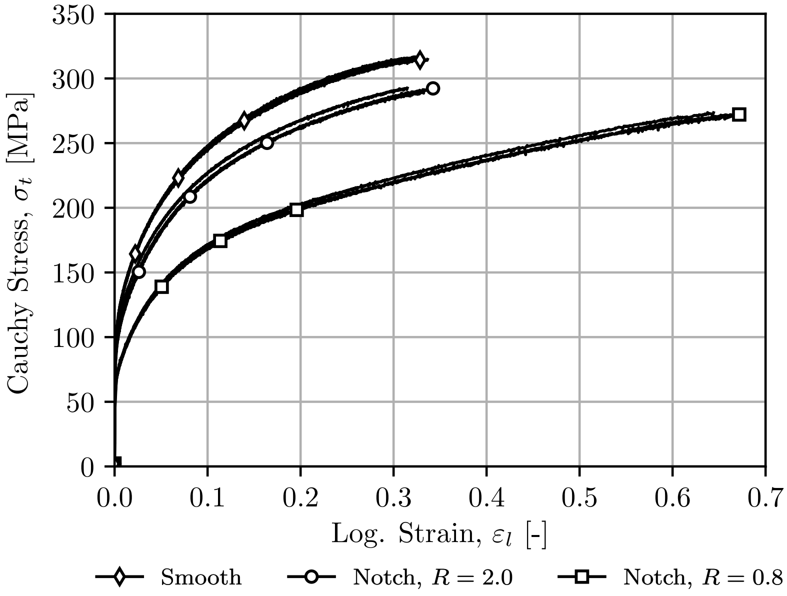

Figure 3.1: *Cauchy stress, σ_t, versus the logarithmic strain, ε_l, for all axisymmetric specimens. The post-processed data is obtained from Westermann et al. [38].*

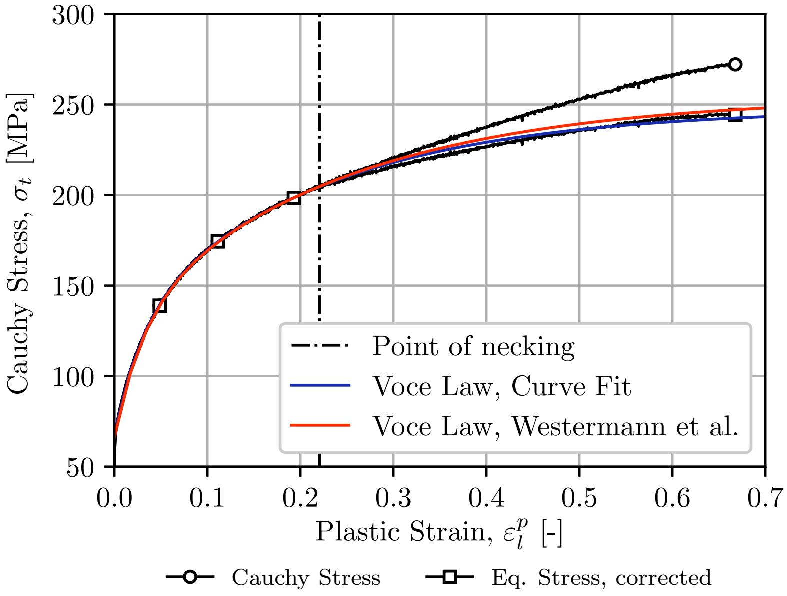

Figure 3.2: *Measured and corrected stress versus the plastic strain, ε_l^p, for a smooth specimen. The blue curve represents the material curve when Voce rule is fitted to the corrected stresses using the Bridgman correction with Le Roy's model for the a/R-ratio. The red curve is obtained using the work-hardening parameters from Westermann et al. [38]. All work-hardening parameters are given in Table 3.3.*

The hardening parameters Q_i and C_i in Equation (2.4) have been fitted using the experimental data from the smooth specimens. For this purpose, the minimize function in the Python SciPy package [63] is utilized with the following cost function

$$e = \frac{1}{3}\sum_{i=1}^{3} \frac{\int_0^{p_f} \left|\sigma_{mes} - \sigma_{model}\right|_i dp}{\int_0^{p_f} \frac{1}{2}\left(\sigma_{mes} + \sigma_{model}\right)_i dp} \tag{3.1}$$

where p_f is the equivalent plastic strain at failure. The measured stress and the stress predicted from Voce rule are denoted σ_{mes} and σ_{model}, respectively. The model-parameters that result in the lowest error e are given in Table 3.3.

Westermann et al. [38] fitted the work-hardening parameters using an inverse modeling approach. These work-hardening parameters are given in Table 3.3 as well. This approach is believed to be more accurate since it captures the equivalent stress state in the neck more accurately, whereas the direct approach, using the Bridgeman correction, is based on several assumptions. Figure 3.2 compares both models with the corrected flow stress. The work-hardening is accurately captured in either case. However, the parameters given by Westermann et al. gives saturation at a slightly higher stress, 254.7 MPa compared to 247.89 MPa. The work-hardening parameters given by Westermann et al. will be used in this thesis from this point on. The logarithmic strain at fracture for all tests are summarized in Table 3.4.

Table 3.3: *Work hardening parameters found using curve fit and the parameters given by Westermann et al. [38].*

	σ_0	Q_1	C_1	Q_2	C_2	$\sigma_{0.2}$
Curve fit	68.55 MPa	58.25 MPa	32.90	121.09 MPa	4.66	-
Westermann	66.26 MPa	62.00 MPa	32.36	126.46 MPa	4.21	71.21 MPa

Table 3.4: *The fracture strain for all axisymmetric specimen tests. The strains are given as logarithmic strains.*

Specimen type	Test #1	Test #2	Test #3	Average value
Smooth	0.6717	0.6761	0.6441	0.6640
$R2$ Notch	0.3424	0.3324	0.3148	0.3299
$R08$ Notch	0.3292	0.3365	0.3267	0.3308

3.2.1 Numerical Model and Mesh Study

Simulations of the smooth and notched specimens have been conducted using the finite element code Abaqus/Standard [58]. A mesh study on three different mesh sizes has been done to ensure convergence. The meshes are denoted M24, M48, and M96, which corresponds to 24, 48 and 96 elements over the minimum cross-section, respectively. This corresponds to a characteristic element size of 0.125, 0.0625 and 0.0313 mm. The models are discretized using a reduced 4-node axisymmetric element type (CAX4R) with hourglass control. The different meshes are illustrated in Figures 3.7–3.9. The results using classical J2 flow theory are presented here. The Gurson-Tvergaard model yields similar results regarding the mesh sensitivity.

As shown in Figure 3.3, convergence of the global response was obtained for the smallest mesh size. Some minor deviations were found between M24 and M48 for the notched specimens. This disparity is rather small, and the M24 model is preferred due to the computational efficiency. The same conclusion holds true for the local response when considering the triaxiality ratio and the Lode parameter across the minimal cross-section, as illustrated in Figure 3.4. These figures plot the Lode parameter and stress triaxiality ratio against the plastic strain in the element. The elements at the center, at the boundary surface, and in between have been used, denoted center, outer, and middle element, respectively. Some differences can be found between the different

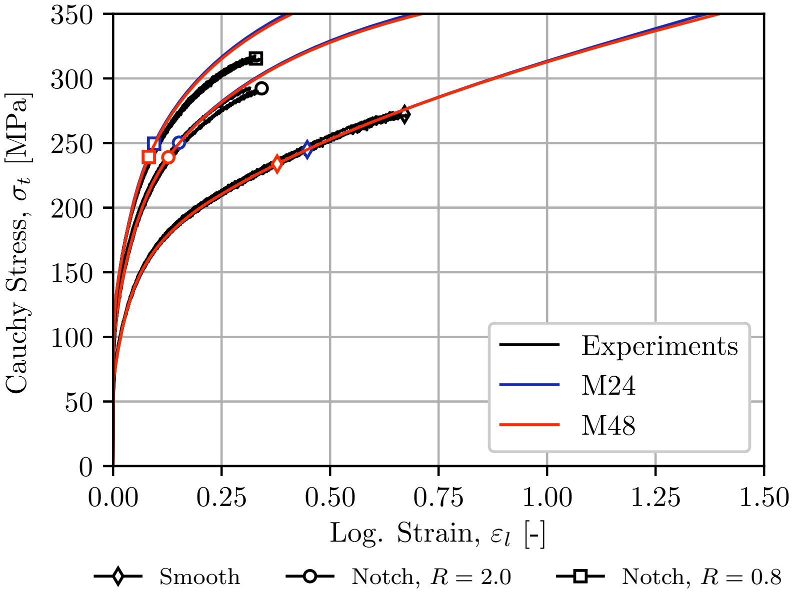

Figure 3.3: *Cauchy stress, σ_t, as a function of the logarithmic strain, ε_l, obtained for the M24 and M48 mesh for the different specimens in Figure 3.2 when applying J2 flow theory. Mesh M48 and M96 showed indistinguishable results. M96 is therefor not included in the figure.*

meshes for the outer element at large strains. The invariants are sampled at the center of each element, at the integration point. Consequently, they are not measured in the same location, which may explain the differences. The coarsest mesh provides sufficient accuracy and will be used hereafter.

The Lode parameter and stress triaxiality are essential factors for void growth and ductile fracture, as mentioned in Section 2.1.3. General knowledge on how these values evolve across the cross-section during a tensile test is important. In the case of a smooth specimen, these invariants are constant across the cross-section up to incipient necking. In uniaxial tension, $\sigma_I > 0$ and $\sigma_{II} = \sigma_{III} = 0$. Consequently, Equation (2.18) yields a triaxiality ratio equal to 1/3. Figure 3.4a shows the same result. The stress triaxiality will rapidly increase in the center of the cross section once the neck is formed, as illustrated by the blue line in Figure 3.5b. A slight decrease of the triaxiality ratio occurs near the surface.

In contrast, the stress triaxiality is not the same over the cross-section for the notched specimens. Moreover, the triaxiality ratio is somewhat unstable in the lower strain regime. The state after this transient phase is plotted as dashed green and red lines in Figure 3.5 and is slowly transforming into a parabolic curve as one approaches maximum force. The triaxiality is found to be largest in the center of the cross-section for the majority of the deformation process. This is especially clear in Figure 3.4, where the triaxiality ratio is almost exclusively largest in the center element for all plastic element strains. A similar response is obtained for either of the notched specimens, but the triaxiality ratio is somewhat higher for the $R08$ geometry. It should be emphasized, as Figure 3.5a illustrates, that the largest plastic strains are located in the outermost element in the case of the notched specimens.

The Lode parameter remains negative unity, i.e., the state of generalized tension, in the center element for all specimens, even after necking. This is predicted by Equation (2.19) in the case where $\sigma_{II} = \sigma_{III}$ and $\sigma_I > 0$

$$L = \frac{2\sigma_{II} - \sigma_I - \sigma_{II}}{\sigma_I - \sigma_{II}} = -1$$

The Lode parameter increases as one approaches the surface of the specimen. In the case of a smooth specimen, the Lode parameter remains -1 up to necking. Subsequently, the Lode parameter increases slightly in the outer region, as shown by Figure 3.5c. The notched specimens experience an opposite effect, where L was found to decrease as the plastic straining increases.

The von Mises yield criterion, given by Equation (2.5) with $m = 2$, has been used in all simulations so far. In general, it is assumed that axisymmetric tensile bars have a

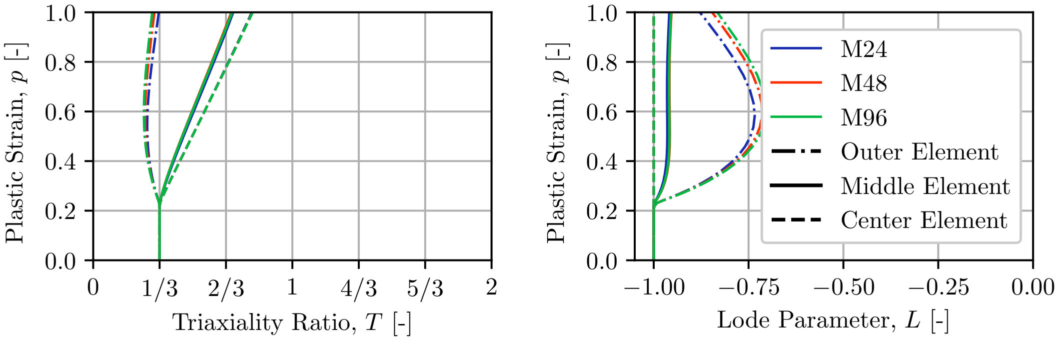

(a) *Smooth specimen*

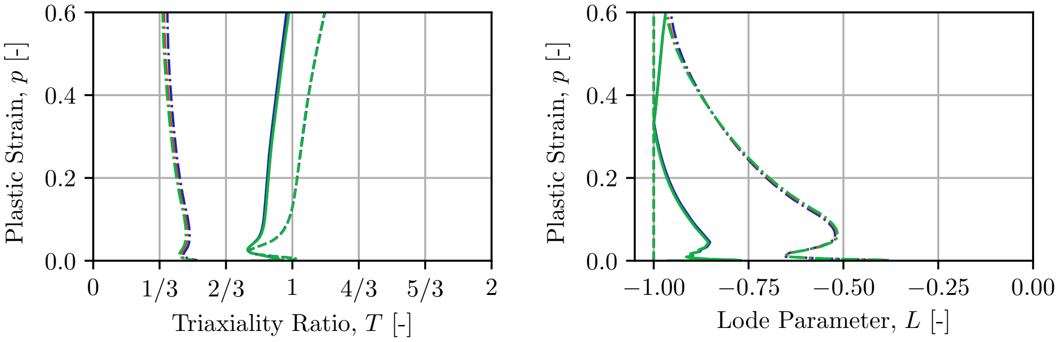

(b) *Notched specimen with* $R = 2.0$ *mm*

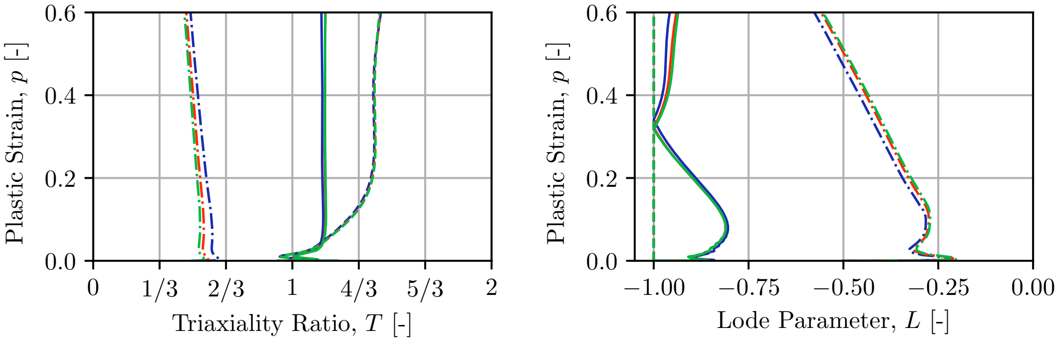

(c) *Notched specimen with* $R = 0.8$ *mm*

Figure 3.4: *Evolution of the triaxiality ratio,* T*, and Lode parameter,* L*, as a function of the plastic strain* p *in different elements of the tensile specimens. The element at the mid-section, at the surface and in between have been used, denoted center, outer and middle element, respectively. The plastic strain,* p*, is given as the plastic strain in the element and is most likely different in each element at a certain point in time.*

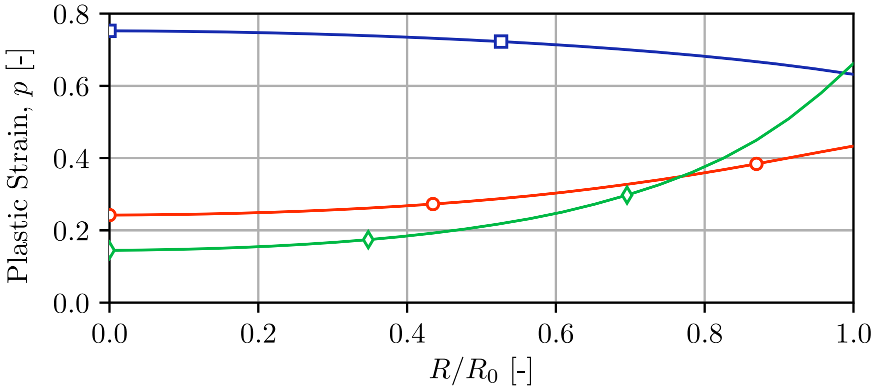

(a) *Plastic strain in each element over the cross section*

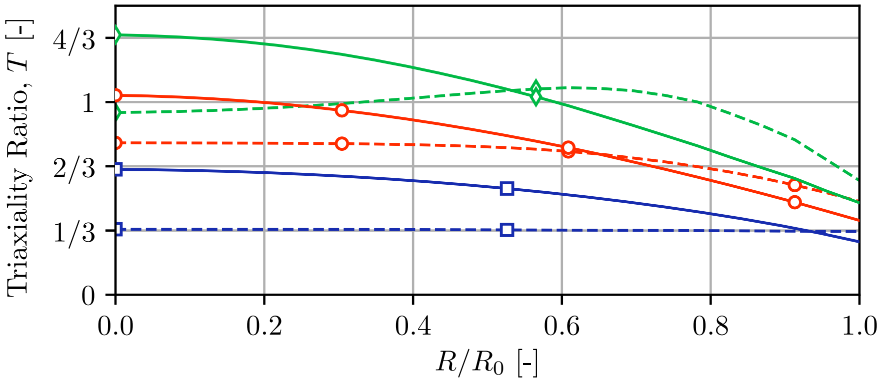

(b) *Triaxiality ratio over the cross section*

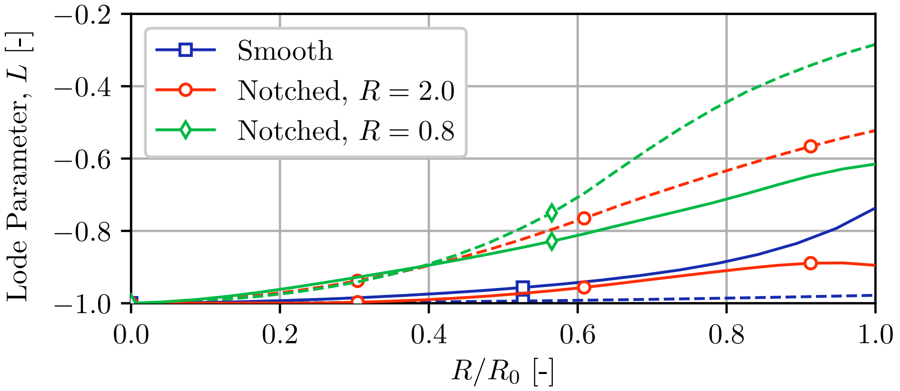

(c) *Lode parameter over the cross section*

Figure 3.5: *Evolution of different measures over the cross-section. Note that the ratio* $R/R_0 = 0$ *corresponds to the center of the specimen, whereas* $R/R_0 = 1$ *represents the specimen surface. Solid lines show the state at the fracture strain in Table 3.4. Dashed lines show the state at necking in the case of a smooth specimen, and right after the transient phase for the notched specimens.*

stress state with a Lode parameter equal to -1. As Figure 2.1 illustrates, Equation (2.5) predicts the same equivalent stress σ_{eq} for all m in this state. Nevertheless, as discussed herein, the state of $L = -1$ only applies to the center element. Elements further away from the center experience larger L. Consequently, yielding will occur at lower stresses for these elements if a Hershey yield surface with $m = 8$ is assumed. Figure 3.6 shows how the yield surface influences the response of the three different test specimens. The smooth specimen is not affected by the change in yield surface, most likely due to small variations in L. On the other hand, the $R08$ notched specimen shows notable softening. This specimen type also experienced the largest deviation in L. Despite this, the von Mises yield surface will be used for all the axisymmetric tensile bars hereafter.

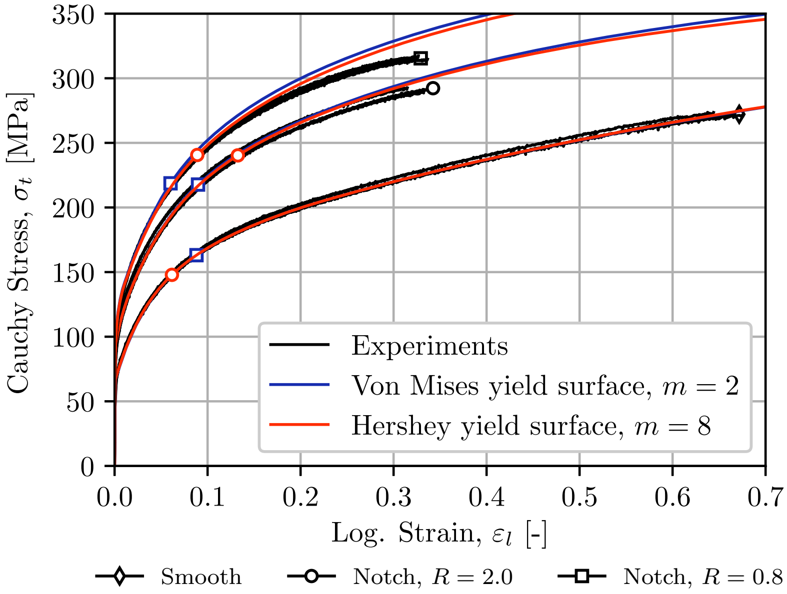

Figure 3.6: *Cauchy stress, σ_t, versus the logarithmic strain, ε_l, from simulations of all specimen types when the Hershey yield criterion in Equation* (2.5) *is applied. A user-defined subroutine from the SIMLab metal model (SMM) library has been used to include a Hershey yield surface in the simulations.*

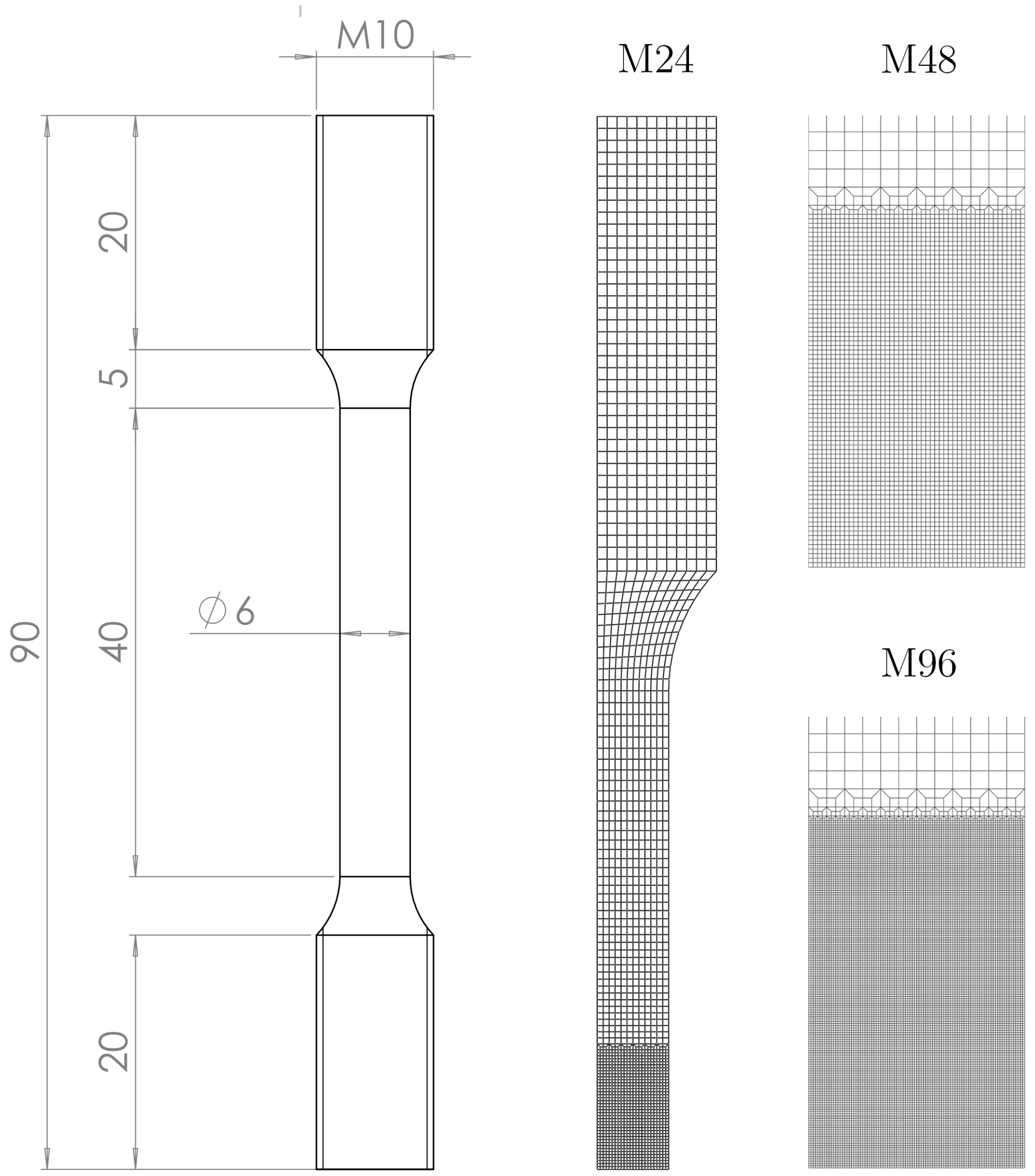

Figure 3.7: *Smooth specimen Geometry and mesh. All measurements are in mm.*

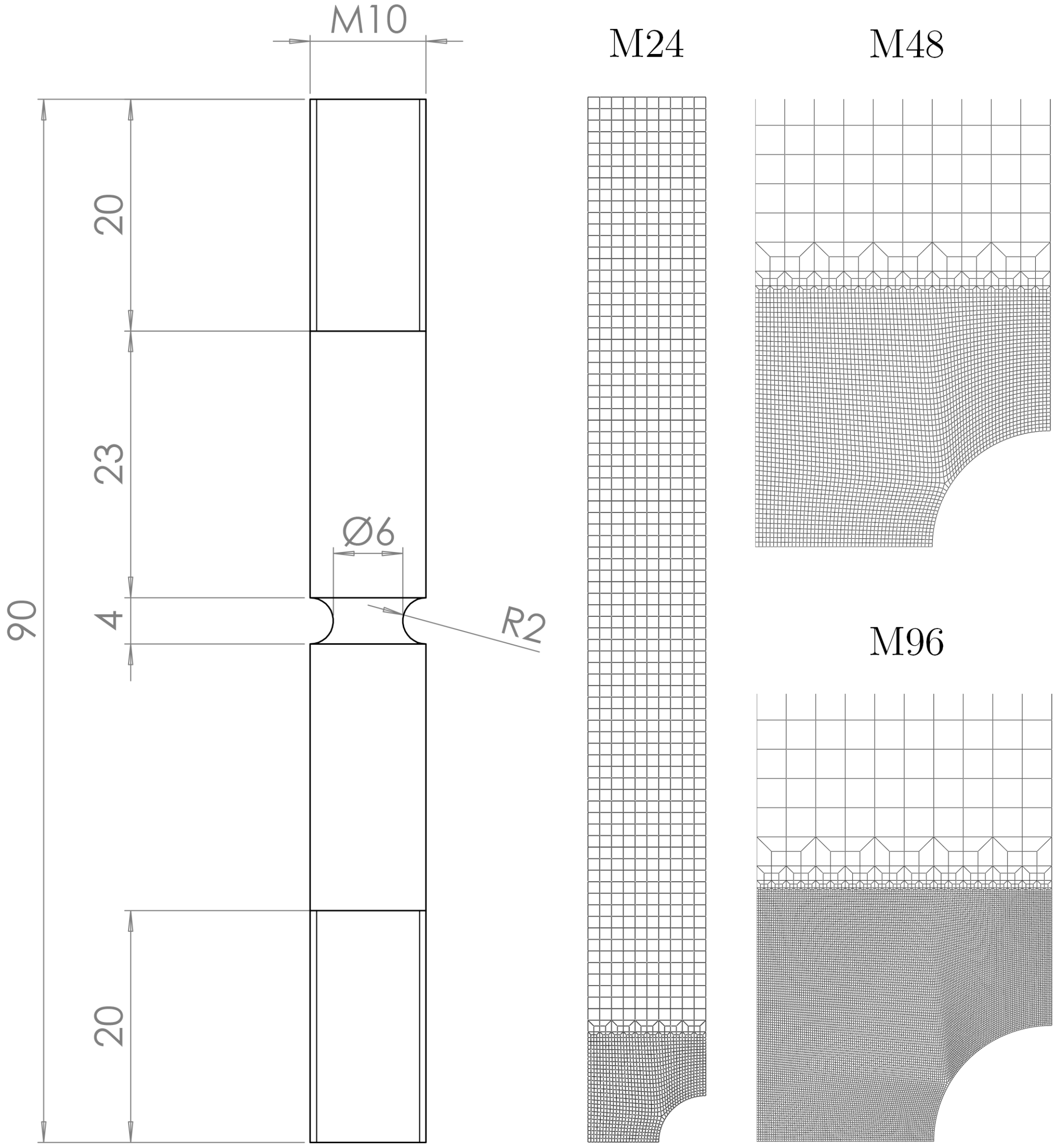

Figure 3.8: *Notched specimen with radius $R = 2.0$. Geometry and mesh. All measurements are in mm.*

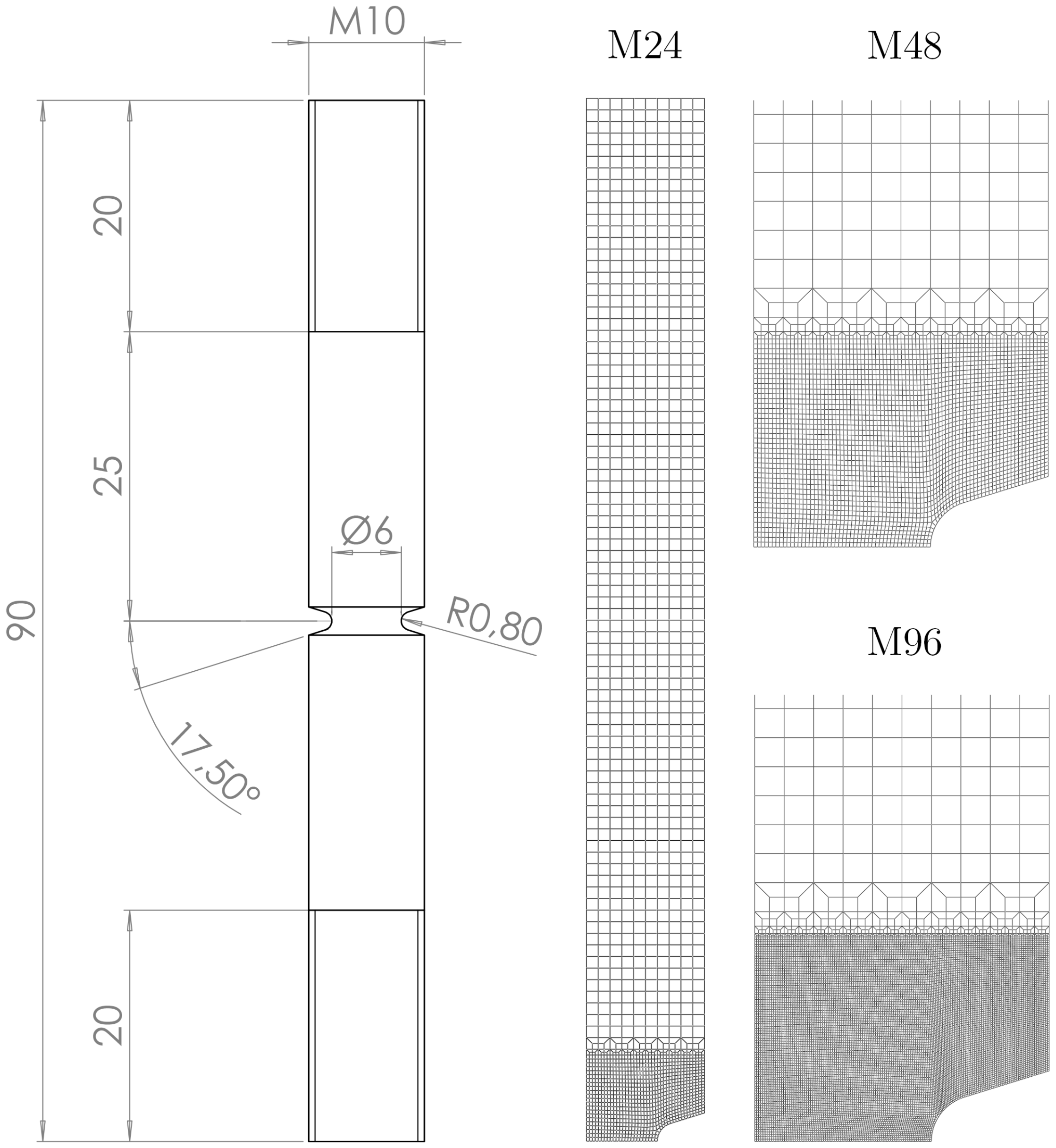

Figure 3.9: *Notched specimen with radius* $R = 0.8$. *Geometry and mesh. All measurements are in mm.*

3.3 Plane Strain Tension Tests

A plane strain tension test (PST) can be used in order to investigate the effect of the Lode parameter. Holmen et al. [39] considered such a test in a separate study using the same material. Figure 3.13 on page 52 shows the specimen geometry. The force was measured using a calibrated load cell. The displacement was found using digital image correlation (DIC) analyses, where a 5 – 6 mm long virtual extensometer was placed in the gauge area. Moreover, a 3D-DIC study confirmed the plane strain assumption [39]. Figure 3.10 plots the force-displacement curve from the experiments.

The specimen was simulated in Abaqus/Standard using 8-node linear continuum elements (C3D8R) with reduced integration and hourglass control. Symmetry was exploited for all three planes to reduce the computational time. Hence, only 1/8 of the model was simulated. The problem was discretized using 4, 8 and 12 elements over the thickness of half the gauge area, corresponding to a characteristic element size of 0.25, 0.125 and 0.063 mm, respectively. The numerical results are plotted in Figure 3.10, where the displacement was extracted in the same manner as done in the experiments. Minor differences were found between the different mesh sizes within reasonable

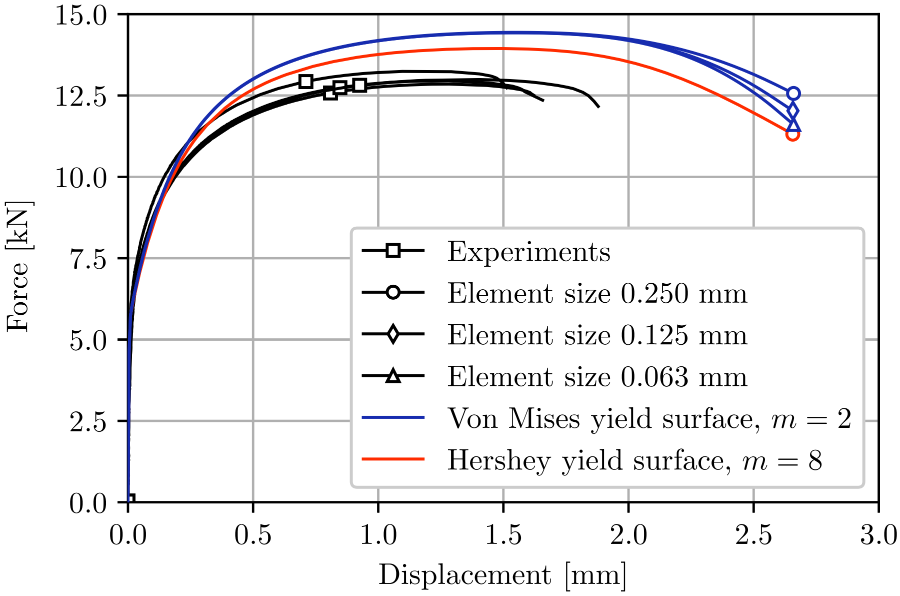

Figure 3.10: *Force versus displacement plot for the PST tests and simulations. The black lines correspond to the results from experiments. The blue colored plots show the results from simulations when J2 flow theory is applied. The red curve illustrates the results for a Hershey yield surface with* $m = 8$ *using the coarsest mesh. A user-defined subroutine from the SIMLab metal model (SMM) library has been used to include a Hershey yield surface in the simulation.*

displacement.

Classical J2 flow theory overestimated the force by more than 10%. A Hershey yield surface with $m = 8$ tends to decrease the strength in plane strain tests compared to the von Mises yield surface due to the introduction of the third deviatoric invariant J_3. The red line in Figure 3.10 illustrates this. The majority of the cross section experiences a stress state with Lode parameter between -0.5 and 0, as indicated in Figure 3.12b. The FE-model still predicts too large force. However, the results are greatly improved by considering the influence of the third deviatoric invariant on the yield surface.

It can be readily shown that $\sigma_I = 2\sigma_{II}$ in plane strain tension where $\sigma_{III} = 0$ using the associated flow rule. Assuming von Mises equivalent flow stress, Equation (2.18) and (2.19) yield $T = \sqrt{3}/3 \approx 0.577$ and $L = 0$. Figure 3.12b and 3.12c show the Lode parameter and stress triaxiality across the cross-section of the gauge area at three distinct cases; at yielding, at maximum force and at the end of the simulation. The Lode parameter is approximately -1 at the outer edges of the gauge area during the whole deformation process. At the start, $L \approx -0.5$ in the center of the specimen, but will increase rapidly as the strain increases. Figure 3.11 shows how the Lode parameter increases with the plastic strain in the center element. As the strain increases, L approaches the state of generalized shear. The red × in the figure indicates the point of maximum force where L is approximately -0.17.

The triaxiality is found to be largest in the center of the specimen at all time, as shown in Figure 3.12c. Moreover, the triaxiality ratio is initially 0.5 in the center element, and linearly increasing with the plastic straining. At the maximum force $T \approx 0.553$, which is slightly below the analytical solution.

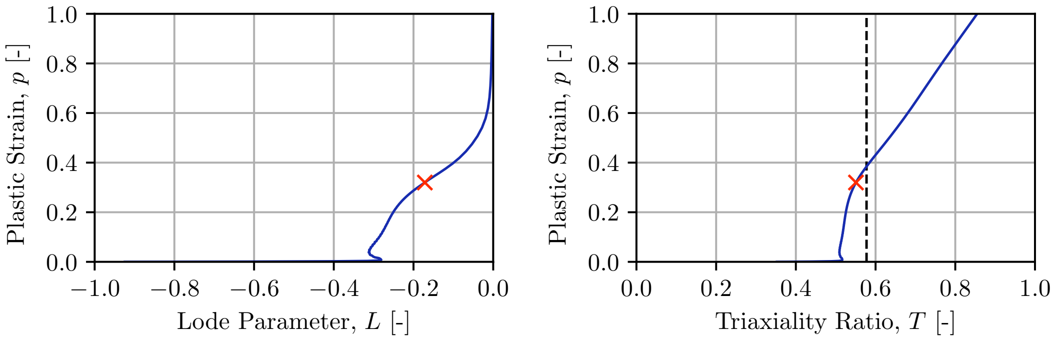

Figure 3.11: The Lode parameter, L, and stress triaxiality ratio, T, as a function of the plastic straining in the center element. The point of maximum force is marked by a red ×. The vertical dashed line represents the point in which $T = \sqrt{3}/3 \approx 0.577$

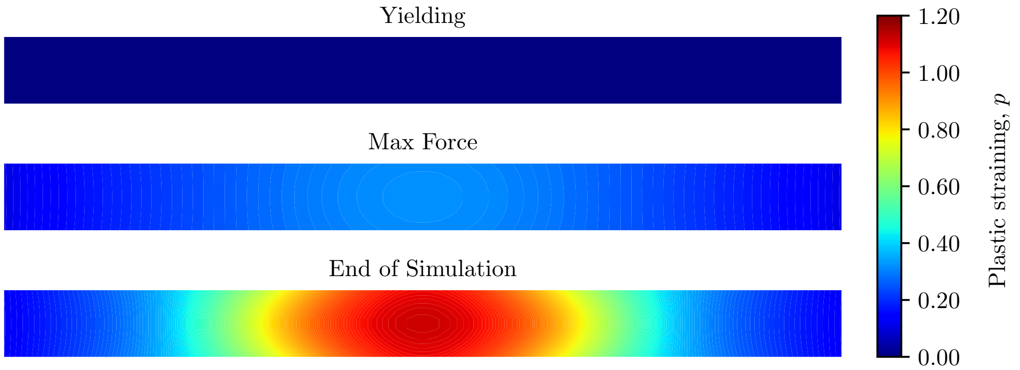

(a) *The equivalent plastic strain p over the cross section of the gauge area.*

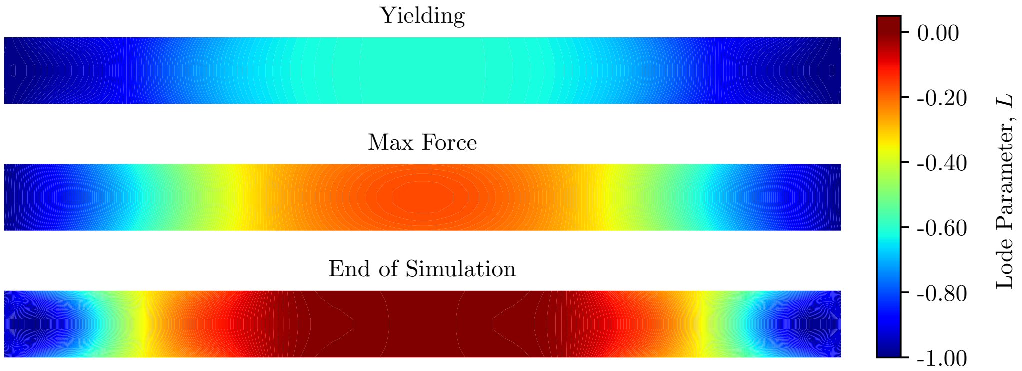

(b) *Lode parameter L over the cross section of the gauge area.*

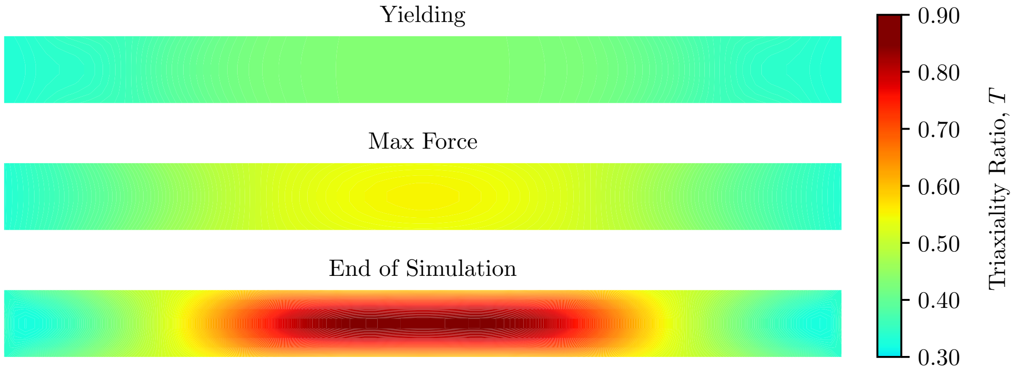

(c) *The stress triaxiality T over the cross section of the gauge area.*

Figure 3.12: *Contour plots of (a) the equivalent plastic strain p, (b) the Lode parameter L and (c) the triaxiality ratio T over the cross-section of the gauge area for three distinct cases; at yielding, at maximum force, and at the end of the simulation.*

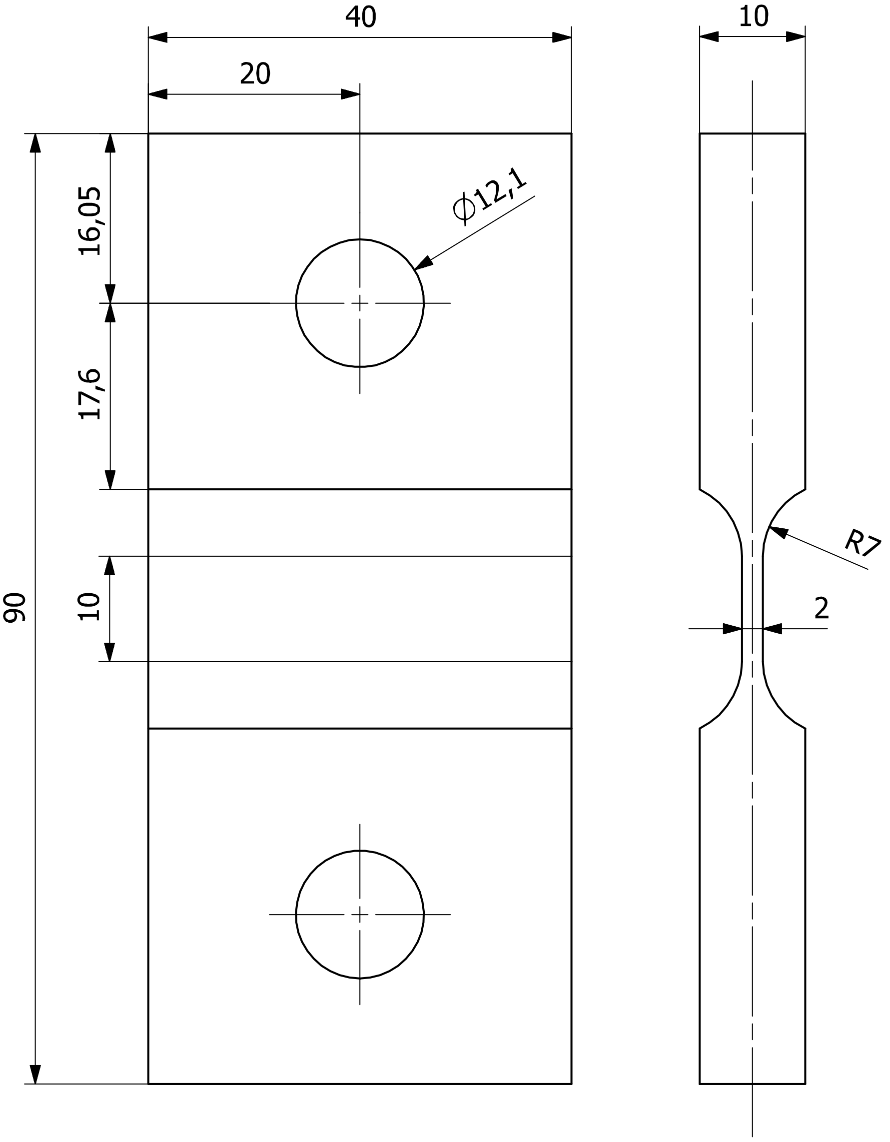

Figure 3.13: The geometry of the PST tensile specimen. All measurements are in mm.

4 Calibration of the GT Model

This chapter will present a micromechanical approach of calibrating the Gurson-Tvergaard material model from Section 2.1.6. For this purpose, the computational unit cell model introduced in Section 2.2 will be utilized to assess the mechanics of void growth and coalescence that occur on a microscopic level. The response of a single material element can then be matched to these cell simulations by choosing a suitable set of parameters for the Gurson-Tvergaard material model. The aim is to use this model to describe the macroscopic material response through these micromechanisms for different proportional load cases with constant Lode parameter L and stress triaxiality T.

Then, the performance of this unit cell approach of calibrating the Gurson-Tvergaard model will be evaluated by calibrating the same set of material constants using experimental data. An outline of the results will be presented at the end of this chapter.

4.1 Unit Cell Simulations

In order to study the mechanics of void growth on a microscopic level, a series of unit cell simulations have been conducted using the implicit solver Abaqus/Standard [58]. The theoretical background for the unit cell model used in this chapter is given in Section 2.2. It is desirable to investigate a wide range of stress states since void growth and damage evolution are dependent on both the Lode parameter, L, and stress triaxiality ratio, T. Proportional macroscopic stress states with constant L and T have therefore been imposed to the unit cell simulations.

As discussed in Chapter 3, the Lode parameter in the center of all axisymmetric tensile specimens was found to be equal to -1. Higher values of L were observed towards the specimen surface of the minimal cross-section. The same parameter in the center of the plane strain tensile specimen approaches 0 as the straining increased. However, the Gurson-Tvergard model, in its original form, does not depend on L. Due to this fact, the state of generalized tension will be the main subject of discussion in this study.

The stress triaxiality ranged from 0.33 to 1.5 for the different specimen geometries used. A sharper notch yields higher triaxiality. Consequently, V-notched and cracked specimens might experience even larger stress triaxiality ratio. The stress triaxiality may not exceed ~ 4.0 under realistic circumstances due to the decrease in strain-hardening rate at considerable plastic strain found in real materials [10]. Four stress triaxiality ratios, corresponding to 2/3, 1, 5/3 and 3, will for these reasons be imposed to the unit cell.

Investigating stress states of lower triaxialities would be beneficial. However, lower triaxialities will result in closing of voids and cannot be represented by the initially voided unit cell. This effect is illustrated in Figure 4.1, where the red shaded area represents the void surface before and after deformation. A remedy is to include a particle inside the void, but this will be omitted in this thesis. Moreover, the Gurson-Tvergaard model tends to overestimate the rate of void growth when the triaxiality becomes low [10] due to the assumption of spherical void evolution. This assumption becomes less true in the lower triaxiality domain. Consequently, the Gurson-Tvergaard model is better suited for intermediate to high stress triaxialities [25].

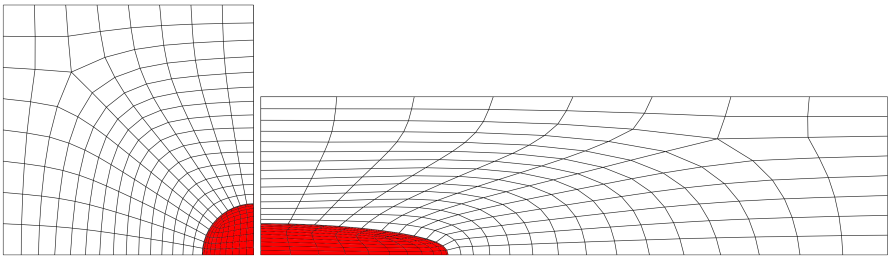

Figure 4.1: *Deformation of a unit cell under generalized tension when* $T = 1/3$*. Notice how the void is closing as the unit cell is deformed.*

Figure 4.2 displays the 1/8 computational cell model used in this thesis. It was established using a Python script provided by postdoctoral researcher Lars Edvard Dæhli [64]. A mesh study was carried out to ensure convergence. The details from this study are presented in Section 4.1.1. Based on these results, a unit cell mesh discretization consisting of 1580 linear 8-node brick elements (C3D8) was employed.

The initial unit cell length was chosen to be $\bar{L}_0 = 1$. ALSTRUC estimated an initial void fraction of $f_0 = 0.00452$. Thus, from Equation (2.54), the radius of the spherical void is $\bar{R}_0 = 0.205$. Symmetry conditions were employed to the three inner faces of the unit cell as shown in Figure 4.2b. A red color marks these faces. Further, a user-defined multi-point constraint (MPC) subroutine was utilized to ensure proportional loading of

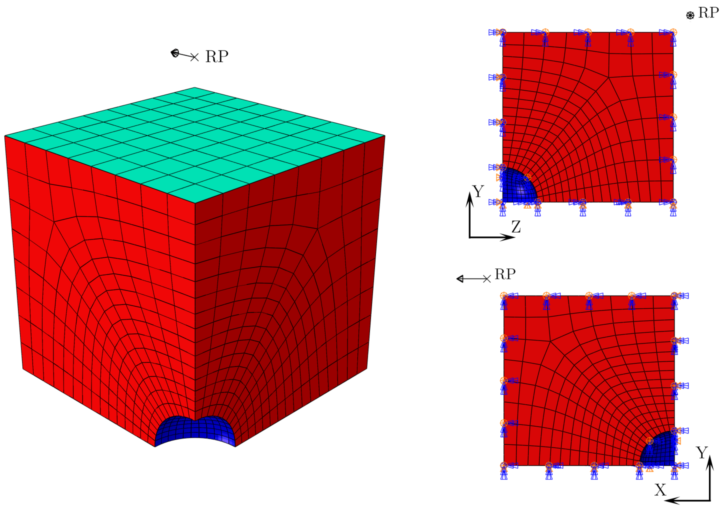

(a) ***(b)***

Figure 4.2: *The* 1/8 *unit cell model used in this thesis. Red color marks the inner faces of the unit cell. Symmetry conditions are employed on these faces, as shown in (b). Turquoise and blue color mark the outer faces and the void surface, respectively. The rigid point just outside the unit cell is denoted as RP.*

the cell. This constraint connects the three outer faces of the cell model to a rigid point (RP), located just outside of the unit cell. A turquoise color marks the outer faces in Figure 4.2. To ensure the assumption of a periodic array of unit cells, these faces must remain straight and move as rigid planes. Equation (2.60) describes the relationship between the displacement of the rigid point and the boundary displacements.

The macroscopic stress of the unit cell can be found by taking the volume average of the stress at the integration points for all elements by the following equation

$$\boldsymbol{\Sigma} = \frac{1}{V_{mat}} \sum_{j=1}^{n_{int} n_{els}} \boldsymbol{\sigma}_j V_j, \qquad V_{mat} = \sum_{j=1}^{n_{int} n_{els}} V_j \tag{4.1}$$

where V_{mat} is the material volume, n_{int} is the number of integration points for each element and n_{els} is the number of elements. Moreover, $\boldsymbol{\sigma}_j$ and V_j are the microscopic stress tensor and volume associated with integration point j, respectively. Lastly, $\boldsymbol{\Sigma}$ is the macroscopic stress tensor of the unit cell. The macroscopic von Mises equivalent stress Σ_{eq}^{VM} can then easily be calculated using Equation (2.55).

Furthermore, the macroscopic principal logarithmic strains are found by

$$E_i = \ln\left(1 + \frac{\Delta D_i}{\bar{L}_i}\right) \tag{4.2}$$

where ΔD_i and $\bar{L}_i$ are the boundary displacement and unit cell length in direction i, respectively. Moreover, E_i is the principal strain in direction i. The work conjugate macroscopic strain to the von Mises stress, E_{eq}^{VM}, can then be calculated using Equation (2.56).

The matrix material has been modeled using the Voce work-hardening rule given by Equation (2.4). To this end, the material constants given in Table 3.3 for the AlMgSi alloy have been used. Accordingly, it is assumed that the voids have only minor effects on the work-hardening at the low triaxialities that occur in the smooth specimen [38, 65].

4.1.1 Mesh Convergence Study

A mesh convergence study was conducted on the unit cell model to ensure adequate results within a reasonable amount of computational effort. The mesh density was increased by doubling the number of elements at the edges of the cell. The three meshes, denoted mesh 1, 2 and 3, are shown in Figure 4.4. All meshes were simulated using a linear 8-node brick element (C3D8). Only mesh 2 was simulated using a reduced integrated quadratic 20-node brick element (C3D20R). The case of generalized tension is presented herein. However, the findings for generalized compression and shear were similar to that of generalized tension. Figure 4.3 presents the results as a plot of the normalized von Mises stresses and porosity as a function of the equivalent strain.

The discrepancies between the four different cases of discretization are small, especially at high triaxiality ratios. The computational cost was, however, heavily increased with

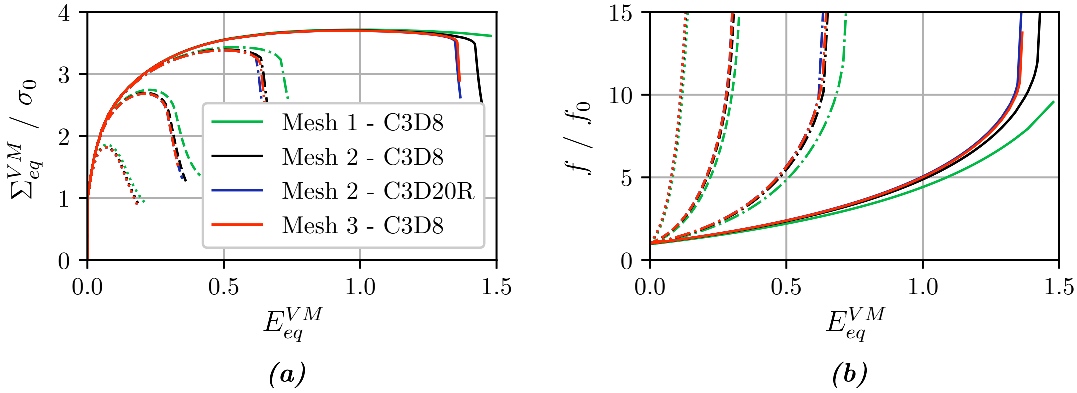

Figure 4.3: *(a) Normalized macroscopic von Mises equivalent stress and (b) normalized porosity as a function of the macroscopic equivalent strain for the different meshes. Only the case of generalized tension is included. The triaxiality ratio ranges from $T = 3$ in the left to $T = 3/2$ in the right.*

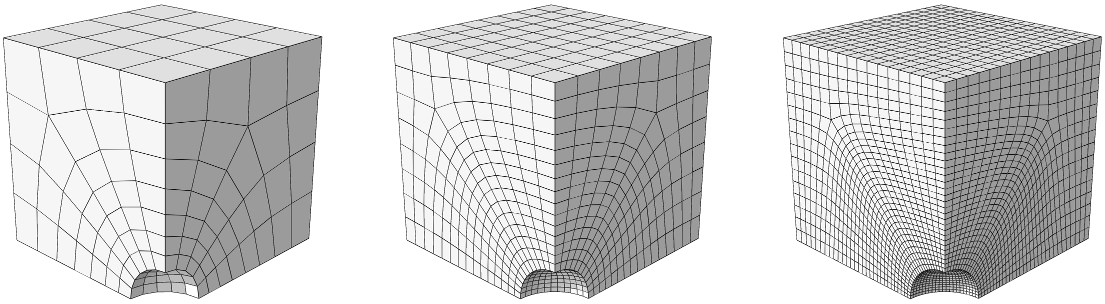

(a) Mesh 1 *(b) Mesh 2* *(c) Mesh 3*

Figure 4.4: *The three meshes used in the mesh convergence study. Mesh 1 consists of 172 elements, Mesh 2 of 1580 elements and Mesh 3 of 11070 elements.*

the refinement of the mesh. The average wall clock time for mesh 1 was 26 seconds, whereas the average wall clock time for mesh 2 and 3 was 167 and 1686 seconds, respectively. Despite this, mesh 2 is not too computationally expensive and can easily be carried out on a laptop. Due to the deviation between Mesh 1 and 2 at large strains, and the fact that a coarse mesh cannot represent the void volume accurately, mesh 2 with C3D8 elements is the preferred discretization of the unit cell.

4.1.2 Unit Cell Results

The case of generalized tension will be considered. Figure 4.7 on page 60 illustrates the deformation and void evolution of the unit cell in the case of $T = 2/3$ and $T = 3$ at three different stages; initial condition, at maximum stress and at the point of void coalescence. The effect of the stress triaxiality on the cell response can be seen in Figure 4.5.

Figure 4.5a shows how the macroscopic equivalent stress versus the equivalent strain response is affected by the triaxiality ratio. The higher the triaxiality, the lower the straining. Furthermore, Figure 4.5b illustrates how the porosity evolves as the cell deforms. As the porosity grows, the macroscopic response softens. A clear competition between the effect of the strain hardening of the matrix material and the softening induced by void growth is visible. The latter effect is more prominent at high triaxialities. This observation corresponds well with the main response seen experimentally, where the ductility decreases with increasing stress triaxiality due to extensive void growth [26].

Figure 4.5c illustrates how the principal strain E_{II} in Y-direction, and thus the principal strain E_{III} in Z-direction, evolves with the macroscopic equivalent strain E_{eq}^{VM}. At one point, marked by a red ×, the homogeneous deformation terminates, and the deformation proceeds in a uniaxial deformation mode in the X-direction. This mode is illustrated by the rightmost cell configuration in Figure 4.7. Localization of the deformation in the inter-void ligament in the Y- and Z-direction occurs after this point, while the material outside the ligament unloads elastically. Physically, this represents the link-up with a neighboring void from an adjacent unit cell [2]. This transition has been referred to as the onset of coalescence in other literature [66]. As shown in Figure 4.5a and 4.5b, at this point the void volume fraction f increases rapidly and the cell starts to lose its load carrying capacity. This point is especially prominent at lower triaxiality ratios.

The stress triaxiality ratio also influences the change in aspect ratio w of the void shape, as illustrated in Figure 4.5d. The aspect ratio is defined as

$$w = \frac{R_x}{R_y} \tag{4.3}$$

where R_x and R_y are the radius of the void in X- and Y-direction, respectively. The void will evolve into a prolate shape in the case of $T = 2/3$ and $T = 1$. Figure 4.7a illustrates this. On the contrary, an oblate shape is obtained for $T = 3$, as shown in Figure 4.7b. It is rather counterintuitive that the void grows laterally when the principal loading direction is vertical. At high triaxiality, however, the hydrostatic stress is sufficient to cause this behavior. Moreover, an almost spherical void growth is obtained for $T = 5/3$ before coalescence. Note that all these findings correspond well with the results for the axisymmetric cell model used by Benzerga et al. [10].

The macroscopic equivalent strain and porosity at the onset of void coalescence as a function of the stress triaxiality ratio are shown in Figure 4.6a and 4.6b, respectively. Clearly, higher triaxialities decrease the critical strain E^c_{eq}. This is due to the rapid void growth at large T, as already discussed. The critical void volume fraction f_c seems to be somewhat unaffected by the triaxiality, revealing an almost constant f_c. It must be emphasized that the porosity f increases rapidly once coalescence starts, making the critical void volume fraction hard to evaluate accurately. A constant f_c is, however, favorable for practical purposes.

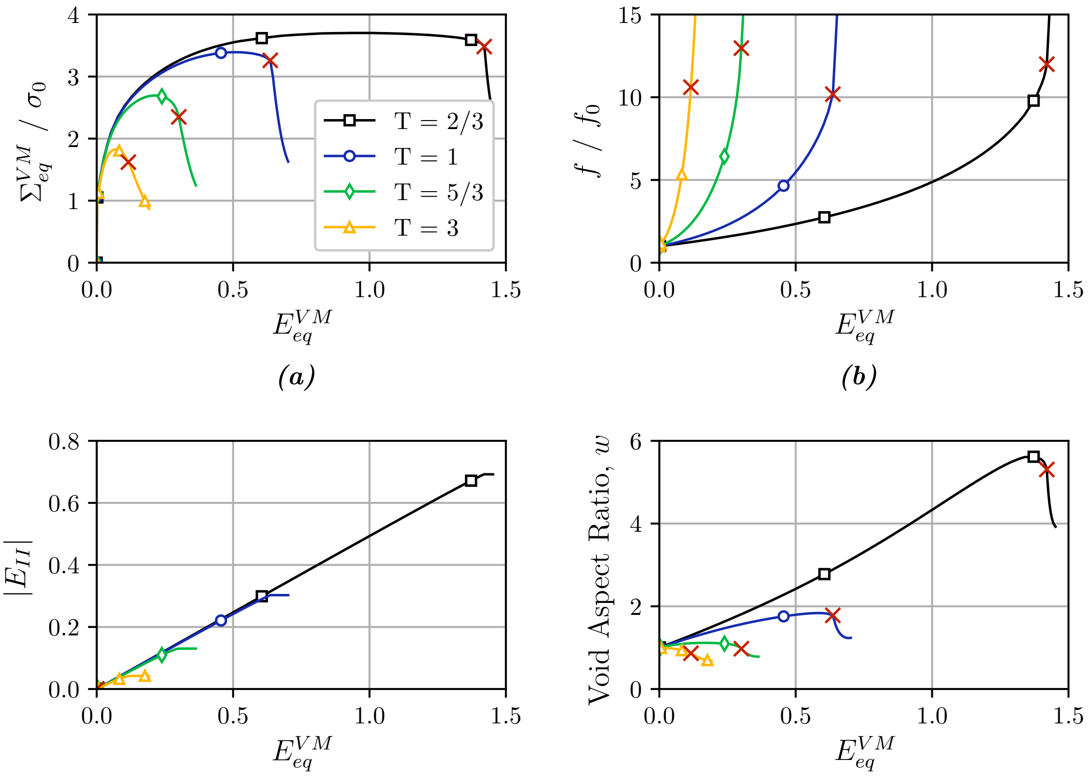

(a) *(b)* *(c)* *(d)*

Figure 4.5: *Plots of the unit cell response under generalized tension showing the effect of the stress triaxiality ratio T. The onset of coalescence is marked by a red ×. (a) Normalized equivalent von Mises stress versus equivalent strain, E_{eq}^{VM}. The initial yield stress of the matrix is denoted σ_0. (b) Normalized void volume fraction versus E_{eq}^{VM}, where f_0 is the initial porosity. (c) Principal strain E_{22} versus E_{eq}^{VM}. (d) Void aspect ratio, $w = R_1/R_2$, versus E_{eq}^{VM}.*

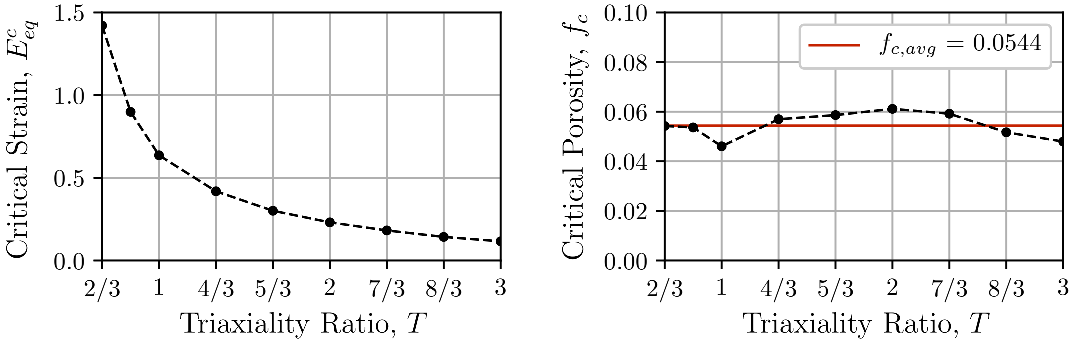

(a) *Critical strain, E_{eq}^c*

(b) *Critical porosity, f_c*

Figure 4.6: *(a) The critical strain, E_{eq}^c, and (b) critical porosity, f_c, versus the triaxiality ratio T for $L = -1$.*

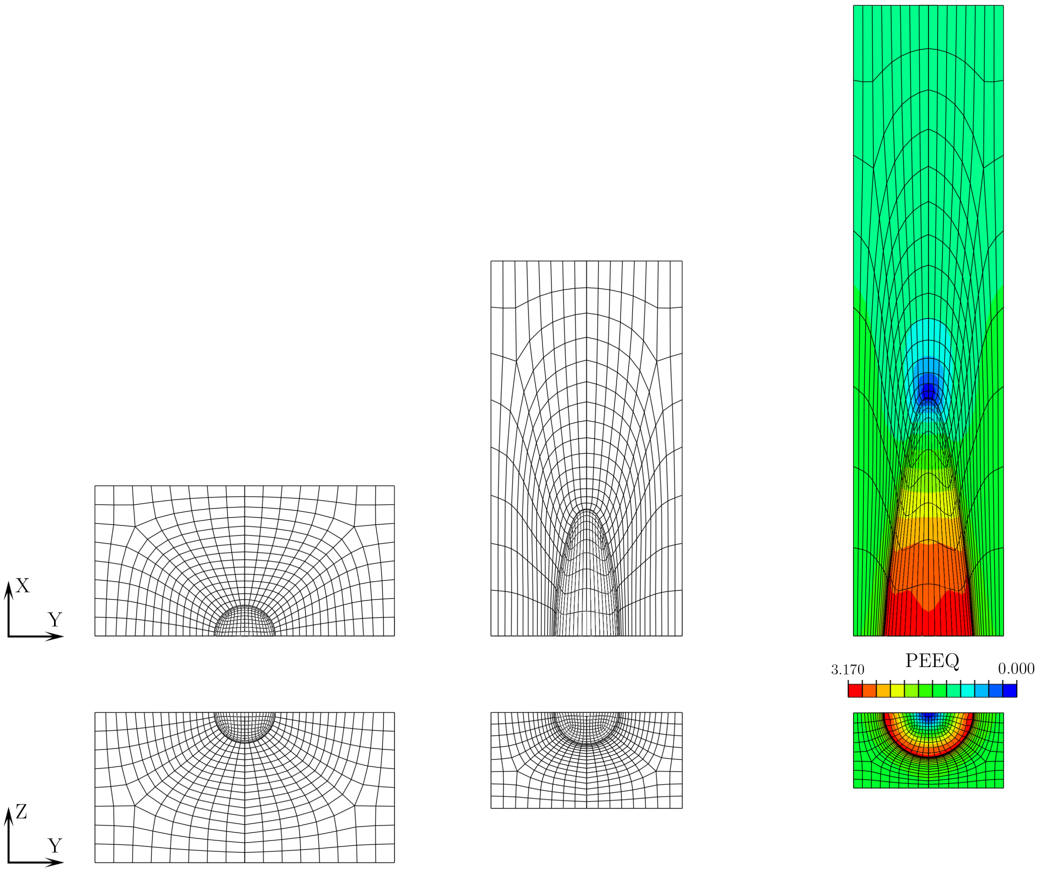

(a) $T = 2/3$

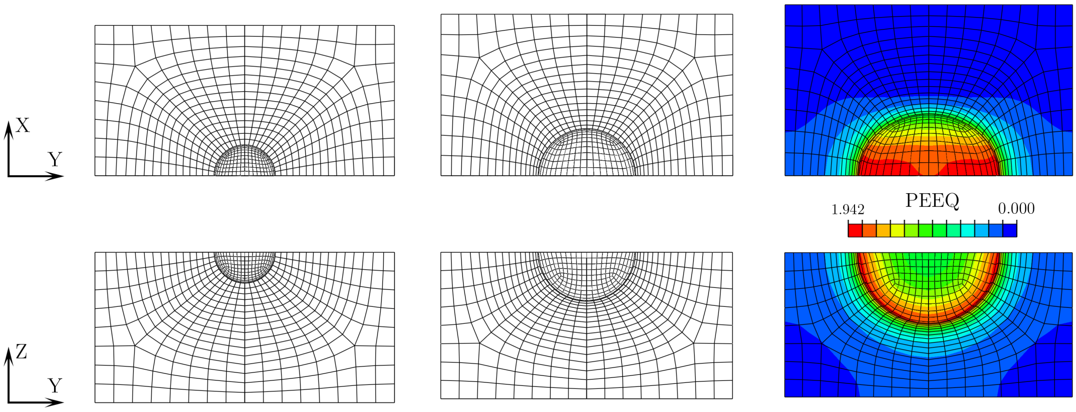

(b) $T = 3$

Figure 4.7: *Void growth for (a)* $T = 2/3$ *and (b)* $T = 3$ *under generalized tension in the XY- and YZ-plane. The leftmost figures represent the initial conditions. The middle figures represent the deformation at maximum stress. The rightmost figures represent the deformation at void coalescence.*

4.2 Calibration of the GT-Model Using Unit Cells

4.2.1 Calibration Procedure

Assuming that the results from the unit cell analyses presented in Section 4.1.2 provide an adequate representation of material response and void growth on a microscopic level, these curves can be used to calibrate the material constants in the Gurson-Tvergaard model. The initial porosity, f_0, is known from before. Thus, only the two model parameters q_1 and q_2 need to be determined. The main essence is that a material element should be able to render the cell response accurately when a porous plasticity model is applied to this element. Thus, one can determine the optimal set of q_i by comparing the response of a single element with the unit cell response under different proportional loading cases.

The two residuals e_Σ and e_f will be introduced to evaluate the discrepancies between the porous plasticity model and the unit cell model concerning both stress-strain history and evolution of porosity. These residuals are defined as a weighted averages in the same manner as done by Dæhli et al. [24]

$$e_\Sigma = \frac{1}{N_{SS}} \sum_{i=1}^{N_{SS}} \frac{\displaystyle\int_0^{E_{eq}^{max}} \left| \Sigma_{eq}^{PPM} - \Sigma_{eq}^{UC} \right|_i dE_{eq}}{\displaystyle\int_0^{E_{eq}^{max}} \frac{1}{2} \left(\Sigma_{eq}^{PPM} + \Sigma_{eq}^{UC} \right)_i dE_{eq}} = \frac{1}{N_{SS}} \sum_{i=1}^{N_{SS}} \frac{\text{▨}_i}{\text{▨}_i} \tag{4.4a}$$

$$e_f = \frac{1}{N_{SS}} \sum_{i=1}^{N_{SS}} \frac{\displaystyle\int_0^{E_{eq}^{max}} \left| f^{PPM} - f^{UC} \right|_i dE_{eq}}{\displaystyle\int_0^{E_{eq}^{max}} \frac{1}{2} \left(f^{PPM} + f^{UC} \right)_i dE_{eq}} = \frac{1}{N_{SS}} \sum_{i=1}^{N_{SS}} \frac{\text{▨}_i}{\text{▨}_i} \tag{4.4b}$$

Here, N_{SS} is the total number of stress states. The equivalent stress Σ_{eq}, equivalent strain E_{eq} and porosity f are defined in the same manner as earlier. The shaded squares is defined by the area under the graph in Figure 4.8. Data from the porous plasticity model and unit cell are denoted PPM and UC, respectively. The integral limit E_{eq}^{max} is defined as the point when the stress in the unit cell is reduced by 5% of its maximum value due to softening, i.e., $E_{eq}^{max} = E_{eq}(0.95\Sigma_{eq}^{max})$. This point is indicated by a red dot in Figure 4.8. The maximum stress is achieved when $\dot{\Sigma}_{eq}^{VM} = 0$. This way both void growth and material softening are accounted for in the calibration. Figure 4.8 shows an example of the macroscopic stress-strain relation and porosity evolution from a UC and a PPM simulation. To put the errors in Equation (4.4) into scale, the errors in this particular case are $e_\Sigma = 0.17$ and $e_f = 0.36$. The error due to void growth was in

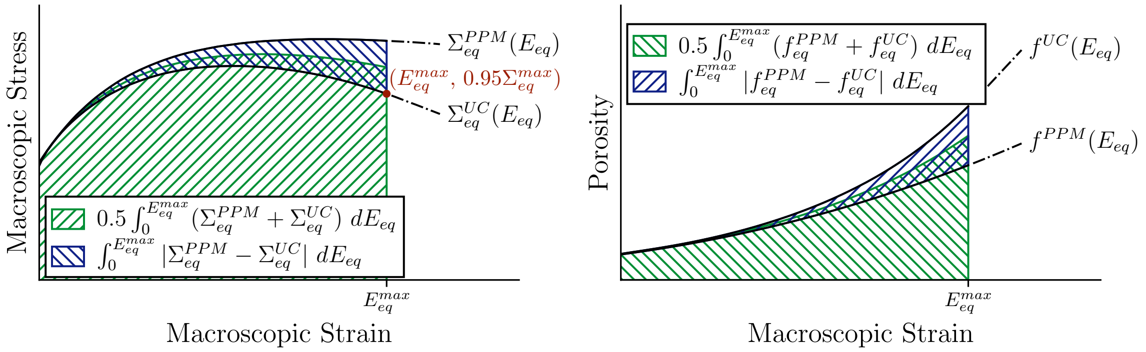

Figure 4.8: *The macroscopic stress and porosity as a function of the macroscopic strain for a unit cell (UC) and a porous plasticity model (PPM) analysis. The numerator and denominator from Equation* (4.4) *are shaded with a blue and green color, respectively. The error in this example was found to be* $e_\Sigma = 0.17$ *and* $e_f = 0.36$.

general found to be the largest. Furthermore, the total error is defined as

$$e = w_\Sigma e_\Sigma + w_f e_f = w_\Sigma e_\Sigma + (1 - w_\Sigma)e_f \tag{4.5}$$

where w_Σ and w_f are the weight of the error due to the stress response and void growth, respectively. Equal weight has been utilized in this thesis, i.e., $w_\Sigma = w_f = 1/2$. Only minor differences in the calibrated q_1 and q_2 values were found when varying these weights.

Only the state of generalized tension has been accounted for in this calibration process. All triaxiality ratios covered in Section 4.1 are used. Contour plots of the total error are displayed in Figure 4.9 for different ranges of q_1 and q_2. These plots have been obtained by running numerous single element simulations over a certain domain in the q_i-space. A Python script has been used to pre-process the data from the simulations and to make the error plot. This script can be found in Appendix B.1. Figure 4.9a shows a broad spectrum of q_i-values. From this, one can conclude that there exist a large number of sets with q_i-values which will result in a low error. This low error region, which stretched over the q_i domain, will from now on be referred to as the band of minimum error. Values in the lower center domain of the plot predict the best fit between the unit cell and porosity simulations. Figure 4.9b shows a more refined domain with higher resolution of data points. The total error was found to increase more rapidly in the upper right domain from the band of minimum error. This is believed to do with extensive softening of the PPM model.

A sequential least-square optimization procedure has been employed to determine the set of q_i-values which is related to the lowest error. The SLSQP minimization solver in the Scipy Python package [63] has been used for this purpose. It must be emphasized

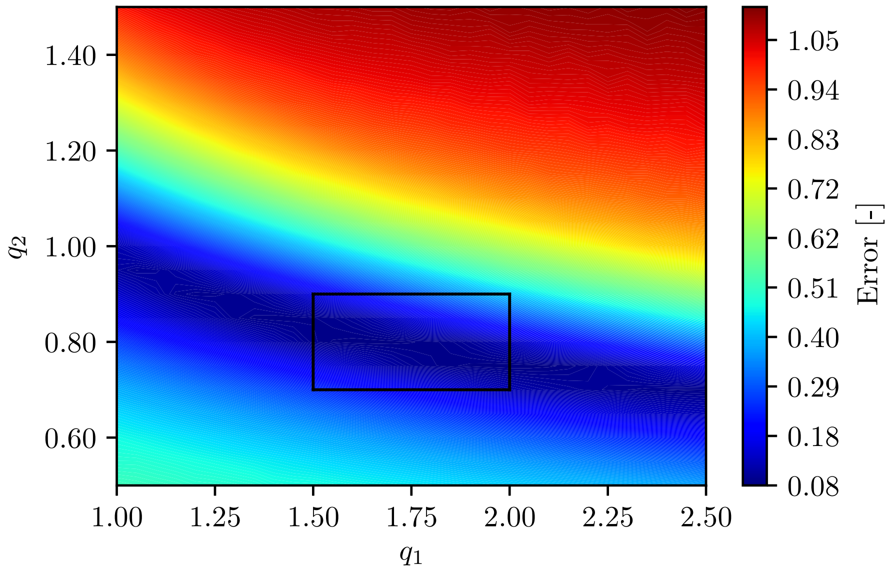

(a) *Global error plot*

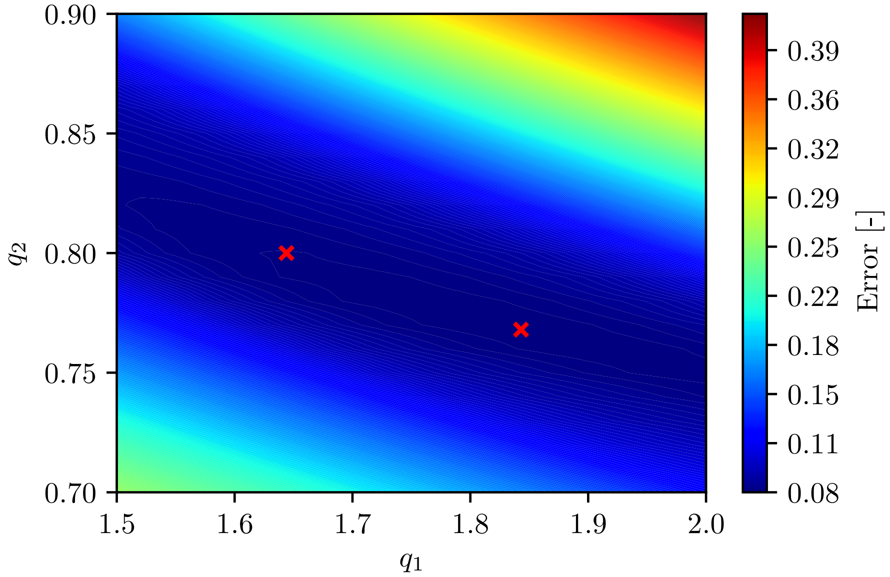

(b) *Local error plot*

Figure 4.9: *Contour plots of the error in the* q_i*-space. In (a),* $q_1 \in [1.0, 2.5]$ *and* $q_2 \in [0.5, 1.5]$ *with a resolution of* 31×21 *points. In (b),* $q_1 \in [1.5, 2.0]$ *and* $q_2 \in [0.7, 0.9]$ *with a resolution of* 51×21 *points. This corresponds to* $\Delta q_i = 0.01$ *and a total of* 4284 *single element simulations. The domain of figure (b) is marked by a black square in figure (a). Red* × *corresponds to the case of* $[1.843, 0.768]$ *(rigth* ×*) and* $[1.644, 0.800]$ *(left* ×*). The error at these two points is given in Table 4.1.*

that the error-surface in the q_i-space is not entirely smooth, and there exist many local minimums as q_1 and q_2 are refined. This makes the iteration process somewhat ambiguous. Nevertheless, q_1 and q_2 down to three decimals have been determined.

Moreover, as the low error region spans over the q_i-space it might be sufficient to only vary one of the variables. This will make the calibration process less laborious. Figure 4.10 shows the error versus q_1 when $q_2 = 0.8$. The results from these two procedures are given in Table 4.1. The set of q_i-values are marked by a red × in Figure 4.9b.

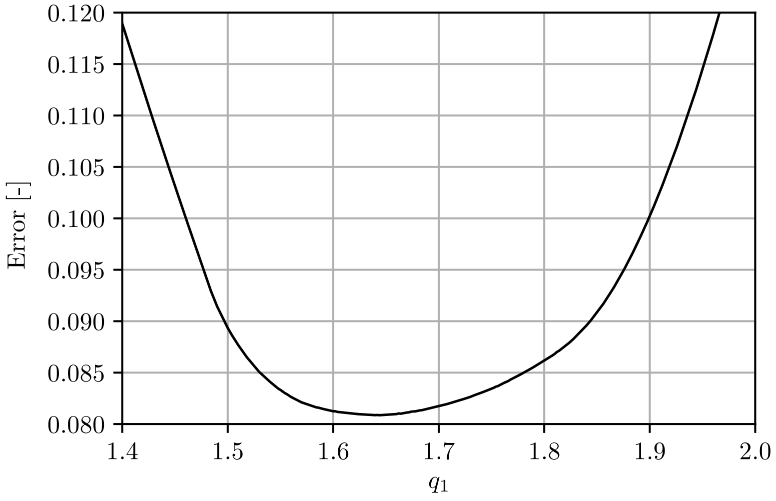

Figure 4.10: *Error as a function of* q_1 *when* q_2 *is kept constant, equal to 0.8.*

Table 4.1: *Results from the fitting process when optimizing in the* q_i*-space and along the* $q_2 = 0.8$ *line with corresponding errors.*

	q_1	q_2	e_Σ	e_f	e
Global calibration	1.843	0.768	0.0151	0.1440	0.0795
$q_2 = 0.8$ calibration	1.644	0.800	0.0136	0.1482	0.0809

Figure 4.11 compares the porous plasticity model with the unit cell model. The Gurson-Tvergaard material model is obviously able to represent the unit cell response. However, the cases of $T = 5/3$ and $T = 2/3$ yield the most significant discrepancies. Moreover, the porous plasticity model softens too much in the case of $T = 2/3$ and too little in the case of $T = 5/3$ and 3. The same trend appears in the void growth, where the lowest triaxiality ratio experience too extensive void growth. A stress triaxiality equal to unity yields good result in terms of the stress-strain response. Additionally, only minor differences are found between the two sets of optimized q_i-values. Figure 4.11b shows a somewhat better fit in the lower triaxiality domain, but the differences are probably negligible.

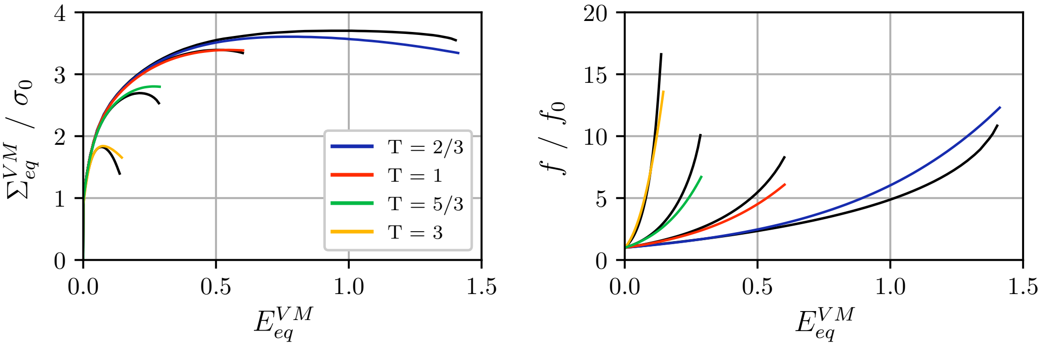

(a) *Global calibration;* $q_1 = 1.843$ *and* $q_2 = 0.768$

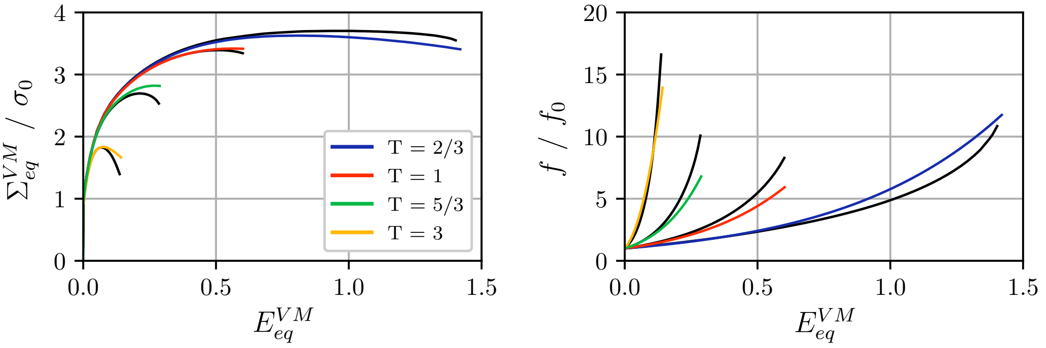

(b) $q_2 = 0.8$ *calibration;* $q_1 = 1.644$ *and* $q_2 = 0.800$

Figure 4.11: *The normalized macroscopic von Mises equivalent stress and porosity versus equivalent macroscopic strain in the case of (a) a global calibration and (b) when* $q_2 = 0.8$ *is kept constant. Black lines represent the unit cell response.*

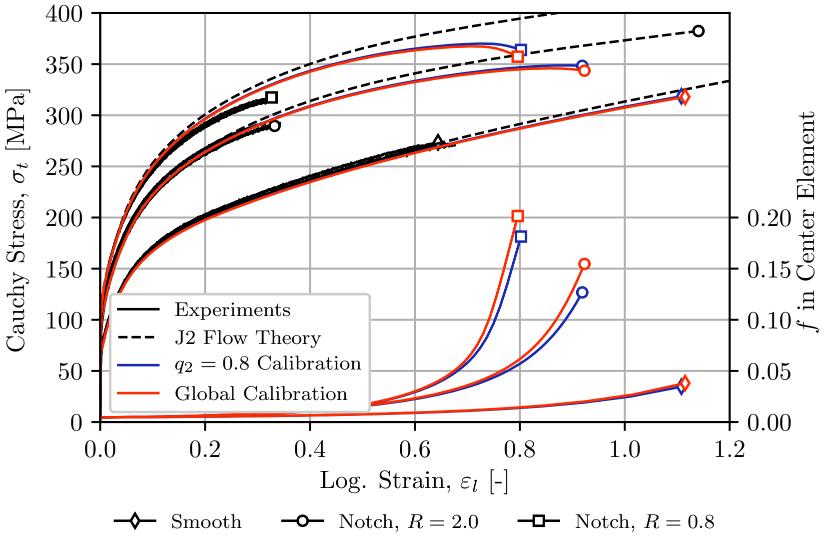

Figure 4.12: *The Cauchy stress,* σ_t*, versus the logarithmic strain,* ε_l*, for the smooth and notched specimens. The dashed lines represent the results obtained from J2 flow theory, i.e., when the initial void content is 0. Solid lines show the results when a porous plasticity material model is used with the constants in Table 4.1.*

Figure 4.12 shows the response of the tensile specimens from Section 3.2 when the Gurson-Tvergaard model is used. The specimens experience some softening compared to the results obtained by the classical J2 flow theory. Furthermore, the softening is more prominent in the notched specimens as expected. The two sets of q_i-parameters in Table 4.1 give almost indistinguishable results.

Figure 4.13 compares the porous plasticity model for five different configurations of the model parameters. The q_1 and q_2 parameters are linearly increased towards the far right and upper plot, respectively. The softening effect is more prominent as the q_1 and q_2 increase. Moreover, the PPM simulations reveal somewhat similar response for the very left and lower plot. The same can be said for the very right and upper plot as well. Consequently, there may exist many configurations of q_1 and q_2 that give almost the same response. This can be related to the change in yield surface shown in Figure 2.6. As discussed in Section 2.1.6, a change in q_2 yields a greater influence on the yield surface compared to a change in q_1. The same trend is visible in the figure below as well. This also explains why a band of minimum error occurs in the q_i-space.

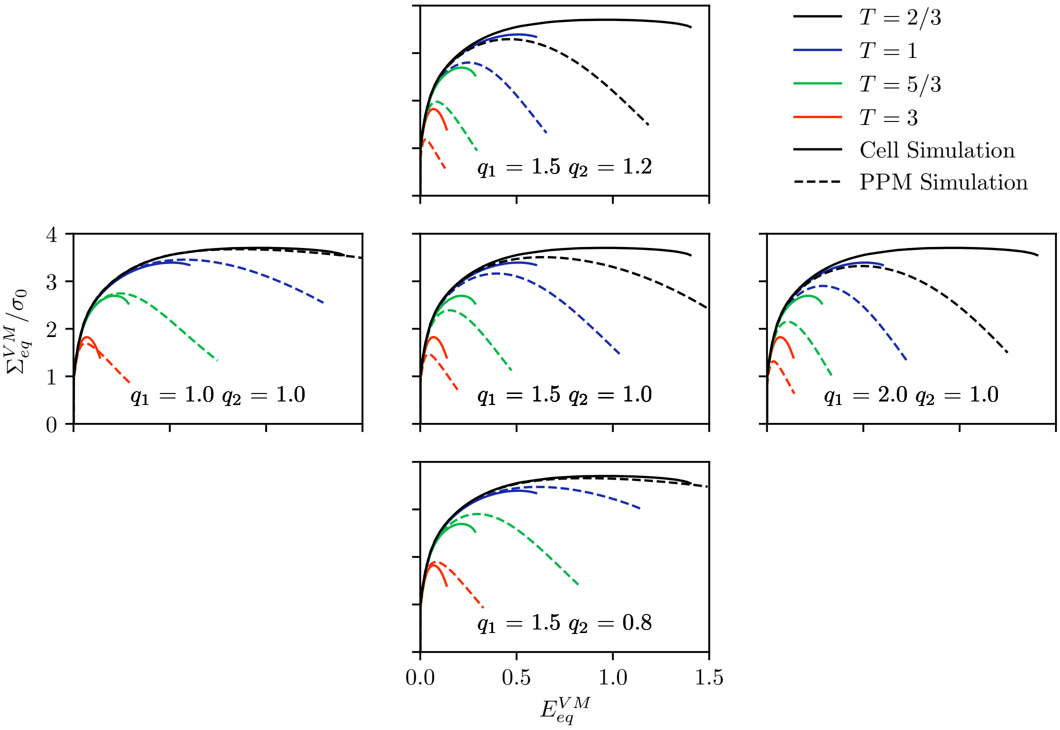

Figure 4.13: *The PPM response for different configurations of q_1 and q_2. The q_1 is increased from 1 to 2 (from left to right plot) and q_2 is increased from 0.8 to 1.2 (from lower to upper plot). Solid lines represent the results obtained from unit cell simulations and are the same in all plots. Dashed lines show the result from PPM simulations.*

4.2.2 Parametric Study

The approach of calibrating the Tvergaard parameters taken in the previous section is rather straightforward. This section will examine some important parameters and how these will influence the error in q_i-space. Parameters directly associated with the calibration process, such as the stress states and the influence of non-proportional loading path, will be investigated using the hardening parameters and initial void content as previously. Moreover, a study of the initial void content and the matrix material response will be presented afterward.

Influence of Stress States

The range of stress triaxialities covered herein is quite extensive. Many practical applications may not experience triaxialities as high as 2. As Figure 4.14 indicates, the error plot depends on the stress states used in the calibration process. Figure 4.14a and 4.14b show the error when only T equal to 1 and 3 is considered, respectively. The orientation and position of the band of minimum error are different in the two cases. A correlation between the orientation of the band and the stress triaxiality ratios used in the calibration could not be obtained. However, the q_i-values will be optimized in a more average sense by including a large range of stress triaxialities, consequently making the optimization process less prone to the stress state.

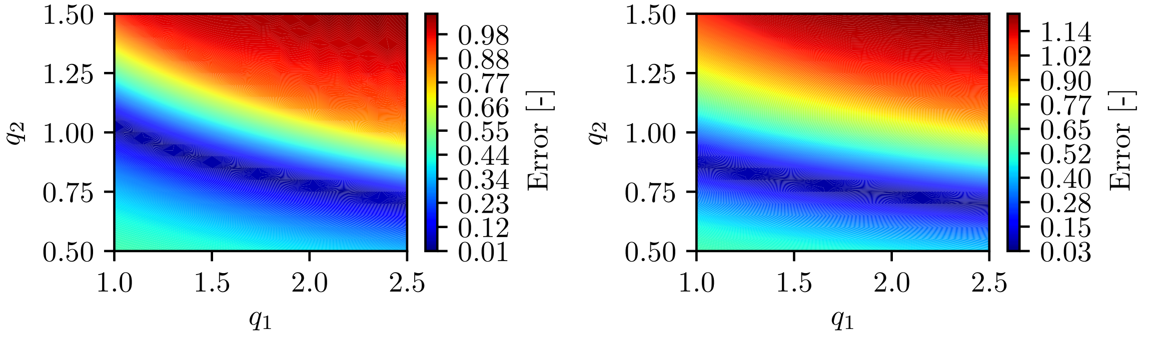

(a) *Calibrated for $T = 1$ only* ***(b)*** *Calibrated for $T = 3$ only*

Figure 4.14: *Contour plots of the error in q_i-space when proportional loading with (a) $T = 1$ and (b) $T = 3$ have been used in the calculation of the error. Only the state of generalized tension has been considered in both cases.*

The method used herein can easily be extended for a range of Lode parameter L as well. Figure 4.15 illustrates the unit cell response for different L, which shows that the unit cell is less prone to softening in generalized compression. Including these three L values in the calibration process of q_1 and q_2 will shift the band of minimum error in the negative direction of q_2. However, the change is not too significant since only the stress-strain response up to a 5% softening in stress has been used in the calibration.

As discusses earlier, the Gurson-Tvergaard model is independent of the Lode parameter. Fitting this model to a wide range of the Lode parameter is therefore somewhat pointless. An effect of L could be obtained heuristically by modifying the Gurson-Tvergaard model by replacing the von Mises equivalent stress with the Hershey equivalent stress. Such a modification is given in Equation (2.53).

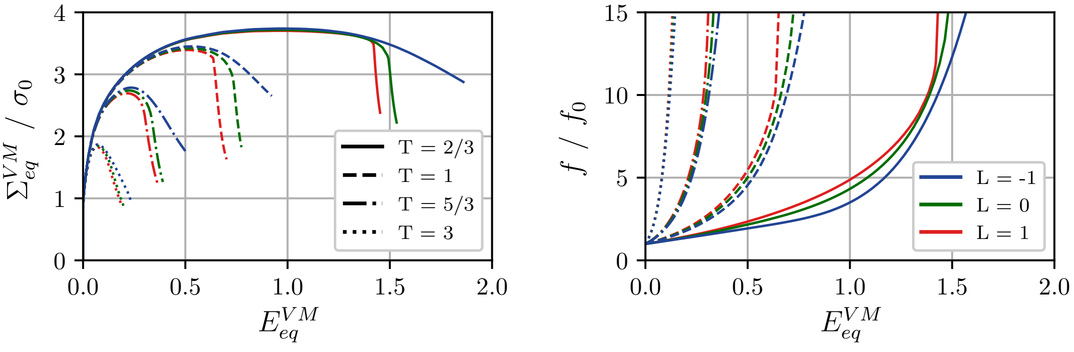

(a) ***(b)***

Figure 4.15: *(a) The normalized macroscopic equivalent stress and (b) normalized evolution of porosity as a function of the macroscopic strain,* E_{eq}^{VM}*, for the case of* $L = -1$*,* 0 *and* 1*.*

Non-Proportional Loading Path

A material element experiences in general non-proportional loading as shown in Figure 3.4. Calibration of the q_1 and q_2 parameters from a proportional loading path might provide incorrect results. The effect of a non-proportional loading path will be investigated here by imposing the triaxiality history $T(p)$ from the center element of the smooth and notched specimens to the unit cell and PPM analyses. It should be noted that $L = -1$ in all center elements.

Figure 4.16 illustrates the response of the unit cell model. A red cross marks the point when coalescence occurs. The smooth specimen experience void closing since the majority of the stress triaxiality ratio is small, i.e., 1/3. Consequently, no coalescence occurs within reasonable deformation of the cell. A remedy for this is to include a particle inside the void. The macroscopic plastic strain, E_{eq}^{c}, at coalescence for the $R08$ and $R2$ notch was found to be 0.411 and 0.594, respectively. Moreover, the critical porosity, f_c, was found to be approximately 0.056 in both cases.

The error plot in the q_i-space is shown in Figure 4.17. The band of minimum error is somewhat shifted in the positive q_2 direction compared to the case of proportional loading. Since the error plot is somewhat dependent on the triaxiality ratios included in the calibration, as shown in Figure 4.14, this discrepancy is most likely not due to the proportional loading by itself.

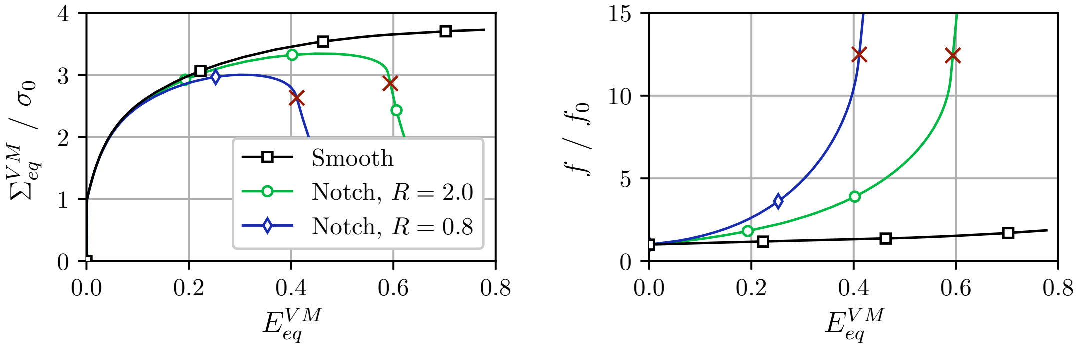

(a) ***(b)***

Figure 4.16: *(a) The normalized macroscopic equivalent stress and (b) normalized evolution of porosity as a function of the macroscopic strain, E_{eq}^{VM}, when non-proportional loading path is imposed to the unit cell and PPM analyses. The load history of the center element has been used. The triaxiality as a function of the plastic strain, $T(p)$, is plotted in Figure 3.4.*

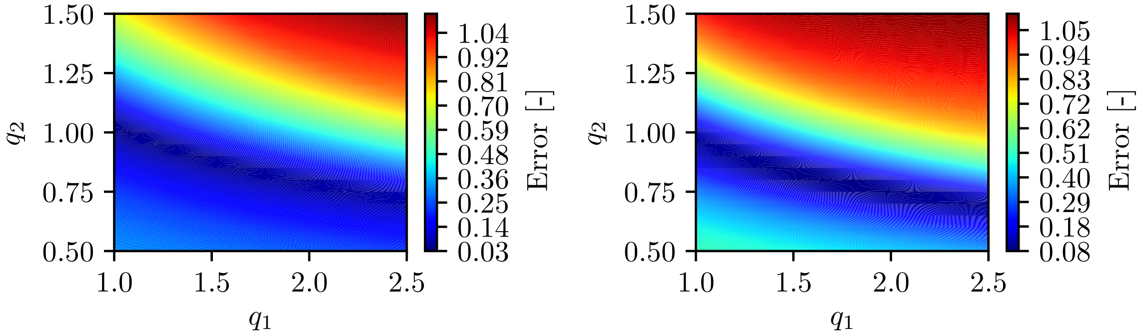

(a) *Non-proportional Loading* ***(b)*** *Proportional Loading*

Figure 4.17: *Contour plot of the error in q_i-space when proportional and non-proportional loading paths are imposed. Figure (b) is the same as Figure 4.9a.*

Initial Porosity

The initial porosity of 0.00452 was based on the prediction from Alstruc. How well this estimate corresponds to the actual void content is unknown. It should be emphasized that the result from Alstruc is not a prediction of initial porosity per se, but rather an estimate of the average particle content that potentially can form voids. How the initial porosity affects the cell response and the calibrated q_1 and q_2 values will be investigated in the following.

Three different porosity levels have been considered; $f_0 = 0.001$, 0.00452 and 0.01. The cell response under generalized tension is plotted with solid lines in Figure 4.19 for the case of $T = 2/3$, 1, 5/3 and 3. A larger initial void fraction results in a softer response of the unit cell and more extensive void growth. Moreover, coalescence occurs at lower strains as the size of the void is increased, thus resulting in lower ductility. This corresponds well with what one would expect.

The dashed lines in Figure 4.19 show the material response of a single element when the Gurson-Tvergaard model is used with $q_1 = 1.65$ and $q_2 = 0.8$. Evidently, the material becomes softer with increasing f_0. Additionally, the change in response of the porous plasticity model follows the same trend as the cell model when f_0 is altered. This is particularly evident from the error plot in Figure 4.18. The band of minimum error spans over the same region despite the significant difference in porosity. The response of the porous plasticity model was found to be somewhat similar for parameters within this band. Thus, the initial porosity is believed to not affect the calibration of q_1 and q_2 too much.

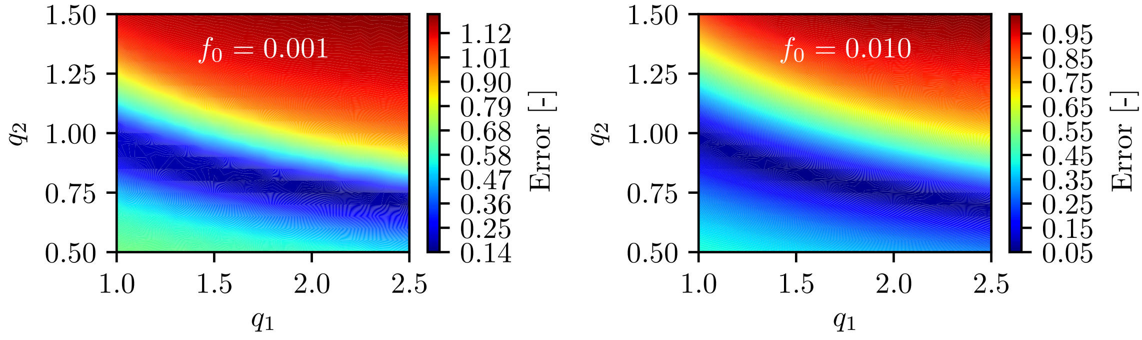

(a) $f_0 = 0.001$ *(b)* $f_0 = 0.010$

Figure 4.18: *Contour plot of the error in q_i-space when $f_0 = 0.001$ and 0.01.*

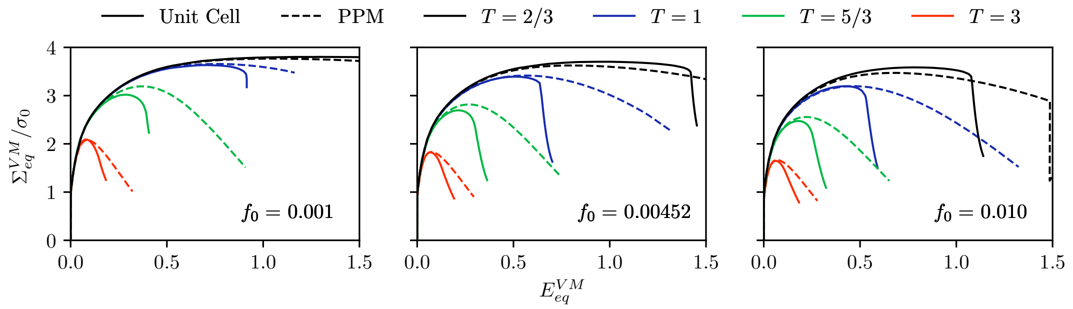

(a) *Macroscopic stress versus macroscopic strain*

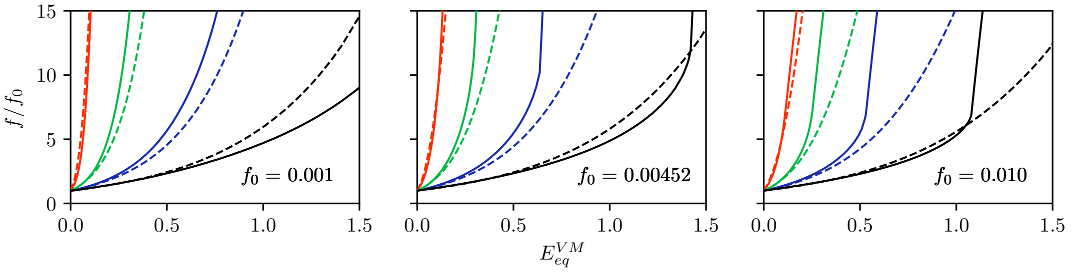

(b) *Evolution of porosity*

Figure 4.19: *(a) The normalized macroscopic equivalent stress and (b) normalized evolution of porosity as a function of the macroscopic strain,* E_{eq}^{VM}*, for three different initial porosity levels. Solid lines represent the cell response. Dashed lines show the results from the Gurson-Tvergaard model where* $q_1 = 1.65$ *and* $q_2 = 0.8$

Matrix Material Response

The last parameter studied is the response of the matrix material, more particular the point of yielding and rate of work hardening. For this purpose, the 6082 aluminium alloy in Chapter 7 has been used as the matrix material. The material parameters can be found in Table 7.2 on Page 135. Figure 4.20 shows the equivalent stress as a function of the plastic strain for the AlMgSi and 6082 aluminium alloy. While the AlMgSi aluminium alloy exhibits extensive work hardening, but low yield stress, the peak-aged 6082 alloy experience much larger yield stress, but a lower hardening.

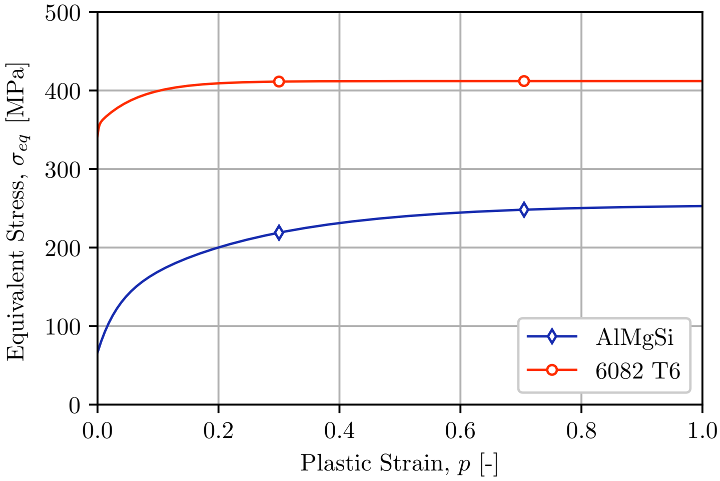

Figure 4.20: *An illustration on how the AlMgSi and 6082 aluminium alloy work hardens. The material parameters can be found in Table 3.3 and 7.2.*

The error between the unit cell simulations and PPM is plotted in Figure 4.22. Figure 4.22a shows the results for the AlMgSi alloy and is the same plot as given in Figure 4.9a. The peak-aged 6082 alloy, represented by Figure 4.22b, has been calibrated using an initial porosity of 0.00922. However, the effect of initial porosity was found to be small.

The band of minimum error shifts in positive q_2 direction for the 6082 aluminium alloy. A higher softening rate in the Gurson-Tvergaard model is preferred to obtain a good correlation with the unit cell simulations. This is especially true in the intermediate to high stress triaxiality region, as indicated by Figure 4.21. From the plots in this figure, the overall most accurate results are obtained when $q_1 = 1.5$ and $q_2 = 1.0$. In the lower triaxiality domain, however, smaller q_1 and q_2 values give best agreements with the unit cell response. The black curves indicate this in the leftmost and lowermost plot. It is also worth mentioning that Figure 4.21 displays the same trends seen by the AlMgSi alloy in Figure 4.13. More extensive softening is achieved by increasing q_1

and q_2. Several q_i configurations are also believed to yield similar material behavior. A separate study showed that both the rise in yield stress and change in work hardening contribute to this shift of the minimal error band. Evidently, the matrix material response influences the calibration of the Tvergaard parameters more than the other parameters investigated herein.

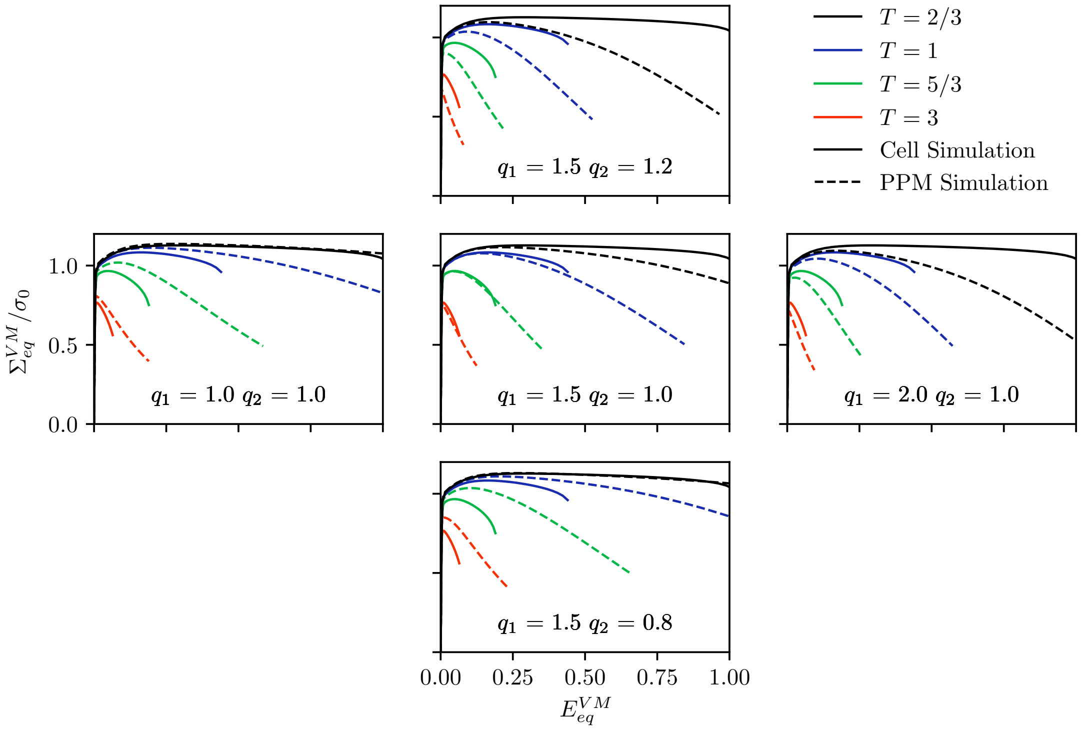

Figure 4.21: *The PPM response for different configurations of q_1 and q_2 when the matrix material for a 6082 aluminium alloy is used. The q_1 is increased from 1 to 2 (from left to right plot) and q_2 is increased from 0.8 to 1.2 (from lower to upper plot). Solid lines represent the results obtained from unit cell simulations and are the same in all plots. Dashed lines show the result from PPM simulations.*

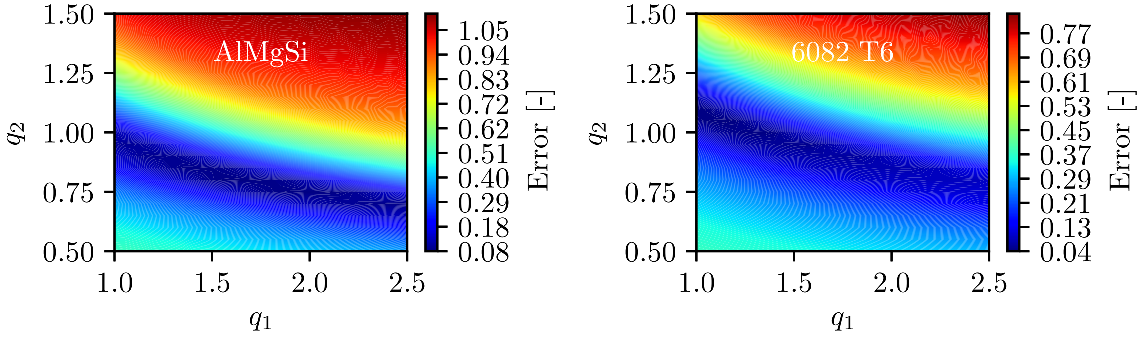

(a) *AlMgSi Alloy* ***(b)*** *6082 T6 Alloy*

Figure 4.22: *Contour plots of the error. Figure (a) is the same as Figure 4.9a.*

4.3 Calibration of the GT Model From Tests

Experimental data from various types of test specimens can also be used to calibrate the Gurson-Tvergaard model. Smooth and different types of notched axisymmetric tensile specimens are usually used for this purpose. It is convenient to fit as few variables as possible due to the limitation of data from tests. One way is to match the initial porosity f_0 for a given set of q_1 and q_2 variables, usually the Tvergaard constants, i.e., $q_1 = 1.5$ and $q_2 = 1$. In this section, however, q_1 and q_2 will be fitted by assuming the initial porosity from Alstruc. The following cost function defines the discrepancies between the simulations and the measured stress

$$e = \frac{1}{N_{TT}} \sum_{i=1}^{N_{TT}} \frac{\displaystyle\int_0^{\varepsilon_l^{max}} \left| \sigma_t^{PPM} - \sigma_t^{EXP} \right|_i d\varepsilon_l}{\displaystyle\int_0^{\varepsilon_l^{max}} \frac{1}{2} \left(\sigma_t^{PPM} + \sigma_t^{EXP} \right)_i d\varepsilon_l} \tag{4.6}$$

Here, N_{TT} is the total number of tensile test. The true stress from simulations and experiments are denoted σ_t^{PPM} and σ_t^{EXP}, respectively. The logarithmic strain at fracture is defined as ε_l^{max}. Section 2.1.2 defines these measurements. Equation (4.6) is equivalent to the cost functions given in Equation (4.4). A total of nine experiments have been carried out on the three specimen types presented in Section 3.2, and all of them are utilized in the optimization process. Thus $N_{TT} = 9$.

Figure 4.23 illustrates how the error evolves in the q_i-space. A similar band of minimum error spans across the contour plot. The band is, however, shifted and does not resemble the result in Figure 4.9 using the unit cell approach to calibrate the same variables. Figure 4.24 shows the stress-strain response for different sets of q_1 and q_2. Evidently, increasing one of these parameters results in a softer behavior. This softening is rather modest at small strains. The point at which the strain starts to localize, indicated by the rapid decrease in stress, is more affected by the change in q_1 and q_2. The error is greatly influenced if this extensive softening occurs before the fracture strain. This is indicated by a black region in the upper-left corner of Figure 4.23.

The softening in the tensile specimens before localization occurs may resemble the same trends seen in the unit cell approach in Figure 4.13. Even so, the unit cell approach experiences more extensive softening, and thus a more significant error, as q_1 and q_2 are changed. This approach also favors lower q_1 and q_2 values.

It is more convenient to only fit q_1 by keeping q_2 constant. Figure 4.25 shows the error plot for $q_2 = 0.8$, 1.0 and 1.2. All local minima are listed in Table 4.2. It should be noted that the q_1 parameter is much larger than values proposed in the literature

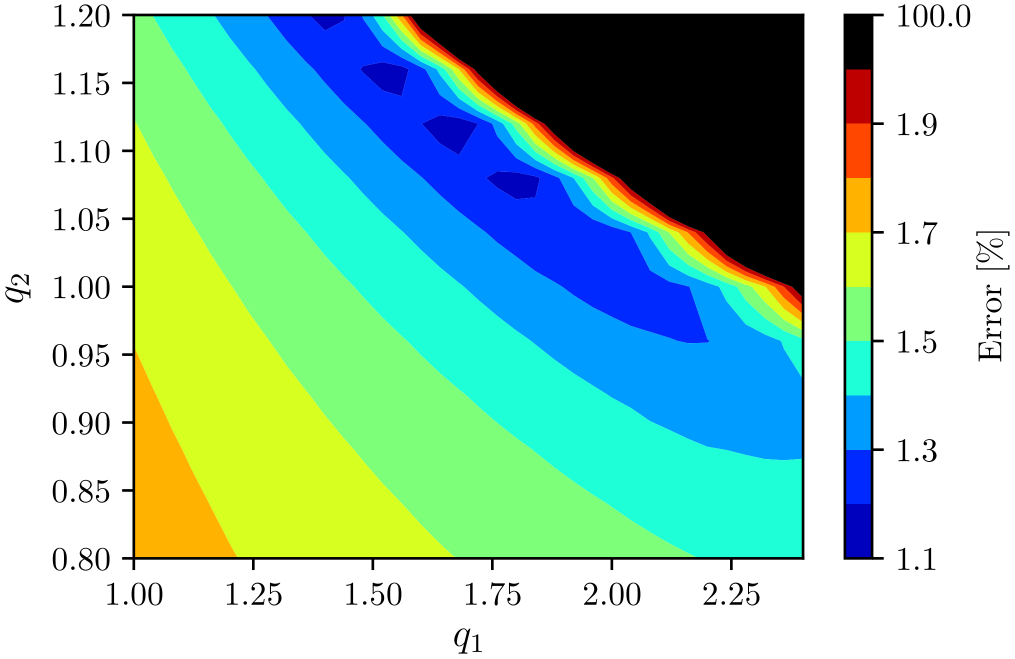

Figure 4.23: *Contour plot of the error in the q_i-space for $q_1 \in [1.0, 2.4]$ and $q_2 \in [0.8, 1.2]$. The resolution of data points is 36×11, which corresponds to a $\Delta q_i = 0.04$.*

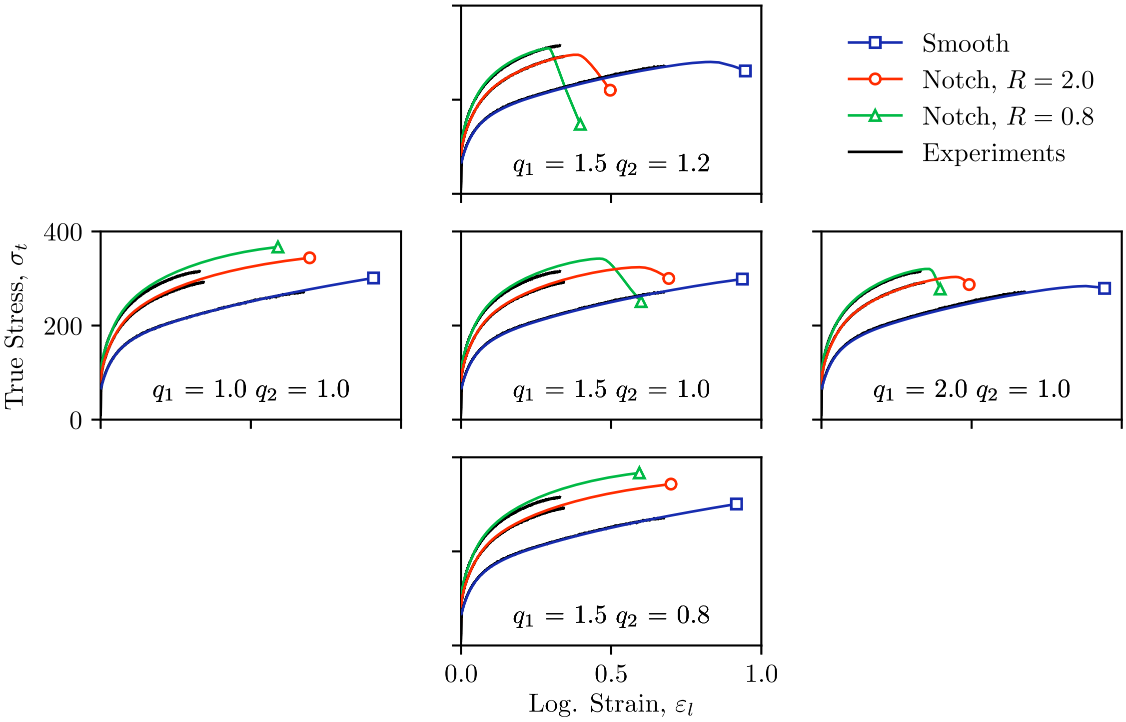

Figure 4.24: *A comparison of the tensile experiments to the simulations using the Gurson-Tvergaard model with different sets of q_1 and q_2, where q_1 is increased from 1 to 2 (from left to right plot) and q_2 is increased from 0.8 to 1.2 (from lower to upper plot).*

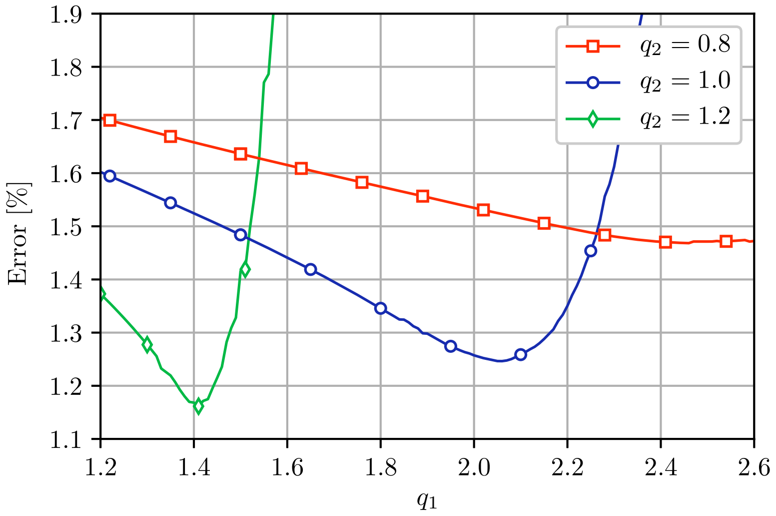

Figure 4.25: *The error as a function of q_1 for three different constant q_2 values.*

[2]. Figure 4.26 compares the axisymmetric tensile test results using the optimized q_1 values for $q_2 = 0.8$ and $q_2 = 1.0$. The difference in error is only about 0.22%. However, this results in considerable deviations in the predicted stress-strain response since the softening mainly takes place at higher strains. No rapid loss of load-carrying capacity is observed for the plane strain tensile specimen simulations in Figure 4.27. Consequently, the two different sets of q_1 and q_2 variables do not give too different results.

It is evident that the finite element simulations can predict the global stress-strain response from experiments more accurately once softening due to void growth is included. The predictions for the axisymmetric specimens are quite good. However, the force is still overestimated in the PST simulations. A Lode dependent porous plasticity model might correct this. As shown in Figure 4.15, the softening in the unit cell simulation is less in generalized shear than in generalized tension. This observation suggests that additional softening terms in the constitutive relation should also be considered. Moreover, the approach of using experimental data to fit the model parameters gives much better agreements with the real stress-strain response than the unit cell approach in Figure 4.12, which is rather obvious. A discussion about this will follow in Section 4.4.

Table 4.2: *Local minima in Figure 4.25 with corresponding error.*

	f_0	q_1	q_2	e [%]
$q_2 = 0.8$	0.00452	2.46	0.80	1.468
$q_2 = 1.0$	0.00452	2.06	1.00	1.246
$q_2 = 1.2$	0.00452	1.41	1.20	1.162

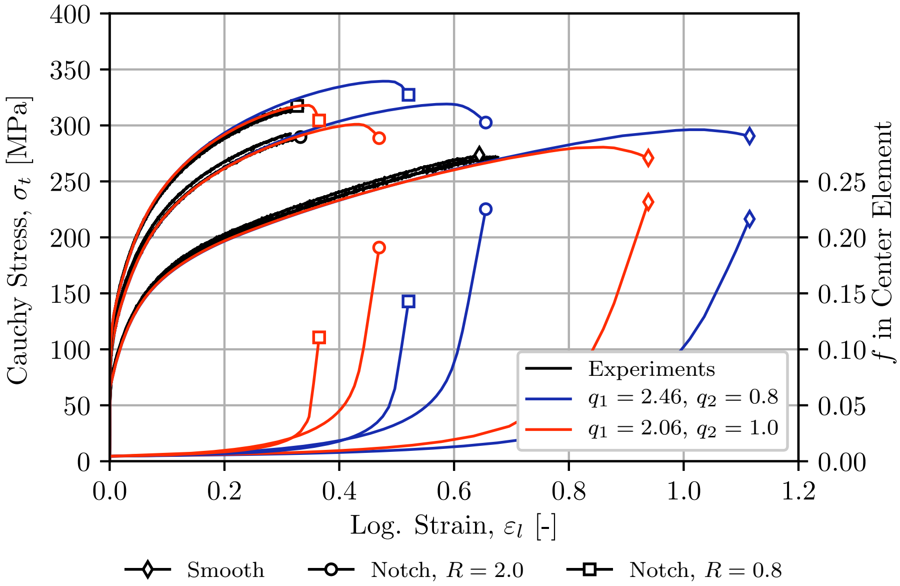

Figure 4.26: *The Cauchy stress, σ_t, and porosity, f, in the center element versus the logarithmic strain, ε_l, for the smooth and notched specimens. Solid black lines show the results from experiments. The colored lines show the results from simulations with different sets of q_1 and q_2.*

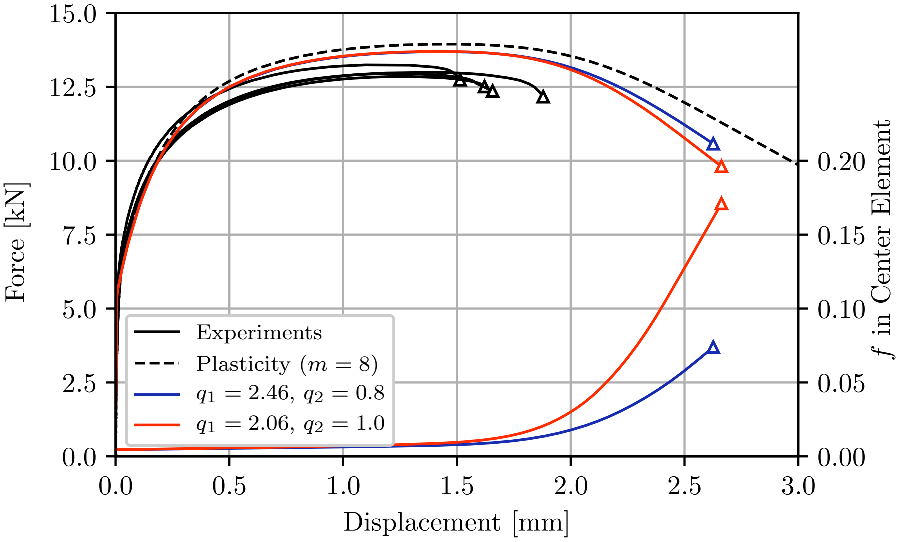

Figure 4.27: *The force and porosity f in the center element versus the displacement for the plane strain tensile test. The solid black lines show the results from experiments. The dashed black line shows the results from simulation when the effect of voids are neglected. Colored lines show the results from simulations with different sets of q_1 and q_2. Here, the Gurson model has been heuristically modified with a Hershey yield surface ($m = 8$) as described by Equation* (2.53).

4.3.1 Influence of Initial Void Volume Fraction

The optimized parameters for the porous plasticity model revealed almost no dependency on the initial porosity in the unit cell calibration approach. Figure 4.28 shows the error in the q_i-space for an initial porosity of 0.01 when using the approach in this section. The optimization approach using experimental data is obviously strongly dependent on the initial porosity. In the unit cell approach, the response of the unit cell and the porous plasticity model are affected by the change in initial porosity in a similar fashion. However, this is not the case here since the chosen porosity does not influence the experimental data.

Figure 4.29 illustrates that more extensive softening occurs as the porosity is increased. Thus, increasing any of the three parameters in the Gurson-Tverrgaard model results in higher softening rate due to the evolution of damage. Even though there perhaps exists a set of material parameters that results in the lowest error, it might be sufficient only to optimize one parameter as long as the other parameters are within reasonable limits.

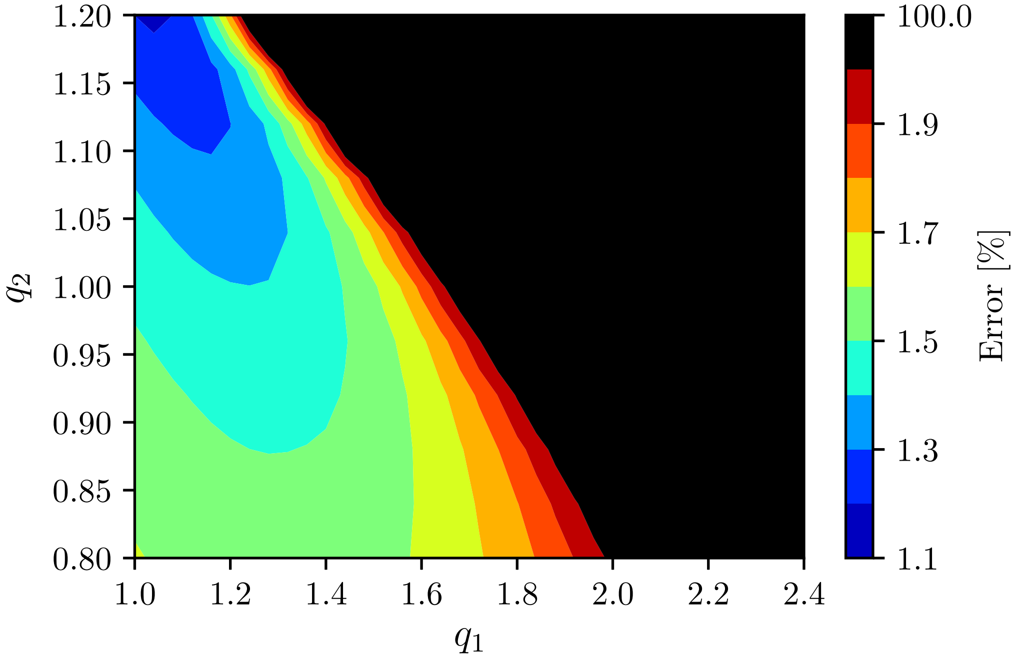

Figure 4.28: Contour plot of the error in the q_i-space when the initial porosity, f_0, equals to 0.01 *for $q_1 \in [1.0, 2.4]$ and $q_2 \in [0.8, 1.2]$. The resolution of data points is* 36×11*, which corresponds to $\Delta q_i = 0.04$.*

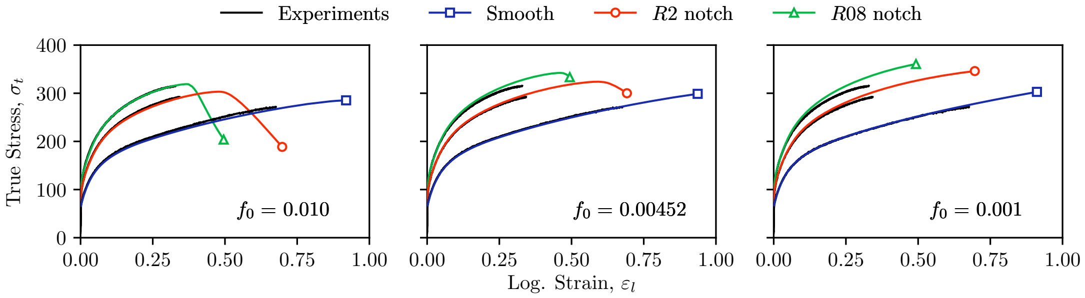

Figure 4.29: *True stress-strain response for all specimens with different initial porosity f_0. q_1 and q_2 are 1.5 and 1.0, respectively.*

4.4 Discussion

A unit cell approach for optimizing the parameters in the Gurson-Tvergaard model has been used and compared with the same parameters optimized from material tests for an AlMgSi alloy. The two methods yield some clear differences. For instance, the unit cell approach underestimates the softening compared to real material response. Moreover, while the unit cell approach does not show any large dependency on in the initial porosity, calibration from material tests is very sensitive to this parameter.

It should be emphasized that the unit cell approach used herein is simplified with respect to the micromechanical mechanisms that occur in a real material. First, the material is assumed to be initially voided and the effect a particle has on the void growth due to contact and friction is neglected. Moreover, no cohesion between the matrix and particles is assumed, thus ignoring the bonding energy. The voids are also considered to be of even size and distribution within the bulk material. They are also initially modeled as spheres. Other studies have found that the initial void shape will influence the unit cell response [2, 10]. In general, the softening effect appears to be more prominent as the initial aspect ratio of the void is decreased, i.e., as the void become more oblate. Consequently, the point of coalescence occurs at lower macroscopic strains. Very oblate voids, also known as penny shape cracks [1], can be important in cases where the material is exposed to particle cracking. These assumptions presented above may not be accurate for a real material. Moreover, it is probably impossible to account for the random size and distribution of voids in a unit cell approach. To further complicate matters, the changes in void shape induce anisotropy to the material. The original Gurson model maintains isotropic by assuming spherical void growth, and can therefore not account for the non-spherical void evolution observed for low triaxialities. Calibration of the material parameters from physical tests may account for all these factors in an average sense in a way the unit cell approach will never accomplish.

It has been reported that the evolution of porosity is lower for a 3D unit cell model than an axisymmetric unit cell model since the 3D model contains more material to constrain the void growth, and thus delay coalescence [2]. Therefore, an axisymmetric model could provide a higher softening rate. It should be emphasized, however, that this effect alone will probably not correct for all the discrepancy seen between the two approaches taken here.

The material may also experience other softening effects. A higher mesh density and the use of a Hershey yield surface result in slightly softer response for the notched specimens as shown in Figure 3.3 and 3.6. This softening would properly shift the band of minimum error in Figure 4.23 in the direction of decreasing q_1 and q_2.

A fracture criterion can be calibrated based on the occurrence of coalescence in the unit cells under generalized tension. One can either find a critical porosity level f_c, or generate a failure strain locus $p_f(T)$. This is shown in Figure 4.6. The approach herein only considers localization in one orientation. However, localization can occur in different orientations depending on the load. Consequently, the predictions will be non-conservative.

Lastly, it may be sufficient to only calibrate one of the three parameters in the Gurson-Tvergaard model, as long as the other two are within reasonable limits. In the unit cell approach, q_1 may be fitted while q_2 is kept constant, say $q_2 = 1$. The optimized parameters that will be used in the following chapter are listed in Table 4.3

Table 4.3: *A summary of the optimized material parameters for the Gurson-Tvergaard model used in the following chapter.*

	f_0	q_1	q_2	$q_3 = q_1^2$
Unit cell approach (Table 4.1)	0.00452	1.843	0.768	3.397
Material test approach (Table 4.2)	0.00452	2.060	1.000	4.244

5 | Numerical Approach to Fracture

In this part, the results from Chapter 4 will be used to calibrate fracture criteria for the AlMgSi aluminium alloy. Different approaches are examined and compared with the experimental results. First, the occurrence of coalescence from the unit cell analysis will be used to define the onset of fracture. Next, the strain localization analysis from Section 2.3 will be used with the calibrated porous plasticity model to identify a failure strain surface in the space of stress triaxiality and Lode parameter. An approach that utilizes only a smooth specimen test to calibrate all material and fracture parameters is discussed in greater details in Section 5.3. In the end, some of the fracture criteria in Section 2.1.5 will be calibrated to illustrate how well they can resemble the fracture surface obtained from localization analysis.

5.1 Unit Cell Approach

Section 4.1.2 defines the occurrence of coalescence in the unit cell as the point in which homogeneous deformation is terminated. The advantage with a coalescence approach to fracture is that it is based on physical mechanisms that can be identified in numerical simulations of void evolution. The unit cell in this thesis only considers coalescence in one orientation. Other orientations may result in earlier coalescence, making this approach non-conservative. Also, the occurrence of coalescence, as defined in Section 4.1.2, cannot be easily identified for other stress states than generalized tension. An approach that accounts for the orientation of the localization and other stress states is proposed in the literature [25, 67]. However, the unit cell approach becomes quite tedious and computational expensive once an extensive range of orientations must be analyzed, which is a significant disadvantage.

Two ways of defining material failure in a finite element analysis for a porous material will be examined in the following; using a critical porosity level and damage accumulation from a fracture surface.

5.1.1 Critical Porosity

The unit cell analyses indicated that the critical porosity, f_c, remains approximately constant over the vast specter of stress triaxiality examined. Figure 4.6b shows that the average critical porosity at coalescence is 0.0544. The exact porosity is somewhat difficult to accurately determine due to rapid void growth upon coalescence, especially for high T. Figure 4.5b illustrates this problem more clearly.

Figure 5.1 plots the global engineering stress and evolution of porosity in the critical element as a function of the engineering strain. Blue and red lines show the results using the material parameters calibrated from unit cell and experimental data, respectively. The parameters from the unit cell approach yield lack of growth in porosity. Consequently, the fracture strain is significantly overestimated. No reasonable critical porosity returns good results using this set of q_i-parameters. The same holds true for the PST specimen in Figure 5.2.

In contrast, the optimized q_1 and q_2 from experiments give somewhat reasonable agreements with the notched specimens. This is because extensive void growth occurs near the point of specimen failure. Thus, a small change in critical porosity will not impact the fracture strain too much. The point of failure for the smooth specimen, however, is overestimated. Since the void growth, in this case, is not as prominent, the fracture strain is more affected by the critical porosity.

The experiments indicate that the fracture strain for the $R2$ and $R08$ notched specimen is almost the same. Figure 5.1 shows that the porosity level in the critical element for these two specimens is the same when the strain is approximately 0.38. Even if the stress triaxiality ratio is higher in the $R08$ notched specimen, the plastic strain in the center evolves more slowly. Consequently, the rate of void growth is initially lower. Figure 5.3 and 5.4 show the results when $f_c = 0.03$ for the axisymmetric and PST specimens, respectively. The q_i parameters optimized from experiments are used in these simulations. From these plots, a constant critical porosity yields good prediction of the failure strain as long as the porous plasticity model predicts sufficient growth in porosity with the increase in strain. It should be emphasized that these results have been determined purely by fitting the material constants to experimental data.

It should be emphasized that the PST specimen in this current section has been modeled with a Gurson-type model that has been heuristically modified with a Hershey yield surface. Equation (2.53) describes such a model. A Hershey exponent of $m = 8$ is used as previously suggested. This has been done in order to induce additional softening to the PST specimen response. The q_i-parameters have been calibrated to a von Mises matrix material, making this approach somewhat non-consistent.

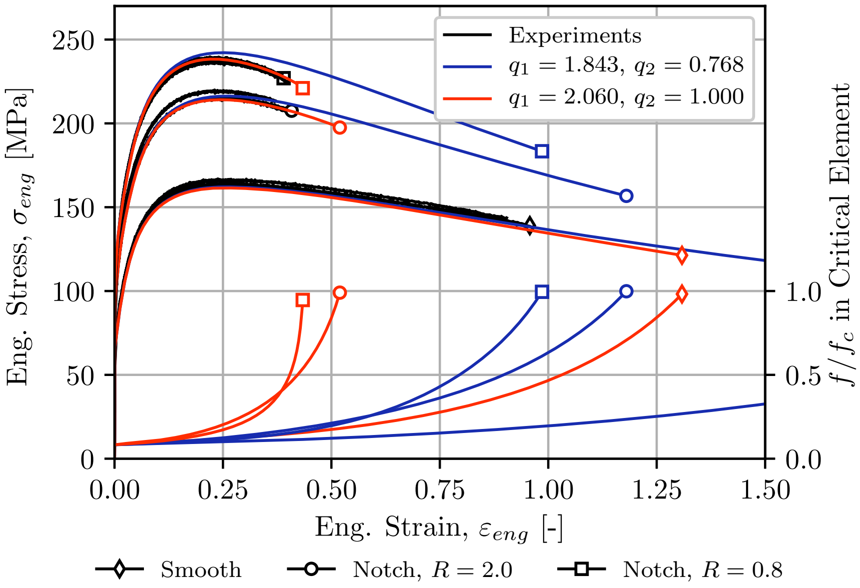

Figure 5.1: *Global engineering stress,* σ_{eng}*, and porosity ratio in the critical element,* f/f_c*, versus engineering strain,* ε_{eng}*, up to failure. The critical porosity is* $f_c = 0.0544$*, as shown in Figure 4.6b. A marker at the end of the graph differentiates the different specimens and indicates the point of failure of the critical element. Separate colors represent the different combination of* q_1 *and* q_2*.*

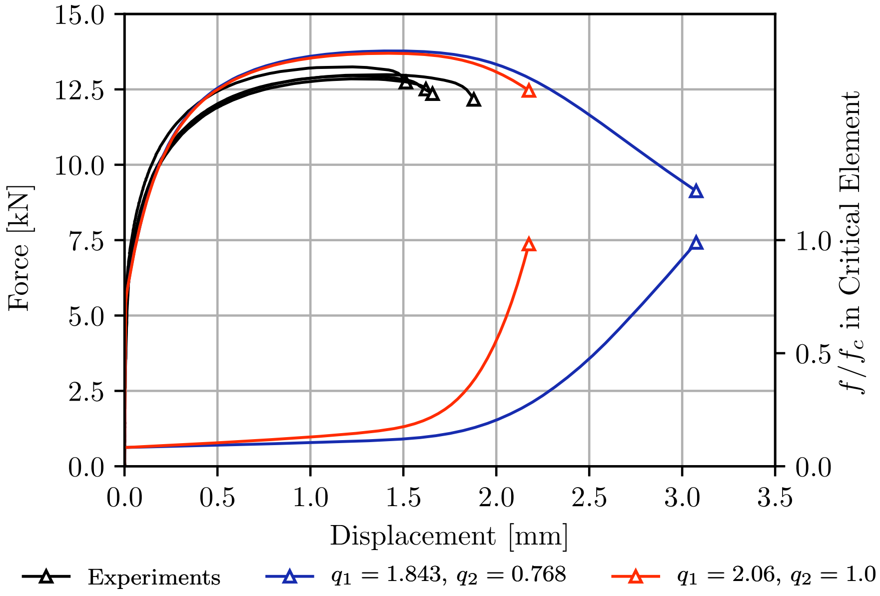

Figure 5.2: *Global force and porosity ratio in the critical element,* f/f_c*, versus the displacement up to failure. The critical porosity is* $f_c = 0.0544$*, as shown in Figure 4.6b. It must be emphasized that the Gurson model has been heuristically modified with a Hershey yield surface* ($m = 8$) *as described by Equation* (2.53)*.*

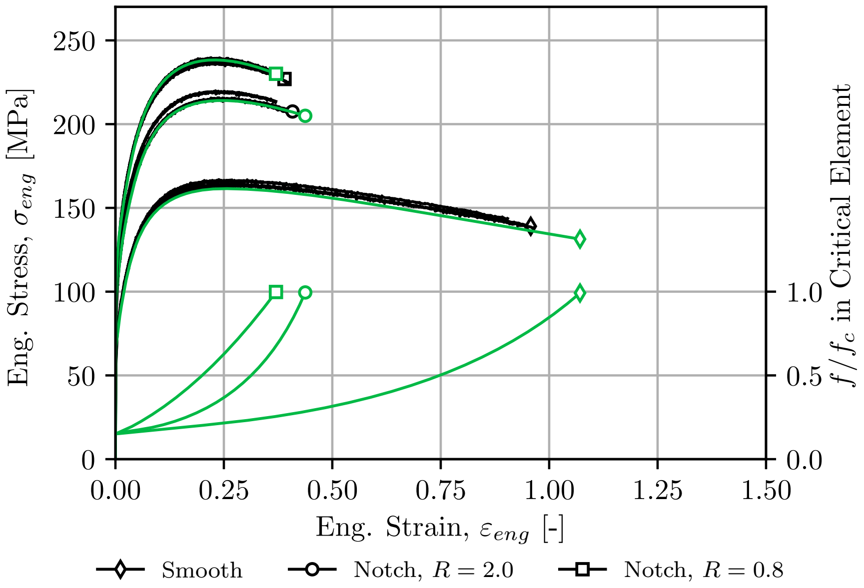

Figure 5.3: *Global engineering stress, σ_{eng}, and porosity ratio in the critical element, f/f_c, versus engineering strain, ε_{eng}, up to failure. The critical porosity is $f_c = 0.03$. A marker at the end of the graph differentiates the different specimens and indicates the point of failure for the critical element. Only the case where $q_1 = 2.06$ and $q_2 = 1.0$ is included here.*

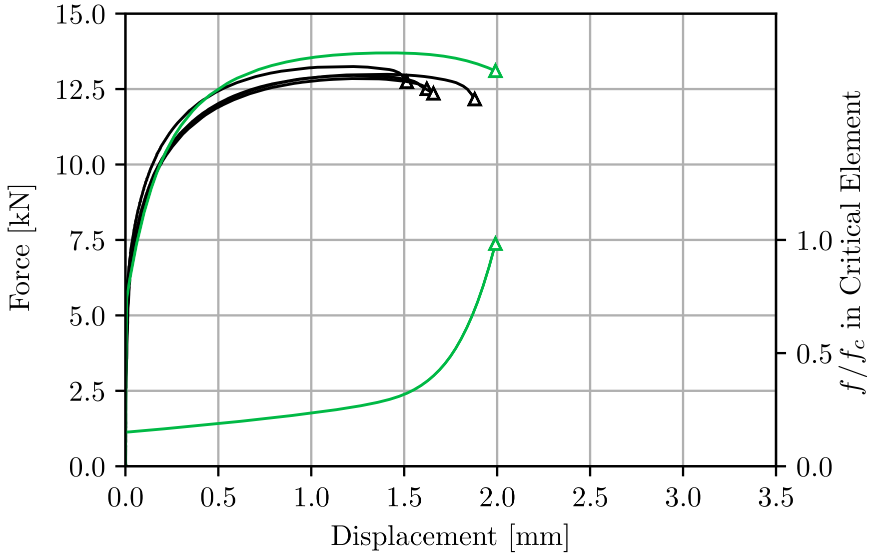

Figure 5.4: *Global force and porosity ratio in the critical element, f/f_c, versus the displacement up to failure. The critical porosity is $f_c = 0.03$. Only the case where $q_1 = 2.06$ and $q_2 = 1.0$ is included here. In this simulation, the Gurson model has been heuristically modified with a Hershey yield surface ($m = 8$) as described by Equation* (2.53)

Figure 5.5 illustrates how the porosity evolves as a function of the engineering stress in the outmost and center element. The critical element for the $R2$ notched specimen is located in the center for almost any critical porosity. The same holds true for the smooth and PST tests. In contrast, the $R08$ notched specimen shows a higher growth rate of voids in the elements near the specimen surface initially. This is due to the extensive plastic deformation at the outer surface of the specimen, as illustrated in Figure 3.5a. Consequently, the critical element is located near the specimen outer surface in the case of $f_c = 0.03$.

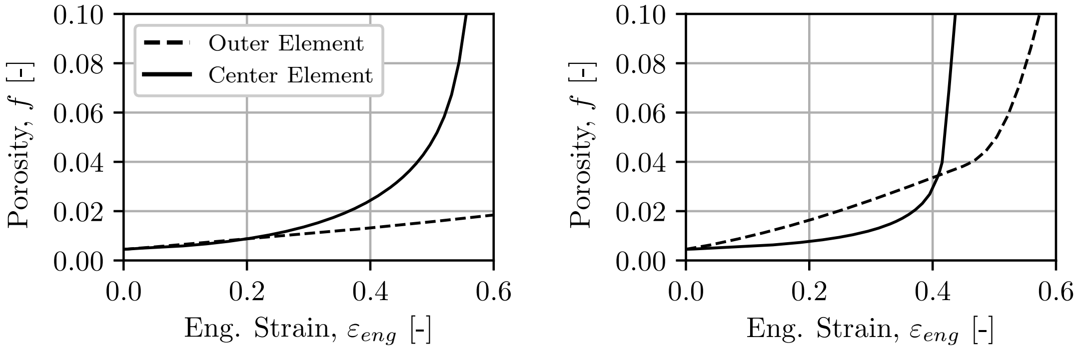

(a) *Notch,* $R = 2.0$ ***(b)*** *Notch,* $R = 0.8$

Figure 5.5: *Porosity,* f*, as a function of the global engineering strain,* ε_{eng}*, for the outer and center element when* $q_1 = 2.06$ *and* $q_2 = 1.0$*. In general, the porosity is larger in the center element for the* $R2$ *notched specimen, as seen in (a). The center element for the* $R08$ *notch specimen (b) experience only highest void content for larger strains, whereas the outer element is more prone to void growth in the lower strain domain.*

5.1.2 Critical Fracture Strain

The critical strain from Figure 4.6a has been used to calibrate the Johnson-Cook fracture model in Equation (2.24). The effects of temperature, strain-rate, and Lode parameter have been neglected, reducing the model to a simple exponential law with respect to the stress triaxiality. Figure 5.6 compares the model with the data from the unit cell simulations. The damage ω is linearly accumulated using Equation 2.23.

Figure 5.7 shows the results from finite element simulations of the axisymmetric specimens. The classical J2 flow theory represents the material in these simulations. The damage is not coupled to the constitutive equations. Consequently, no softening occurs due to increase in material damage. The same applies to the rest of the plots in this chapter. Again, the strain at fracture is overestimated. Moreover, the damage evolution in the critical element is nearly linear, compared to the exponential increase in porosity observed in Figure 5.1 – 5.4. This is most likely because the damage is linearly accumulated and uncoupled to the material response.

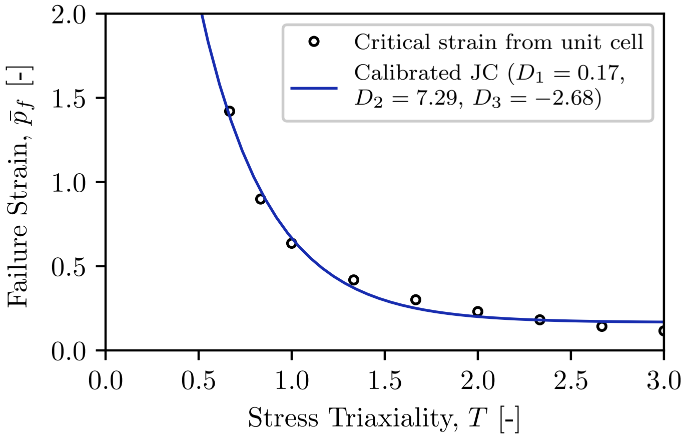

Figure 5.6: *Johnson-Cook fracture model calibrated to the strain at coalescence in the unit cell simulations in Figure 4.6a. Note that the temperature, rate dependency, and the effect of Lode parameter are ignored, i.e.,* $D_4 = D_5 = D_6 = 0$.

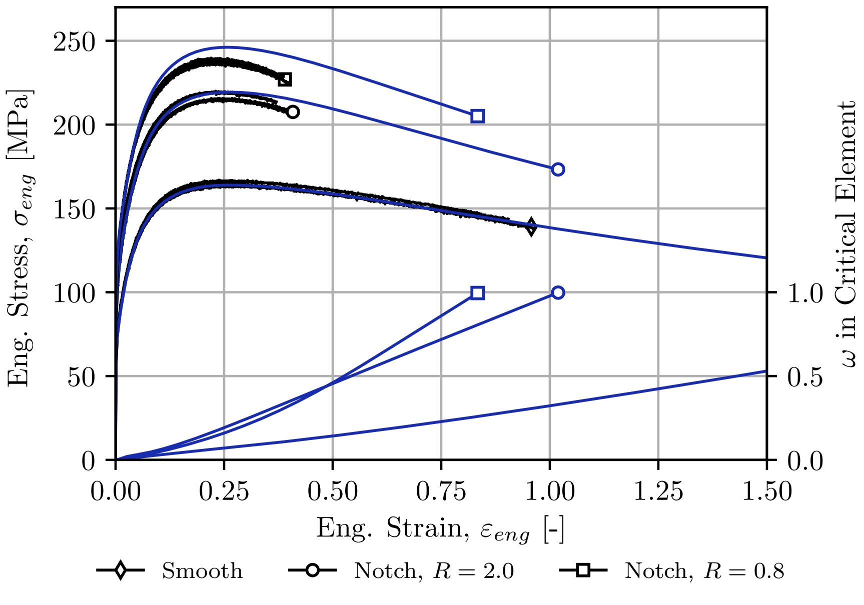

Figure 5.7: *Global engineering stress,* σ_{eng}*, and accumulated damage in the critical element,* ω*, versus engineering strain,* ε_{eng}*, up to failure. The Johnson-Cook fracture model from Figure 5.6 is used. Classical J2 flow theory is utilized to represent the material in the finite element simulations.*

5.2 Strain Localization Analysis

The imperfection band analysis in Section 2.3.1 will be used to generate a fracture surface. A separate FORTRAN code provided by professor David Morin [52] is used for this purpose. The reader is referred to Morin et al. [32] for more information about the numerical implementation. The Gurson-Tvergaard model in Chapter 4 represents the imperfection band material to induce material softening, and thus localization of deformation. Classical J2 flow theory is used to model the material outside the band, and it is assumed that any voiding mechanism taking place in here is negligible. The input cards for the FORTRAN code used are listed in Appendix C.

First, a fracture surface will be generated in a straightforward fashion by assuming an initial porosity. The effect of using a continuous nucleation model and softening in shear will also be examined. Another approach is to calibrate the initial porosity, f_0, or the nucleation rate, A_n, to the fracture strain from a smooth axisymmetric specimen test. This method has been proven to give good results by Morin et al. [68], and will be covered in Section 5.3.

5.2.1 Initial Porosity

The material inside the band is represented by the Gurson-Tvergaard model with the material constants in Table 4.3. Contour lines of the fracture surface with respect to the triaxiality ratio and Lode parameter are plotted in Figure 5.8 and 5.9. The former shows the surface when q_1 and q_2 are optimized from unit cell simulations. Apparently,

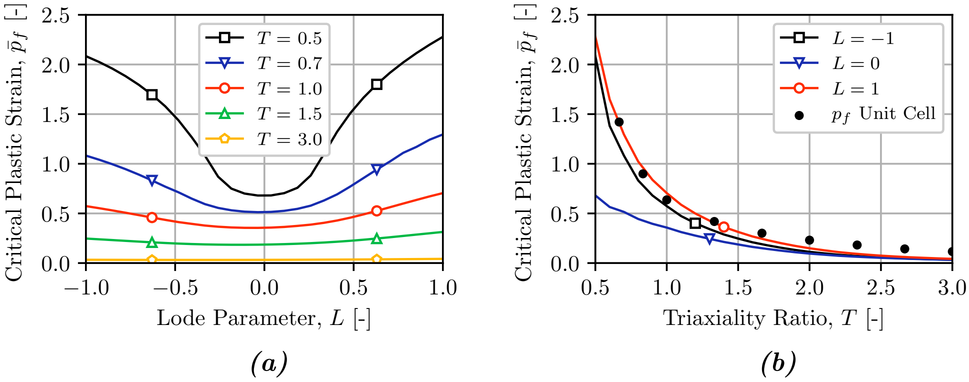

Figure 5.8: *Plastic failure strain, $\bar{p}_f$, obtained from proportional loading in the localization analysis when initially voided band material is used with $q_1 = 1.843$ and $q_2 = 0.768$. The proportional fracture strain, $\bar{p}_f$, is presented for (a) various triaxiality ratios in L-space and (b) various Lode parameter in T-space.*

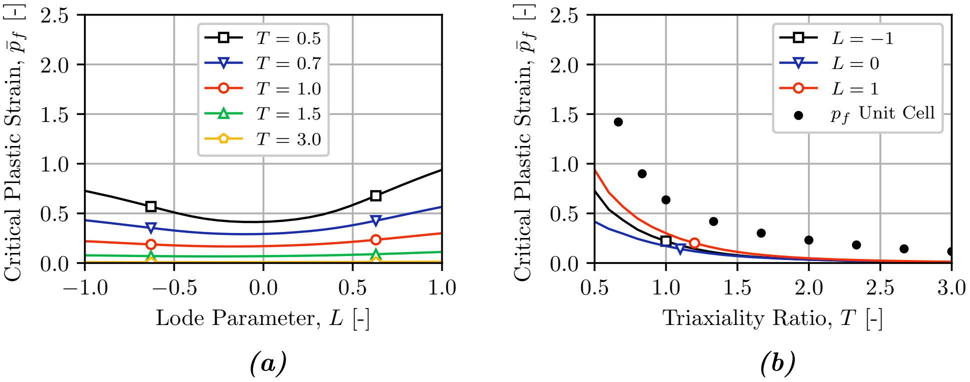

Figure 5.9: *Plastic failure strain, $\bar{p}_f$, obtained from proportional loading in the localization analysis when initially voided band material is used with $q_1 = 2.06$ and $q_2 = 1.0$. The proportional fracture strain, $\bar{p}_f$, is presented for (a) various triaxiality ratios in L-space and (b) various Lode parameter in T-space.*

the predicted fracture strain $\bar{p}_f = \bar{p}_f(T, L)$ is quite affected by the material constants in the Gurson-Tvergaard model. A higher material softening was obtained when the model was fitted to experimental data. Consequently, the fracture strain $\bar{p}_f$ is reduced, as shown in Figure 5.9.

For comparison, the predicted failure strain from the unit cell analysis is included in Figure 5.8b and 5.9b. As shown previously, such strains heavily overestimate the point of fracture for all test specimens. As a result, using the fracture surface in Figure 5.8 will result in too large fracture strain as well. This is verified in Figure 5.10 by the red curves. Moreover, the fracture surface from Figure 5.9 yields good predictions for the $R2$ notch, whereas the estimated fracture strain for the smooth specimen is too large. Failure occurs too early in the $R08$ notched specimen. On top of that, the fracture is initiated in the element near the outer surface of the $R08$ notch.

Figure 5.11 shows how the damage is accumulated in the center element, represented by solid lines. The color code is the same as in Figure 5.10. The dashed lines represent either the outmost element or, in the case of the blue line in Figure 5.11b, the critical element. Clearly, the critical element is located in the center of the $R2$ notched specimen. The largest triaxiality is also located in this element, as indicated by Figure 3.4b, and the plastic strain near the specimen surfaces is not accumulated fast enough to cause extensive damage in this location.

The $R08$ notched specimen yields a different behavior. The critical element is located in the third position from the specimen outer surface when the fracture surface from Figure 5.9 is used. This is not the case when the fracture surface in Figure 5.8 is applied in the simulation. According to Equation (2.23), more damage will be accumulated for a smaller increment of plastic strain dp since the fracture strain $\bar{p}_f(T, L)$ is lower. Consequently, the higher stress triaxiality in the center is not enough to overcome the effect of more extensive plastic straining near the surface. The trend is different for the red curve. The damage at the surface starts to saturate, whereas the damage in the center increases with a steady state.

It must be emphasized that it is not uncommon for the fracture to initiate outside the center for strongly notched specimens [52]. Westermann et al. [38] reported that the main global fracture appearance was a cup-and-cone fracture mode. This often implies that the fracture starts in the center. However, it is unknown if this is the actual case. Only the case where the Gurson-Tvergaard parameters are optimized from tensile tests will be used in Section 5.2.2 and 5.2.3, i.e., $q_1 = 2.06$ and $q_2 = 1.0$.

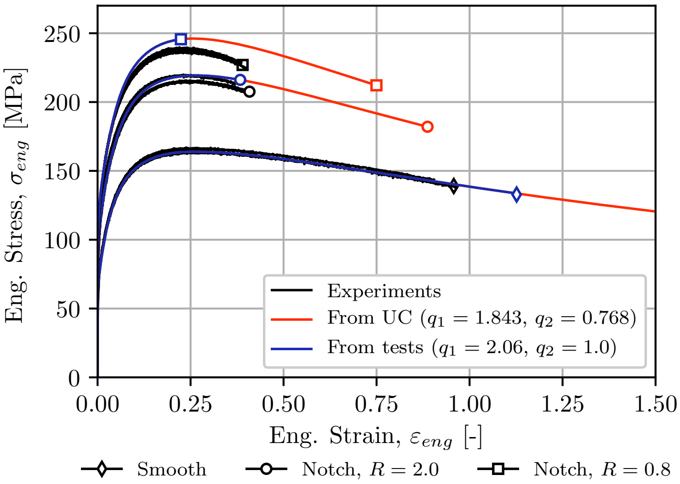

Figure 5.10: *Global engineering stress, σ_{eng}, versus engineering strain, ε_{eng}, up to failure when using the failure surface in Figure 5.8 (red color) and 5.9 (blue color).*

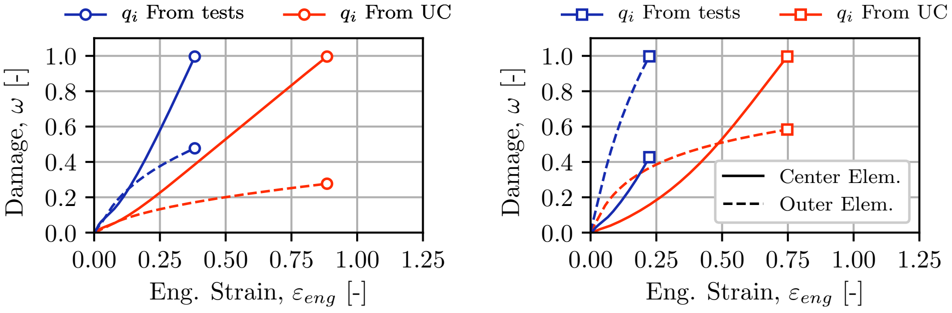

(a) *Notch, $R = 2.0$* ***(b)*** *Notch, $R = 0.8$*

Figure 5.11: *Accumulated damage, ω, in center element (solid line) and outer element (dashed line) for (a) R2 notch and (b) R08 notch.*

5.2.2 Softening in Shear

Equation (2.51) presents an extension to the Gurson-Tvergaard model that takes the evolution of damage $\dot{f}$ due to shear softening into account. This contribution also influences the predicted fracture surface from the localization analysis. Figure 5.12 illustrates that the critical plastic strain $\bar{p}_f$ is decreased as the shear contribution constant k_s is increased. The Tvergaard parameters are here optimized from tensile tests, i.e., $q_1 = 2.06$ and $q_2 = 1.0$. The effect of shear is more prominent as one approaches the case of generalized shear, i.e., $L = 0$. Furthermore, the softening effect is less notable at intermediate to high stress triaxiality ratios.

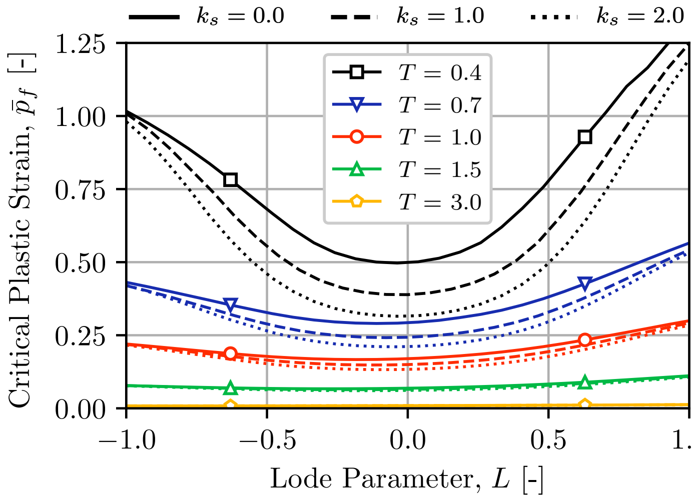

Figure 5.12: *Plastic failure strain, $\bar{p}_f$, obtained from proportional loading in the localization analysis for different shear contribution factors k_s. The band material is initially voided with $q_1 = 2.06$ and $q_2 = 1.0$.*

Figure 5.13 and 5.14 show the effect of shear contribution on the simulation of the tensile specimens. Minor effects are observed for the smooth and $R2$ notched specimens, since the Lode parameter equals to -1 in the center element during the whole deformation process. The point of fracture for the $R08$ notched specimen, however, is more affected by the shearing effect. The critical element for the $R08$ notch is located at the specimen outer surface where the Lode parameter ranges from -0.25 to -0.5, as shown in Figure 3.4c. Consequently, this makes the global fracture strain more prone to damage contribution due to shear softening.

The plane strain tensile test is also more affected by the shear contribution since the Lode parameter is closer to zero at the specimen center. Figure 5.14 shows that the predicted displacement at fracture is better represented compared to the majority of the test results. Consequently, some influence of softening in shear may be beneficial.

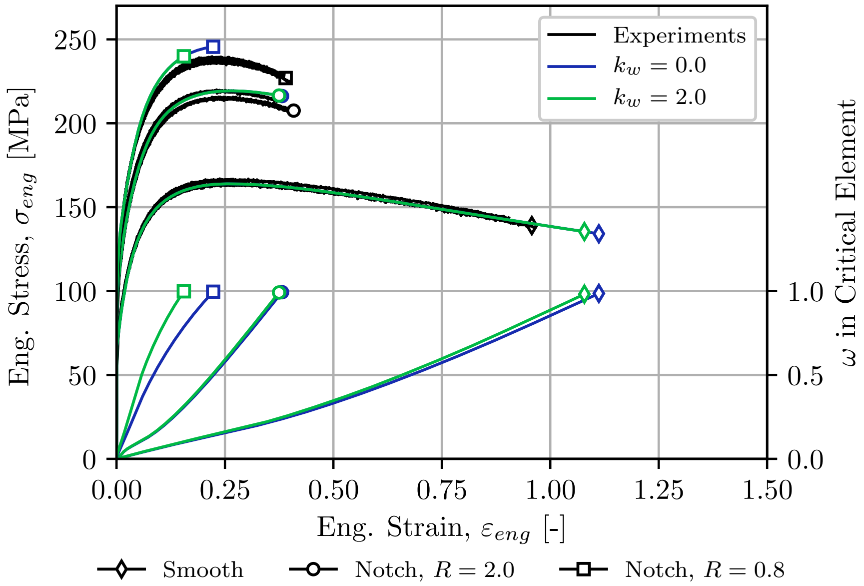

Figure 5.13: *Global engineering stress, σ_{eng}, and accumulated damage in the critical element, ω, versus engineering strain, ε_{eng}, up to failure when using the failure surface in Figure 5.12 for $k_s = 0$ and 2. Classical J2 flow theory is used to represent the material in the finite element simulations.*

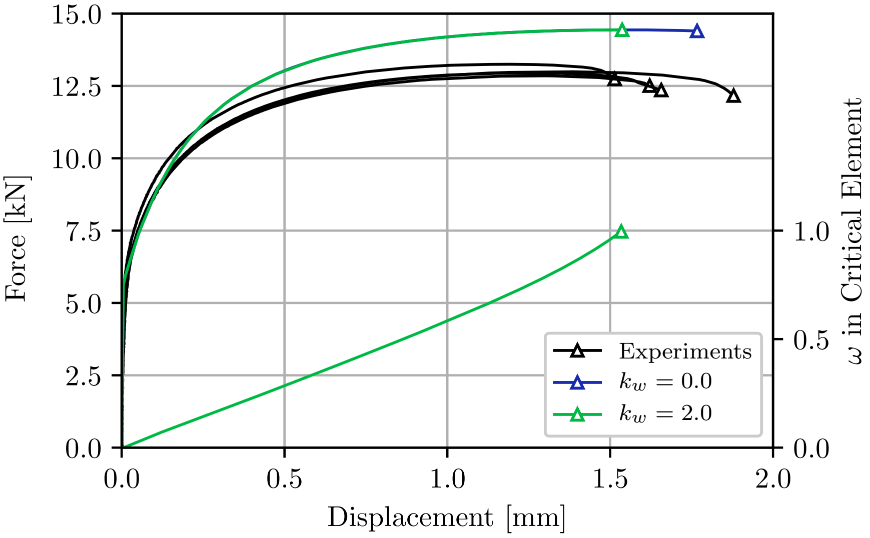

Figure 5.14: *Global force and accumulated damage in the critical element, ω, versus the displacement up to failure when using the failure surface in Figure 5.12 for $k_s = 0$ and 2. Classical J2 flow theory is used to represent the material in the finite element simulations.*

5.2.3 Continuous Nucleation Model

So far, the effect of void nucleation has been neglected by assuming an initially voided material. The effect of nucleation will be included here using the continuous nucleation model presented in Equation (2.46). The rate of nucleation to plastic strain p depends on the constant A_n. The Gurson-Tvergaard parameters optimized from experiments are used, and 0.00452 is the maximum volume fraction that can be nucleated based on the prediction from ALSTRUC. Softening due to shear is not included, i.e., $k_s = 0$.

Figure 5.15 shows how the critical plastic strain $\bar{p}_f$ is increased when $A_n = 0.01$ is used. Accordingly, all voids have been nucleated when the plastic strain $p = 0.00452/0.01 = 0.452$. The effect of nucleation on the Lode parameter is somewhat small and the shift in L-p_f-space is rather continuous. Furthermore, the critical plastic strain is increased significantly with respect to the stress triaxiality ratio T once nucleation is included, as illustrated for generalized tension in Figure 5.16a. Lower A_n results in higher ductility. The fracture surface approaches the results of an initially voided material as $A_n \to \infty$.

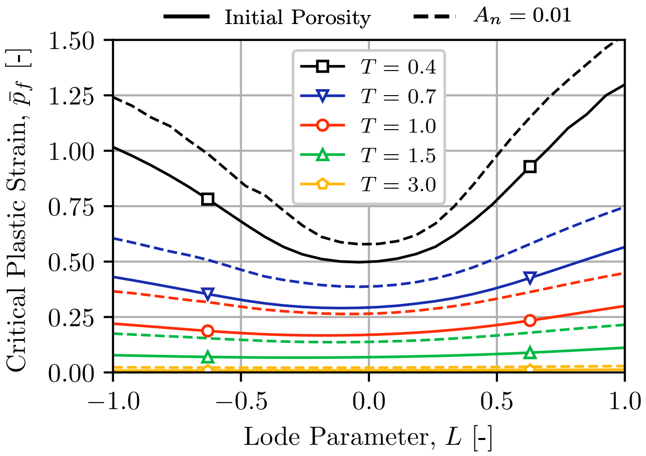

Figure 5.15: *Plastic failure strain, $\bar{p}_f$, obtained from proportional loading in the localization analysis. The band material is modeled as both initially voided and with a continuous nucleation law with $A_n = 0.01$. The porous material is represented with $q_1 = 2.06$ and $q_2 = 1.0$.*

The tendency of overestimating the fracture strain in the case of a smooth specimen, while underestimating the fracture strain for the notched specimens, is a repeating pattern. The blue curves in Figure 5.10 highlight this more clearly, ignoring the fact that fracture occurs near the surface for the sharpest notched specimen. Consequently, it will be beneficial to increase the ductility at intermediate to high stress triaxialities without rising the ductility in the lower triaxiality region. Figure 5.16b illustrates the increase in critical plastic strain compared to the initially voided case. Here, $\bar{p}_f^{A_n}$ and $\bar{p}_f^{init}$ are the critical plastic strain for a given A_n and for an initially voided band material, respectively. The difference in ductility is more prominent for higher triaxialities.

The global response for the axisymmetric specimens is plotted in Figure 5.17. The increase in fracture strains is notable. Using a higher initial porosity could account for this increase, as shown in Section 5.3. Moreover, the fracture is still initiated near the specimen surface for the $R08$ notched specimen.

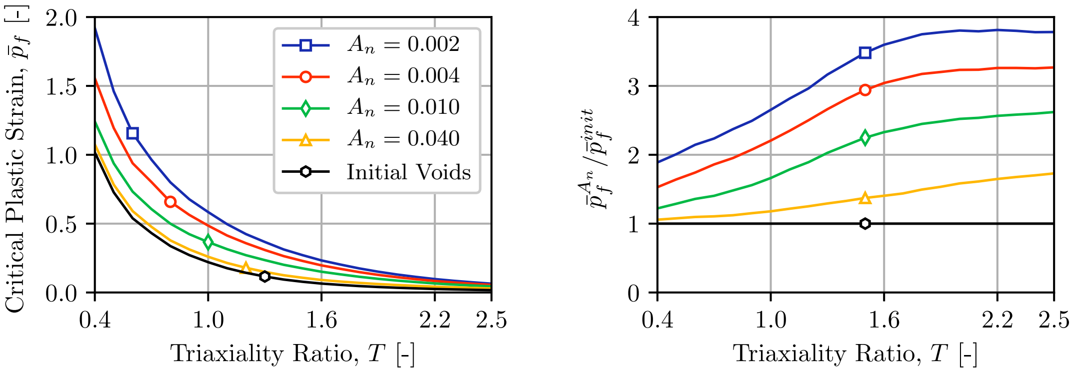

(a) *(b)*

Figure 5.16: *(a) The plastic failure strain for different values of A_n under generalized tension, and (b) the ratio between the fracture strain obtained for the nucleation band material $\bar{p}_f^{A_n}$ and the initially voided band material $\bar{p}_f^{init}$, as a function of T.*

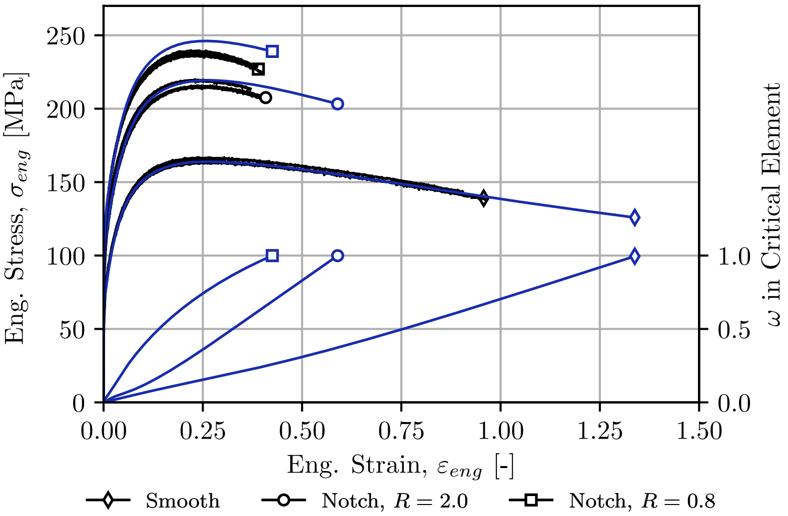

Figure 5.17: *Global engineering stress, σ_{eng}, and accumulated damage in the critical element, ω, versus engineering strain, ε_{eng}, up to failure when using the failure surface for continuous nucleation in Figure 5.15, represented by dashed lines.*

5.3 A Localization Approach to f_0 and A_n

The fracture strain of the smooth tensile specimen has been overestimated in all the previous studies. The lack of softening in the imperfection band is believed to cause this discrepancy. Figure 5.8 and 5.9 in Section 5.2.1 clearly illustrate the effect of a material with higher softening rate in the imperfection band. The higher the q_1 and q_2 parameters, the lower the fracture strain $\bar{p}_f$. Another way of obtaining higher softening is to increase the initial porosity f_0 or nucleation rate A_n. These parameters can, for instance, be fitted using the localization analysis together with the fracture strain from a single smooth specimen. This method has been shown to give good results for a medium-carbon A572 Grade-50 steel by Morin et al. [68].

5.3.1 Methodology

Figure 5.18 illustrates the method used in this section. First, unit cell analyses will be used to optimize the material parameters in the Gurson-Tvergaard model. Section 4.2 proposes an approach for such a process. The matrix material response is calibrated to the smooth tensile test. The predicted particle content from Alstruc will be used as a first estimate for the porosity f_0. A new porosity level will be calibrated later on. However, the optimization of the q_i parameters do not depend too much on the initial porosity, as discussed in Section 4.2.2.

Finite element simulations of the tensile bar are executed to access the deformation gradient $\mathbf{F}(t)$ in the center, which will then be imposed to the material outside the imperfection band in the strain localization analysis. The material properties in the imperfection band, here f_0 and A_n, can then be iteratively adjusted. The optimized parameter is obtained once the plastic strain in the material outside the band at localization equals the plastic strain in the center element at fracture, named p_f.

The deformation gradient, $\mathbf{F}(t)$, from the critical element in the notched specimens can then be enforced to the material outside the imperfection band with the new material parameters to estimate the plastic failure strain in this current element. Since material failure can occur in other locations than the center element, all elements over the cross-section must be examined. A failure surface for proportional loading may also be constructed in the same manner as before with the new parameters.

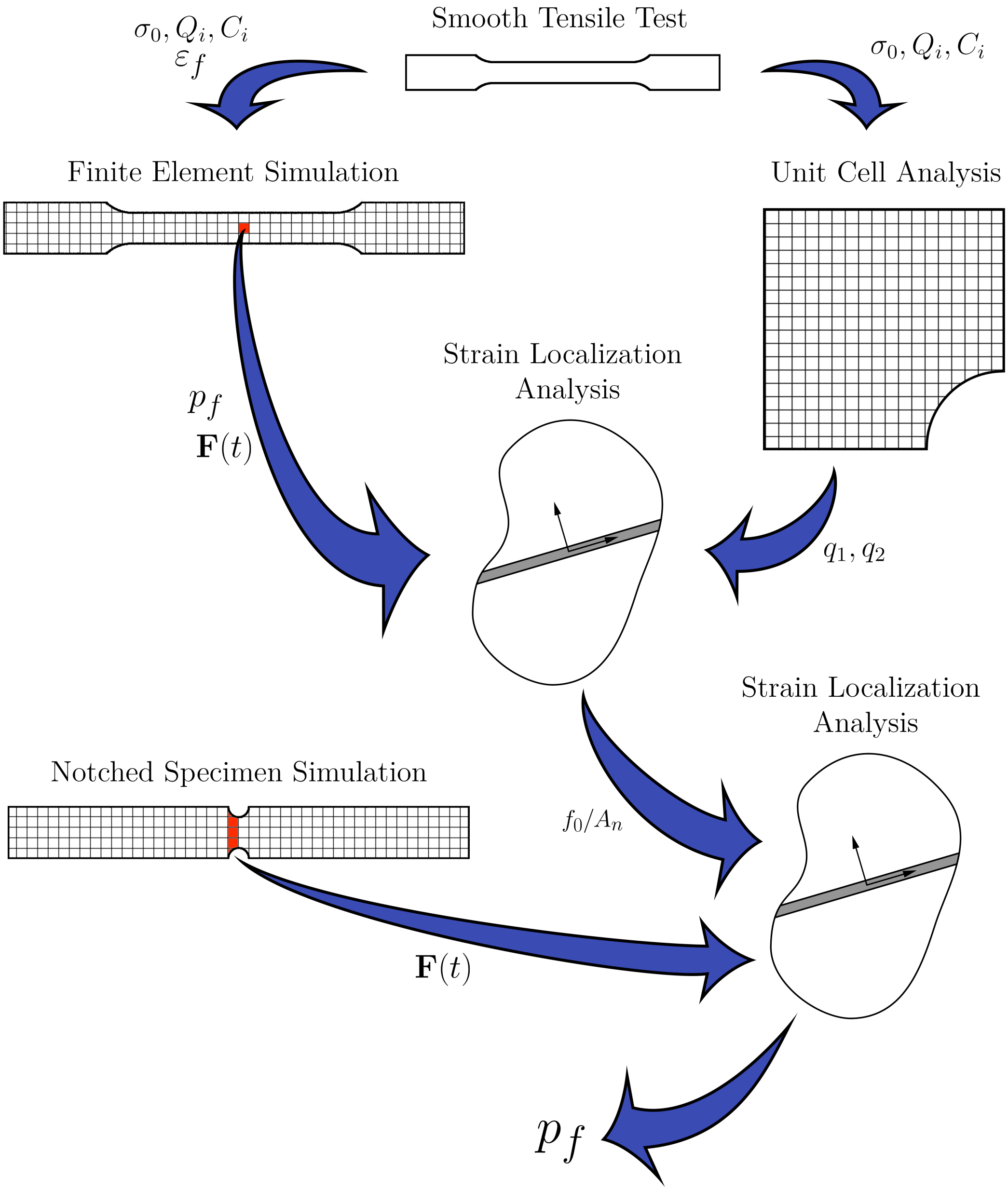

Figure 5.18: *A methodology for predicting the plastic failure strain, p_f, from localization analysis using the experimental result from a single smooth tensile specimen. The global fracture strain ε_f and material response (σ_0, Q_i and C_i) are obtained from the experiment. Finite element simulation is used to find the deformation gradient and plastic failure strain in the critical element. The q_1 and q_2 parameters from unit cell analyses in Section 4.2 will be used.*

5.3.2 Optimization of f_0 and A_n

The material parameters in Table 3.3 will be imposed to the material both inside and outside the band in the strain localization analysis. Softening in the imperfection band is modeled using the Gurson-Tvergaard model with the q_i parameters obtained from unit cell simulations. All parameters are summarized in Table 5.1. The deformation gradient $\mathbf{F}(t)$ in the center element is imposed to the localization analysis.

The plastic strain in the center element at fracture is 0.724 for one of the smooth tensile specimens. The red curve in Figure 5.19 shows that the initial porosity must be 0.01727 to get localization for the same plastic strain outside of the band in the localization analysis. This level of porosity is relatively high compared to the particle content of 0.00452 predicted by ALSTRUC. Other mechanisms than spherical void growth will most likely also contribute to the fracture process. Consequently, using a meaningful physical porosity might be inadequate, whereas calibrating this parameter to experiments may account for other contributions in an average sense. Moreover, the rate of softening in the material inside the band is low. Using larger q_1 and q_2 parameters will also reduce the initial porosity needed, as later shown in Table 5.3. Figure 5.20a illustrates how the stress and porosity evolve inside the band as a function of the plastic strain in the outside material for the optimized and predicted porosity level. The difference is noticeable.

Figure 5.19 also shows the optimization of the nucleation rate A_n, represented by the blue curve, which was found to be 0.03470. A maximum void volume fraction of 0.05 is allowed be nucleated. The dashed line in Figure 5.20b represents the volume fraction of nucleated particles. From this figure, the main contribution to the increase in porosity comes from nucleation up to an equivalent strain of 0.45 − 0.5. Growth dominates subsequently until localization occurs.

The stress response inside the band is similar for the initial porosity and nucleation approaches of modeling. The softening is more prominent at lower strains for the initially voided band. However, the discrepancy becomes smaller once the rate of void growth becomes more prominent.

Table 5.1: *Material parameters used in this section. The Tvergaard parameters are found from unit cell simulation in Section 4.2. The Voce hardening rule constants are given in Table 3.3.*

GT Parameter			Voce Hardening rule				
q_1	q_2	$q_3 = q_1^2$	σ_0	Q_1	C_1	Q_2	C_2
1.843	0.768	3.397	66.26 MPa	62.00 MPa	32.36	126.46 MPa	4.21

Table 5.2: *Calibrated initial porosity, f_0, and nucleation rate, A_n, from localization analysis. The calibration process is shown in Figure 5.19.*

Initial porosity f_0	Nucleation rate A_n
0.01727	0.03470

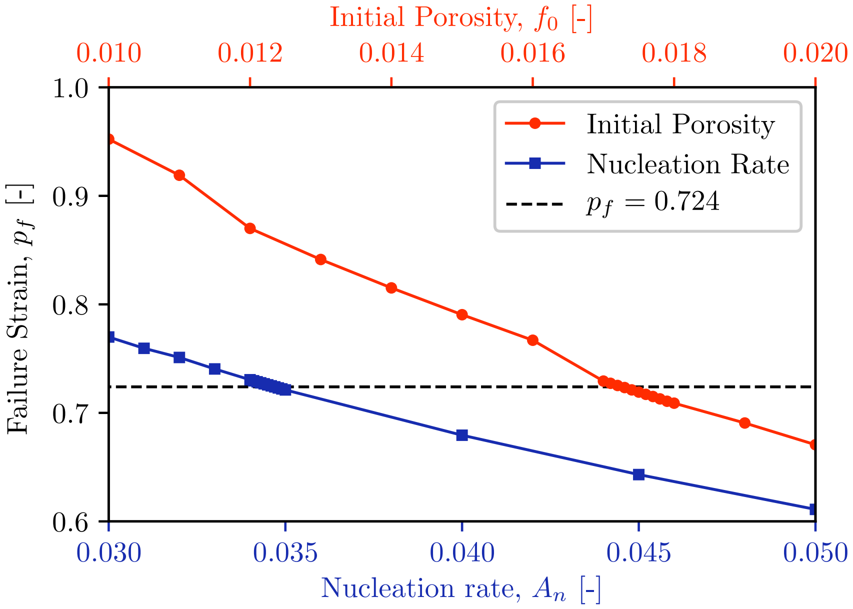

Figure 5.19: *Calibration of the nucleation rate A_n (primary horizontal axis/blue graph) and initial porosity f_0 (secondary horizontal axis/red graph). The calibrated values are given in Table 5.2. The dashed horizontal line represents the plastic failure strain in the center element of the smooth specimen.*

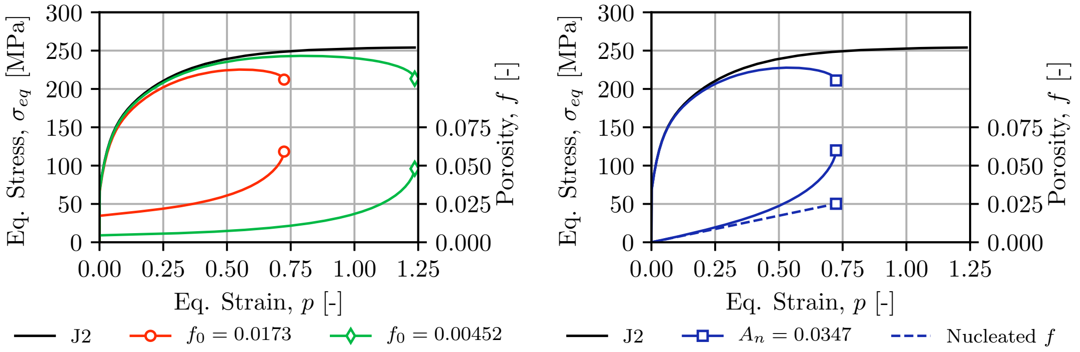

(a) *Initially voided band material.* **(b)** *Nucleation of voids in the band material.*

Figure 5.20: *Equivalent stress, σ_{eq}, and porosity, f, inside the band material. The solid black line represents the J2 plasticity response which the material outside the band encounters. Two different initial porosities are shown in (a); the optimized f_0 from Table 5.2 and the predicted f_0 from* ALSTRUC. *The dashed blue line in (b) represents the porosity nucleated.*

5.3.3 Fracture Strain From Localization Analysis

The deformation gradient in the integration point of the critical element can be imposed to the localization analysis together with the calibrated initial porosity f_0 or nucleation rate A_n to predict the critical plastic strain p_f in this element. The approach is identical to that of before. Once the plastic failure strain of the critical element is obtained, the global failure strain ε_f of the specimen can be determined.

All elements over the cross-section must be checked for the notched axisymmetric specimens since the critical element is unknown a priori. It is safe to assume that the critical element in the plane strain tension test is located in the center. As earlier shown in Figure 3.12, the center element is prone to the highest triaxiality ratio and plastic strain. Furthermore, this element also experiences Lode parameter closest to generalized shear.

Figure 5.21 shows the predicted global failure strain ε_f over the cross-section. Here, R/R_0 equal to 0 and 1 corresponds to the center and outer surface of the specimen, respectively. The center element experiences the lowest fracture strain in the case of a $R2$ notched specimen. On the contrary, the lowest strain at localization occurs at the surface for the $R08$ notched specimen. This is the same behavior as earlier observed. Moreover, the use of nucleation predicts more ductile behavior in both cases. The disparities between the blue and red curves, however, is less near the specimen surface. Larger plastic strains are allowed in these outer elements since the triaxiality is less compared to the center of the specimen, making the void growth phase not as dominant. Consequently, more particles are nucleated before localization occurs, making the differences less outstanding. Also, the predicted failure strain is almost the

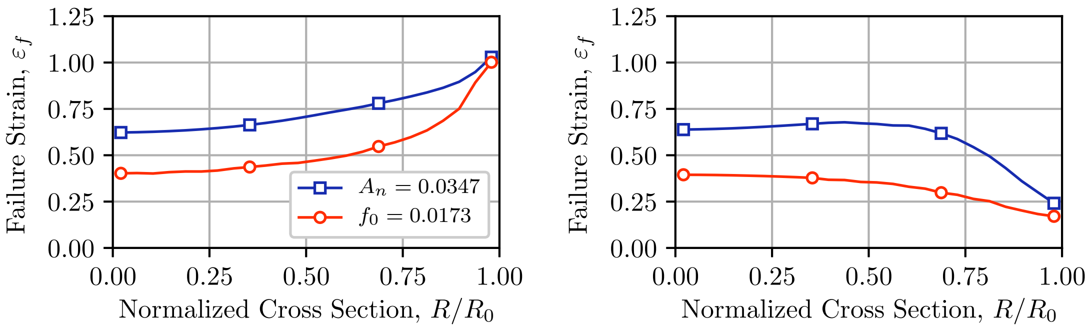

(a) *Notch,* $R = 2$ ***(b)*** *Notch,* $R = 0.8$

Figure 5.21: *Predicted global fracture strain,* ε_f*, from localization analyses across the cross-section of the notched asymmetric specimens for initial voids and void nucleation in the band material. Fracture is initiated where* ε_f *is at its lowest point. Consequently, fracture is initiated in the center for the* $R2$ *and at the surface for the* $R08$ *specimen.*

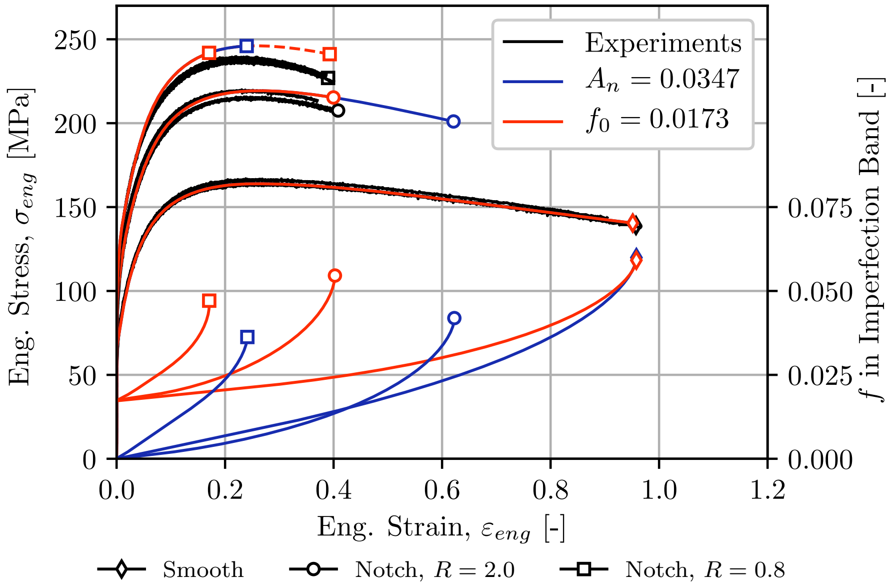

Figure 5.22: *Global engineering stress, σ_{eng}, and porosity in the critical element, f, versus engineering strain, ε_{eng}, up to failure when the deformation gradient $\mathbf{F}(t)$ of the critical element is imposed to the strain localization analysis. The red color represents an initially voided band material. The blue color shows the results when a continuous nucleation law is used. The dashed red line shows the predicted results if the center element is assumed to be the critical element for the $R08$ notched specimen.*

same in the center for both specimens. This can be supported by the fact that the global fracture strain from experiments is similar for these specimen types.

Figure 5.22 shows that excellent prediction is obtained for the $R2$ notched specimen using an initial porosity, whereas the results for the $R08$ notched specimen is somewhat conservative. This is because fracture is initiated at the specimen surface. If the occurrence of localization in the center element is used instead, good prediction is achieved for this specimen type as well. The red dashed line in Figure 5.22 illustrates this.

Non-conservative results are obtained for the $R2$ notch when using void nucleation, whereas the prediction for the sharper notched specimen is conservative. As previously discussed, the fracture process starts at the specimen outmost element, which has been proven to provide conservative estimates. Compared to the initially voided band material approach, the predicted fracture strain is increased when a nucleation approach is used to model the imperfection band. This is expected since A_n is calibrated from the smooth specimen, which experiences large plastic strains before localization. Consequently, more voids are allowed to nucleate before void growth becomes the main contributor to the increase in f. Once the stress triaxiality is increased, void growth becomes more extensive, and the plastic failure strain decreases. Thus, fewer particles are nucleated in the notched specimens before the occurrence of localization, resulting in a higher failure strain compared to the initially voided material.

Figure 5.23 shows the results for the plane strain tension specimen. The prediction is good in either case, but the initially voided band predicts failure earlier. The difference in fracture strain between the two approaches is less than for the notched specimens. The observed plastic failure strain in the center element is higher, and more particles are allowed to nucleate before void growth takes over.

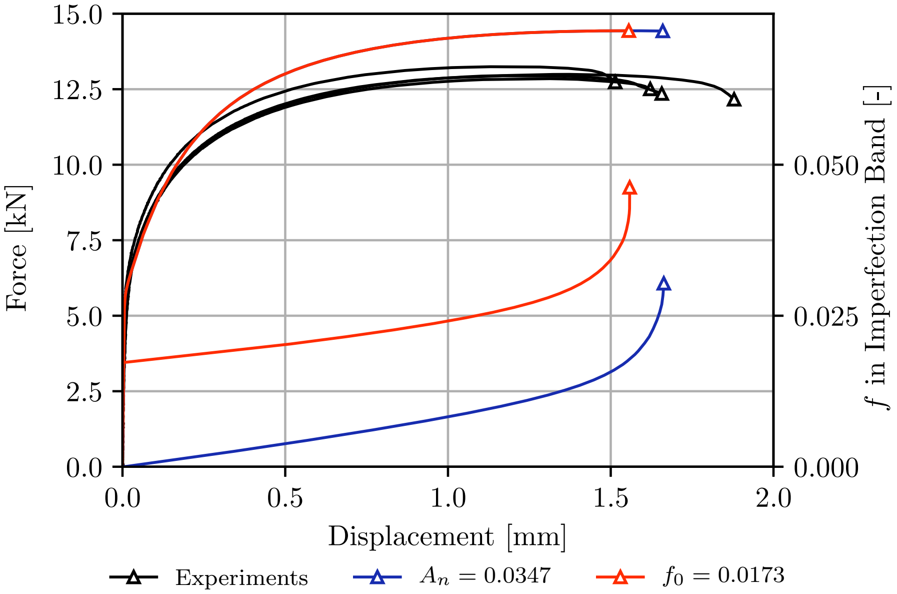

Figure 5.23: *Global force and porosity in the critical element, f, versus the displacement up to failure when the deformation gradient $\mathbf{F}(t)$ of the center element is imposed to the strain localization analysis. A localization band modeled with initially voided and continuous nucleation material are shown in this figure.*

5.3.4 Fracture Surface in FE-Simulations

A fracture surface should be constructed for finite element purposes. Such a surface can be obtained in the same way as done in Section 5.2 by imposing proportional loads in the localization analysis. Figure 5.24a shows the plastic failure strain $\bar{p}_f$ as a function of the Lode parameter for different triaxiality ratios for the optimized f_0 and A_n. The shape of the curves is similar in the intermediate to high stress triaxialities. Larger differences are found in the low triaxiality domain, and the initial void approach of modeling the band material appears to be more Lode dependent. Moreover, this approach predicts higher ductility in the low triaxiality domain, as shown in Figure 5.24b. This figure shows the critical plastic strain as a function of T for the case of generalized tension, i.e., $L = -1$. Evidently, using a nucleation law in the band material predicts more ductile response in the vast majority of triaxiality ratios.

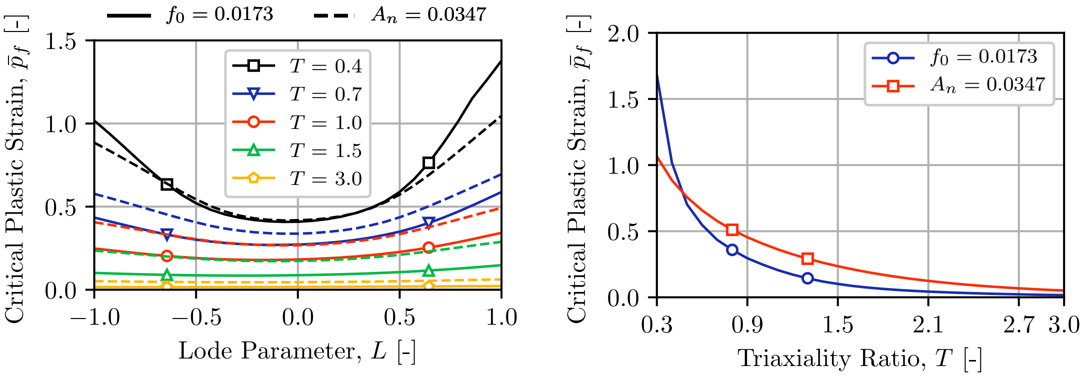

(a) *(b)*

Figure 5.24: *Plastic failure strain, $\bar{p}_f$, obtained from proportional loading in the localization analysis. The band material is modeled as both initially voided and with a continuous nucleation law with the optimized parameters in Table 5.2. Figure (a) shows $\bar{p}_f$ for different T in L-space. Figure (b) shows the case of generalized tension for increasing triaxiality ratio.*

The two curves in Figure 5.24b cross at a slightly higher plastic failure strain than 0.724, as predicted in the center element of the smooth specimen. This is natural since these curves have been constructed using a proportional loading path, whereas f_0 and A_n have been obtained using the actual loading path of the center element. Consequently, both fracture surfaces predict almost the same fracture strain for the smooth tensile test, as shown in Figure 5.25. The point of failure for the smooth specimen is, however, somewhat overestimated. It should be emphasized that the approach of predicting failure in the localization analysis and finite element simulation is different. In the imperfection band analysis used herein, failure is connected to instability in the constitutive law due to imperfections in the material. Consequently, deformation is concentrated to this slightly softer material once it reaches a critical level. On the contrary, a linear damage accumulation rule is applied to the finite element simulations, as explained in Section 2.1.5. No physical mechanisms are directly associated with this approach. A non-linear approach of accumulating damage might correct this, but would also be harder to calibrate.

The differences between these two approaches are particularly prominent when comparing the void growth inside the band material in Figure 5.22 and the accumulated damage in Figure 5.25. Whereas the damage accumulates rather continuously, the porosity inside the band material experiences rapid changes upon failure. The ductility is also somewhat higher for the two notched and plane strain specimens compared to the prediction from localization analyses, as indicated in Figure 5.25 and 5.26. The differences are, however, small.

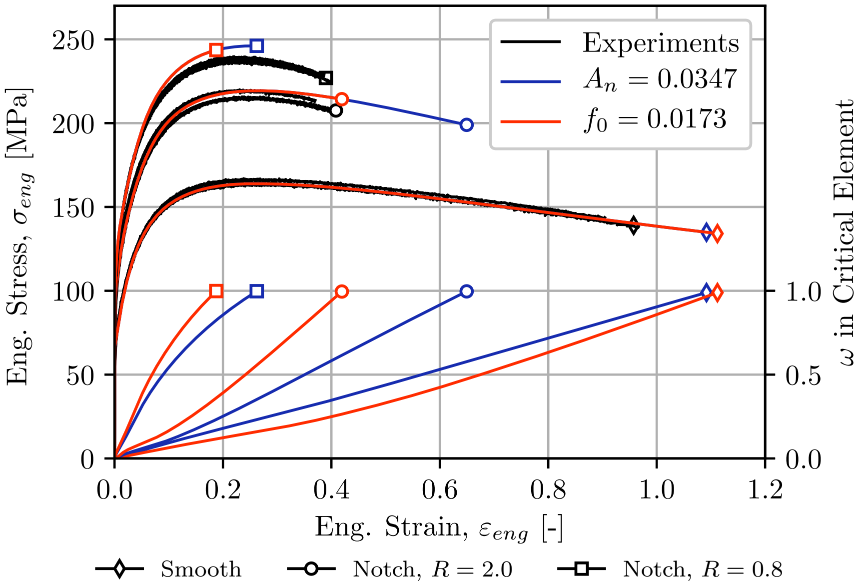

__Figure 5.25:__ Global engineering stress, σ_{eng}, and accumulated damage in the critical element, ω, versus engineering strain, ε_{eng}, up to material failure for the axisymmetric specimens when the fracture surfaces in Figure 5.24 is used in the finite element simulations.

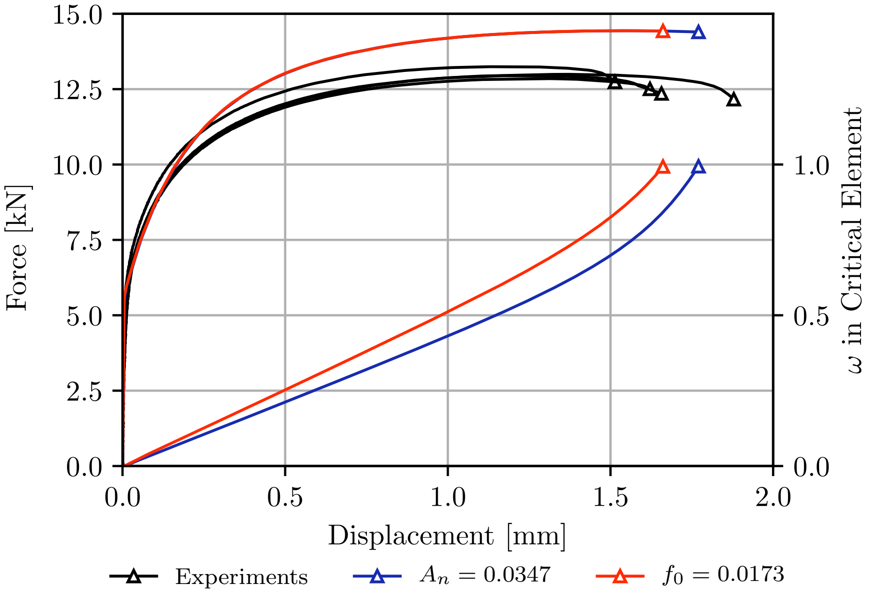

__Figure 5.26:__ Global force and accumulated damage in the critical element, ω, versus the displacement up to material failure for the plane strain specimen when the fracture surfaces in Figure 5.24 is used in the finite element simulations.

5.3.5 Parametric Study

A parametric study has been performed to determine how different parameters affect the performance of the procedure presented in this section. The case of initially voided band material will be used in this study. The nucleation approach of modeling the band material will be included in the investigation of the effect of q_1 and q_2.

Influence of Shear Modification

The effect of k_s due to softening in shear has been documented in Section 5.2.2. This contribution was found less prominent at intermediate to high stress triaxiality ratios but tends to reduce the ductility in the lower triaxiality domain. Moreover, the effect of the Lode parameter is stronger for higher k_s values. Figure 5.27 shows the fracture surface for k_s equal to 0 and 2 when the optimized f_0 from Table 5.2 is used. The fracture strain $\bar{p}_f$ for generalized tension is reduced by 21.0% and 4.7% for $T = 0.3$ and 1.0, respectively. This reduction is beneficial since the global fracture strain for the smooth specimen was overestimated when using a fracture surface in the finite element simulations. Hence, including some shear contribution will reduce the fracture strain for the smooth specimen without affecting the notched tests too much.

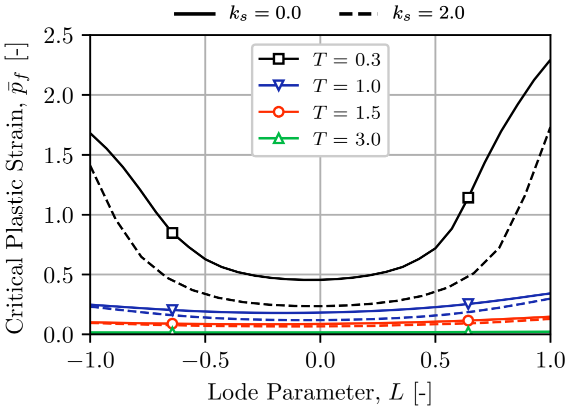

Figure 5.27: *Plastic failure strain, $\bar{p}_f$, obtained from proportional loading in the localization analysis. The band material is modeled with no shear contribution and a shear factor $k_s = 2$. The initial porosity f_0 is 0.0173 in both cases. Note that the plot is similar to Figure 5.12, but with a different initial porosity.*

The stress-strain response of all axisymmetric test are plotted in Figure 5.28 for the two different values of k_s. The smooth specimen fails earlier, whereas the $R2$ notch is barely affected. Furthermore, the $R08$ notch fails at a much lower strain as well. This is rather expected since the critical element is located at the specimen surface where the Lode parameter is closer to 0. The plane strain element is, in general, more affected by the k_s for the same reason. Figure 5.29 shows that the displacement at fracture is underestimated. Quickly summarized, including some softening due to shear yields more conservative estimations.

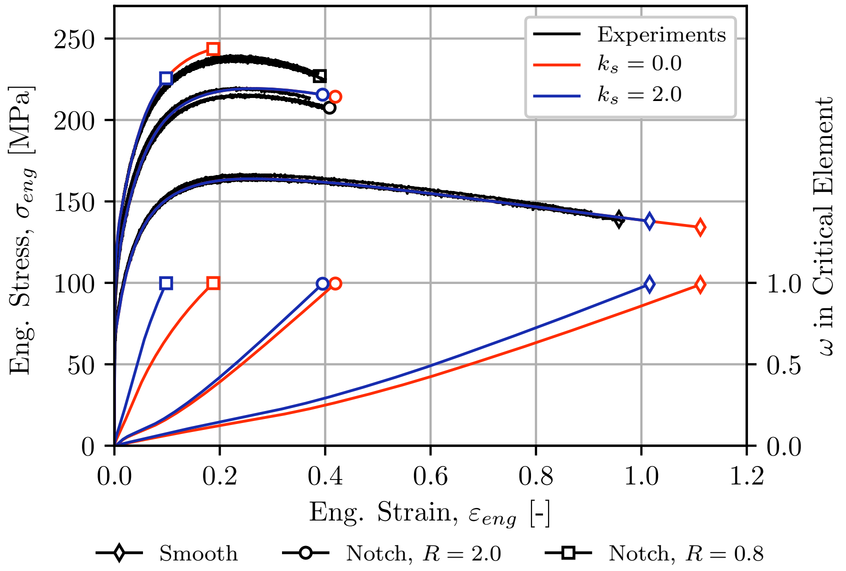

Figure 5.28: *Global engineering stress, σ_{eng}, and accumulated damage in the critical element, ω, versus engineering strain, ε_{eng}, up to material failure when the failure surfaces in Figure 5.27 are used in the finite element simulations.*

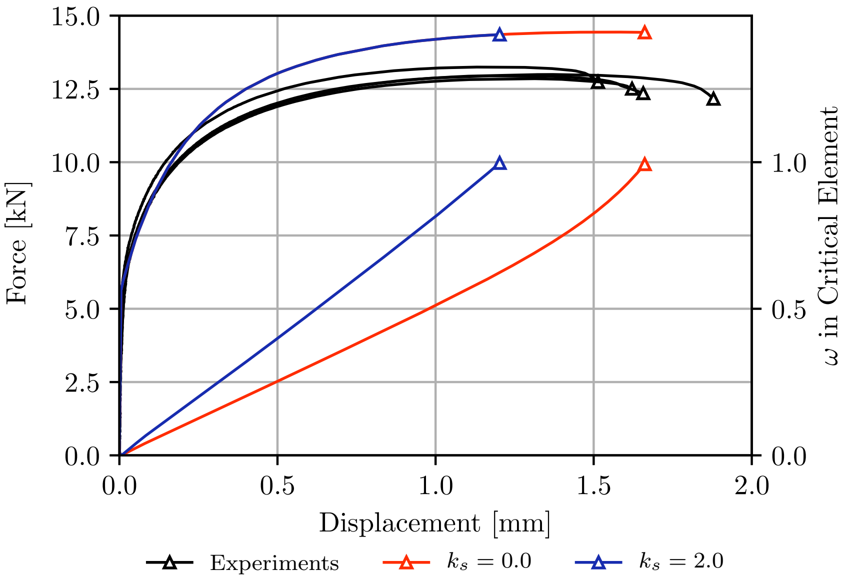

Figure 5.29: *Global force and accumulated damage in the critical element, ω, versus the displacement up to material failure when the failure surfaces in Figure 5.27 are used in the finite element simulations.*

Influence of q_1 and q_2

It has previously been shown that the porous plasticity parameters q_1 and q_2 govern the rate of softening. The higher the values, the higher the void growth and softening. Chapter 4 demonstrates that q_1 and q_2 found from unit cell simulation did not correspond well with experiments. It is thus interesting to examine how these parameters affect the prediction of fracture. The optimized q_1 and q_2 from experiments and unit cell are compared below. Moreover, the original Gurson model, i.e., $q_1 = q_2 = 1$, and the parameters proposed by Tvergaard [15], i.e., $q_1 = 1.5$ and $q_2 = 1$, are also included in this study.

Table 5.3 summarizes the corresponding f_0 and A_n for all models. They are sorted from least to most soft according to the trend seen in Figure 4.24. In general, higher softening due to q_1 and q_2 results in lower f_0 and A_n. This result is rather obvious since increasing both f_0 and A_n tends to soften the material response. It is also noteworthy that the predicted parameters from experiments yield only slightly higher initial porosity compared to the particle content from ALSTRUC. This similarity does not indicate whether the estimate on initial porosity is good or not, since q_1 and q_2 are dependent of the initial porosity when experiments are used to calibrate them, as indicated in Figure 4.28. However, it might highlight the very nature of the band imperfection analysis in the sense that the band material has properties that yield a slightly softer material response.

Figure 5.30 and 5.31 show that the different sets of q_1 and q_2 predict similar global fracture strain when the localization analysis is used to predict the failure strain. Only the case of initially voided material is shown herein. The void nucleation approach of modeling the band material yields similar results.

Table 5.3: *Optimized initial porosity f_0 and nucleation rate A_n for different combinations of q_1 and q_2. The different models are sorted from most to least soft.*

	q_1	q_2	$q_3 = q_1^2$	f_0	A_n
Optimized from Experiments	2.06	1.0	4.244	0.00529	0.01330
Tvergaard Parameters [15]	1.5	1.0	2.25	0.01174	0.02565
Optimized from Unit Cells	1.843	0.768	3.397	0.01727	0.03470
Gurson Parameters	1.0	1.0	1.0	0.02874	0.05206

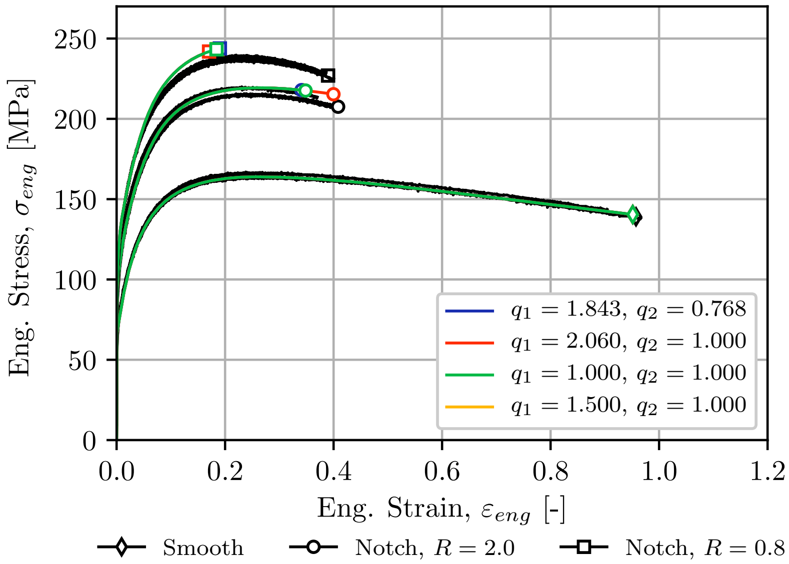

Figure 5.30: *Global engineering stress, σ_{eng}, versus engineering strain, ε_{eng}, up to failure for the axisymmetric specimens. The fracture strain is predicted by imposing the deformation gradient $\mathbf{F}(t)$ from the critical element to the localization analysis.*

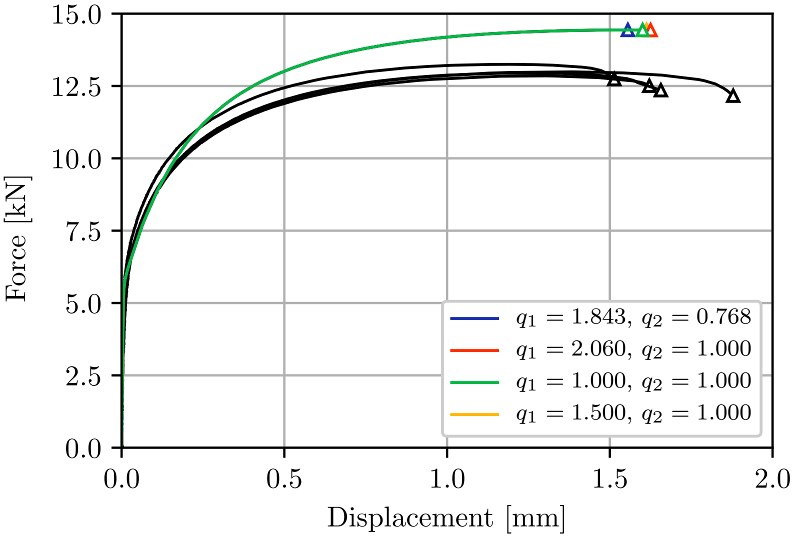

Figure 5.31: *Global force versus the displacement up to failure for the plane strain specimen. The point of fracture is predicted by imposing the deformation gradient $\mathbf{F}(t)$ from the center element to the localization analysis.*

Influence of the Lode Parameter

As previously observed, the fracture process is initiated in the outer element for the $R08$ notched specimen. This element experiences both a Lode parameter closer to zero and higher plastic strains, resulting in a very conservative estimate of the global fracture strain. Studies also yield excellent prediction if the center element is assumed as the critical element, as indicated by the red dashed line in Figure 5.22. Many fracture models do not include any dependencies of the Lode parameter, which could result in less accumulated damage closer to the specimen boundaries where the Lode parameter deviates from generalized tension. Therefore, it is interesting to see how well the calibrated fracture surface performs when removing the Lode dependency. The case of generalized tension of the initially voided band material from Section 5.3.2 will be used for this purpose.

As Figure 5.32 and 5.33 suggest, removing the Lode dependency of the yield surface increases the predicted fracture strain of the $R08$ notched and PST specimens, while keeping the results unchanged for the other two test specimens. This is as expected since the critical element in the smooth and $R2$ notched specimens is located in the center where $L = -1$. However, the fracture is still initiated near the outer surface of the $R08$ specimen. Moreover, the predicted fracture strain for the PST specimen becomes non-conservative once the Lode dependency is removed, suggesting that the effect of L should not be ignored.

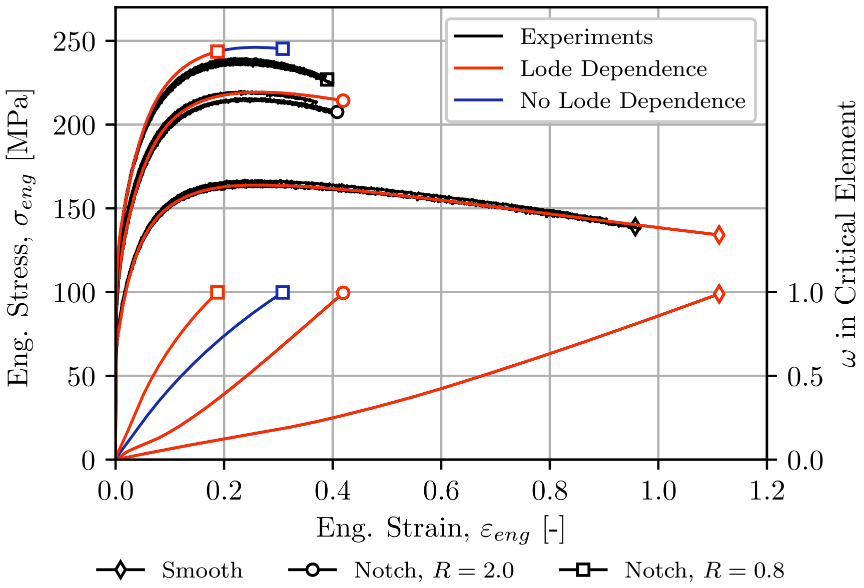

Figure 5.32: *Global engineering stress, σ_{eng}, and accumulated damage in the critical element, ω, versus engineering strain, ε_{eng}, up to material failure when the fracture surfaces for $L = -1$ in Figure 5.24b is used in the finite element simulations.*

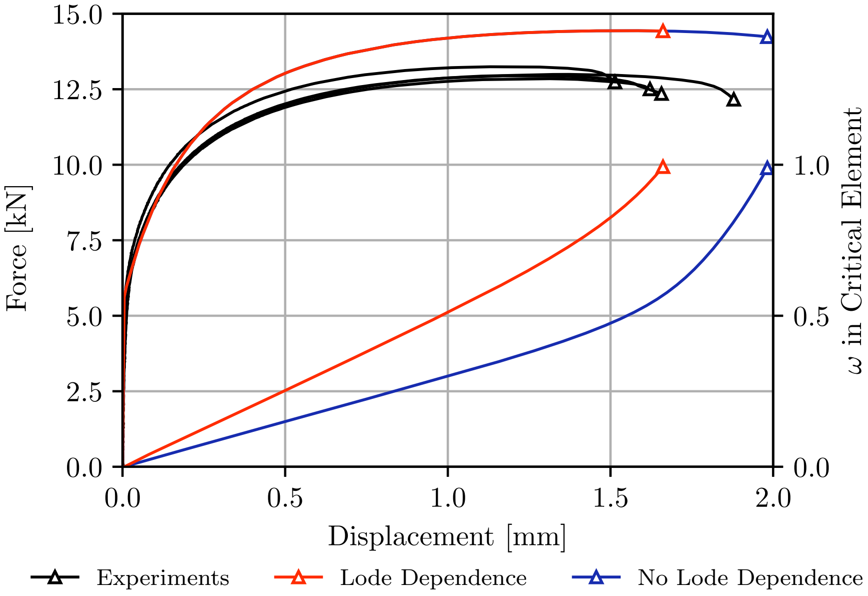

Figure 5.33: *Global force and accumulated damage in the critical element, ω, versus the displacement up to material failure when the fracture surfaces for $L = -1$ in Figure 5.24b is used in the finite element simulations.*

5.4 Failure Models

Experimental data from various specimen geometries are commonly used to calibrate different fracture models. Section 2.1.5 presented some common criteria that have been extensively reported in the literature, along with extensions to make them more versatile to the Lode dependency. It is from an engineering standpoint beneficial to restrain the number of model parameters to reduce the number of material test necessary in the calibration process. For instance, the original Cockcroft-Latham criterion in Equation (2.29) can be calibrated from only a single test. It follows that the model is restricted to a limited range of applications, depending on the test used in the calibration.

It is rather obvious that no simple model can describe the complex fracture surfaces predicted from the localization analysis in this chapter. Figure 5.34–5.36 illustrate the fracture loci for the Extended Cockcroft-Latham (ECL), Extended^2 Rice-Tracey (E^{2}RT), and Modified Johnson-Cook (MJC), respectively. These surfaces have been obtained using a least-square optimization procedure from the L-BFGS-B solver in the Scipy Python package [63]. The surface in Figure 5.24 for an initially voided band material has been used as the reference. Only T between 0.4 and 2.0 have been weighed, whereas the whole range of Lode parameters is included. A better fit was obtained by excluding triaxialities lower than 0.4. Moreover, excluding the lower range of triaxialities is beneficial since it will correct some of the discrepancies observed using a linear accumulation of damage rule in the finite element simulations.

Both the ECL and E^{2}RT criteria represent the failure surface accurately in the intermediate to high triaxiality domain, whereas the MJC criterion exhibits too large Lode dependency. More substantial differences emerge at low triaxiality, i.e., $T = 0.4$. The MJC criterion is the least accurate model in this particular case and the only model that is not tilted in the L-plane. This could be corrected by adding an additional term to Equation (2.24). Moreover, the ECL criterion is accurate for positive values of the Lode parameter, but too conservative at generalized tension. The E^{2}RT criterion might be the best model for this particular fracture surface. Still, the case of generalized tension and compression are not well represented at lower T due to the way $\omega_{s1}(L)$ is defined. A parabolic function might be a better option in this case.

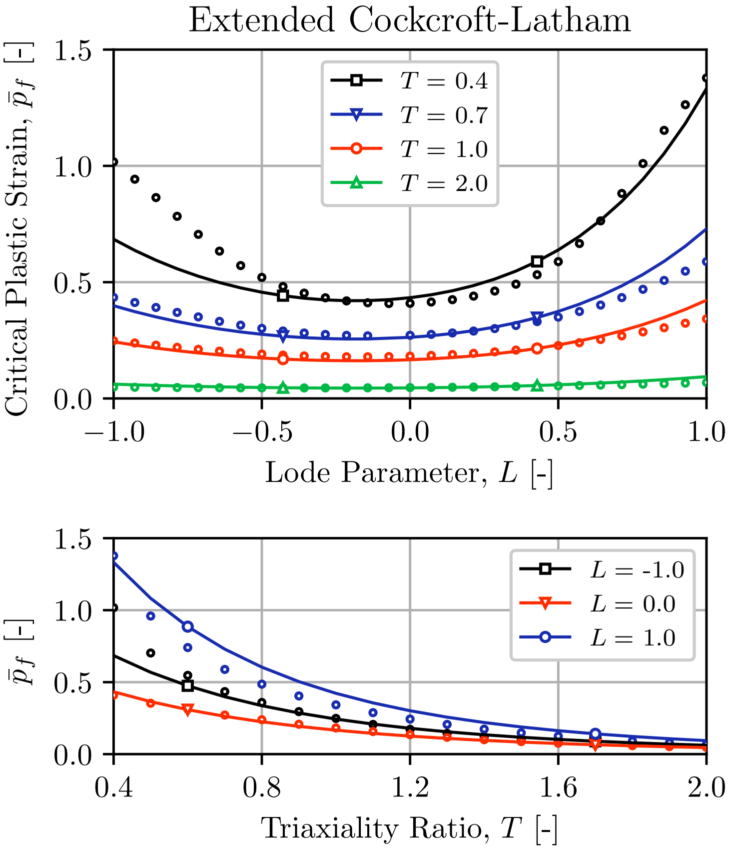

Figure 5.34: *The Extended Cockcroft-Latham model in Equation (2.33) fitted to the fracture surface in Figure 5.24 with an initially voided band material. The solid lines represent the fitted model and the dots are the actual surface.*

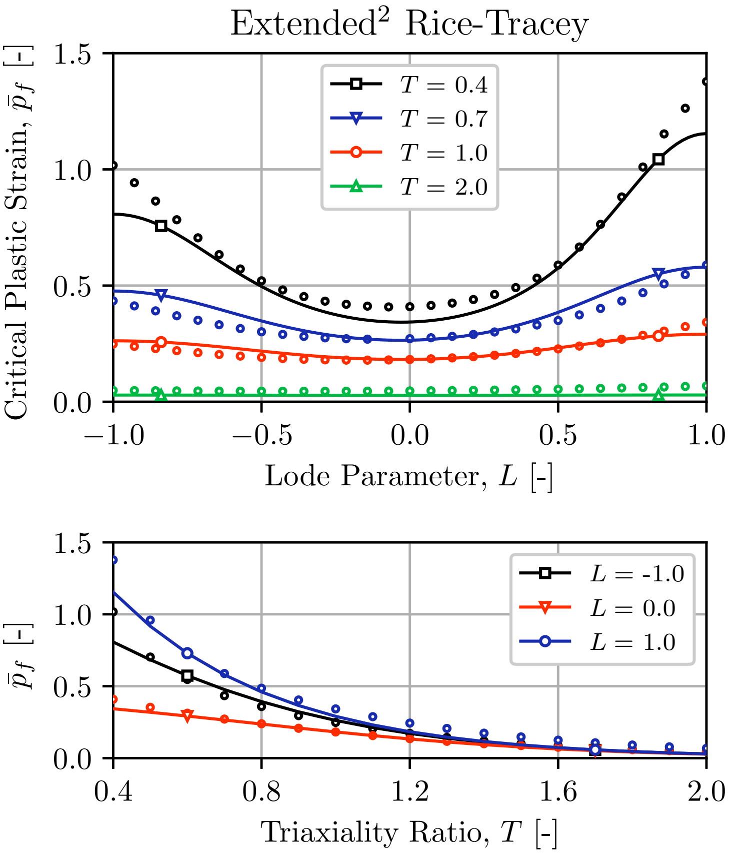

Figure 5.35: *The Extended*^{2} *Rice-Tracey model in Equation* (2.39) *fitted to the fracture surface in Figure 5.24 with an initially voided band material. The sold lines represent the fitted model and the dots are the actual surface.*

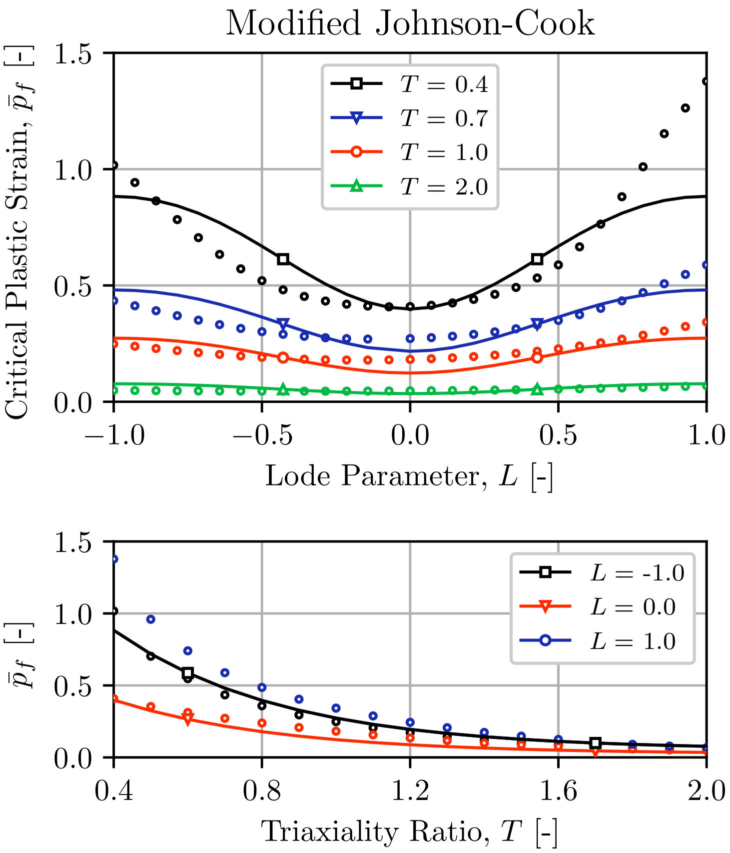

Figure 5.36: *The modified Johnson-Cook model in Equation* (2.24) *fitted to the fracture surface in Figure 5.24 with an initially voided band material. The sold lines represent the fitted model and the dots are the actual surface.*

5.5 Discussion

This section will address the performance of a micro-mechanical framework to fracture. The prediction from coalescence in unit cell simulations results in an overestimation of the global fracture strain, both when using f_c and $\bar{p}_f$. This over-prediction is expected since the necking down of material between voids, and thus localization of deformation, can occur in other directions than the one investigated. Satisfactory results were obtained by using a constant critical porosity calibrated from experiments. This approach was also able to capture the coinciding fracture strain for the $R2$ and $R08$ notched specimens. Figure 5.3 and 5.4 highlight this. It should be noted that neither f_c nor q_1 and q_2, were calibrated using a micro-mechanical framework in this particular case.

The strain localization approach based on the framework of Rice [50] showed reasonable results when using the Gurson-Tvergaard model calibrated from experiments. Again, this is not a purely micro-mechanical approach, but the complex failure surface obtained is still an accomplishment considering the limited number of tests conducted. Further, including the shear softening in the constitutive relations gave more conservative results and enhanced the accuracy of the plane strain specimen simulation. A recurring trend in both the unit cell and strain localization approach is that the use of f_0 from ALSTRUC together with the q_1 and q_2 calibrated from unit cell simulations give unsatisfactory fracture strains. This conclusion suggests that a pure micro-mechanical framework, where any form of material test is precluded, is somewhat ambitious. Consequently, some sort of material testing must be done to account for the complex mechanisms of failure in an average sense.

A methodology where only one single smooth tensile specimen is necessary to calibrate the initial porosity or nucleation rate is proposed in Figure 5.18. This approach, which is analogous to the work of Morin et al. [68], showed good results when an initially voided imperfection band was assumed. This is illustrated in Figure 5.22. Failure was found to be initiated at the surface of the $R08$ notched specimen, consequently resulting in too conservative estimates on the global failure strain. In fact, almost all predictions of failure for the $R08$ notched specimen were too conservative due to this, and the few approaches that anticipated the onset of failure in the center of this specimen overestimated all the fracture strains as well. It is unknown from the experiments if the fracture actually started at the specimen surface. However, the reoccurring underestimations of the global fracture strain for the $R08$ notch and the excellent prediction of the fracture strain for the center element using the localization analysis (dashed line in Figure 5.22) suggest otherwise.

It has been proven that excluding the effect of the Lode parameter does not influence where the fracture commences. This suggests that plastic strain must be accumulated faster in the center and slower at the surface to initiate failure in the specimen center of the $R08$ specimen. Section 7.5 reveals that the real geometry can be markedly different from the requested geometry. It is suggested from Figure 3.5a that a less sharp notch results in an increase of plastic strain in the center element, whereas the elements near the surface exhibit a decrease in p. If the geometry deviates significantly, this may help to explain why fracture is not initiated in the center in the simulations. It should be emphasized that a greater radius of the notch also decreases the triaxiality and the exact outcome of a slightly larger radius is unknown. Moreover, the deformation gradient imposed to the localization analysis was determined using J2 plasticity, which has been proven to give a too stiff material response. A higher plastic strain rate in the center might be obtained by including softening, for instance, due to material damage. Marini et al. [69] found that "a reduction in the work-hardening capability of the material gave rise to an increase in the stress triaxiality ratio" in the center of notched specimens. A higher stress triaxiality ratio results in an increase in accumulated damage, but it is unclear how this would affect the stress state near the surface.

A "best practice" approach for a numerical framework to fracture should probably use some sort of material test to calibrate the necessary material parameters. The fracture surface from localization analysis predicts, however, too large failure strain at low stress triaxialities when used in a finite element application with a linear accumulation of damage to account for non-proportional loading. This deficiency could be corrected by including some softening in shear or by excluding the lowest triaxiality domain when constructing a failure surface.

6 | Case Study - Blast Load

Applications such as protective structures against blast loads and projectiles, car crashes, and other impact problems are often prone to material failure. The fracture loci constructed in Chapter 5 could be implemented in simulations of such large-scale problems.

This chapter will investigate how the different failure criteria perform for a pre-damaged plate subjected to a blast load. No experiments have been carried out. Thus, this chapter will only examine how the models compare to each other. It should be emphasized that the calibrated material models in this thesis do not account for rate effects and temperature softening due to adiabatic heating. A study by Vilamosa et al. [70] illustrated that a 6060 aluminium alloy "exhibited negligible strain-rate sensitivity (SRS) for temperatures lower than 200°C”. A similar result was reported by Chen et al. [71], where they concluded that a 6060 T6 aluminium alloy "could probably be modeled as rate-insensitive with good accuracy". These articles do not, however, say how the strain rate and temperature affect the failure strain. Furthermore, studies on plates subjected to blast loads have indicated that the plastic strain rate is not too extensive, and the rise in temperature due to adiabatic heating is believed to be neglectable. Therefore, this simplified material model is expected to describe the problem adequately for the purpose herein.

6.1 Problem Definition

A 300 × 300 mm plate with a thickness of 1.5 mm will be investigated in this chapter. Ph.D. candidate Henrik Granum [72] provided the model. Four X-shaped slits are initially located on the plate to initiate crack growth, as shown in Figure 6.2a. Due to the symmetry of the problem, only 1/4 of the plate is modeled. The red surfaces in Figure 6.2b are prohibited from displacement and rotation in all directions. Symmetry conditions have been applied to the two blue surfaces.

The blast load is represented by a uniform pressure $P(t)$ applied to one of the faces. The pressure-time curve is represented by the Friedlander equation [73], defined as

$$P(t) = P_r \left(1 - \frac{t}{t_+}\right) \exp\left(-b\frac{t}{t_+}\right) \tag{6.1}$$

Here, P_r is the peak reflective pressure, t_+ is the duration of the positive phase, and b is the exponential decay coefficient. Figure 6.1 plots the pressure-time curve used in this case study.

It should be pointed out that the pressure acts perpendicular to the plate surface at all time. This assumption is not entirely correct after the slits open since the pressure will try to wrap the plate back into itself. An interaction between fluid and structure must be accounted for to represent the problem accurately. Such a model will, however, make the problem overly complicated for the current purpose and is omitted herein. The model also excludes the clamping system which could be a source of error [74].

The mesh is generated using a sweep method, which gives a somewhat random distribution of the elements. This might be beneficial concerning crack growth compared to a structured mesh. Figure 6.3 illustrates how the mesh looks initially and after a crack has formed. Three elements are used over the thickness, resulting in an approximate element size of 0.5 mm. It should be taken into account that the fracture criteria have been calibrated to an element size of 0.125 mm. Ideally, these criteria should be calibrated using the same element size as the large-scale problem. The simulation was run in ABAQUS/Explicit using reduced 8-node linear continuum elements (C3D8R) with hourglass control. An element erosion technique is utilized to represent crack growth. Once the integration point of an element reaches a critical value, the element is eroded, and its stress tensor is set to zero. This integration point can no longer carry any load.

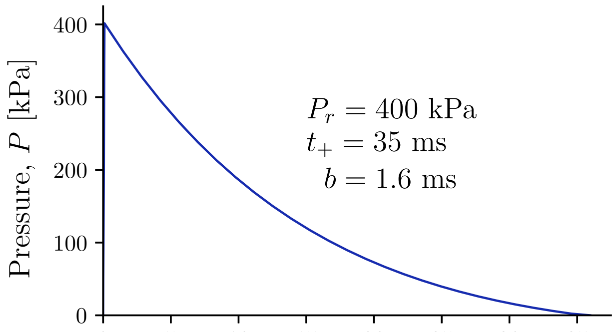

Figure 6.1: *Pressure-time plot of the load $P(t)$.*

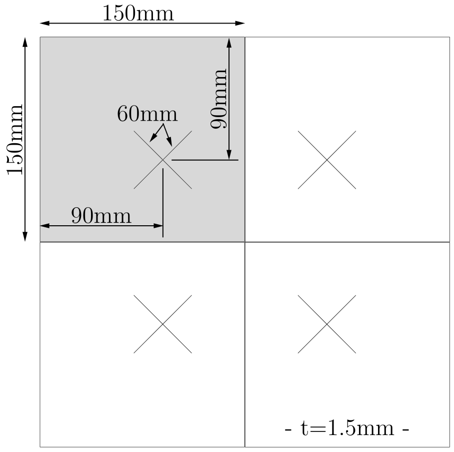

(a) Measurements of the model

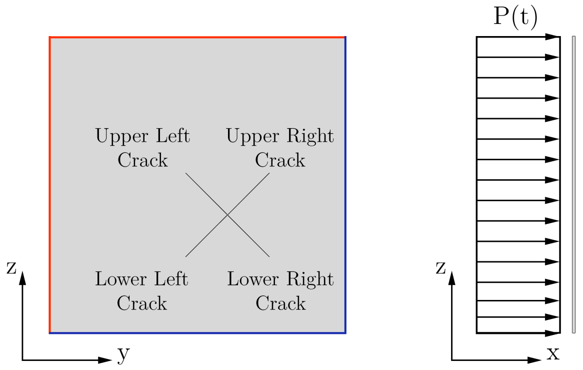

(b) Boundary condition *(c) Load*

Figure 6.2: *(a) Plate geometry, (b) 1/4 model, and (c) pressure load. Fixed boundary conditions have been applied to the red surfaces, whereas symmetry conditions are enforced to the blue surfaces.*

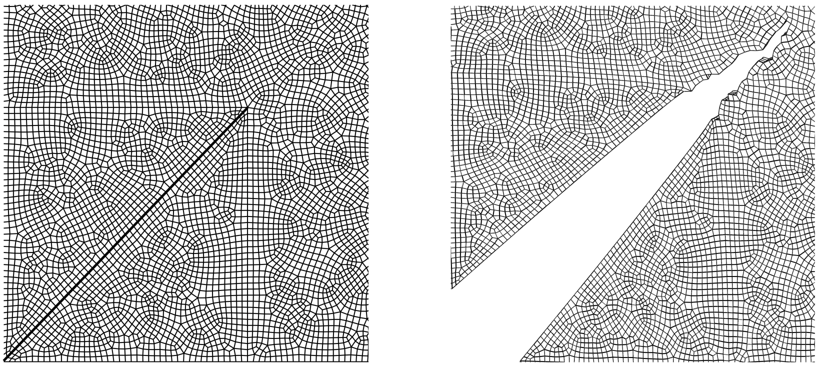

(a) Initial mesh *(b) Mesh after cracking of plate*

Figure 6.3: *The mesh at the slit (a) initially and (b) after a crack has formed.*

6.2 Results

6.2.1 Critical Porosity Approach

In this section, the plate material will be represented by the Gurson-Tvergaard porosity model. An element is eroded once a critical porosity f_c is reached at its integration point. Two different sets of material parameters are used. Figure 6.4a and 6.5a show the results when q_1, q_2, and f_c are calibrated just from unit cell simulations. Limited formation of cracks can be observed from this simulation, and the elements become highly deformed before they get eroded. As shown by the blue curve in Figure 5.1 and 5.2, this particular set of parameters does not predict accurate results for the material test either. The triaxiality in front of the crack tip was found to be in the range of 0.5 to 1.0, which is in between the smooth and $R2$ notched specimen. The void growth in the center element for these specimens is quite modest and the critical porosity of 0.0544 is high.

In contrast, Figure 6.4b and 6.5b show the crack growth and plate deformation when the same parameters are calibrated purely from experiments. The simulations of the material test are shown in Figure 5.3 and 5.4. The cracks that occur in this simulation look more realistic. It should be noted that the growth stops after approximately 15 ms, and the plate is still intact.

Consequently, the numerical approach using only unit cell simulations examined herein is not adequate to present any realistic material behavior. It should also be noted that these approaches are independent of the Lode parameter L and the critical porosity is considered as a constant value. However, the damage is coupled to the stress state, in particular, the triaxiality ratio, through the constitutive relation.

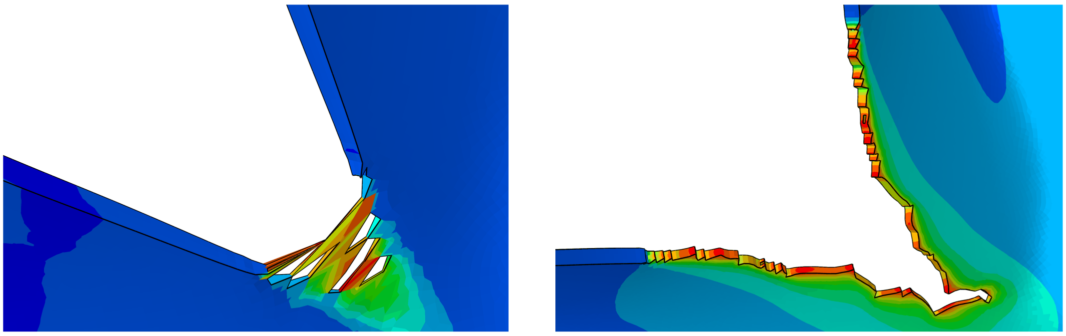

(a) Calibrated from Unit Cell *(b) Calibrated from Experiments*

Figure 6.4: *An illustration on how the lower right crack propagates for different material constants and critical porosity.*

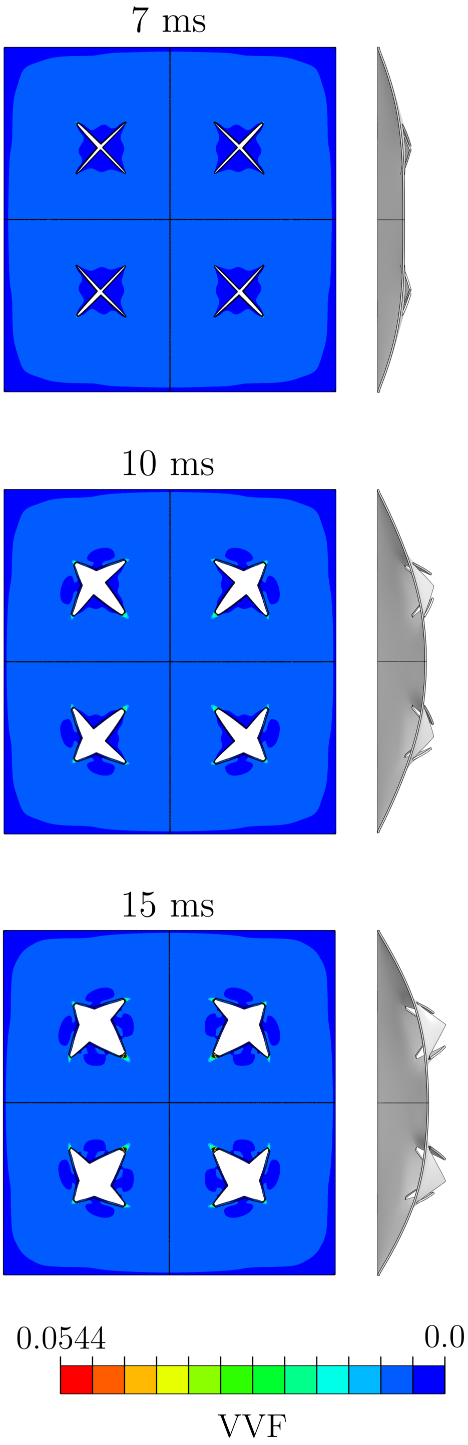

(a) Calibrated from unit cell

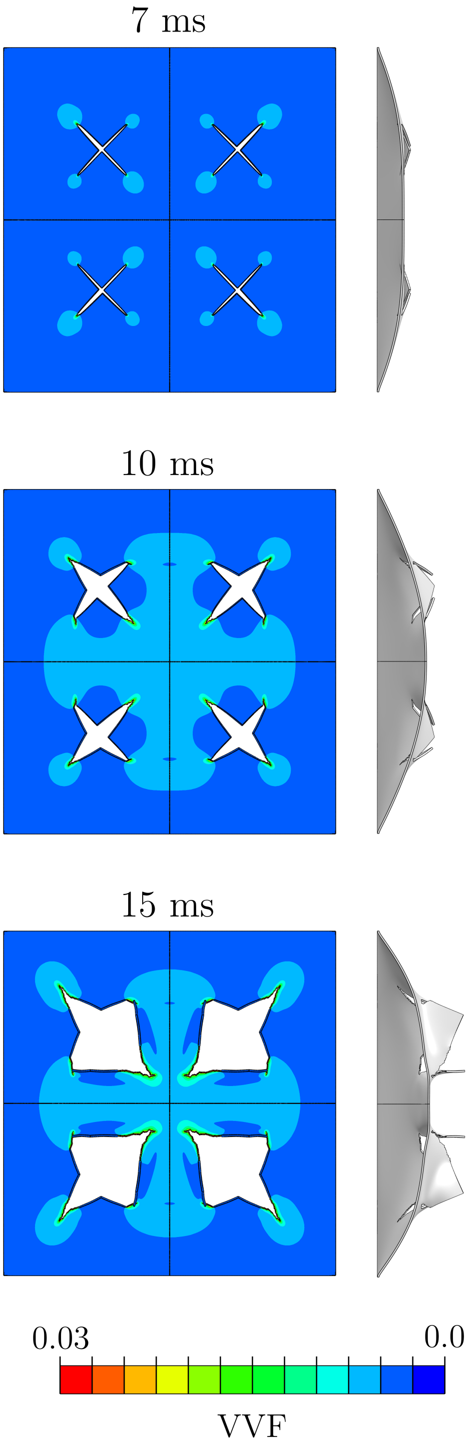

(b) Calibrated from experiments

Figure 6.5: *The deformation pattern of the plate for different material constants and critical porosities. Figure (a) shows the results when the unit cell is used to calibrate the material parameters. Experimental data is used to calibrate the material model in figure (b).*

6.2.2 Fracture Surface Approach

A classical J2 plasticity model will be used to represent the plate material in this section. Some of the fracture surfaces calibrated in Section 5.3 for an initially voided band material are used to predict material failure and crack growth. To account for the non-proportional stress state, a linear accumulation rule, given by Equation (2.23), is utilized to define the total damage as previously. The following four cases will be considered:

(a) An initially voided band material represented by the solid lines in Figure 5.27 on page 104. The initial porosity has been calibrated using a single smooth tensile test.

(b) An initially voided band material with shear softening represented by the dashed lines in Figure 5.27 on page 104. A shear constant of $k_s = 2$ is used.

(c) The calibrated Extended^2 Rice-Tracey criterion shown in Figure 5.35.

(d) An voided band material with initial porosity estimated from ALSTRUC and Tvergaard parameters optimized from unit cell simulations. This fracture surface is represented by Figure 5.8 in Section 5.2.1 and highlights a, more or less, pure microstructure-based calibration process.

Figure 6.6 – 6.8 show the lower left crack, crack propagation and plate deformation, respectively. The same letters in the list above apply the figures. The crack growth appears, in general, to be more severe in the case of a fracture locus compared to the critical porosity approach in Figure 6.5b, where the plate is still intact at the end of the simulation. Moreover, the lower right slit is more prone to crack growth, as shown in Figure 6.4b. The exact reason for this is unknown, but the lack of Lode dependency in the porous plasticity model could be one possible explanation, making the constant critical porosity approach somewhat inadequate.

Case (a) and (b) illustrate how softening in shear affects the problem. Including this softening effect results in higher crack growth rate. This is rather obvious from Figure 5.27, where the fracture strain $\bar{p}_f$ is decreased in the lower triaxiality domain. Moreover, the crack path changes somewhat as shown in Figure 6.7. Consequently, the midsection of the plate takes a more spherical shape compared to the original case (a). The plate also fails at the clamping at 9 – 10 ms when shear effects are included, which might explain the difference in the crack path. The Extended^2 Rice-Tracey criterion in case (c) gives a similar deformation pattern as the original case (a). The lower left crack in Figure 6.6 is similar as well. However, the lower right crack propagates faster than the upper one. Consequently, the released midsection takes a different shape, as indicated by the green shaded part in Figure 6.7c. The reason for this discrepancy is unknown. Case (d) is based on a failure surface obtained from the localization analysis with q_1 and q_2 calibrated from unit cell simulations and f_0 from ALSTRUC. The failure strain was found to be vastly overestimated, as Figure 5.10 illustrates. Consequently, the plate is less prone to the growth of cracks since less damage is accumulated.

It is somewhat hard to give any conclusion from this brief study without experiments. The various fracture surfaces give different fracture appearances of the plate, making the problem particularly sensitive to changes in the failure loci used. Stensjøen and Thorgeirsson performed experiments on the same type of pre-damaged plate [75]. Even though they used a 6016 T4 aluminium alloy which exhibits a different material response, the deformation pattern and the crack growth they observed are quite similar to case (a). This is a good indication that the results herein are realistic.

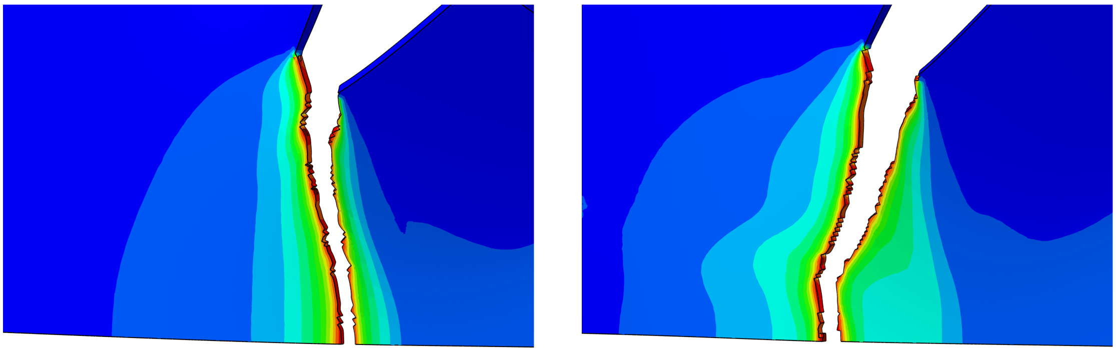

(a) *Initially voided band material,* $k_s = 0$ ***(b)*** *Initially voided band material,* $k_s = 2$

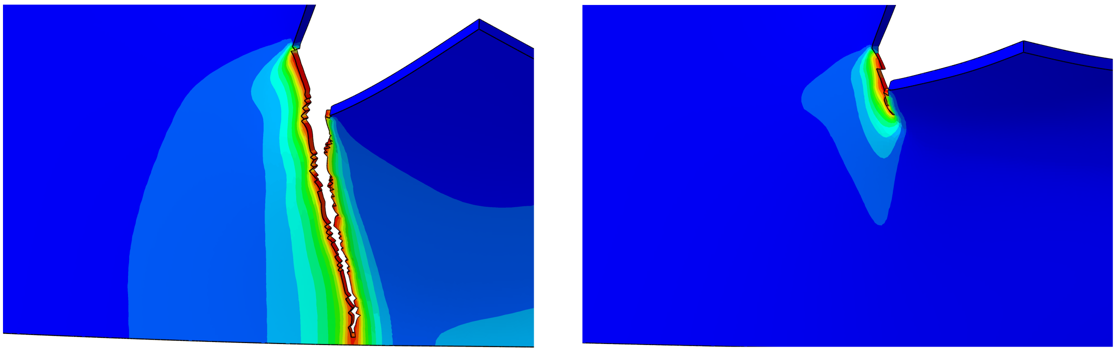

(c) *Calibrated* E^2RT ***(d)*** *Initially voided band material from UC*

Figure 6.6: *Illustrations on how the lower left crack has propagated for the four different cases in this section.*

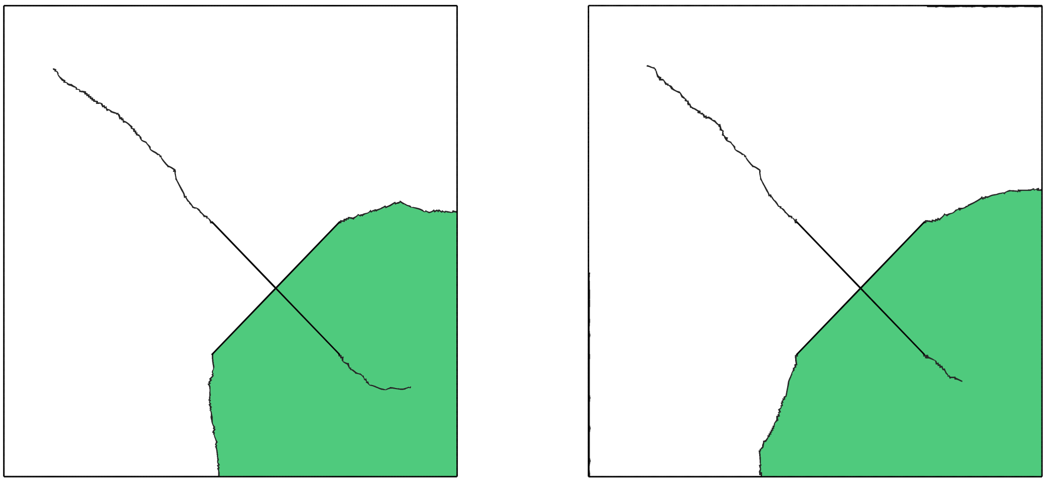

(a) Initially voided band material, $k_s = 0$ *(b) Initially voided band material, $k_s = 2$*

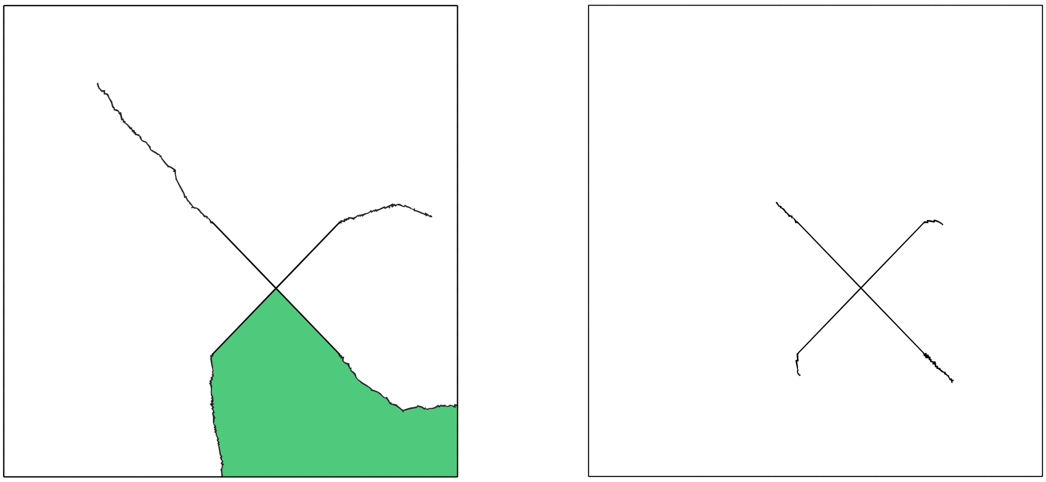

(c) Calibrated E^2RT *(d) Initially voided band material from UC*

Figure 6.7: *These figures show how the cracks in the 1/4 model have propagated for the four different cases in this section. The green shaded area represents the part that has been torn away from the plate.*

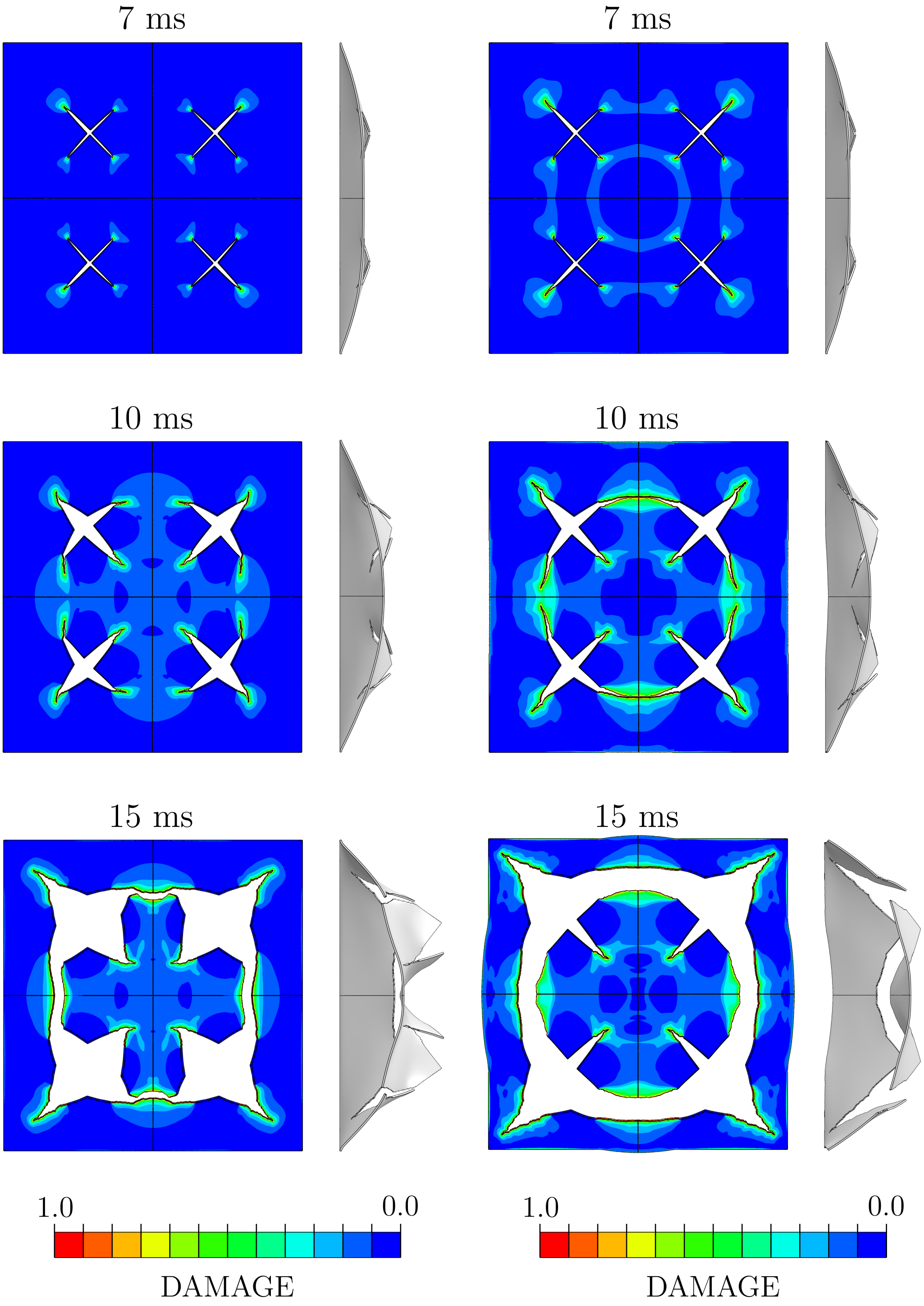

(a) *Initially voided band material,* $k_s = 0$ ***(b)*** *Initially voided band material,* $k_s = 2$

Figure 6.8: *The deformation pattern of the plate for different failure surfaces. Figure (a) shows the results when the initial porosity has been calibrated from the localization analysis without contribution due to softening in shear. The shear effects are included in figure (b). See next page for figure (c) and (d).*

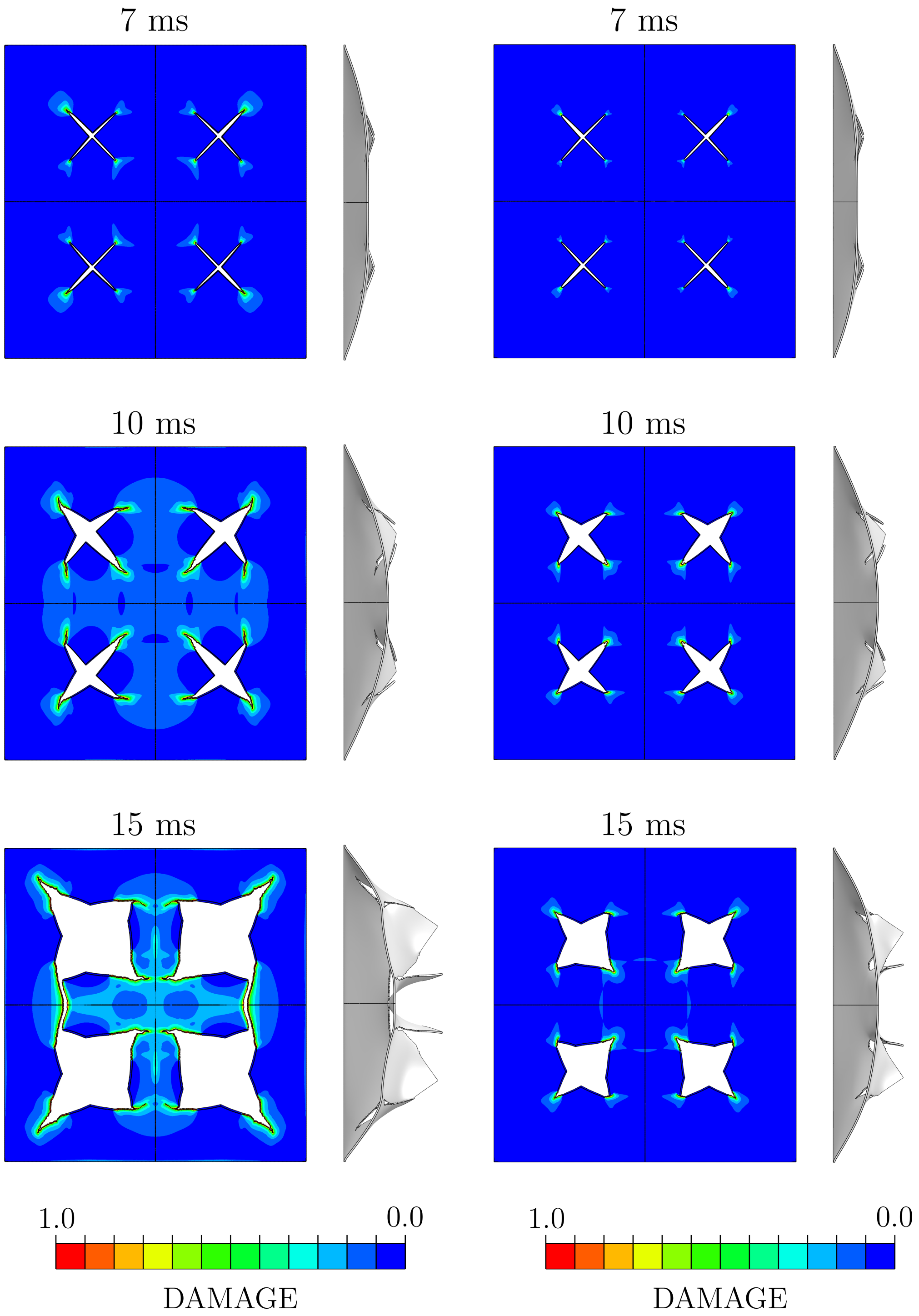

(c) *Calibrated E^2RT*

(d) *Initially voided band material from UC*

Figure 6.8: *The deformation pattern of the plate for different failure surfaces. Figure (c) shows the results when a surface calibrated to the E^2RT criteria is used. Figure (d) shows the results when a failure surface calibrated from the localization analysis with q_1 and q_2 calibrated from unit cell simulations and f_0 from* Alstruc*. See previous page for figure (a) and (b).*

7 | Aluminium Alloy 6082 T6

A 6082 aluminium alloy in a cast and homogenized state was initially intended for this thesis. However, as will be shown later, the material experienced a brittle fracture behavior, and only limited ductility was observed from the tensile tests. The test material was artificially peak-aged to a T6 temper. This chapter will document this particular alloy. Details about the material and tempering process will be explained first. Then, results from tensile tests of various smooth and notched specimens will be looked into together with an examination of the fracture surface using scanning electron microscope (SEM). Material response predicted by NaMo will be compared to the results from experiments. Lastly, some remarks will be made regarding the inaccuracies of the notched specimen geometry.

7.1 Material and Tempering Process

Hydro aluminium provided the aluminium alloy as a casted and homogenized ingot. The composition is given in Table 7.1. After machining of the different tensile test specimens, the material was further peak-aged to a T6 temper. Figure 7.1 illustrates the tempering process.

The tempering treatment was performed using a laboratory furnace. First, the specimens were solution heat treated by heating them to 540°C. Holding the samples at that temperature for an adequate amount of time allows the alloying elements to enter into a solid solution. This will distribute the alloying elements evenly, making the material uniform. Water quenching (WQ), represented by the T1-T2 period in Figure 7.1, brings the specimens rapidly to room temperature, making sure that the constituents stay in

Table 7.1: *The composition in wt% of the 6082 aluminium alloy.*

Si	Mg	Fe	Cu	Mn	Zn	Ti	Cr	Al
0.991	0.662	0.204	0.014	0.543	0.003	0.017	0.010	Bal.

solution. The specimens were stored at room temperature (RT) for 10 minutes before the artificial aging process. The aging process was performed by leaving the samples in a furnace heated to 185°C for 5 hours. This will allow larger particles to form and increase the number density of precipitates, consequently impeding the movement of dislocation and increasing the yield strength of the material.

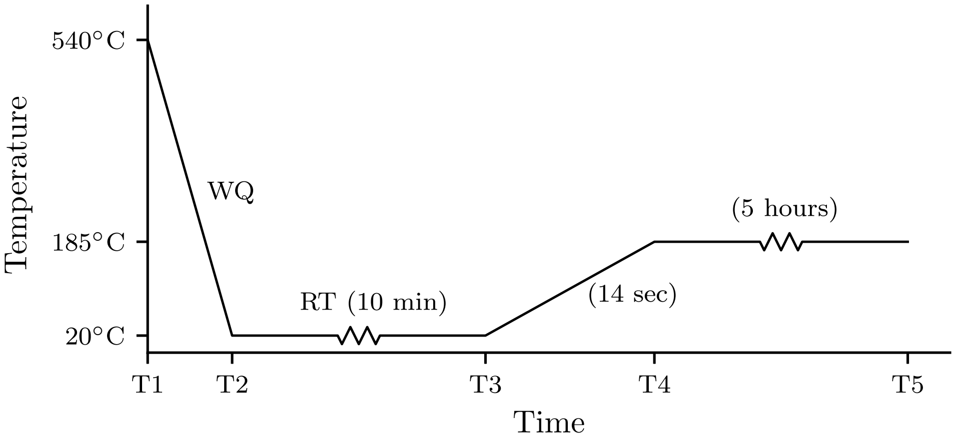

Figure 7.1: *The heat treatment of the 6082 aluminium alloy. The x-axis is not in scale.*

7.2 Tensile Tests

Quasi-static tensile tests were performed on a smooth and various notched axisymmetric tensile specimens to investigate the material behavior for different stress triaxiality ratios. The geometry of the different specimens is shown in Figure 3.7 – 3.9 and 7.2. Tests on three specimens of each type were carried out, resulting in a total of 12 tests. The tensile tests were performed in an INSTRON 5985 universal tensile machine using a 250 kN load cell. The smooth specimens were stretched with a cross-head velocity of 1.0 mm/min, corresponding to an initial strain rate of approximately 5×10^{-4}. The velocity of the cross-head for the notched specimens was 0.15 mm/s. All experiments were carried out at room temperature.

Pictures of the specimens were taken during the deformation process with a frequency of 1 frame per second. A Prosilica GC2450 camera with a Samyang 100 mm f/2.8 ED UMC macro lens was used for this purpose. Two perpendicular directions of the specimens were monitored using mirrors. The edges of the specimens were track by digital image correlation (DIC) in the software eCorr [76]. The minimum cross-section diameter could then be obtained.

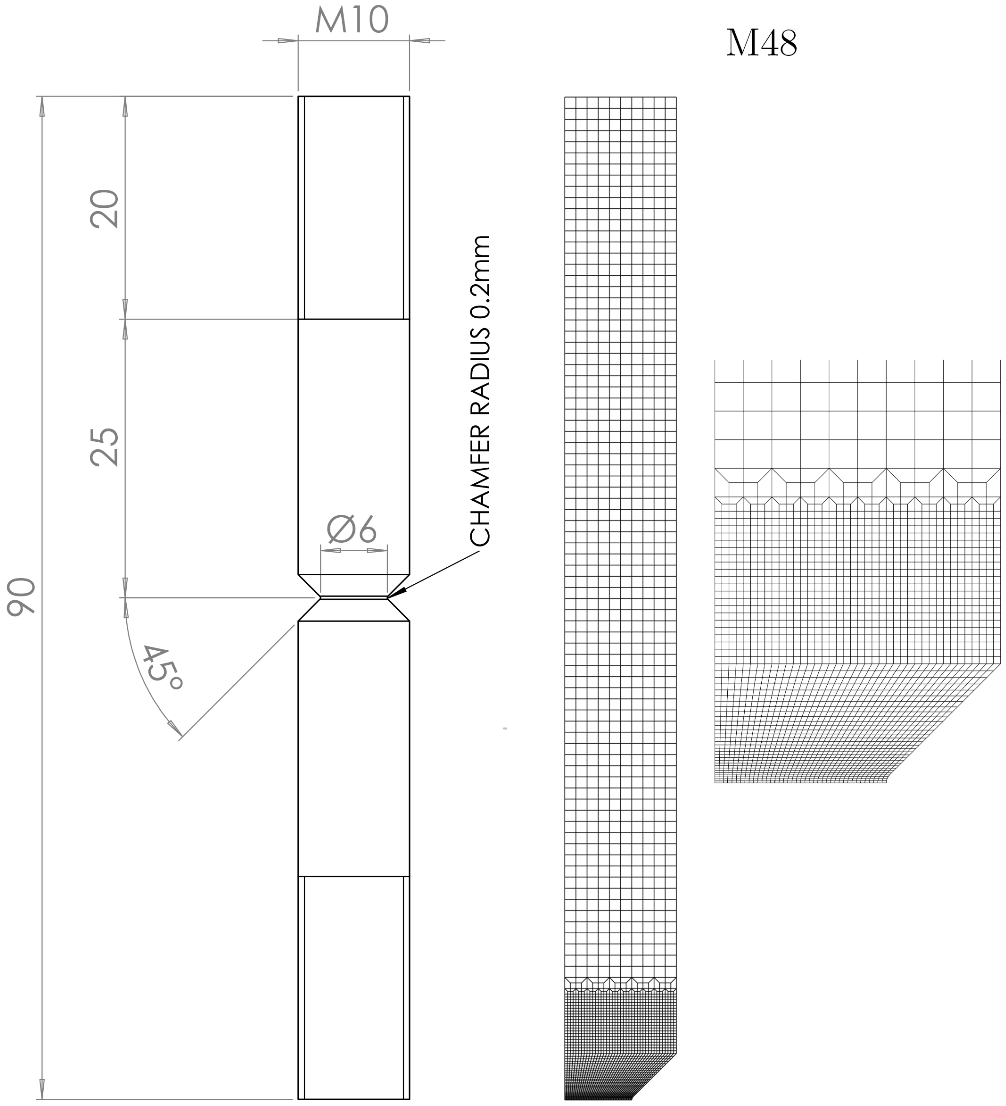

Figure 7.2: *V-notched specimen with radius $R = 0.2$. Geometry and mesh. All measurements are in mm.*

Figure 7.4 shows the engineering stress-strain curves for all 12 tests. The stress and strain have been found using Equation (2.11). Limited ductility is observed from this plot, and the smooth specimens barely surpass the point of maximum force before failure. As seen in Figure 7.3a, no clear neck is recognized in the gauge area, and the fracture surface is rather flat. The $R2$ notched specimen is the only notched type that reached maximum force before failure. Failure occurs rather soon after this point. Moreover, the stress-strain response of the smooth and $R2$ notched specimens is consistent, but the failure strains diverge somewhat, especially in the case of the smooth specimens. The $R08$ and V-notch tests yield, however, more substantial disagreements in the stress-strain response. Moreover, the material hardening response of the $R08$ and V-notched specimens is somewhat similar, but the V-notched specimens fail at lower strains. The material appears to be very notch sensitive, and the introduction of a notch increases the applied forces significantly while reducing the strain at failure.

Figure 7.5 shows the r-value, defined here as the ratio between the two perpendicular diameter D_1 and D_2, as a function of the strain. The material is surely isotropic.

(a) Smooth specimen *(b) Notch, $R = 2.0$* *(c) Notch, $R = 0.8$* *(d) V-notch, $R = 0.2$*

Figure 7.3: *The specimens after failure.*

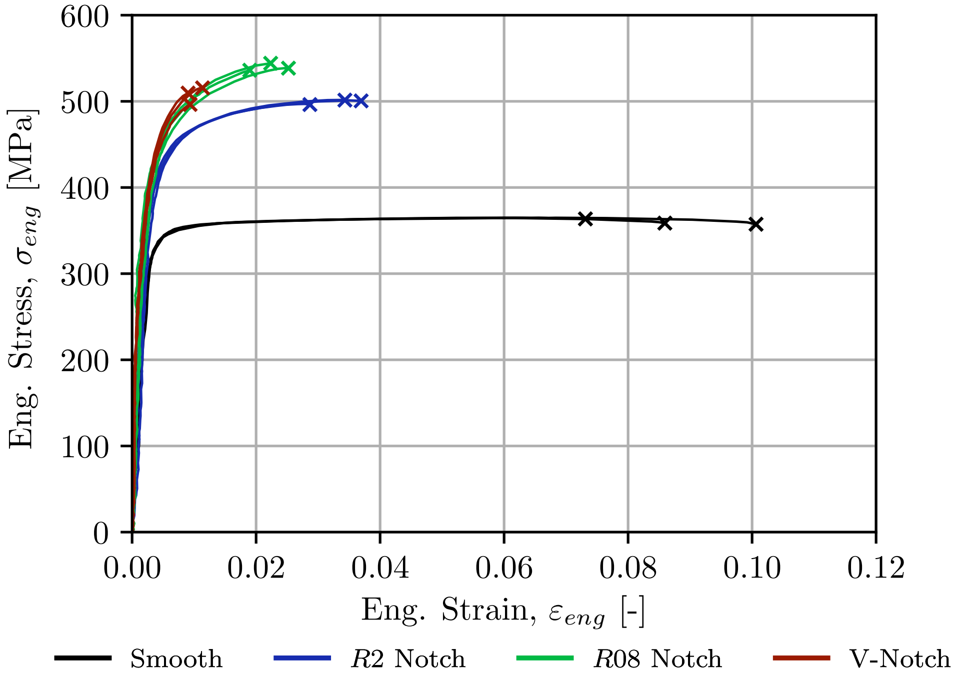

Figure 7.4: *Engineering stress, σ_{eng}, versus engineering strain, ε_{eng}, for all 12 tensile tests. The point of fracture is marked by a ×.*

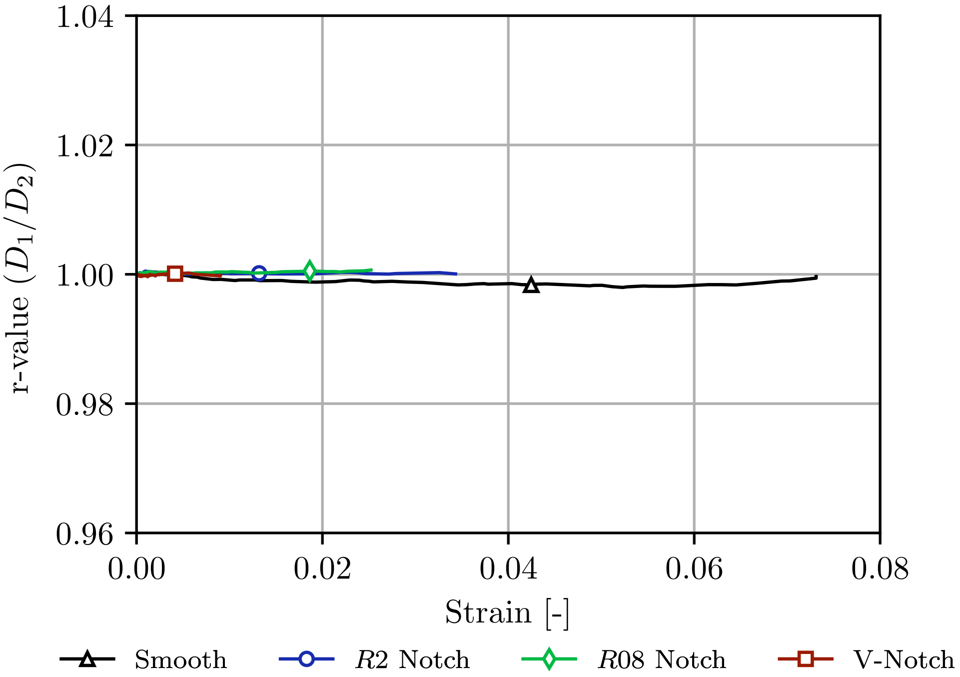

Figure 7.5: *The r-value, defined here as the ratio D_1/D_2, as a function of the strain. The material is considered plastical isotropic if $r = 1$. Only the one sample of each tensile test is included in this plot, but all tests confirm the same.*

7.3 Fracture Surface

A fractographic study was performed to get a better understanding of the failure mechanisms that occur. A Zeiss Gemini Supra 55 VP Scanning Electron Microscope (SEM) operation at 20 kV was used for this purpose. This work was done by Ph.D. candidate Susanne Thomesen [77]. The Scanning Electron Microscope uses a focused electron beam to make an image of the surface it is scanning. Since electrons have a shorter wavelength than light, SEM can provide much better resolution compared to the traditional optical microscopes. The specimens were cleaned beforehand with acetone and placed in an ultrasound bath for 10 minutes. It is essential to remove any grease and organic particles since this can disrupt the image. After cleaning, the specimens were placed in a vacuum chamber while scanning to prevent interactions between air molecules and the electrons.

Figure 7.6 shows the fracture surface of the smooth and V-notched specimen. The surfaces of the smooth specimens were flat and minor deformations prior to fracture were observed. A more rough fracture surface with visible grooves was seen for the notched specimen types. None of the samples experienced a cup-and-cone fracture appearance, which is often associated with ductile fracture.

Figure 7.7 shows fractographs of the smooth and V-notched specimens with a magnification factor of 700. No evidence of ductile void growth as the main fracture mechanism is found in these pictures. All specimen types are believed to experience an intergranular fracture, as illustrated in Figure 2.3a, meaning that the grain boundaries are the preferred path for crack growth. Precipitation free zones form adjacent to the grain boundaries, consequently resulting in zones that are softer than the matrix material and thus prone to strain localization [78, 79]. This is especially true if the matrix material exhibit high strength. SEM photographies of all specimen types at different magnifications are included in Appendix A.

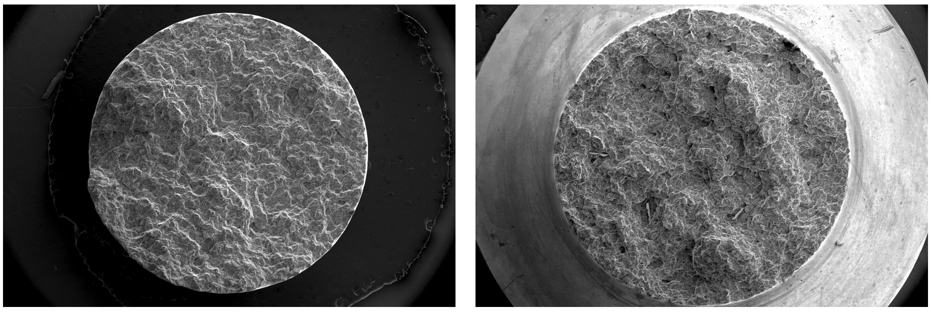

(a) *Smooth specimen* ***(b)*** *V-notched specimen*

Figure 7.6: *Pictures of the fracture surface of the smooth and V-notched specimen.*

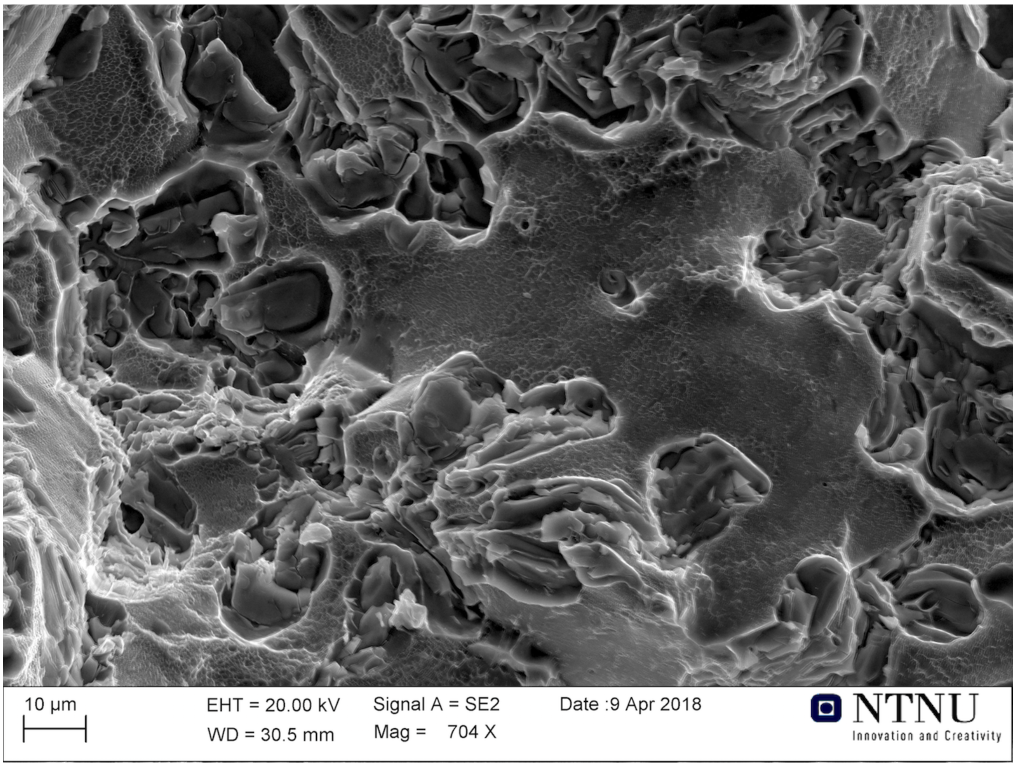

(a) *Smooth specimen*

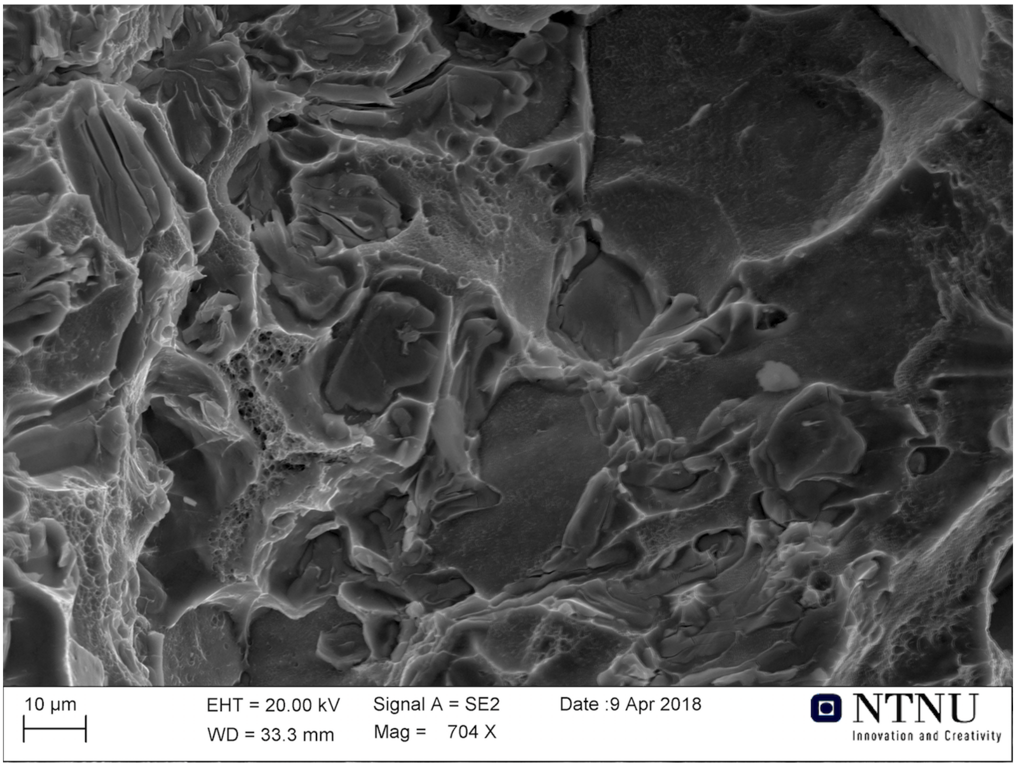

(b) *V-notched specimen*

Figure 7.7: *700x magnified SEM pictures of the fracture surface of the smooth and V-notched specimen.*

7.4 NaMo

The main objective of this thesis is to model an aluminium alloy using a numerical framework. The response of the AlMgSi alloy in Chapter 3 was predicted from tensile tests of a smooth axisymmetric specimen. In spite of that, the material strength could be estimated numerical using the nano-scale material model NaMo. This section will address the capability in predicting the yield strength and work hardening for the 6082 aluminium alloy. A summary on the foundation of NaMo will be presented first. The reader is referred to Myhr et al. [33, 34, 35, 80] for a more comprehensive review.

7.4.1 Theoretical Outline of NaMo

The nano-scale material model NaMo is used to determine the stress response of Al-Mg-Si alloys based on the chemical composition and thermal history. The model was developed by Hydro and NTNU, and is fully integrated into a user-friendly computer code. The stress-strain relation predicted by NaMo may subsequently be used as input in FE-simulations. NaMo is physically based and proves good predictive capabilities for the 6xxx series, which has been comprehensively verified and validated in various papers [33, 34, 35, 80, 81]. Figure 7.8 illustrates the main outline of the model.

The model consists of three sub-models; a precipitation model, a yield strength model and a work hardening model. These three models are listed in Figure 7.8. The precipitation model predicts the particle size distribution (PSD) in the alloy and is the key component for the other two sub-models. Based on the PSD, essential precipitation parameters are extracted and transferred to the yield strength and work hardening models. The user must define the chemical composition and thermal history to predict the PSD. The precipitation model consists of three components, which eventually defines the evolution of hardening precipitates [34]

1. A nucleation law is used to predict the number of stable nuclei that form in the alloy.
2. A nucleated particle will either dissolve or grow. A rate law calculates the dissolution or the growth rate of each discrete particle size class, defined by the particle radius r.
3. A continuity equation keeps a record on the amount of solute being tied up as precipitates.

The reader is referred to Myhr et al. [33, 34] for a summary of the main constitutive equations, which are not reported herein.

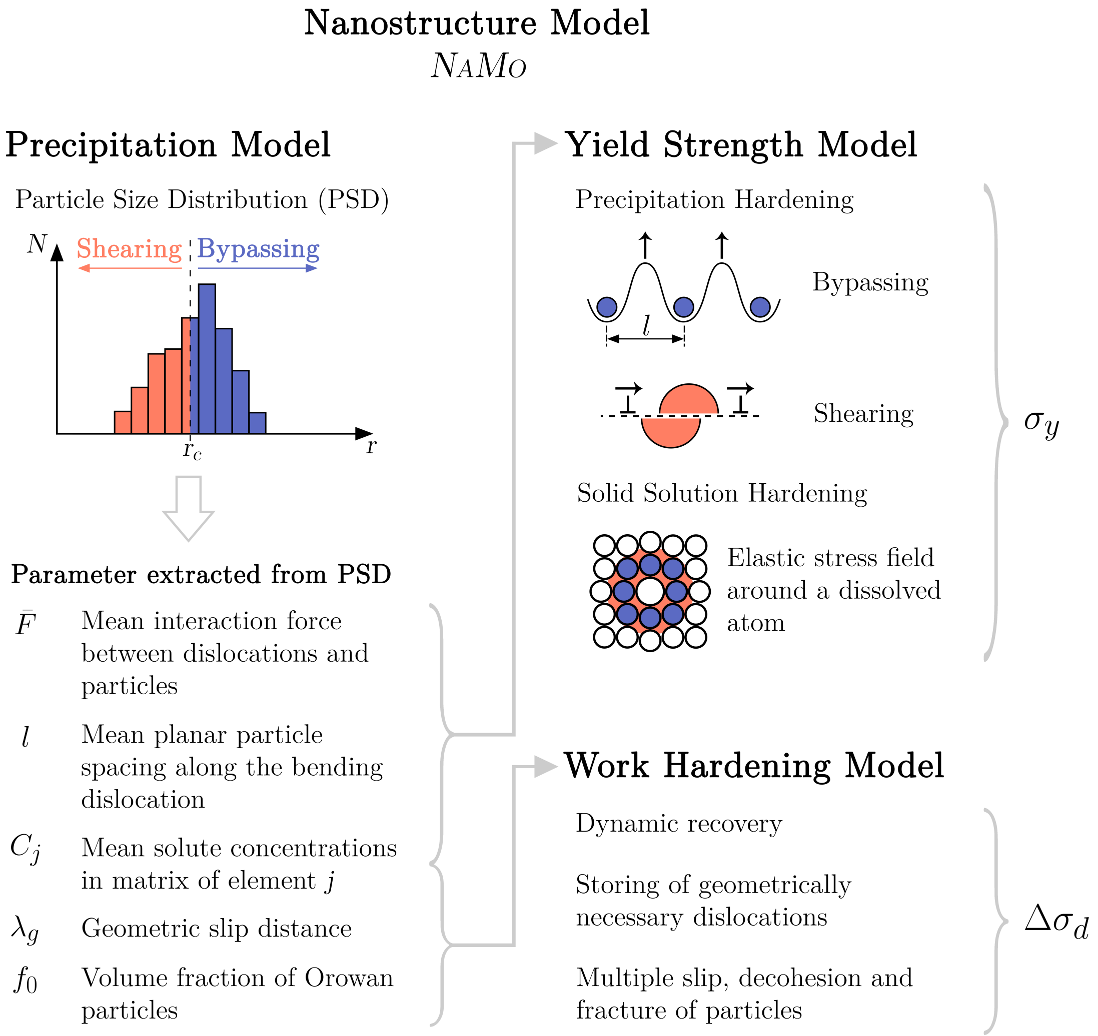

Figure 7.8: *An illustration on the main outline of* NaMo. *The figure is inspired by Johnsen et al. [35].*

The yield strength model uses relevant output parameters from the precipitation model, indicated by the arrow in Figure 7.8, to predict the yield strength of the tempered alloy at room temperature. The overall macroscopic yield strength is defined as

$$\sigma_y = \sigma_i + \sigma_{ss} + \sigma_p \tag{7.1}$$

Hence, the model, which is based on dislocation mechanics, considered three distinct contributions that are individually added [34]

1. σ_i is the intrinsic yield strength of pure aluminium.

2. σ_p is the overall precipitation hardening contribution due to shearing and bypassing of particles.
3. σ_{ss} is the solid solution hardening contribution from each alloying elements.

The work hardening model is based on the assumption that the work hardening behavior of Al-Mg-Si alloys can be evaluated by considering the total dislocation density ρ_t as the only internal variable of the system. The total dislocation density is taken as the sum of the geometrically necessary dislocation density ρ_g and the statically stored dislocation density ρ_s [34]. The total contribution from work hardening on the net stress, $\Delta\sigma_d$, is given by

$$\Delta\sigma_d = \sigma_{eq} - \sigma_y = \alpha M G \mathbf{b}\sqrt{\rho_t} = \alpha M G \mathbf{b}\sqrt{\rho_g + \rho_s} \tag{7.2}$$

where α is a constant, M is the Taylor factor, G is the shear modulus and $\mathbf{b}$ is the magnitude of the burger vector. These parameters are defined by Myhr et al. [34]. In the same article, they show how to relate the evolution of ρ_g and ρ_s to the plastic strain, ε_p, based on well-established evolution laws. "The evolution of statistically stored dislocations (ρ_s) is predicted as the balance between statistical storage and dynamic recovery of dislocations, while the generation of geometrically necessary dislocations (ρ_g) during plastic deformation is assumed to be associated with non-shearable particles."[35]. Thus, it is possible to determine the rise in stress $\Delta\sigma_d$ due to work hardening as a function of the plastic strain. The reader is again referred to the work of Myhr et al. [33, 34] and references therein for a more comprehensive review of the work hardening model. Finally, the flow stress, σ_{eq}, is calculated as follows

$$\sigma_{eq} = \sigma_y + \Delta\sigma_d \tag{7.3}$$

7.4.2 Results From NaMo

The blue curve in Figure 7.9 shows the predicted material response using NaMo with the composition in Table 7.1 and thermal history in Figure 7.1. The red curve shows the estimated flow stress when Voce rule is used to extrapolate the data from the smooth tensile tests. All material parameters are given in Table 7.2. The plastic equivalent strain p from experiments has been calculated using Equation (2.12). Only data prior to necking, which is marked by black dots in Figure 7.9, have been used in the calibration of the material parameters.

The prediction from NaMo is non-conservative and the saturation stress, σ_{sat}, is overestimated by 3.1% compared to the experimental data. On the other hand, the 0.2%

proof stress, $\sigma_{0.2}$, is almost exact compared to the experiments, as shown in Table 7.2. It should be emphasized that due to low ductility, the calibrated material model might be somewhat inaccurate. The increase in flow stress predicted by NaMo suddenly diminishes when the plastic strain is between 0.12 and 0.13. As the material is plastically deformed, dislocations loop around the precipitates, which contribute to work hardening and thus increasing the flow stress. This accumulation of dislocations loops ceases at some critical plastic strain [34]. Consequently, the work hardening stops and saturation is reached.

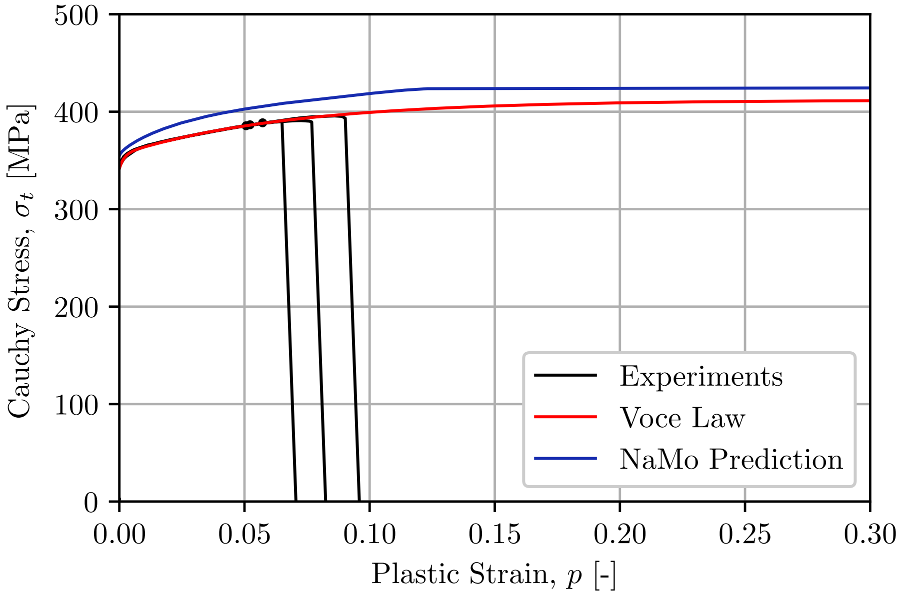

Figure 7.9: *The Cauchy stress, σ_t, as a function of the equivalent plastic strain, p. The blue curve shows the predictions from* NaMo. *The calibrated Voce rule is plotted as a red curve. Black curves show the results from test on the smooth specimens. The point of maximum force is marked by a black* ●.

Table 7.2: *The 0.2% proof stress, $\sigma_{0.2}$, saturation stress, σ_{sat}, from* NaMo *and experiments, and the calibrated material hardening parameters using Voce rule in Equation* (2.4).

	$\sigma_{0.2}$	σ_{sat}	σ_0	Q_1	C_1	Q_2	C_2
Experiment	351.6 MPa	412.0 MPa	341.8	14.4	514.2	55.8	14.9
NaMo	352.8 MPa	424.7 MPa	MPa	MPa	-	MPa	-

7.5 Specimen Geometry and Numerical Results

An examination on the actual geometry of the various notched specimens revealed slightly divergence from the requested, or nominal, geometry in Figure 3.8, 3.9 and 7.2. Figure 7.10 demonstrates this deviation where the blue contour lines represent the requested geometry, and the red contour lines are the actual geometry. The actual radius of the notch was found to be approximately 2.25mm, 1.05mm, and 0.23mm for the $R2$, $R08$ and V-notched specimens, respectively. The specimen in Figure 7.10b experiences the most significant discrepancies, whereas the tolerance of the V-notched specimen in Figure 7.10c is rather good.

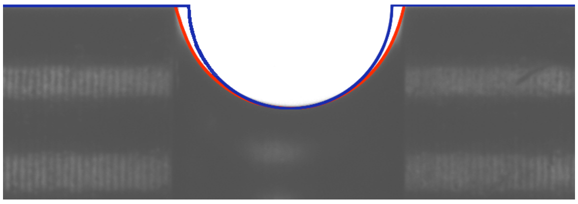

(a) *Notch,* $R = 2.0$

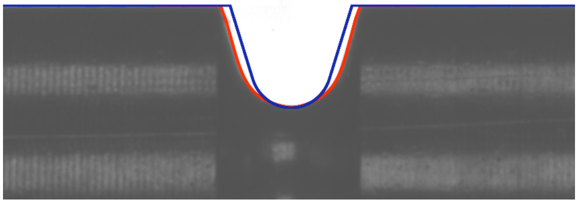

(b) *Notch,* $R = 0.8$

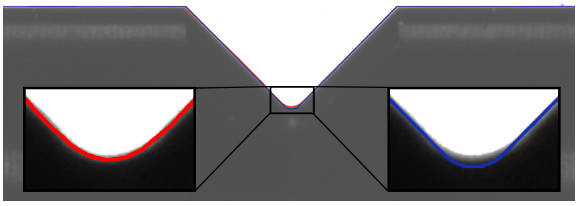

(c) V*-notch,* $R = 0.2$

Figure 7.10: *Contour lines of the geometry of the various notched specimen. Blue and red contour lines represent the requested and actual geometry, respectively.*

The influence of this divergence in specimen geometry on the component response has been studied using a finite element method. A stand-alone python script that evaluates a picture of the specimen has been used to map the outline of the geometry accurately. Ph.D. candidate Sondre Bergo [82] provided this code. The specimen shape can then be imported into a pre-possessing software and discretized into a finite element model. Reduced 4-node axisymmetric elements (CAX4R) with hourglass control have been used in all simulations. No further symmetry assumptions are applied to the model. 48 elements have been used over the cross-section in all models to represent the sharp V-notch in Figure 7.2 accurately.

Figure 7.11 shows the global stress-strain response when applying J2 plasticity theory. The stress and strain have been obtained as described in Section 2.1.2. The $R2$ and $R08$ notched specimens experience a notable reduction in stress when the actual geometry of the notch is used, represented by the red curves. These two specimen types also experienced the most considerable divergence in notch radius compared to the requested geometry. The reduction in stress triaxiality ratio, as shown in Figure 7.12a and 7.12b, is believed to cause this decrease in global stress. The radius of the notch in the actual geometry model is slightly larger. Consequently, the triaxiality ratio is expected to be reduced in the center due to less contribution from radial and transverse stress components. It follows from Equation (2.15) that the longitudinal stress required for plastic flow is decreased.

The stress triaxiality in the V-notched specimen is only minor affected by the increase in notch radius as shown in Figure 7.12c, and the two models predict more or less the same stress-strain response. Furthermore, the stress triaxiality for the element at the specimen surface is less prone to the divergence in notch radius for all specimen types.

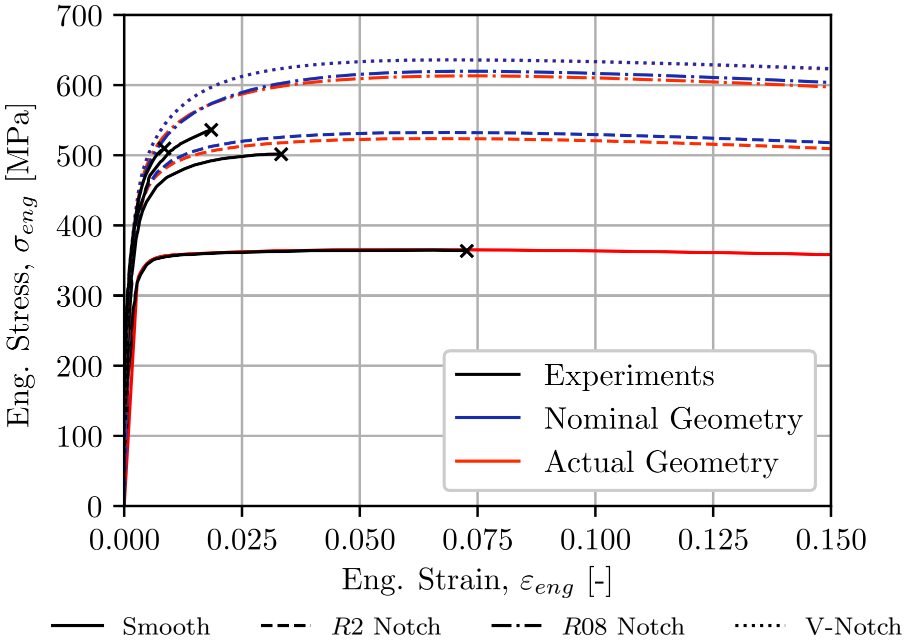

Figure 7.11: *Engineering stress, σ_{eng}, versus engineering strain, ε_{eng}, for the actual and requested geometry. Black lines show the results from experiments. The point of failure is indicated by a black ×.*

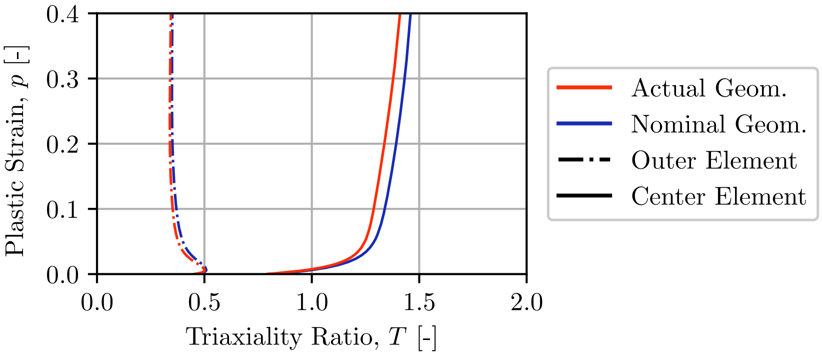

(a) *Notched,* $R = 2.0$

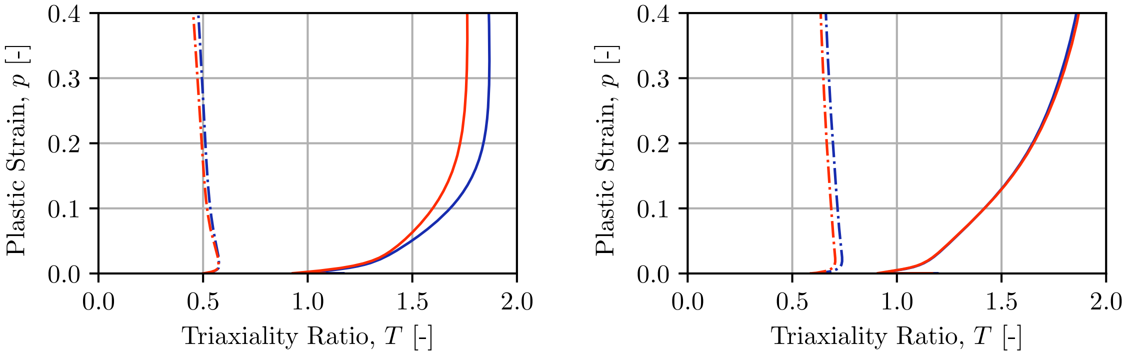

(b) *Notched,* $R = 0.8$ ***(c)*** *V-notched,* $R = 0.2$

Figure 7.12: *Stress triaxiality ratio, T, as a function of the plastic strain, p, in the element at the center and at the specimen surface. Information extracted from the actual and nominal geometry model is plotted as red and blue curves, respectively.*

7.6 Influence of a Prolonged RT Storage Time

The first batch of tensile specimens was stored at room temperature (RT) for 10 minutes before the artificial aging. It has been suggested that the short storage time could make the alloy more prone to intergranular failure. Test on a new smooth specimen with a 24 hour room storage time has been carried out. As Figure 7.13 indicates, this does not improve the ductility. Furthermore, the material strength is reduced by approximately 7%. A prolonged room-temperature storage time will increase the number density of clusters prior to the aging process. Since these clusters tend to survive for a certain period during the artificial aging, some of the solutes are tied-up which would otherwise be used in the formation of β” particles. The nucleation rate of the β” particles is therefore reduced, consequently lowering the final yield strength of the material [83].

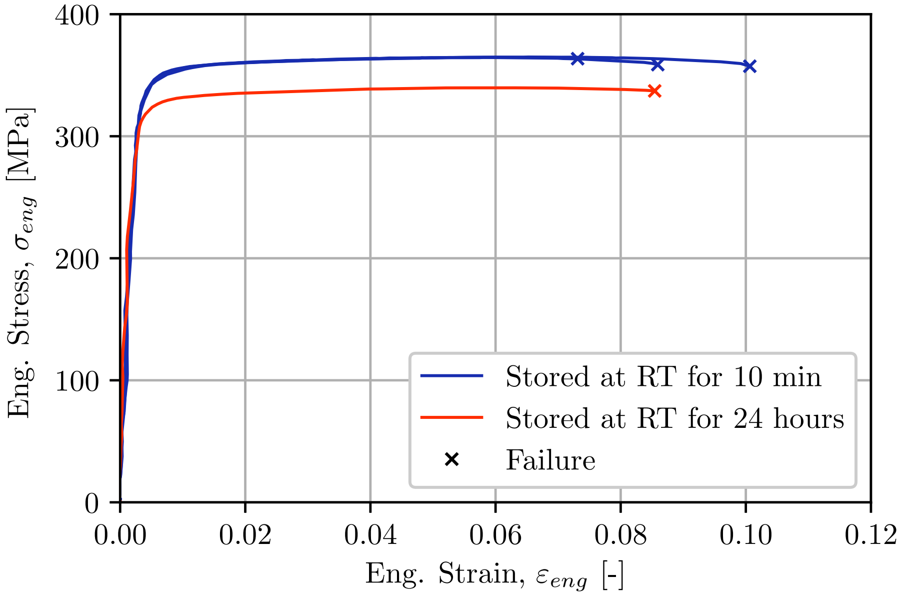

Figure 7.13: *The engineering stress, σ_{eng}, versus the engineering strain, ε_{eng}, for the smooth tensile specimen when the test has been stored for 10 minutes (blue curve) and 24 hours (red curve) before the artificial aging process.*

8 | Concluding Remarks

The primary objective of this thesis was to examine a microstructure-based modeling framework. Unit cell simulations have been used to investigate the void growth and occurrence of coalescence. Strain localization analyses have been performed to determine when the strain localizes into a narrow band, which is a frequent precursor to failure. The different failure models have been applied in a blast load problem to access how well they function in large-scale simulations. This chapter presents the most important findings and conclusions.

A peak-aged 6082 T6 aluminium alloy was initially intended for this thesis. However, experiments revealed a brittle behavior. This was confirmed by SEM fractographies which showed no tendency to void growth and coalescence as the primary failure mode. Therefore, this thesis mainly concerns an AlMgSi aluminium alloy which has been reported by Westermann et al. [38] and Holmen et al. [39]. A smooth and two types of notched axisymmetric tensile specimens, as well as experimental data from plane strain tension tests, have been used to validate the results obtained from unit cell simulations and localization analyses.

Unit Cell Analyses

A broad specter of stress triaxiality ratios, ranging from 2/3 to 3, has been imposed to the unit cell. Lower triaxialities resulted in closing of the void and have not been examined herein. At a certain strain, homogeneous deformation of the unit cell is terminated and extensive softening occurs. This point defines the onset of coalescence. The macroscopic strain at coalescence was found to decrease with increasing triaxiality ratio. This is in good agreement with experiments, where the introduction of a notch reduces the fracture strain. The critical porosity at this point was found to be somewhat constant. Furthermore, the unit cell takes different shapes, depending on the imposed triaxiality ratio. A prolate shape was obtained in the lower triaxiality region, whereas the void became oblate when T was increased.

The Gurson-Tvergaard model was calibrated to the unit cell response using an approach proposed by Dæhli et al. [24]. The estimated particle content from ALSTRUC [36, 37] was used as the initial porosity, and only the material parameters q_1 and q_2 were calibrated to the unit cell results. The optimization process revealed that a large set of q_1 and q_2 parameters would give a minimal discrepancy between the response of the unit cell and the Gurson-Tvergaard model. Consequently, it should be sufficient to only calibrate q_1 while holding q_2 constant, making the calibration procedure less laborious. A parametric study indicated that the initial porosity level does not influence the prediction of q_1 and q_2 very much. Of all the parameters examined here, only the change in matrix material response gave any notable changes in the predicted q_i-values.

The unit cell approach of calibrating q_1 and q_2 was found to give too limited material softening compared to the experimental data. The same parameters were optimized by fitting the Gurson-Tvergaard model to the material tests of the axisymmetric specimens. These results revealed that greater values of q_1 and q_2 are needed to achieve a satisfactory accuracy of the stress-strain response. This might suggest that the very simplified unit cell approach used in this thesis is not adequate.

Numerical Approach to Fracture

The occurrence of coalescence in the unit cell analyses has been used to find both a critical porosity and a failure strain. In general, using q_1 and q_2 optimized from the unit cell did not give an accurate prediction on the global failure strain in either case. Conservative results were expected since only one orientation of coalescence was considered in the unit cell simulations. By contrast, a constant critical porosity showed promising results for all the material tests when the material parameters were calibrated from experiments.

The strain localization analysis was used to construct a fracture surface by imposing the calibrated Gurson-Tvergaard model to the band material. The material parameters optimized from the unit cell did not provide enough softening, resulting in a vastly overestimated failure strain. On the contrary, the q_i-values optimized from experiments proved promising results. However, the failure strain for the smooth specimen was somewhat too large, whereas the $R08$ notch revealed conservative results because failure was initiated at the specimen surface and not in the center.

The initial porosity f_0 and constant nucleation rate factor A_n were calibrated using the failure strain and deformation gradient of the center element to the smooth specimen with the localization analysis. The localization analysis was also used to predict failure in the other specimens using the same approach with these new calibrated parameters.

An initially voided band material demonstrated good predictive capabilities. However, the $R08$ notch revealed to conservative results since failure was initiated at the specimen surface. If the center element is assumed to be the critical element, good results were also achieved for this specimen type. On the other hand, using a continuous nucleation law in the band material resulted in non-conservative results. A parametric study on this calibration approach showed that the q_1 and q_2 parameters did not affect the failure strain of the different specimens too much. The calibrated f_0 and A_n must, however, be adjusted to account for the change in softening when different q_i-values are used.

Implementing a failure surface from the localization analysis for proportional loads into a finite element simulation tends to increase the failure strain for the smooth specimen. This is believed to do with the way ABAQUS linearly accumulate damage. A remedy could be to include some softening in shear when constructing the failure surface, or by simply extrapolating the locus in the lower triaxiality domain by only considering intermediate to high triaxiality ratios.

A blast load problem of a pre-damaged plate showed deviating response on crack growth when different fracture models was applied. This indicates that an accurate representation of the material is essential. Some of the calibrated models revealed reasonable crack propagation and final deformation of the plate. However, a proper conclusion can not be given without experimental data.

According to the findings in this thesis, a purely microstructure-based modeling framework to ductile fracture without any material test is believed to be ambitious. There exist too many uncertainties that will influence the ductile failure processes which cannot be taken into account by a simple modeling framework. Relating the material parameters to the real material response from experiments might account for these uncertainties in an average sense. Moreover, the brittle failure in the 6082 alloy would be hard to predict without any form of testing. The complex failure surface that was obtained from just a single smooth tensile test is, however, believed to be a great achievement in itself. Though, further validations for other ductile materials and stress states are still necessary.

Future Work

More work needs to be done on a microstructure-based modeling framework for ductile failure. Many improvements to the Gurson model are proposed in the literature which could be appealing for such a framework. However, these improvements are usually not available in standard finite element software and require implementation of complex subroutines. The following suggestions for further work will therefore only consider improvements and validations on the job done in this thesis.

- The unit cell approach for optimizing the parameters in the Gurson-Tvergaard model showed a dependency on the matrix material response. Moreover, the predicted Tvergaard constants yielded too limited softening compared to experiments. The same optimization procedure should be check for other ductile materials. Westermann et al. [38] examined three other aluminium alloys which could be used for this purpose.
- The coalescence analyses of the unit cell simulations revealed too conservative results of the critical strain since only one orientation of localization was considered. Other approaches that investigate a broad specter of orientations have been proposed in the literature (See for instance [25, 39, 49, 68]). Such approaches would result in a lower failure strain and provide a useful set of data which could be used to compare the results from the strain localization analysis.
- The Gurson-Tvergaard model does not depend on the Lode parameter in its original form. Moreover, it has been proposed that aluminium alloys exhibit a non-quadratic yield surface which can be described by the Hershey yield surface with $m = 8$. The Gurson-Tvergaard model in the unit cell calibration approach could, for instance, be heuristically modified to account for the third deviatoric stress invariant J3 by replacing the von Mises equivalent stress with the Hershey equivalent stress.
- The material outside the band in the strain localization analysis has been modeled using classical J2 flow theory, whereas a porous plasticity model represents the band material. Another approach would be to apply the Gurson-Tvergaard

model to both materials, where the band has a slightly larger porosity to induce the softer material response. This approach would also agree more with real materials. The percentage increase in porosity for the band could, for instance, be determined using the same method as shown in Section 5.3. Such an approach could also be used to calibrate the critical porosity f_c by evaluate the porosity in the outside band material at localization.

- It would be beneficial to compare the stain localization procedure proposed in Section 5.3 to other materials as well. Again, the aluminium alloys reported by Westermann et al. [38] could be used for this purpose.
- According to the simulations, failure was initiated at the surface of the $R08$ notched specimen. Consequently, the global failure strain becomes too conservative. A softer material response may reveal failure in the center. One way of checking this theory is to calibrate the Voce rule to the experimental data of the $R08$ notch, which could then be used to find a new deformation gradient $\mathbf{F}(t)$ for the localization analysis.
- The localization analysis herein has only been compared to material tests that exhibit negative Lode parameter and intermediate stress triaxialities. Other tests should be performed to verify the results for cases in the positive range of the Lode parameter and for very low triaxiality ratios.
- The blast load simulations revealed some dependency on the applied failure model. Without any experimental data, however, it is hard to evaluate the difference in performance. Therefore, the models should be evaluated to real large-scale experiments. Moreover, a study on the influence of the Lode parameter on the crack propagation should be performed.

Bibliography

[1] T.L. Anderson. *Fracture Mechanics: Fundamentals and Applications.* Taylor Francis Group, 2004.

[2] Z. Chen and C. Butcher. Micromechanics modelling of ductile fracture, 2013.

[3] Fractal. `https://www.ntnu.edu/kt/fractal`, 2016. Accessed: 20-05-2018.

[4] Toppforsk grant benefits sfi casa research. `http://sfi-casa.no/toppforsk-grant-benefits-sfi-casa-research/`, 2016. Accessed: 20-05-2018.

[5] Prosjektbanken. `https://www.forskningsradet.no/prosjektbanken/#/project/NFR/250553/Sprak=en`, 2016. Accessed: 20-05-2018.

[6] The norwegian research council. `https://www.forskningsradet.no/prognett-fripro/Nyheter/En_milliard_til_sterke_forskningsmiljoer/1254015683057/p1226994096468`, 2016. Accessed: 20-05-2018.

[7] G.R. Johnson and W.H. Cook. Fracture characteristics of three metals subjected to various strains, strain rates, temperatures and pressures. *Engineering Fracture Mechanics*, 21(1):31–48, 1985.

[8] M.G. Cockcroft and D.J. Lathan. Ductility and the workability of metals. *Journal of the Institute of Metals*, 96:33–39, 1968.

[9] G. Gruben, O.S. Hopperstad, and T. Børvik. Evaluation of uncoupled ductile fracture criteria for the dual-phase steel docol 600dl. *International Journal of Mechanical Sciences*, 62(1):133–146, 2012.

[10] A.A. Benzerga and J.B. Leblond. Ductile Fracture by Void Growth to Coalescence. *Advances in Applied Mechanics*, 44:169–305, 2010.

[11] A. L. Gurson. Continuum theory of ductile rupture by void nucleation and growth: Part i - yield criteria and flow rules for porous ductile media. *Journal of Engineering Materials and Technology*, 99(1), 1977.

[12] V. Tvergaard. Influence of voids on shear band instabilities under plane strain conditions. *International Journal of Fracture*, 17(4):389–407, 1981.

[13] V. Tvergaard. On localization in ductile materials containing spherical voids. *International Journal of Fracture*, 18(4):237–252, 1982.

[14] C. Chu and A. Needleman. Void nucleation effects in biaxially stretched sheets. *Journal of Engineering Materials and Technology (Transactions of the ASME)*, 102(3):249–256, 1980.

[15] V. Tvergaard and A. Needleman. Analysis of the cup-cone fracture in a round tensile bar. *Acta Metallurgica*, 32(1):157–169, 1984.

[16] K. Nahshon and J.W. Hutchinson. Modification of the gurson model for shear failure. *European Journal of Mechanics / A Solids*, 27(1):1–17, 2008.

[17] A.A. Benzerga and J. Besson. Plastic potentials for anisotropic porous solids. *European Journal of Mechanics - A/Solids*, 20(3):397–434, 2001.

[18] A.A. Benzerga, J. Besson, and A. Pineau. Anisotropic ductile fracture: Part ii: Theory. *Acta Materialia*, 52(15):4639–4650, 2004.

[19] J. Wen, Y. Huang, K.C. Hwang, C. Liu, and M. Li. The modified gurson model accounting for the void size effect. *International Journal of Plasticity*, 21(2):381–395, 2005.

[20] J. Pan, M. Saje, and A. Needleman. Localization of deformation in rate sensitive porous plastic solids. *International Journal of Fracture*, 21(4):261–278, 1983.

[21] M.E. Mear and J.W. Hutchinson. Influence of yield surface curvature on flow localization in dilatant plasticity. *Mechanics of Materials*, 4(3):395–407, 1985.

[22] A. Benallal. Constitutive equations for porous solids with matrix behaviour dependent on the second and third stress invariants. *International Journal of Impact Engineering*, 108:47–62, 2017.

[23] A. Needleman. Void growth in an elasic-plastic medium. *Journal of Applied Mechanics, Transactions ASME*, 39(4):964–970, 1972.

[24] L.E.B. Dæhli, J. Faleskog, T. Børvik, and O.S. Hopperstad. Unit cell simulations and porous plasticity modelling for strongly anisotropic fcc metals. *European Journal of Mechanics / A Solids*, 65:360–383, 2017.

[25] L.E.B Dæhli, D. Morin, T. Børvik, and O.S. Hopperstad. Influence of yield surface curvature on the macroscopic yielding and ductile failure of isotropic porous plastic materials. *Journal of the Mechanics and Physics of Solids*, 107:253–283, 2017.

[26] O.S. Hopperstad and T. Børvik. Materials Mechanics, Part II, 2017.

[27] J.K. Solberg, J.R. Leinum, J.D. Embury, S. Dey, T. Børvik, and O.S. Hopperstad. Localised shear banding in weldox steel plates impacted by projectiles. *Mechanics of Materials*, 39(9):865–880, 2007.

[28] R. Hill. On discontinuous plastic states, with special reference to localized necking in thin sheets. *Journal of the Mechanics and Physics of Solids*, 1(1):19–30, 1952.

[29] Z. Marciniak and Kuczyński K. Limit strains in the processes of stretch-forming sheet metal. *International Journal of Mechanical Sciences*, 9(9):609–620, 1967.

[30] J.W. Rudnicki and J.R. Rice. Conditions for the localization of deformation in pressure-sensitive dilatant materials. *Journal of the Mechanics and Physics of Solids*, 23(6):371–394, 1975.

[31] J.R. Rice. The localization of plastic deformation. *Theoretical and Applied Mechanics*, 1:207–220, 1976.

[32] D. Morin, O.S. Hopperstad, and A. Benallal. On the description of ductile fracture in metals by the strain localization theory. *International Journal of Fracture*, 209 (1):27–51, 2018.

[33] O.R. Myhr, Ø. Grong, and S.J. Andersen. Modelling of the age hardening behaviour of al-mg-si alloys. *Acta Materialia*, 49(1):65–75, 2001.

[34] O.R. Myhr, Ø. Grong, and K.O. Pedersen. A combined precipitation, yield strength, and work hardening model for al-mg-si alloys. *Metallurgical and Materials Transactions A*, 41(9):2276–2289, 2010.

[35] J. Johnsen, J.K. Holmen, O.R. Myhr, O.S. Hopperstad, and T. Børvik. A nanoscale material model applied in finite element analysis of aluminium plates under impact loading. *Computational Materials Science*, 79:724–735, 2013.

[36] A.L. Dons, E.K. Jensen, Y. Langsrud, E. Trømborg, and S. Brusethaug. The alstruc microstructure solidification model for industrial aluminum alloys. *Metallurgical and Materials Transactions A*, 30(8):2135–2146, 1999.

[37] A.L. Dons. The alstruc homogenization model for industrial aluminum alloys. *Journal of Light Metals*, 1(2):133–149, 2001.

[38] I. Westermann, K.O. Pedersen, T. Furu, T. Børvik, and O.S. Hopperstad. Effects of particles and solutes on strength, work-hardening and ductile fracture of aluminium alloys. *Mechanics of Materials*, 79:58–72, 2014.

[39] J.K. Holmen, L.E.B. Dæhli, O.S. Hopperstad, and T. Børvik. Prediction of ductile

failure using a phenomenological model calibrated from micromechanical simulations. *Procedia Structural Integrity*, 2:2543–2549, 2016.

[40] O.S. Hopperstad and T. Børvik. Materials Mechanics, Part I, 2017.

[41] W.F. Hosford. *The Mechanics of Crystals and Textured Polycrystals.* Oxford University Press, 1993.

[42] *SIMLab Metal Model (SMM) – Theory, user's and example manual.* STRUCTURAL IMPACT LABORATORY, 3 edition, January 2017.

[43] P.W. Bridgman. The stress distribution at the neck of a tension specimen. *Trans. Am. Soc. Met.*, 32:553–574, 1944.

[44] G. Le Roy, J.D. Embury, G. Edwards, and M.F. Ashby. A model of ductile fracture based on the nucleation and growth of voids. *Acta Metallurgica*, 29(8):1509–1522, 1981.

[45] W.M. Garrison and N.R. Moody. Ductile fracture. *Journal of Physics and Chemistry of Solids*, 48(11):1035–1074, 1987.

[46] J.W. Hancock and D.K. Brown. On the role of strain and stress state in ductile failure. *Journal of the Mechanics and Physics of Solids*, 31(1):1–24, 1983.

[47] B. Marini, F. Mudry, and A. Pineau. Experimental study of cavity growth in ductile rupture. *Engineering Fracture Mechanics*, 22(6):989–996, 1985.

[48] Y. Bao and T. Wierzbicki. On fracture locus in the equivalent strain and stress triaxiality space. *International Journal of Mechanical Sciences*, 46(1):81–98, 2004.

[49] I. Barsoum and J. Faleskog. Rupture mechanisms in combined tension and shear experiments. *International Journal of Solids and Structures*, 44(6):1768–1786, 2007.

[50] J.R. Rice and D.M. Tracey. On the ductile enlargement of voids in triaxial stress fields. *Journal of the Mechanics and Physics of Solids*, 17(3):201–217, 1969.

[51] G. Rousselier. Ductile fracture models and their potential in local approach of fracture. *Nuclear Engineering and Design*, 105(1):97–111, 1987.

[52] David Morin. Private Communication, 2018.

[53] X. Gao and J. Kim. Modeling of ductile fracture: Significance of void coalescence. *International Journal of Solids and Structures*, 43(20):6277–6293, 2006.

[54] Z.L Zhang, C. Thaulow, and J Ødegård. A complete gurson model approach for ductile fracture. *Engineering Fracture Mechanics*, 67(2):155–168, 2000.

[55] M. Brunet, F. Morestin, and H. Walter-Leberre. Failure analysis of anisotropic sheet-metals using a non-local plastic damage model. *Journal of Materials Processing Tech.*, 170(1):457–470, 2005.

[56] *SIMLab Porous Plasticity Model (SPPM) – Theory and user's manual.* STRUCTURAL IMPACT LABORATORY, 1 edition, September 2015.

[57] L.E.B. Dæhli. *Numerical studies on ductile failure of aluminium alloys.* PhD thesis, NTNU, 2017.

[58] Dassault Systèmes Simulia Corp. Abaqus 2017, 2017.

[59] J. Kim, X. Gao, and T.S. Srivatsan. Modeling of void growth in ductile solids: effects of stress triaxiality and initial porosity. *Engineering Fracture Mechanics*, 71(3):379–400, 2004.

[60] D. Morin, M. Fourmeau, T. Børvik, A. Benallal, and O.S. Hopperstad. Anisotropic tensile failure of metals by the strain localization theory: An application to a high-strength aluminium alloy. *European Journal of Mechanics - A/Solids*, 69:99–112, 2017.

[61] K.O. Pedersen, I. Westermann, Børvik T. Furu T., and O.S. Hopperstad. Influence of microstructure on work-hardening and ductile fracture of aluminium alloys. *Materials Design*, 70:31–44, 2015.

[62] I. Westermann, K.O. Pedersen, T. Børvik, and O.S. Hopperstad. Work-hardening and ductility of artificially aged aa6060 aluminium alloy. *Mechanics of Materials*, 97:100–117, 2016.

[63] E. Jones, T. Oliphant, P. Peterson, et al. SciPy: Open source scientific tools for Python, 2001–. URL `http://www.scipy.org/`. 28.05.18.

[64] Lars Edvard Dæhli. Private Communication, 2018.

[65] Z. Xue, M.G. Pontin, F.W. Zok, and J.W. Hutchinson. Calibration procedures for a computational model of ductile fracture. *Engineering Fracture Mechanics*, 77(3):492–509, 2010.

[66] J. Koplik and A. Needleman. Void growth and coalescence in porous plastic solids. *Int. J. Solids Struct*, 24(8):835–853, 1988.

[67] I. Barsoum and J. Faleskog. Rupture mechanisms in combined tension and shear micromechanics. *International Journal of Solids and Structures*, 44(17):5481–5498, 2007.

[68] D. Morin, L.E.B. Dæhli, A. Benallal, and O.S. Hopperstad. Numerical study of ductile failure under non-proportional loading. In progress, 2018.

[69] B. Marini, F. Mudry, and A. Pineau. Ductile rupture of a508 steel under nonradial loading. *Engineering Fracture Mechanics*, 22(3):375–386, 1985.

[70] V. Vilamosa, T. Børvik, O.S. Hopperstad, and A.H. Clausen. Behaviour and modelling of aluminium alloy aa6060 subjected to a wide range of strain rates and temperatures. *EPJ Web of Conferences*, 94, 2015.

[71] Y. Chen, A.H. Clausen, O.S. Hopperstad, and M. Langseth. Stress-strain behaviour of aluminium alloys at a wide range of strain rates. *International Journal of Solids and Structures*, 46:3825–3835, 2009.

[72] Henrik Granum. Private Communication, 2018.

[73] V. Aune, M. Langseth, and T. Børvik. Impact mechanics: An introduction to blast mechanics (lecture notes in tkt4128), 2016.

[74] Tore Børvik. Private Communication, 2018.

[75] J.M. Stensjøen and S.T. Thorgeirsson. An experimental and numerical investigation of the blast response of pre-damaged aluminium plates. Master's thesis, The Norwegian University of Science and Technology, 2017.

[76] Egil Fagerholt. ecorr: Digital image correlation, 2017. URL `http://folk.ntnu.no/egilf/ecorr/doc/index.html`. 01.06.18.

[77] Susanne Thomesen. Private Communication, 2018.

[78] K.O. Pedersen, T. Børvik, and O.S. Hopperstad. Fracture mechanisms of aluminium alloy aa7075-t651 under various loading conditions. *Materials Design*, 32 (1):97–107, 2011.

[79] M.S. Remøe, K. Marthinsen, I. Westermann, K. Pedersen, J. Røysetc, and C. Marioara. The effect of alloying elements on the ductility of al-mg-si alloys. *Materials Science Engineering A*, 693:60–72, 2017.

[80] O.R. Myhr and Ø. Grong. Modelling of non-isothermal transformations in alloys containing a particle distribution. *Acta Materialia*, 48(7):1605–1615, 2000.

[81] O.R. Myhr, Ø. Grong, H.G. Fjær, and C.D. Marioara. Modelling of the microstructure and strength evolution in al-mg-si alloys during multistage thermal processing. *Acta Materialia*, 52(17):4997–5008, 2004.

[82] Sondre Bergo. Private Communication, 2018.

[83] Ole Runar Myhr, Øystein Grong, and Carmen Schäfer. An extended age-hardening model for al-mg-si alloys incorporating the room-temperature storage and cold deformation process stages. *Metallurgical and Materials Transactions A*, 46(12): 6018–6039, 2015.

A | SEM Photography

A.1 UT90

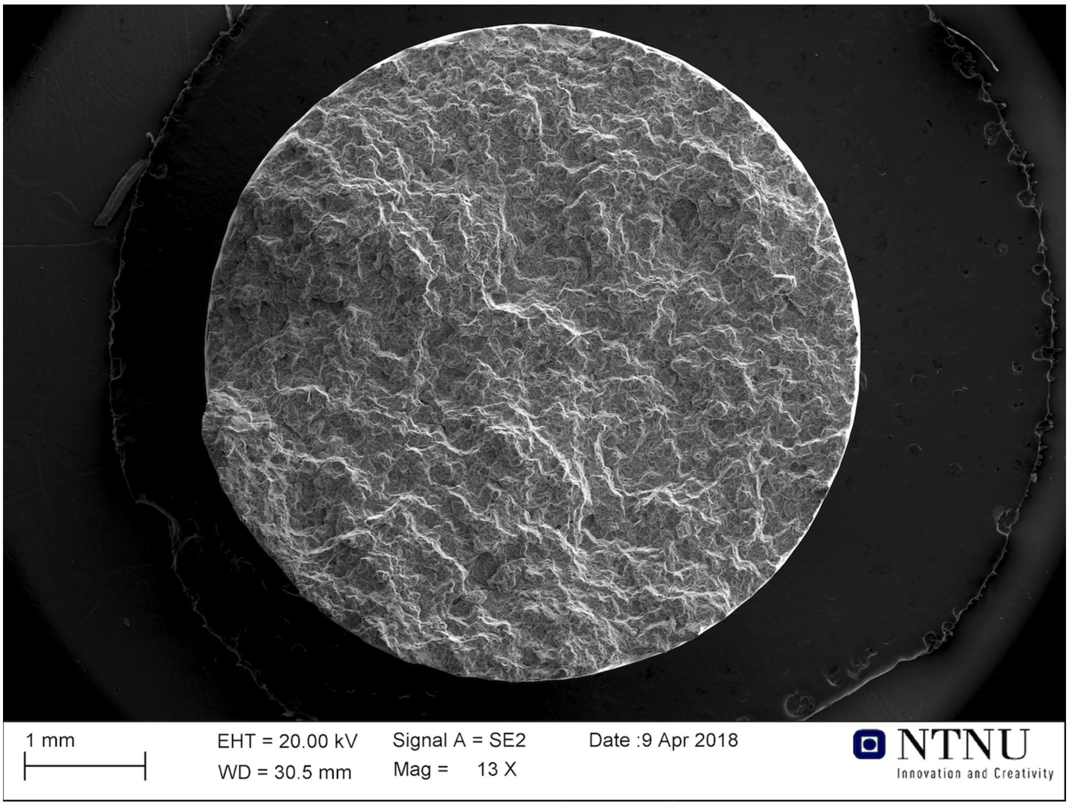

Figure A.1: *Overview of the fracture surface for the smooth specimen.*

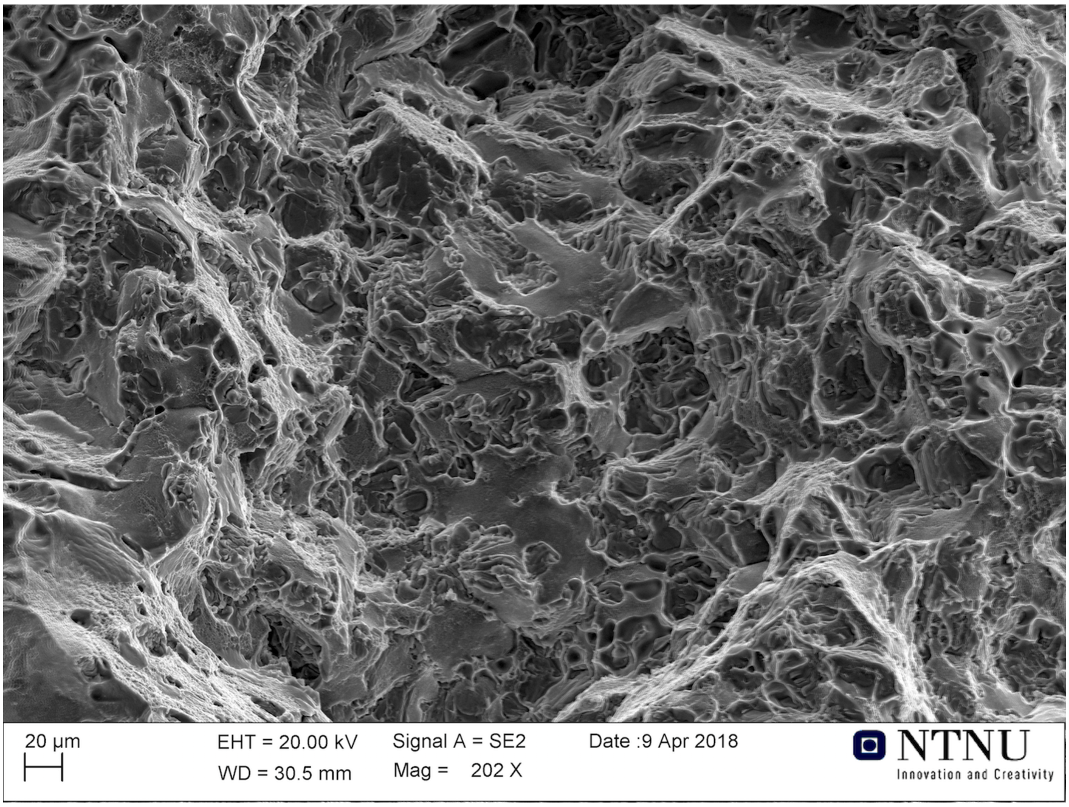

Figure A.2: *200x magnification for the smooth specimen.*

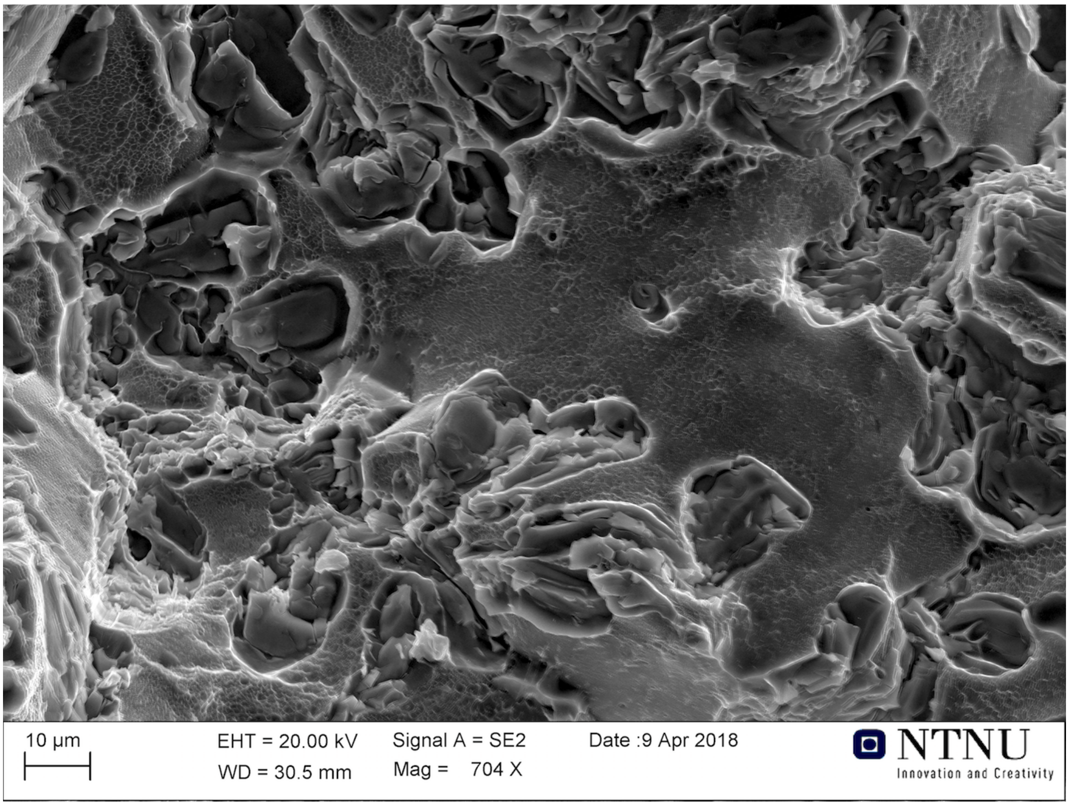

Figure A.3: *700x magnification for the smooth specimen.*

A.2 NT90-2

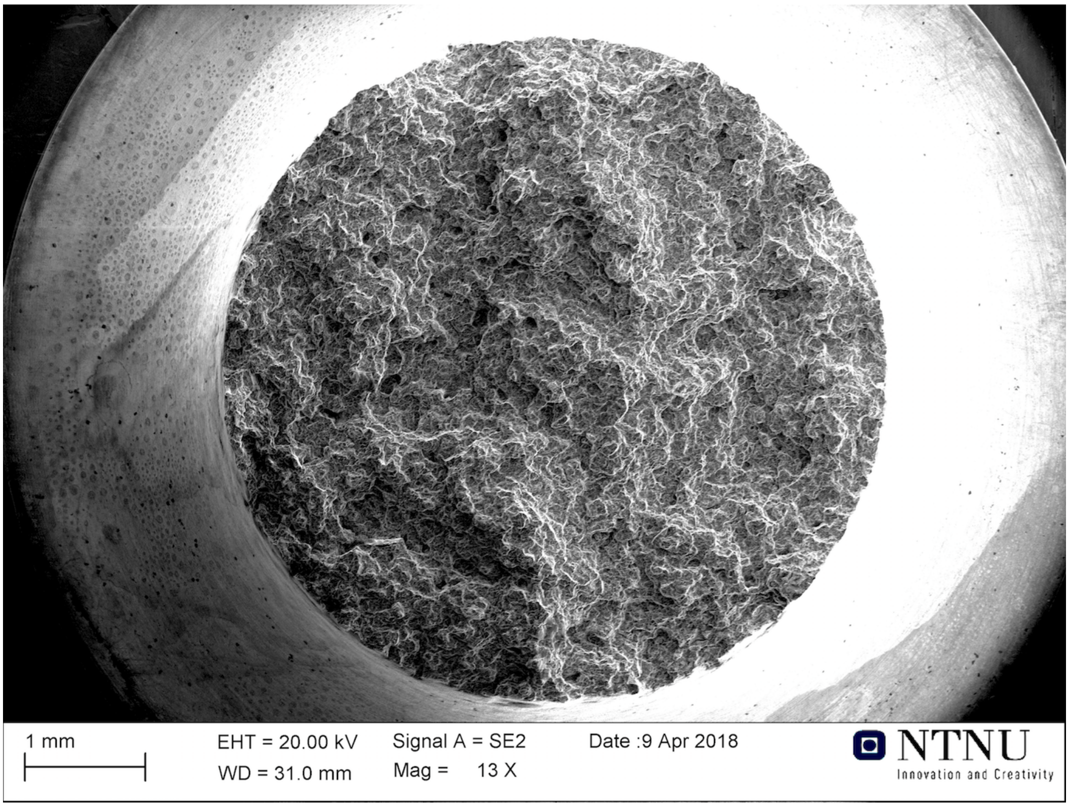

Figure A.4: *Overview of the fracture surface for the R2 notched specimen.*

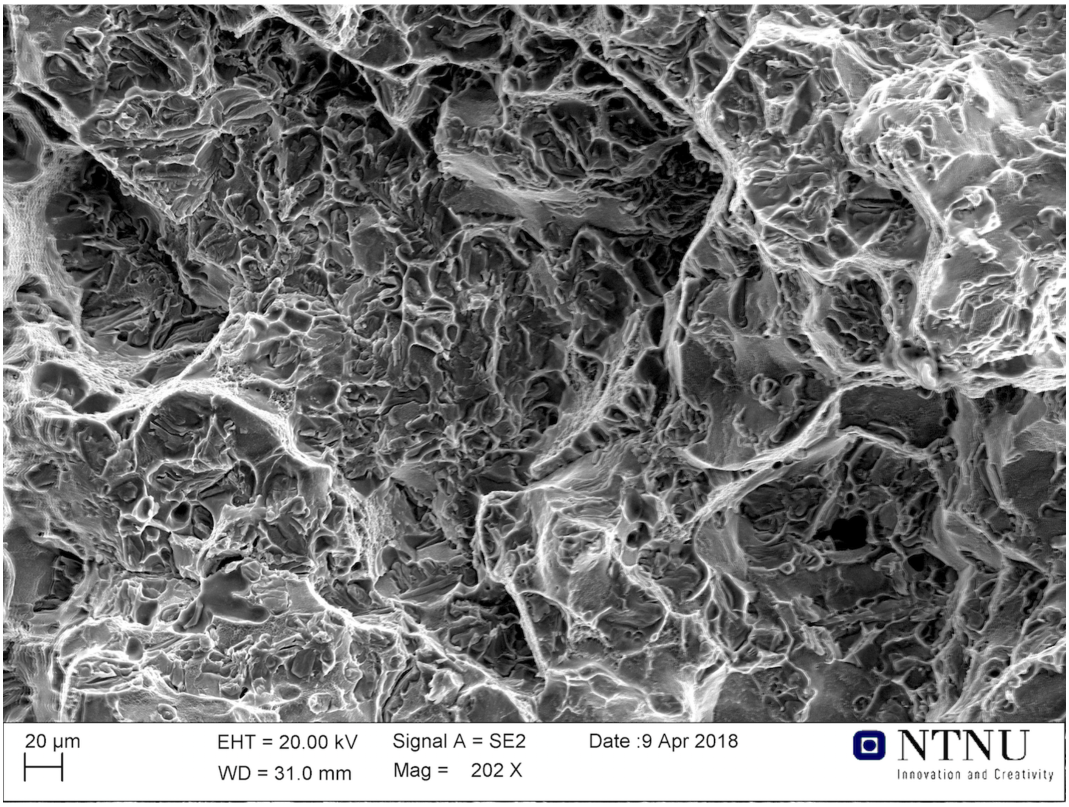

Figure A.5: *200x magnification for the R2 notched specimen.*

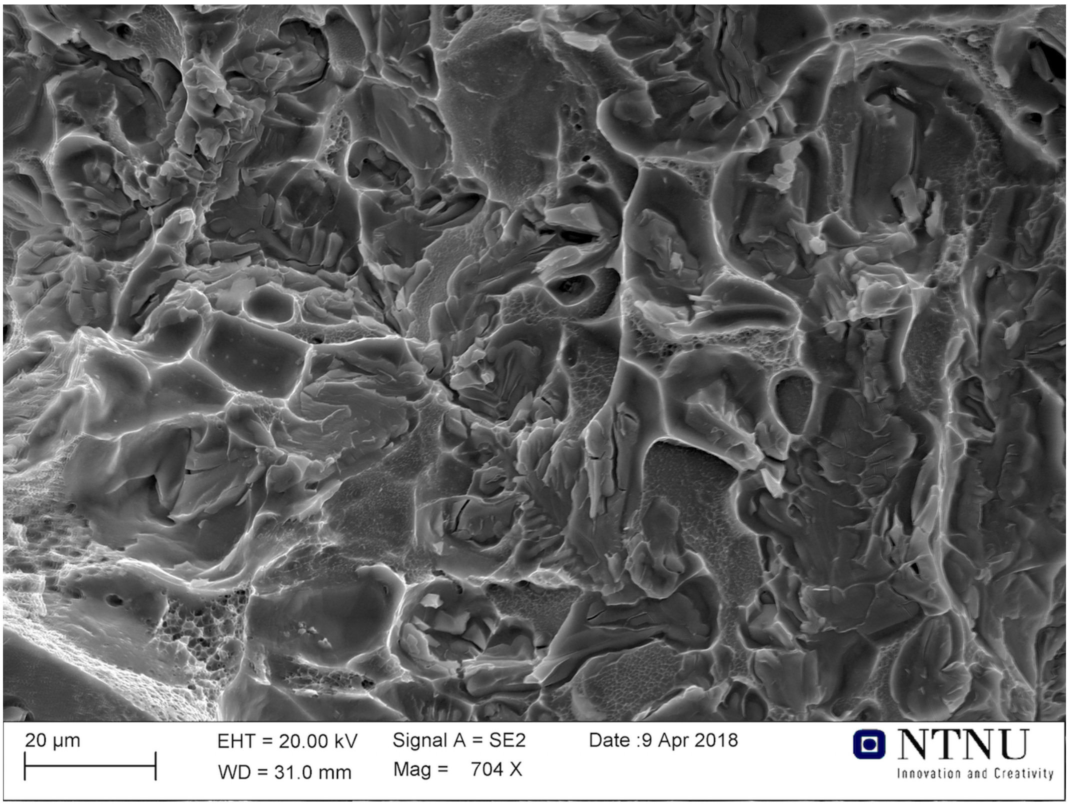

Figure A.6: *700x magnification for the R2 notched specimen.*

A.3 NT90-08

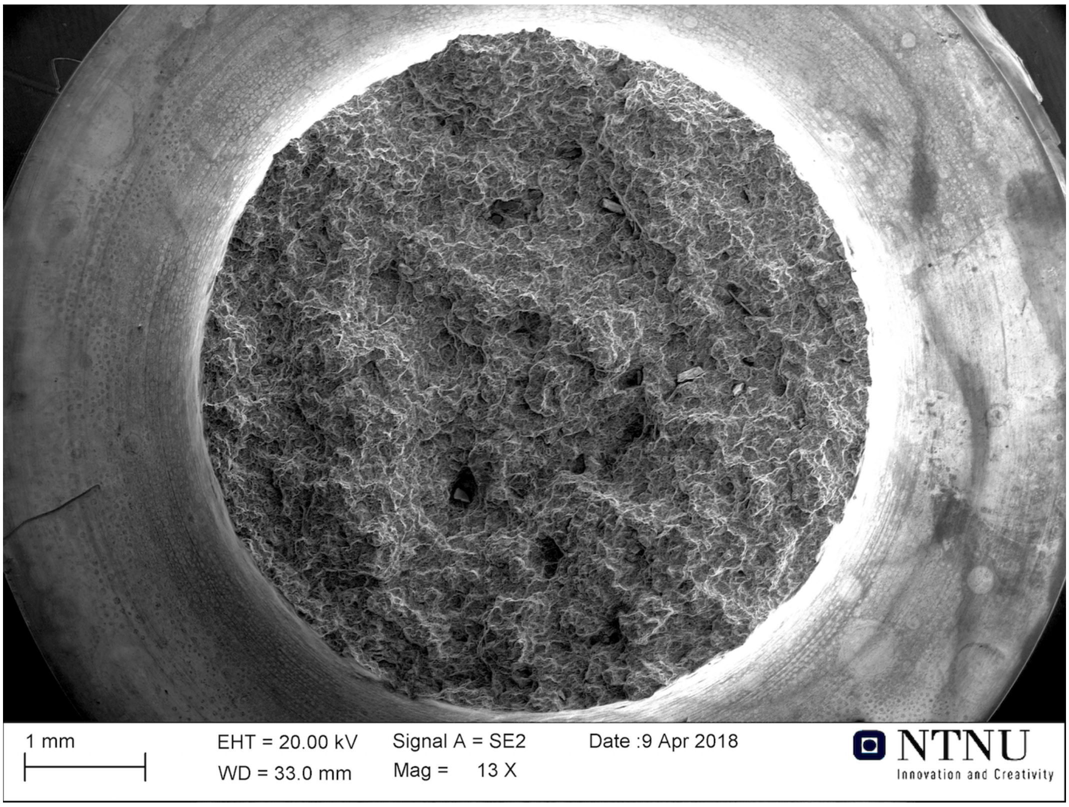

Figure A.7: *Overview of the fracture surface for the R08 notched specimen.*

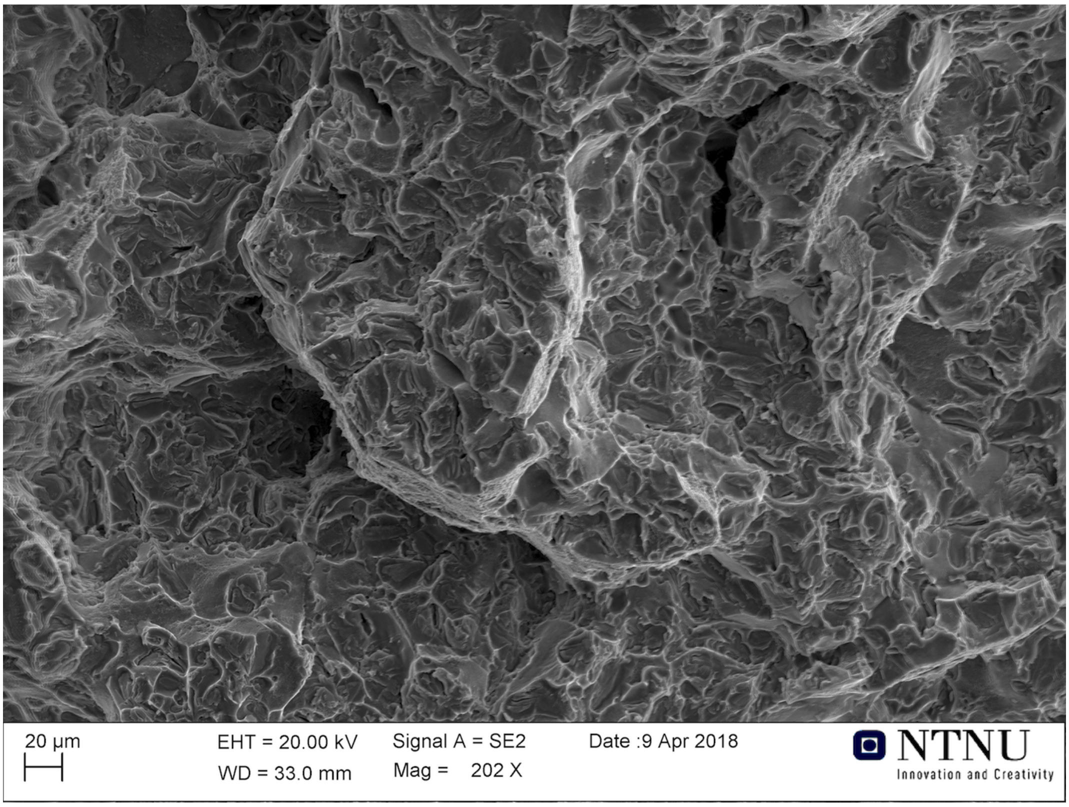

Figure A.8: *200x magnification for the R08 notched specimen.*

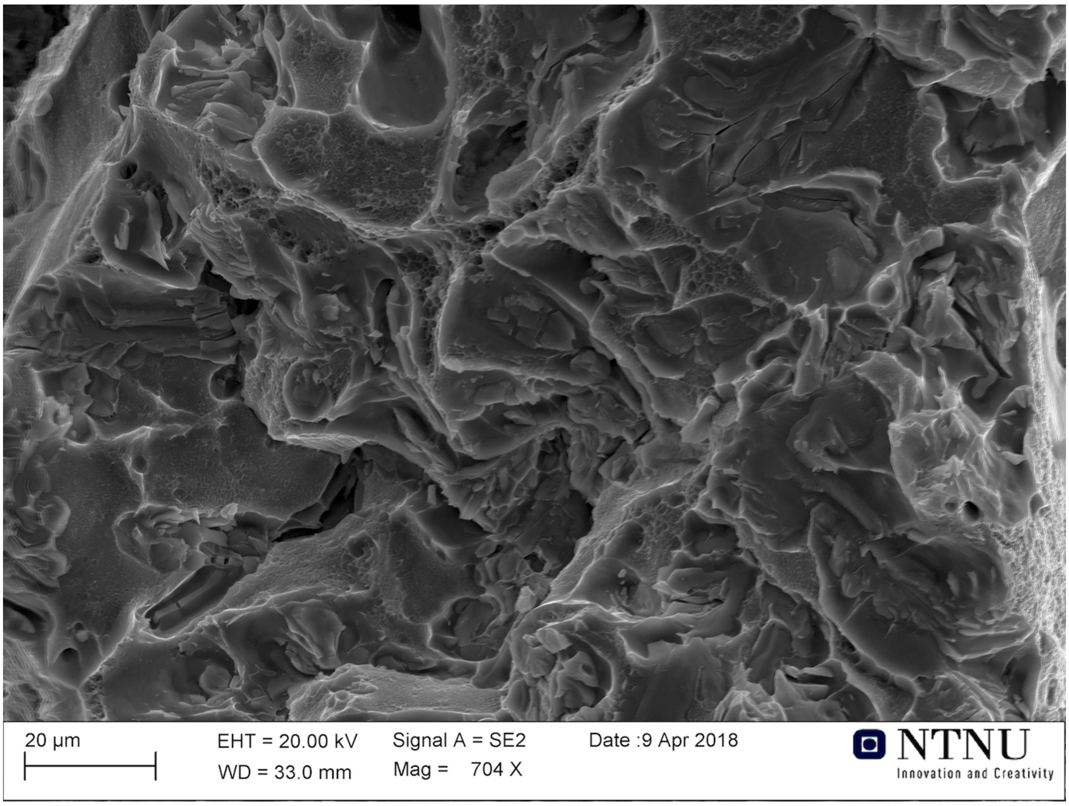

Figure A.9: *700x magnification for the R08 notched specimen.*

A.4 NT90-V

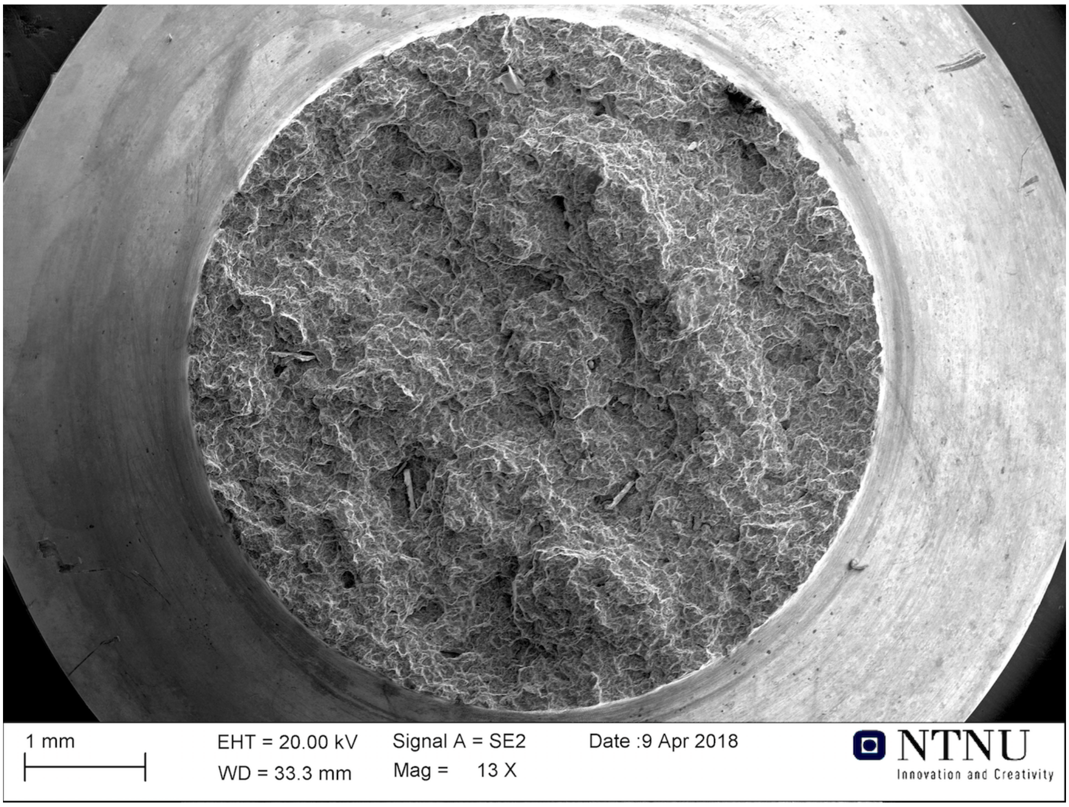

Figure A.10: *Overview of the fracture surface for the V-notch specimen.*

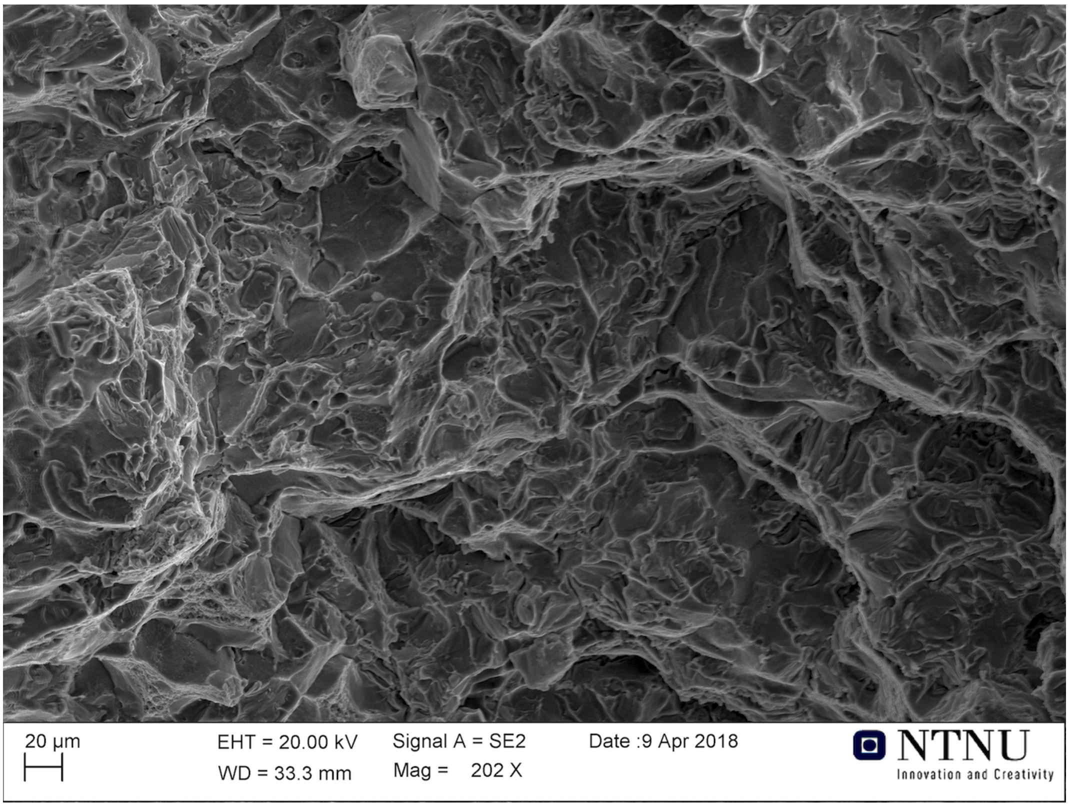

Figure A.11: *200x magnification for the V-notch specimen.*

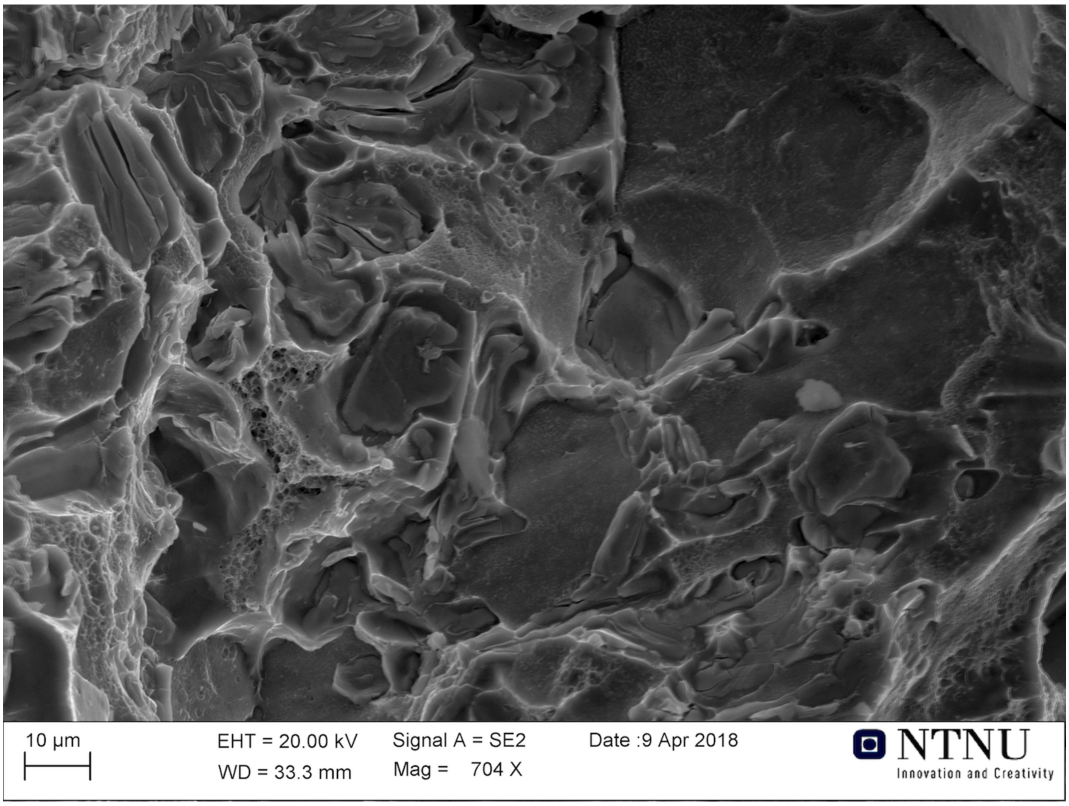

Figure A.12: *700x magnification for the V-notch specimen.*

B | Python Script

B.1 Calibration of q_1 and q_2 From Unit Cell

```
import os
import sys
import numpy as np
import matplotlib.pyplot as plt
from mpl_toolkits.mplot3d import Axes3D
import csv
import scipy.optimize as optimization
import ast
import copy
from matplotlib.ticker import FormatStrFormatter

def file_list(path = '', extension = '.txt'):
    '''
    Returns a list with files with extension "extension".
    Default is '.txt' files.
    '''
    files = os.listdir(path)
    return [f for f in files if f[-4::] == extension]


class simulation:
    '''
    Basic class for one simulation.
    When initiated, the Lode (L) and Triaxiality (T) is found from
    the first step in the simulation.
    '''
    def __init__(self, path, filename):
        self.file = path+filename
        self.L = []
        self.T = []
        self.Seq = []
        self.Eeq = []
        self.f = []

        # Open file
```

```
        with open(self.file) as txtfile:
            reader = csv.reader(txtfile, delimiter= ',')
            counter = 0
            for row in reader:
                # The first 9 lines do not contain relevant data.
                if counter > 9:
                    # Set T and L from the first step.
                    if not self.T:
                        self.T = float(row[0])
                    if not self.L:
                        self.L = float(row[1])

                    # If T change sign (due to large deformation), stop
                     ↪  importing data.
                    if np.sign(self.T) != np.sign(float(row[0])) or
                     ↪  np.sign(self.L) != np.sign(float(row[1])):
                        break

                    # Import Seq and Eeq
                    self.Seq = np.append(self.Seq, float(row[2]))
                    self.Eeq = np.append(self.Eeq, float(row[7]))
                    self.f = np.append(self.f, float(row[11]))
                counter = counter + 1

    def set_lode(self, L):
        self.L = L
    def set_triax(self, T):
        self.T = T


class cell:
    '''
    Class that contains all cell simulation data.
    '''
    def __init__(self, path = '', folder = ''):
        # If no path is given, set path to */CELL/
        if not path:
            path = os.getcwd() + '/CELL/'
        else:
            if folder:
                path = path + folder
            else:
                path = path + '/CELL/'

        # Find all filenames in path
        filenames = file_list(path)
        self.simulations = []

        # Make a new simulation object for all files in path
        for filename in filenames:
            self.simulations.append(simulation(path, filename))
```

```python

    def return_lode_list(self, L):
        # Returns a list with all cell simulation with Lode L
        # Empty list is returned if no simulation is found
        return_list = []
        for simulation in self.simulations:
            if simulation.L == L:
                return_list = np.append(return_list, simulation)
        return return_list

    def return_triax_list(self, T):
        # Returns a list with all cell simulation with Triaxiality T
        # Empty list is returned if no simulation is found
        return_list = []
        for simulation in self.simulations:
            if simulation.T == T:
                return_list = np.append(return_list, simulation)
        return return_list

    def return_simulation(self, L, T):
        # Returns the simulation with L and T
        for simulation in self.simulations:
            if simulation.L == L and simulation.T == T:
                return simulation

        # If simulation not found, raise an error
        raise RuntimeError


class ppm:
    '''
    Contains all data form one q1-q2-set
    '''
    def __init__(self, q1, q2):
        # Construct ppm when first called.
        path = os.getcwd() + '/PPM/'
        self.simulations = []
        self.q1 = q1
        self.q2 = q2

    def add_simulation(self, path, filename):
        # Add a simulation to simulations list
        self.simulations.append(simulation(path, filename))

    def von_mises(self):
        # If von Mises is used, only L=-1 is included
        # This function copies the L=-1 results to
        # L=0 and L=1
        temp = []
        for simulation in self.simulations:
            GS = copy.deepcopy(simulation)
```

```
            GS.set_lode(0)
            temp.append(GS)
            GT = copy.deepcopy(simulation)
            GT.set_lode(1)
            temp.append(GT)
        self.simulations = self.simulations + temp

    def e(self, cells, m, w, lode, triax):
        # Counter to keep track of number of simulations.
        counter = 0
        # Define errors
        self.e_S = 0
        self.e_f = 0
        self.e

        # Loop throug all simulation in simulations
        for simulation in self.simulations:
            # Find current L and T
            L = simulation.L
            T = simulation.T

            # If L or T not included in lode and triax list,
            # go to next step.
            if L not in lode:
                #print 'Lode ' + str(L) + ' not included'
                continue
            if T not in triax:
                #print 'Triax ' + str(T) + ' not included'
                continue

            counter += 1

            # Find the corresponding cell simulation.
            # If missing file in Cell directory, the process will be
            ↪ terminated
            # And an error will be printed
            try:
                cell = cells.return_simulation(L, T)
            except RuntimeError:
                print 'Missing Cell file. Terimate the prosess'
                print 'Lode:   ' + str(L)
                print 'Triax : ' + str(T)
                sys.exit()

            # Interpolate the Eeq_ppm, Seq_ppm, f_ppm data to match up with
            ↪ cell data
            Eeq_ppm, Seq_ppm, f_ppm = interpol(simulation.Eeq,
            ↪ simulation.Seq, simulation.f)
            Eeq_cell, Seq_cell, f_cell = interpol(cell.Eeq, cell.Seq, cell.f)

            # Cut data according to the rules given.
```

```
            # See function for better description.
            Eq_cell, Seq_cell, f_cell, Eq_ppm, Seq_ppm, f_ppm = cut_data_stress(Eq_cell, Seq_cell, f_cell, Eq_ppm, Seq_ppm, f_ppm, m)

            # Find error
            e_S = find_e(Eq_cell, Seq_cell, Seq_ppm)
            e_f = find_e(Eq_cell, f_cell, f_ppm)

            # Add tp total error
            self.e_S = self.e_S + e_S
            self.e_f = self.e_f + e_f

            # If 1 then print plot, else do not print plot.
            if 0:
                print 'q1: ' + str(self.q1) + '\tq2: ' + str(self.q2)
                print 'L:  ' + str(L) + '\t\tT: ' + str(T)
                #print 'e_S: ' + str(e_S)
                #print 'e_f: ' + str(e_f)

                fig, ax1 = plt.subplots(figsize=(7, 4), dpi=150)

                ax2 = ax1.twinx()
                ax1.plot(cell.Eeq, cell.Seq, 'o', color ='blue')
                ax1.plot(Eeq_cell, Seq_cell, '-', color ='blue', label = 'Cell data')
                ax1.plot(simulation.Eeq, simulation.Seq, 'o', color ='red')
                ax1.plot(Eeq_ppm, Seq_ppm, '-', color ='red', label = 'PPM data')
                ax1.plot([Eeq_ppm[-1], Eeq_ppm[-1]], [0, 500], '--', color ='black')

                ax1.set_xlabel('$E_{eq}$')
                ax1.set_ylabel('$S_{eq}$')

                ax2.plot(cell.Eeq, cell.f, 'd', color ='blue')
                ax2.plot(Eeq_cell, f_cell, '--', color ='blue')
                ax2.plot(simulation.Eeq, simulation.f, 'd', color ='red')
                ax2.plot(Eeq_ppm, f_ppm, '--', color ='red')
                ax2.set_ylabel('f')

                #ax1.set_xlim([0,0.5])
                ax1.set_ylim([0,450])

                ax1.legend()
                ax1.grid(True)
                plt.show()

        # Find total error
        self.e_S = self.e_S/counter
        self.e_f = self.e_f/counter
```

```
        self.e = w*self.e_S + (1-w)*self.e_f

        # If 1 then print status for this set of qi.
        if 0:
            print 'q1:  ' + str(self.q1)
            print 'q2:  ' + str(self.q2)
            print 'e_S: ' + str(self.e_S)
            print 'e_f: ' + str(self.e_f)
            print 'e: ' + str(self.e)
            print '--------------------------------------------'
            print '--------------------------------------------'

class ppms:
    '''
    Main Class
    Class that contains the ppm class for all qi-combinations.
    Note that all PPM simulations (single element simulations) are place in folder */PPM
    All cell simulations are placein in folder */CELL
    '''
    def __init__(self, VM = True, m = 200, w = 0.5, lode = [-1,0,1], triax=[0.6667, 1., 1.6667, 3.], path = ''):
        # Set path
        if not path:
            self.path = os.getcwd() + '/PPM/'
        else:
            self.path = path + '/PPM/'

        # Get cell simulation data from parameteric file
        cells = cell(path)
        self.idents, self.q1s, self.q2s = self.read_parametric()

        # ppms is a dict with ppm
        self.ppms = {}

        # Make a ppm-class for each qi combination
        for ident in self.idents:
            q1 = self.idents[ident]['q1']
            q2 = self.idents[ident]['q2']

            self.ppms[ident] = ppm(q1,q2)

        # Sort all ppm-simulation into the correct ppm-class
        folders = os.walk(self.path).next()[1]
        for folder in folders:
            path = self.path + folder + '/'
            files = file_list(path)
            for file in files:
                ident = file.split('_')[-1].split('.')[0]
                self.ppms[ident].add_simulation(path, file)

```

```
        # If von Mises, make GS (L=0) and GC (L=1) simulation based on GT
         ↪  (L=-1)
        if VM:
            for p in self.ppms:
                self.ppms[p].von_mises()

        # Calculate e for all ppms
        for p in self.ppms:
            self.ppms[p].e(cells, m, w, lode, triax)

    def read_parametric(self):
        # This function reads the summary file from parametric study
        # The identity (c1, c2, ...) are collected with
        # Corresponding q1 and q2.
        with open(self.path+'parametric.var') as varfile:
            reader = csv.reader(varfile, delimiter= ';')
            idents = {}
            q1 = set([])
            q2 = set([])

            for row in reader:
                n = row[2].split('_')[-1]
                qs = ast.literal_eval(row[3].strip())
                idents[n] = {}
                idents[n]['q1'] = float(qs[0])
                idents[n]['q2'] = float(qs[1])

                q1.add(qs[0])
                q2.add(qs[1])

        return idents, sorted(q1), sorted(q2)

    def find_ident(self, q1, q2):
        # Returns ident associated the given q1 and q2
        for n in self.idents:
            if self.idents[n]['q1'] == q1 and self.idents[n]['q2'] == q2:
                return n
        return False

def interpol(xdata, y1data, y2data, n = 4):
    '''
    Interpolate x and y data to match up.
    n equals number number of desimals to include
    eq. n=4 gives a e=0.0001
    '''
    m = np.floor(max(xdata)*10**n)
    xret = np.linspace(0, m*10**(-n), m+1)
    y1ret = np.interp(xret, xdata, y1data)
    y2ret = np.interp(xret, xdata, y2data)

    return xret, y1ret, y2ret
```

```

def cut_data_stress(xcell, y1cell, y2cell, xppm, y1ppm, y2ppm, n = 0.95):
    '''
    Cut data so they match up. Based on stress.
    n equals to percentage reduction in stress.
    '''
    index = find_stress_index(y1cell, max(y1cell)*n)
    xcellret = xcell[0:index]
    y1cellret = y1cell[0:index]
    y2cellret = y2cell[0:index]

    if xcellret[-1] <= xppm[-1]:
        xppmret = xppm[0:index]
        y1ppmret = y1ppm[0:index]
        y2ppmret = y2ppm[0:index]

        if len(xppmret) != len(xcellret):
            xppmret = xppmret[0:len(xcellret)]
            y1ppmret = y1ppmret[0:len(xcellret)]
            y2ppmret = y2ppmret[0:len(xcellret)]

    else:
        num = len(xppm)
        xppmret = xppm
        y1ppmret = y1ppm
        y2ppmret = y2ppm
        xcellret = xcellret[0:num]
        y1cellret = y1cellret[0:num]
        y2cellret = y2cellret[0:num]

    return xcellret, y1cellret, y2cellret, xppmret, y1ppmret, y2ppmret

def find_e(xcell, ycell, yppm):
    '''
    Calculate e from formula.
    '''
    numerator = np.trapz(abs(yppm-ycell), xcell)
    denominator = np.trapz(.5*(yppm+ycell), xcell)

    return numerator/denominator

def find_stress_index(ydata, stress):
    # Returns index in ydata associated with value "stress"
    index = 0
    for i, y in enumerate(ydata):
        if y >= stress:
            index = i
    return index

def plot_data(data, name = 'test', size=(4.5, 3), text='', domain = [], corr
 ↪ = 0):
```

```python
    '''
    Function for plotting countour plot of error in qi-space
    Data is a ppms object
    '''
    x = np.asarray(data.q1s)
    y = np.asarray(data.q2s)
    z = np.array([])

    minimum = 10
    q1 = 0
    q2 = 0

    ytemp = 0
    ymin = []
    zmin = []
    minitemp = 10

    for i in x:
        for j in y:
            ident = data.find_ident(i,j)
            z = np.append(z, data.ppms[ident].e)

            if data.ppms[ident].e < minimum:
                minimum = data.ppms[ident].e
                q1 = data.ppms[ident].q1
                q2 = data.ppms[ident].q2
            if data.ppms[ident].e < minitemp:
                minitemp = data.ppms[ident].e
                ytemp = j
        ymin = np.append(ymin, ytemp)
        zmin = np.append(zmin, minitemp)
        minitemp = 10


    X, Y = np.meshgrid(y, x)
    if corr == 1:
        z = (z-min(z))/max(z)
    Z = np.reshape(z, (len(x), len(y)))
    plt.figure(1, figsize=size, dpi=300)
    plt.rc('text', usetex=True)
    plt.rc('font', family='serif')

    cs = plt.contourf(Y, X, Z, 100, cmap='jet')

    cbar = plt.colorbar(format="%.2f",extend='neither',
     ↪  spacing='proportional')
    cbar.ax.set_ylabel('Error [-]', labelpad=8)
    cbar.ax.tick_params(labelsize=10)

    plt.xlabel('$q_{1}$', fontsize=10)
    plt.ylabel('$q_{2}$', fontsize=10)
```

```python
    plt.xticks(size = 10)
    plt.yticks(size = 10)
    axes = plt.gca()
    axes.yaxis.set_major_formatter(FormatStrFormatter('%.2f'))

    if domain:
        print domain[0:2], domain[2::]
        axes.set_xlim(domain[0:2])
        axes.set_ylim(domain[2::])

    if not text == '':
        t = axes.text(.5,0.8, text, horizontalalignment='center',
         ↪  transform=axes.transAxes, fontsize=10, zorder=20, color='white')
        t.set_bbox(dict(facecolor='white', alpha=0., edgecolor='none'))

    plt.savefig(name + '.eps', format='eps', bbox_inches="tight")
    plt.show()

    print str(minimum) + ' ved q1: ' + str(q1) + ' q2: ' + str(q2)
```

B.2 Process SLM Output Files

```python
def file_list(path = '', extension = '.txt'):
    '''
    Return a list file files in path that has a given extension
    '''
    files = os.listdir(path)
    return [f for f in files if f[-4::] == extension]

def print_fracture_locus(Ls, Ts, pfs, name = 'default'):
    '''
    Write the failure locus for Abaqus
    '''
    with open(name + '.txt', 'w') as txt:
        txt.write('*Damage Initiation, Criterion = Ductile, lode
         ↪  dependent\n')
        for i, L in enumerate(Ls):
            T = Ts[i]
            pf = pfs[i]
            if i > 0 and L != Ls[i-1]:
                txt.write('**\n')
            if pf > 0:
                str = '{:f}, {:f}, {:f}, {:f}\n'.format(pf, T, -L, 0.)
                txt.write(str)
        txt.write('*Damage Evolution, type=DISPLACEMENT\n')
        txt.write('0.,')

class simulation:
    '''
```

```
    Defines one simulation with constant L and T.
    '''
    def __init__(self, T, L, p, f, Seq, fout):
        self.L = L
        self.T = T
        self.Seq = Seq
        self.p = p
        self.f = f
        self.fout = fout


class SLM:
    '''
    Main class. Read outputfile from SLM, and make a set of simulations objects.
    '''
    def __init__(self, path, filename, filter = True, GT = False, old = False, exclude = []):
        self.file = path + filename
        self.simulations = []
        self.L = []
        self.T = []
        self.p = []
        self.f = []
        self.Seq = []
        self.fout = []


        with open(self.file) as txtfile:
            reader = csv.reader(txtfile, delimiter= ',')
            for row in reader:
                if not (float(row[2]) == 0 and float(row[3]) == 0 and float(row[4]) == 0) or not filter:
                    if (float(row[0]) not in exclude):
                        if GT == False or float(row[1]) == -1:
                            if old:
                                temp = 0
                            else:
                                temp = float(row[5])
                            self.simulations.append(simulation(
                                float(row[0]),float(row[1]),float(row[2]),
                                float(row[3]),float(row[4]),float(temp)))
                            self.T.append(float(row[0]))
                            self.L.append(float(row[1]))
                            self.p.append(float(row[2]))
                            self.f.append(float(row[3]))
                            self.Seq.append(float(row[4]))
                            self.fout.append(temp)
                elif 0:
                    print 'Triax: ' + str(float(row[0])) + '\tLode: ' + str(float(row[1]))
```

```python

        self.L_list = sorted(set(self.L))
        self.T_list = sorted(set(self.T))


    def extrapolate(self, num = 0):
        '''
        Extrapolate failure surface.
        '''
        if num == 0: num = (max(self.T))/0.1 + 1
        triax = np.linspace(0, max(self.T), num)
        T_ret = np.asarray([])
        L_ret = np.asarray([])
        p_ret = np.asarray([])

        for L in reversed(self.L_list):
            Ts = []
            ps = []
            for T in sorted(set(self.T)):
                if self.return_simulation(L, T):
                    Ts.append(T)
                    ps.append(self.return_simulation(L, T).p)
            f = interpolate.interp1d(Ts, ps, fill_value='extrapolate')

            p_ret = np.concatenate([p_ret, f(triax)])
            T_ret = np.concatenate([T_ret, triax])
            L_ret = np.concatenate([L_ret, np.ones(len(triax))*L])

        return L_ret, T_ret, p_ret


    def return_simulation(self, L, T):
        '''
        Return a simulation object with given L and T.
        '''
        for simulation in self.simulations:
            if simulation.L == L and simulation.T == T:
                return simulation
        return False

    def lode_section(self, L=0):
        '''
        Return all simulation objects with L
        '''
        ret = []
        for T in self.T_list:
            sim = self.return_simulation(L, T)
            if sim:
                ret.append(sim)
        return ret

```

```
    def triax_section(self, T=0):
        '''
        Return all simulation objects with T
        '''
        ret = []
        for L in self.L_list:
            sim = self.return_simulation(L, T)
            if sim:
                ret.append(sim)
        return ret

    def sorted_lists(self):
        '''
        Returns a sorted list of L, T and pf.
        Ls, Ts, pfs can be used with print_fracture_locus(Ls, Ts, pfs) to print failure surface for Abaqus
        '''
        Ls = []
        Ts = []
        pfs = []
        for L in reversed(self.L_list):
            for T in self.T_list:
                pf = self.return_simulation(L, T)
                if pf:
                    Ls.append(L)
                    Ts.append(T)
                    pfs.append(pf.p)
        return Ls, Ts, pfs

    def GT_lists(self):
        '''
        Returns a sorted list L, T and pf where only L=-1 is considdered
        Ls, Ts, pfs can be used with print_fracture_locus(Ls, Ts, pfs) to print failure surface for Abaqus
        '''
        Ls = []
        Ts = []
        pfs = []
        for T in self.T_list:
            pf = self.return_simulation(-1, T)
            if pf:
                Ls.append(-1)
                Ts.append(T)
                pfs.append(pf.p)
        return Ls, Ts, pfs
```

C | SLM Input Cards

The input files for the SIMLab Localization Module (SLM) analysis are included in this appendix. Values that are altered are marked red. Thus, the same card may apply to several analysis but with different parameters.

- **Appendix C.1: Failure Surface - Initially Voided Band Material**
  This card is used to generate a fracture surface when an initially voided material is applied to the band. An extensive range of proportional load simulations with constant Lode parameter and stress triaxiality ratio is simulated.
- **Appendix C.2: Failure Surface - Continuous Nucleation of Voids**
  This card is used to generate a fracture surface when a continuous nucleation law is applied to the band material. An extensive range of proportional load simulations with constant Lode parameter and stress triaxiality ratio is simulated.
- **Appendix C.3: Proportional Loading - Initially Voided Band Material**
  This card is used in localization analyses where non-proportional loading is imposed to the outside material when an initially voided material is applied to the band.
- **Appendix C.4: Proportional Loading - Continuous Nucleation of Voids**
  This card is used in localization analyses where non-proportional loading is imposed to the outside material when a continuous nucleation law is applied to the band material.

C.1 Failure Surface - Initially Voided Band Material

```
*parameters
** istop, maxinum,iprint,iomsg, tolR,  tolKSI,  wc, flag,
       1,      -1,     0,    6, 1e-6,   500.0, 0.8,    1,   0
*mat_outside
**  EFLAG,   PFLAG,    YFLAG, RMAPFLAG,   HFLAG,    VFLAG,   TFLAG,  DFLAG
        1,       1,        1,        5,       4,        0,       0,      1
** STFLAG,       E,       NU,       q1,      q2,       q3,  SIGMA0,    KSI
        0, 70000.0,      0.3,    1.843,   0.768, 3.396649,   66.26,   0.01
**      T1,      Q1,       T2,       Q2,      T3,       Q3,THETAMIN,     W0
  2006.32,   62.00, 532.3966,   126.46,     0.0,      0.0,     0.0,    0.0
**      WN,      PN,       SN,       KS,      WC
      0.0,     0.0,      0.0,      0.0,     0.0,      0.0,     0.0,    0.0
*mat_inside
**  EFLAG,   PFLAG,    YFLAG, RMAPFLAG,   HFLAG,    VFLAG,   TFLAG,  DFLAG
        1,       1,        1,        5,       4,        0,       0,      1
** STFLAG,       E,       NU,       q1,      q2,       q3,  SIGMA0,    KSI
        0, 70000.0,      0.3,    1.843,   0.768, 3.396649,   66.26,  0.001
**      T1,      Q1,       T2,       Q2,      T3,       Q3,THETAMIN,     W0
  2006.32,   62.00, 532.3966,   126.46,     0.0,      0.0,     0.0,     0.00452
**      WN,      PN,       SN,       KS,      WC
      0.0,     0.0,      0.0,    0.000,     0.9,      0.0,     0.0,    0.0
*bands
** minphi,maxphi,mintheta,maxtheta, nphi, ntheta
      0.0,  90.0,    90.0,    90.0,   10,      0
*load_S
** strain, tps, triax, devang,load,   niter
   1.0e-5, 0.1, <<T>>,  <<L>>,   1, 1000000
*optimization
**  niter, dptol
       20,  1e-4
```

C.2 Failure Surface - Continuous Nucleation of Voids

```
*parameters
** istop, maxinum,iprint,iomsg, tolR,  tolKSI,  wc, flag,
       1,       -1,      0,     6, 1e-6,   500.0, 0.8,     1,    0
*mat_outside
**  EFLAG,   PFLAG,    YFLAG, RMAPFLAG,   HFLAG,    VFLAG,   TFLAG, DFLAG
        1,       1,        1,        5,       4,        0,       0,     1
** STFLAG,       E,       NU,       q1,      q2,       q3,  SIGMA0,   KSI
        0, 70000.0,      0.3,    1.843,   0.768, 3.396649,   66.26,  0.01
**     T1,      Q1,       T2,       Q2,      T3,       Q3,THETAMIN,    W0
  2006.32,   62.00, 532.3966,   126.46,     0.0,      0.0,     0.0,   0.0
**     WN,      PN,       SN,       KS,      WC
      0.0,     0.0,      0.0,      0.0,     0.0,      0.0,     0.0,   0.0
*mat_inside
**  EFLAG,   PFLAG,    YFLAG, RMAPFLAG,   HFLAG,    VFLAG,   TFLAG, DFLAG
        1,       1,        3,        5,       1,        0,       0,     8
** STFLAG,       E,       NU,    BETA1,   BETA2,    BETA3,  SIGMA0,     A
        0, 70000.0,      0.3,    1.843,   0.768, 3.396649,   66.26,     2
**    KSI,      T1,       Q1,       T2,      Q2,       T3,      Q3, THETAMIN
    0.001, 2006.32,    62.00, 532.3966,  126.46,      0.0,     0.0,   0.0
**     W0,      AN,      PHI,       FP,      FC,       WC,
      0.0,   0.002,     -1.0,  0.00452,     0.9,      0.9
*bands
** minphi,maxphi,mintheta,maxtheta, nphi, ntheta
      0.0,   90.0,   90.0,    90.0,   10,      0
*load_S
** strain, tps, triax, devang,load,   niter
   1.0e-5, 0.1, <<T>>,  <<L>>,   1, 1000000
*optimization
**  niter, dptol
       20,  1e-4
```

C.3 Proportional Loading - Initially Voided Band Material

```
*parameters
** istop, maxinum,iprint,iomsg, tolR,  tolKSI,  wc, flag,
       1,      -1,     0,     6, 1e-6,   500.0, 0.8,    1,   0
*mat_outside
**   EFLAG,    PFLAG,     YFLAG, RMAPFLAG,    HFLAG,     VFLAG,    TFLAG, DFLAG
         1,        1,         1,        5,        1,         0,        0,     1
** STFLAG,        E,        NU,       q1,       q2,        q3,  SIGMA0,   KSI
         0, 70000.0,       0.3,    1.843,    0.768,  3.396649,   66.26,  0.01
**      T1,       Q1,        T2,       Q2,       T3,        Q3,THETAMIN,    W0
   2006.32,    62.00,  532.3966,   126.46,      0.0,       0.0,      0.0,   0.0
**      WN,       PN,        SN,       KS,       WC
       0.0,      0.0,       0.0,      0.0,      0.0,       0.0,      0.0,   0.0
*mat_inside
**   EFLAG,    PFLAG,     YFLAG, RMAPFLAG,    HFLAG,     VFLAG,    TFLAG, DFLAG
         1,        1,         1,        5,        1,         0,        0,     1
** STFLAG,        E,        NU,       q1,       q2,        q3,  SIGMA0,   KSI
         0, 70000.0,       0.3,    1.843,    0.768,  3.396649,   66.26, 0.001
**      T1,       Q1,        T2,       Q2,       T3,        Q3,THETAMIN,    W0
   2006.32,    62.00,  532.3966,   126.46,      0.0,       0.0,      0.0,     0.00452
**      WN,       PN,        SN,       KS,       WC
       0.0,      0.0,       0.0,    0.000,      0.9,       0.0,      0.0,   0.0
*bands
** minphi,maxphi,mintheta,maxtheta, nphi, ntheta
       0.0, 360.0,      0.0,    90.0,   10,     10
*load_F
**   straininc, nload
        1.0e-5
*optimization
**   niter, dptol
        20,  1e-4
*output
<<S>>_mat_in.csv
*mat_output
<<S>>_mat_out.csv
```

C.4 Proportional Loading - Continuous Nucleation of Voids

```
*parameters
** istop, maxinum,iprint,iomsg, tolR,  tolKSI,  wc, flag,
       1,      -1,     0,    6, 1e-6,   500.0, 0.8,    1,   0
*mat_outside
**  EFLAG,   PFLAG,    YFLAG, RMAPFLAG,   HFLAG,    VFLAG,   TFLAG,  DFLAG
        1,       1,        1,        5,       4,        0,        0,      1
** STFLAG,       E,       NU,       q1,      q2,       q3,  SIGMA0,    KSI
        0, 70000.0,      0.3,    1.843,   0.768, 3.396649,   66.26,   0.01
**     T1,     Q1,       T2,       Q2,      T3,       Q3,THETAMIN,     W0
  2006.32,   62.00, 532.3966,   126.46,     0.0,      0.0,     0.0,    0.0
**     WN,     PN,       SN,       KS,       WC
      0.0,     0.0,      0.0,      0.0,     0.0,      0.0,     0.0,    0.0
*mat_inside
**  EFLAG,   PFLAG,    YFLAG, RMAPFLAG,   HFLAG,    VFLAG,   TFLAG,  DFLAG
        1,       1,        3,        5,       1,        0,        0,      8
** STFLAG,       E,       NU,    BETA1,   BETA2,    BETA3,  SIGMA0,      A
        0, 70000.0,      0.3,    1.843,   0.768, 3.396649,   66.26,      2
**    KSI,     T1,       Q1,       T2,      Q2,       T3,      Q3, THETAMIN
    0.001, 2006.32,    62.00, 532.3966,  126.46,      0.0,     0.0,    0.0
**     W0,     AN,      PHI,       FP,      FC,       WC,
      0.0,   0.002,     -1.0,  0.00452,     0.9,       0.9
*bands
** minphi,maxphi,mintheta,maxtheta, nphi, ntheta
      0.0, 360.0,     0.0,    90.0,   10,     10
*load_F
**  straininc, nload
       1.0e-5
*optimization
**  niter, dptol
       20,  1e-4
*output
<<S>>_mat_in.csv
*mat_output
<<S>>_mat_out.csv
```